



**Università
degli Studi
di Ferrara**

**DOTTORATO DI RICERCA IN
"FISICA"**

CICLO XXXII

COORDINATRICE Prof. Luppi Eleonora

RESEARCH ON THIN FILM HARD MATERIALS AND DEVELOPMENT OF A NON-COMMERCIAL
PHYSICAL VAPOR DEPOSITION SYSTEM FOR THE COATING OF TUNGSTEN CARBIDE
WIRE ROLLS

Settore Scientifico Disciplinare FIS/03

Dottorando

Dott. Azzolini Oscar

Tutore

Prof. Fiorentini Giovanni

Anni 2016/2019

Content

CONTENT	I
LIST OF ACRONYMS	V
ESTRATTO	VII
ABSTRACT	IX
INTRODUCTION	XI
CHAPTER 1: HARD COATINGS	13
CHAPTER 2: INTRODUCTION TO THE PLASMA DISCHARGE	21
CHAPTER 3: PHYSICAL VAPOUR DEPOSITION (PVD) PROCESS	25
3.1 MAGNETRON SPUTTERING SOURCES	27
3.2 REACTIVE MAGNETRON SPUTTERING	33
3.3 CATHODIC VACUUM ARC SOURCES	35
3.4 THIN FILM GROWTH	40
CHAPTER 4: INSTRUMENTATION	45
4.1 PVD SYSTEM PROTOTYPES	45
4.2 SEM AND EDS MICROANALYSIS	48
4.3 X-RAY DIFFRACTOMETER	49
4.4 CATHODIC VACUUM ARC SOURCE	50
4.5 MAGNETRON SPUTTERING SOURCE	53

CHAPTER 5: HARD COATINGS DEPOSITED VIA MAGNETRON SPUTTERING	55
5.1 TiN MAGNETRON SPUTTERING COATINGS	55
5.2 TiCN MAGNETRON SPUTTERING COATINGS	65
5.3 CONCLUSIONS OF MAGNETRON SPUTTERING COATINGS	68
CHAPTER 6: HARD COATINGS DEPOSITED VIA CATHODIC VACUUM ARC (CVA)	71
6.1 TiN CATHODIC VACUUM ARC COATINGS	71
6.2 TiCN CATHODIC VACUUM ARC COATINGS	73
6.3 CrCN CATHODIC VACUUM ARC COATINGS	76
6.4 CONCLUSION OF CATHODIC VACUUM ARC COATINGS	78
CHAPTER 7: WEAR RATE EVALUATION OF THE PVD COATINGS.	79
7.1 CONCLUSIONS OF THE WEAR RATE EVALUATION.	82
CHAPTER 8: MAGNETRON SPUTTERING SOURCE DESIGN	83
8.1 CONCLUSIONS OF THE MAGNETRON SPUTTERING SOURCE DESIGN.	93
CHAPTER 9: DEVELOPMENT OF A NON-COMMERCIAL PHYSICAL VAPOR DEPOSITION SYSTEM	95
9.1 THE VACUUM SYSTEM CHARACTERISTICS	95
9.2 THE DEPOSITION CHAMBER AND THE SAMPLE HOLDER	99
9.3 THE PROCESS POWER SUPPLIES.	108
9.4 EVALUATION OF THE OUTGASSING RATE OF THE PVD SYSTEM	110
9.5 CONCLUSIONS OF THE DEVELOPMENT OF A NON-COMMERCIAL PHYSICAL VAPOR DEPOSITION SYSTEM	112
CONCLUSIONS	115
ACKNOWLEDGMENTS	117

LIST OF FIGURES	119
LIST OF TABLES	123
BIBLIOGRAPHY	125
THESIS ANNEX	131

List of Acronyms

CAD: Computer Aided Design

CVA: Cathodic Vacuum Arc

CVD: Chemical Vapour Deposition

DC: Direct Current

EDS: Energy Dispersion Spectroscopy

FEM: Finite Element Method

HIPIMS: High Power Impulse Magnetron Sputtering

INFN: National Institute of Nuclear Physics

LNL: National Laboratories of Legnaro

MF: Magnetic Field

MGN: Magnetron

PVD: Physical Vapour Deposition

SEM: Scanning Electron Microscopy

SZD: Structure Zone Diagram

XRD: X-Ray Diffraction

Estratto

Il lavoro di dottorato descritto nella seguente tesi si focalizza sulla ricerca di ricoprimenti duri a film sottile depositati attraverso tecniche di deposizione fisica da fase vapore (PVD) e sullo sviluppo di un sistema PVD non commerciale per il rivestimento dei rulli in carburo di tungsteno utilizzati nell'industria del filo.

L'incremento della vita media dei rulli è l'obiettivo della ricerca e l'indicazione immediata sulla bontà delle soluzioni proposte durante questo lavoro di tesi è ottenuta attraverso il tasso di usura stimato con il test di una sfera strisciante su piano ("ball on flat test"). I risultati ottenuti suggeriscono che i rivestimenti duri depositati sulla superficie dei rulli riducono il valore del tasso di usura rispetto a quello ottenuto misurando solo il materiale di base puro. Questa prova è verificata per diversi materiali di base e rivestimenti di materiali duri. Il miglior rivestimento duro ottenuto è il CrCN depositato sul substrato EC10F, uno specifico carburo di tungsteno la cui composizione è riservata.

Lo sviluppo del sistema PVD non commerciale passa attraverso diversi passaggi, alcuni dei quali sono: la progettazione di una sorgente magnetron sputtering del secondo tipo (molto sbilanciata), l'adozione delle sorgenti ad arco catodico commerciali convalidate durante la ricerca sulla deposizione dei film sottili duri, la scelta del corretto sistema di pompaggio, l'uso di materiali specifici (compatibili con il vuoto) per la costruzione del sistema PVD e la procedura di pulizia più appropriata. La velocità di degassificazione ottenuta delle parti interne esposte al vuoto è pari a $6 \cdot 10^{-12} \text{ mbar} \cdot \text{l} \cdot \text{s}^{-1} \cdot \text{cm}^{-2}$ ed è paragonabile al valore tabulato per l'acciaio inossidabile AISI 316L (materiale della camera da vuoto).

Il risultato finale di questa tesi è una macchina PVD perfettamente funzionante e in grado di depositare film sottili di materiali duri che migliorano la durata dei rulli di laminazione prodotti per l'industria del filo.

Abstract

The PhD work described in the following thesis is focused on the research of thin film hard coatings deposited through physical vapor deposition (PVD) techniques, and the development of a noncommercial PVD system for the coating of the tungsten carbide rolls used in the wire industry.

The improvement of the lifetime of the rolls is the goal of the research and the immediate indication on the goodness of the solutions proposed during this work of thesis is obtained through a wear rate ball on flat test. The results suggest that the hard coatings deposited on the surface of the rolls decrease the wear rate value respect to the one obtained measuring only the pure base material. This evidence is verified for different base materials and coatings. The best hard coating obtained is the CrCN deposited on the EC10F substrate, a specific tungsten carbide whose composition is confidential.

The development of the noncommercial PVD system passes through different steps, some of these are: the design of a custom magnetron sputtering source of the second type (very unbalanced), the adoption of the commercial cathodic vacuum arc sources validated during the thin film research, the choice of the correct pumping system, the use of the specific materials (vacuum compatible) for the PVD system construction and the right cleanliness procedure. The obtained outgassing rate of the internal parts exposed to the vacuum is equal to $6 \cdot 10^{-12} \text{ mbar} \cdot \text{l} \cdot \text{s}^{-1} \cdot \text{cm}^{-2}$ and it is comparable with the tabulated value for the stainless steel AISI 316L (material of the vacuum chamber).

The result of this thesis is a PVD machine perfectly working and capable to deposit thin films of hard materials that improve the lifetime of the wire rolls produced for the wire industry.

Introduction

The present work of thesis is the result of the collaboration between the National Institute of Nuclear Physics (INFN) and the Eurolls s.p.a. regulated under the technology transfer contract n° TTA_16LNL_039. The Eurolls company was founded in 1987 by Renato Railz and has its headquarter in the Friuli Region of Italy. The production plants are located in different part of the World: Italy, Mexico, Brazil and China. Since its inception, Eurolls's activity was concentrated on two different fields of applications, the Tube Industry and the Wire Industry base of the research activity of this work of thesis.

The wire rolls are the pulsing heart of the modern wire industry (see Figure 1), they are commonly mounted in special rolling cassettes (see Figure 2) to produce wires with specific dimensions and shapes starting from another wire made of a wide range of base materials essentially discriminated for their hardness. The possibility of rolling more sophisticated materials and improve the lifetime of the wire rolls adopted for the lamination processes, are always a new challenge for this industry. This work tries to give an answer to this necessity, identifying the materials to apply on the surface of the rolls deposited as a thin layer and determining the right physical vapour deposition technology to produce these coatings.



Figure 1: tungsten carbide wire rolls¹.

The wire rolls, base of this research, are the tungsten carbide (WC) wire rolls made of a bulk material with 2350 HV of hardness. For this physical property, the choice of the coating to investigate fell back on the hard materials that present a similar value of hardness and widely used in the machining industry as the nitride and carbonitride of transition metals i.e. TiN (2100 HV), TiCN (3260 HV) and CrCN (2300 HV). The modern PVD industry can produce the thin film coatings essentially adopting two PVD technologies, that are extremely different, due to their opposite regimes of plasma discharge, which are the magnetron sputtering and the cathodic vacuum arc techniques. These two techniques are investigated in this work of thesis in order to determine the best technology to apply for the thin film deposition on the WC rolls. The experimental part of the thesis presents in fact a section dedicated to the deposition of the hard coatings with different PVD technologies, that are discriminated through the wear rate test.

The work of thesis also presents, in parallel to the research activity on the thin film deposition, the development of a noncommercial PVD system, that is currently used from the Eurolls company to deposit the WC rolls with the hard materials, already identified during this research and others new not reported here. This part of the thesis is fundamental as the research part, because the characteristics of the PVD system determine the coating properties from the point of view of the composition and the crystal structure of the material obtained. In fact, the PVD deposition is for example function of the vacuum level reached before the process, of the PVD source adopted for the coating deposition and of the typology and the grade of unbalancing of the magnetron sputtering source.

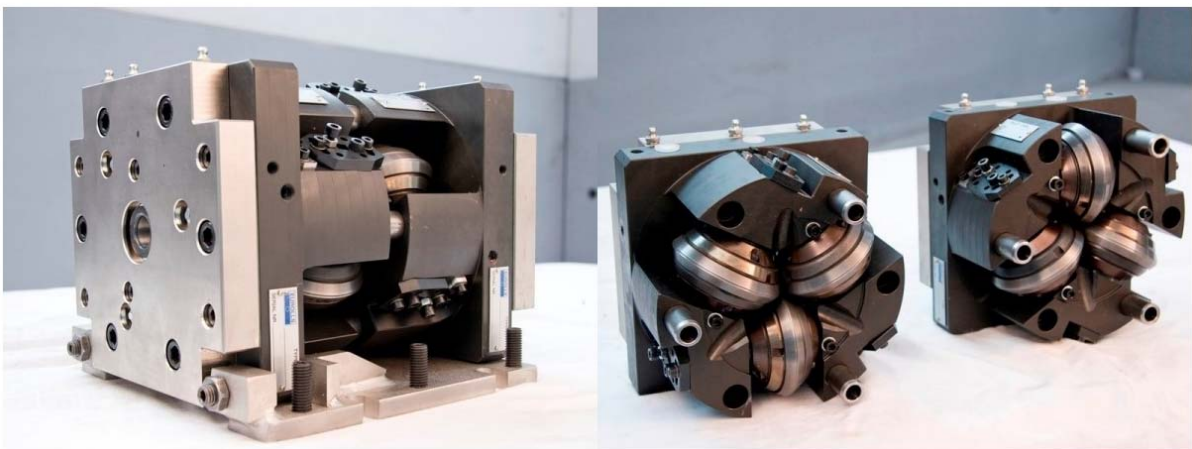


Figure 2: wire rolling cassettes².

Chapter 1: Hard Coatings

The demands of design and production engineers pushed the search of new materials with significantly improved properties. In recent years many new materials have been synthesized, characterized and put into use. In the industrial environment, the protection of tools by hard coatings plays one of the most important roles, by means of improving component performance and working life essentially mitigating the wear resistance and increasing the hardness of the material.

There are two main ways to apply these materials on the industrial components: the first one is to create the component directly with the hard material and the second one is to apply the hard coating in a thin layer on the component made of a different base material. This last option is of course the most interesting, for the cost production and the machining of the components. In fact, it is much simpler machining a steel component and then deposit a hard coating on it, instead of machining directly the same component made of a hard material. Moreover, a large improvement in the life of a cutting tool or a drilling tool (often more than 10 times) after coating with a hard material (eg. TiN), for a fraction of the cost of the tool, has been widely reported in literature³.

The techniques used to create these thin layers usually start from vapour phase and are classified in chemical deposition CVD (Chemical Vapour Deposition) and physical deposition PVD (Physical Vapour Deposition), in function of the bonds between the coating and the surface of the components.

The hard materials applied with coatings can be divided in three groups dependent on the chemical bonding character: metallic hard materials (borides, carbides, and nitrides of the transition metals), covalent hard materials (borides, carbides, and nitrides of Al, Si, and B, as well as diamond), and ionic hard materials (oxides of Al, Zr, Ti, and Be), as resumed in Table 1.

TABLE 1: CLASSIFICATION OF VARIOUS HARD MATERIALS IN FUNCTION OF THE CHEMICAL BOND⁴.

<i>Metallic</i>	<i>Covalent</i>	<i>Ionic</i>
<i>Borides</i> <i>Carbides</i> <i>Nitrides of the transition metals</i>	<i>Borides</i> <i>Carbides</i> <i>Nitrides of Al, Si, B,</i> <i>Diamond</i>	<i>Oxides of Al, Zr, Ti, Be</i>
<i>e.g.</i> <i>TiB₂, TiC, TiN,</i> <i>VC, WC</i>	<i>e.g.</i> <i>B₄C, SiC, BN</i>	<i>e.g.</i> <i>Al₂O₃, ZrO₂, BeO</i>

The field of application and the physical properties of various representatives of these three groups of hard materials as elastic moduli, thermal expansion coefficients, melting point compatibility and hardness are reported in the Tables 3,4 and 5.

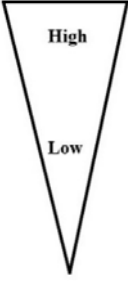
Analyzing in detail the values reported in these tables it is easy to understand how all the compounds stand out for their high hardness and high melting points, while the modulus of elasticity of the ionic hard materials respect to covalent and metallic is the lowest. Moreover, pointing the attention on the linear thermal expansion coefficient, it increases in general from covalent to metallic and ionic hard materials.

Resuming these data, it is possible to give some statements:

1. Each of the different groups of hard materials show advantages and disadvantages in respect of an application as hard coating.
2. The metallic hard materials seem to be the most suitable and versatile layers substances.
3. Ionic hard materials are suitable for the surface, because of high stability and low interaction tendency.
4. Optimum wear resistance can only be achieved by multiphase or multi-layer coatings

Moreover, considering the amount of data reported in these tables, an intuitive and schematic way of comparing all these coating properties is reported in Table 2.

TABLE 2: PROPERTIES AND BEHAVIOR OF VARIOUS GROUPS OF HARD MATERIALS (M = METALLIC; C = COVALENT; I = IONIC)⁵.

Level	Hardness	Brittleness	Melting Point	Stability -ΔG	Thermal Expansion Coefficient	Adherence to Metallic Substrates	Interaction Tendency	Multilayer Suitability
	C	I	M	I	I	M	M	M
	M	C	C	M	M	I	C	I
	I	M	I	C	C	C	I	C

From this table it is easy to understand that the optimal performance of the hard coating with high hardness and high wear resistance can be achieved only with the combination of different hard materials. This means that high abrasion resistance is not only due to high hardness. In fact, as reported in literature, B₄C is the material with the highest hardness, whereas a B₄C containing composite material with lower hardness has three times better abrasion resistance⁴. From the bibliographic research done for this work, I can assume that it does not exist a single hard material that can solve all the problems of the modern industry and that exist different ways to improve/optimize the properties of a hard material.

One method is to substitute the metal lattice of the compound phase with another compatible metal, e.g. in TiN the lattice of Ti is partly substituted by Al, V, Zr or Hf. Another method is to vary the relative concentrations of the non-metallic elements. By doing so, the valence electron concentration (VEC) of the phase changes and thus its mechanical and physical properties change too. As reported in Figure 3 the microhardness values of certain carbides, mixed carbides and carbonitrides vary in function of VEC passing through a maximum. When the VEC value is around 8.4 the coating reached the highest value of hardness, that is related with the highest number of bonds in the material (higher hardness = higher number of bonds). For other properties such as toughness, chemical stability and wear resistance similar diagrams as a function of VEC should be obtained. Considering a single

nitride, depending on the concentration of nitrogen, the properties of the nitride vary. For example, in TiN_x , the value of x determines mechanical and physical properties and as reported in Figure 3 to obtain a TiN coating with the highest hardness, the material deposited has to be under stoichiometric of nitrogen.

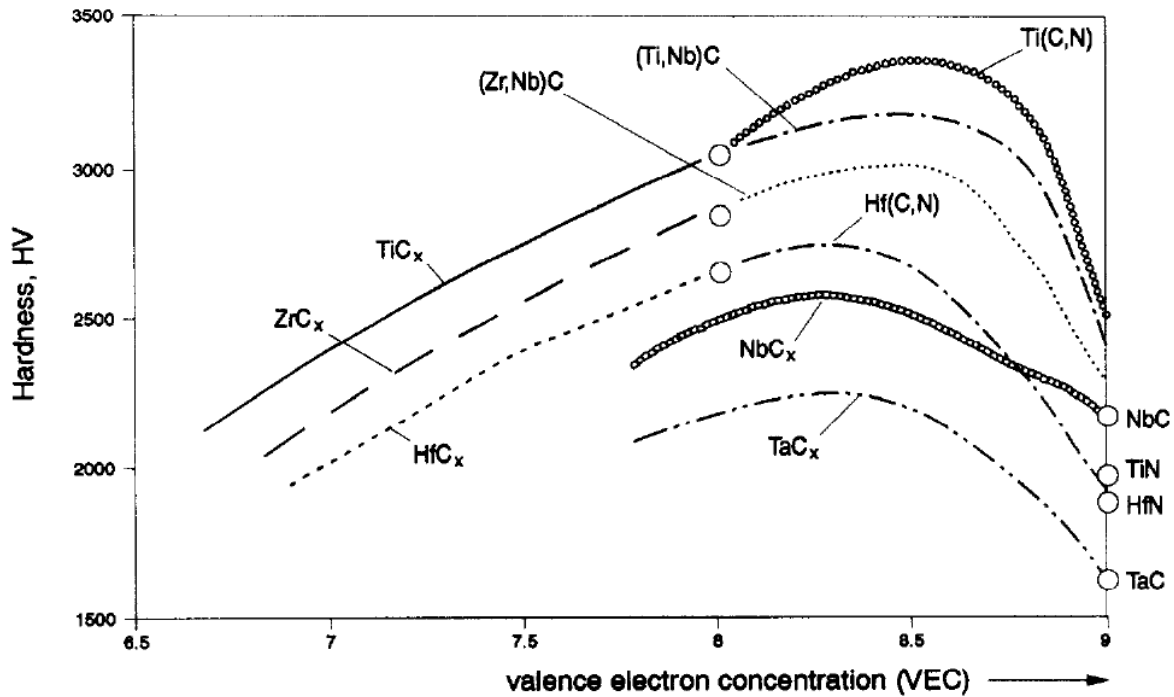


Figure 3: Microhardness of carbides, mixed carbides or carbonitrides as a function of the valence electron concentration⁴.

The last method to optimize the properties of the material deposited is the combination of different hard coatings in a composite or a multilayer structure, mixing the properties of the single material used. The possibility of mixing different materials with different properties is of course an innovative solution, but at the same time it opens another field of discussion. There are different ways to mix two different materials and the results is a material with different structures and interfaces as reported in Figure 4. In this work the important structures to be considered are the ones related with the PVD coatings, that are the multilayer and gradient structures.

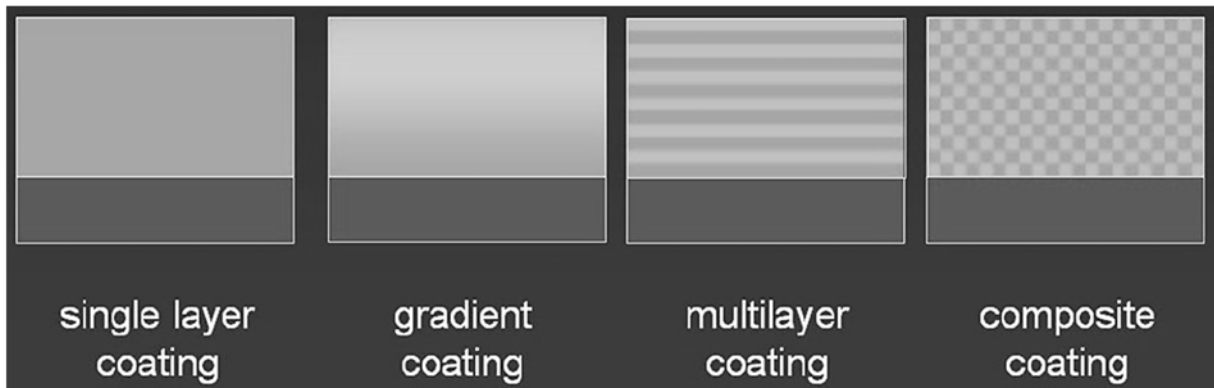


Figure 4: Schematic illustration of the structure of different types of coating.

The difference between the two structures is essentially the interface: in the case of multilayer the deposition of different hard materials follows a sequence predetermined and the result is a structure with sharp interfaces. This structure could present lack of adhesion considering the physical properties of the single hard material deposited. A way to avoid this problem of the PVD multilayer coatings is mixing the interfaces, creating a gradient of material during the transition between one and the other layer of hard material. This effect can be reached depositing simultaneously (co-deposition) the bilayer materials obtaining a gradient structure as reported in Figure 4.

TABLE 3: CARBIDES, NITRIDES, OXIDES AND BORIDES EMPLOYED TO RESIST CORROSION AND WEAR ⁶.

Carbides	Nitrides	Oxides	Borides
Corrosion-resistant ceramics			
SiC	Si ₃ N ₄ , Sialon	Al ₂ O ₃	TiB ₂
HfC	HfN	SiO ₂	MoB
ZrC	ZrN	TiO ₂	WB
	TiN	ZrO ₂	NbB ₂
		SnO ₂	TaB ₂
		MgAl ₂ O ₄	ZrB ₂
		MgO	HfB ₂
		CrO ₂	
Tribological ceramics			
TiC	TiN	Al ₂ O ₃	TiB ₂
HfC	HfN	SiO ₂	MoB
ZrC	Si ₃ N ₄	TiO ₂	WB
SiC	BN	ZrO ₂	NbB ₂
B ₄ C	ZrN	TaO ₂	TaB ₂
B ₂ C	TaN	Cr ₂ O ₃	ZrB ₂
W ₂ C	AlN	HfO ₂	HfB ₂
Cr ₇ C ₃	VN	V ₂ O ₃	VB
Cr ₃ C ₂	NbN		
Cr ₂₃ C ₆			
TaC			
VC			
NbC			
WC			

TABLE 4: PROPERTIES OF METALLIC HARD MATERIALS

Phase	Density (g/cm ³)	Melting Point (°C)	Hardness (HV)	E Modulus (kN/mm ²)	Spec. el. Resistivity (μΩ cm)	Thermal exp. coeff. (10 ⁶ K ⁻¹)
TiB ₂	4.50	3225	3000	560	7	7.8
TiC	4.93	3067	2800	470	52	8.0-8.6
TiN	5.40	2950	2100	590	25	9.4
ZrB ₂	6.11	3245	2300	540	6	5.9
ZrC	6.63	3445	2560	400	42	7.0-7.4
ZrN	7.32	2982	1600	510	21	7.2
VB ₂	5.05	2747	2150	510	13	7.6
VC	5.41	2648	2900	430	59	7.3
VN	6.11	2177	1560	460	85	9.2
NbB ₂	6.98	3036	2600	630	12	8.0
NbC	7.78	3613	1800	580	19	7.2
NbN	8.43	2204	1400	480	58	10.1
TaB ₂	12.58	3037	2100	680	14	8.2
TaC	14.48	3985	1550	560	15	7.1
CrB ₂	5.58	2188	2250	540	18	10.5
Cr ₃ C ₂	6.68	1810	2150	400	75	11.7
CrN	6.12	1050	1100	400	640	2.3
Mo ₂ B ₅	7.45	2140	2350	670	18	8.6
MoC	9.18	2517	1660	540	57	7.8-9.3
W ₂ B ₅	13.03	2365	2700	770	19	7.8
WC	15.72	2776	2350	720	17	3.8-3.9
LaB ₆	4.73	2770	2530	400	15	6.4

TABLE 5: PROPERTIES OF COVALENT HARD MATERIALS

Phase	Density (g/cm ³)	Melting Point (°C)	Hardness (HV)	E Modulus (kN/mm ²)	Spec. el. Resistivity (μΩ cm)	Thermal exp. coeff. (10 ⁶ K ⁻¹)
B ₄ C	2.52	2450	3 - 4000	441	0.5x10 ⁶	4.5(5.6)
BN (Cub.)	3.48	2730	5000	660	10 ¹⁸
C (Diamond)	3.52	3800	8000	910	10 ²⁰	1.0
B	2.34	2100	2700	490	10 ¹²	8.3
AlB ₁₂	2.58	2150	2600	430	2x10 ¹²
SiC	3.22	2760	2600	480	10 ⁵	5.3
SiB ₆	2.43	1900	2300	330	10 ⁷	5.4
Si ₃ N ₄	3.19	1900	1720	210	10 ¹⁸	2.5
AlN	3.26	2250	1230	350	10 ¹⁵	5.7

TABLE 6: PROPERTIES OF IONIC HARD MATERIALS

Phase	Density (g/cm ³)	Melting Point (°C)	Hardness (HV)	E Modulus (kN/mm ²)	Spec. el. Resistivity (μΩ cm)	Thermal exp. coeff. (10 ⁶ K ⁻¹)
Al ₂ O ₃	3.98	2047	2100	400	10 ²⁰	8.4
Al ₂ TiO ₅	3.68	1894	13	10 ¹⁶	0.8
TiO ₂	4.25	1867	1100	205	9.0
ZrO ₂	5.76	2677	1200	190	10 ¹⁶	11 (7.6)
HfO ₂	10.2	2900	780	6.5
ThO ₂	10.0	3300	950	240	10 ¹⁶	9.3
BeO	3.03	2550	1500	390	10 ²³	9.0
MgO	3.77	2827	750	320	10 ¹²	13.0

Chapter 2: Introduction to the Plasma Discharge

The plasma discharge characteristic of the Physical Vapour Deposition (PVD) processes is generated applying a difference of potential between two metal electrodes immersed in a low-pressure gas. When the voltage applied is enough high, the neutral gas atoms (usually argon or krypton) are ionized. The plasma starts when a stray electron is accelerated toward the anode by the applied electric field. Reached the ionization energy the electron impacts with a neutral gas atom extracting a second electron and converting the neutral gas atom into a positively charged ion (A^+). The ionization process can be summarized with the following equation:



The two electrons produced during the ionization are now accelerated and bombard two additional neutral gas atoms, generating more ions and electrons in an avalanche process. The electric field applied between the two electrodes drives the positive ions in the opposite direction respect to the electron to collide with the cathode. These hints simultaneously generate different physical processes including the sputtering of the target atoms and secondary electrons emission that is fundamental for the maintenance of the plasma discharge.

The breakdown occurs when the distance (d) between the electrodes is enough large to accelerate the electrons and reach the necessary level of energy for the ionization cascade. Townsend equation describes mathematically the ionization process⁷:

$$i_0 = i_0 \frac{e^{\alpha d}}{[1 - \gamma_e (e^{\alpha d} - 1)]} \quad \text{Equation 2}$$

Where i_0 is the initial current; α represents the probability per unit length of ionization occurring during an electron-gas atom collision and is called Townsend ionization coefficient; γ_e is the Townsend secondary-electron emission coefficient and is defined as the number of secondary electrons emitted at the cathode per incident ion.

The breakdown voltage (voltage in which appears the plasma discharge) is usually expressed calculating the equation proposed in the Paschen Law. Where the mean free path is related to the ionization probability α , and the critical breakdown voltage can be expressed in terms of a product of the pressure of the system and the interelectrode distance as following:

$$V_B = \frac{APd}{\ln(Pd)+B} \tag{Equation 3}$$

In the Paschen Law A and B are considered constants and plotting the potential obtained from the equation in function of the P·d product we can obtain a curve as reported in Figure 5, and for different gases the curve is different due to the different ionization constant.

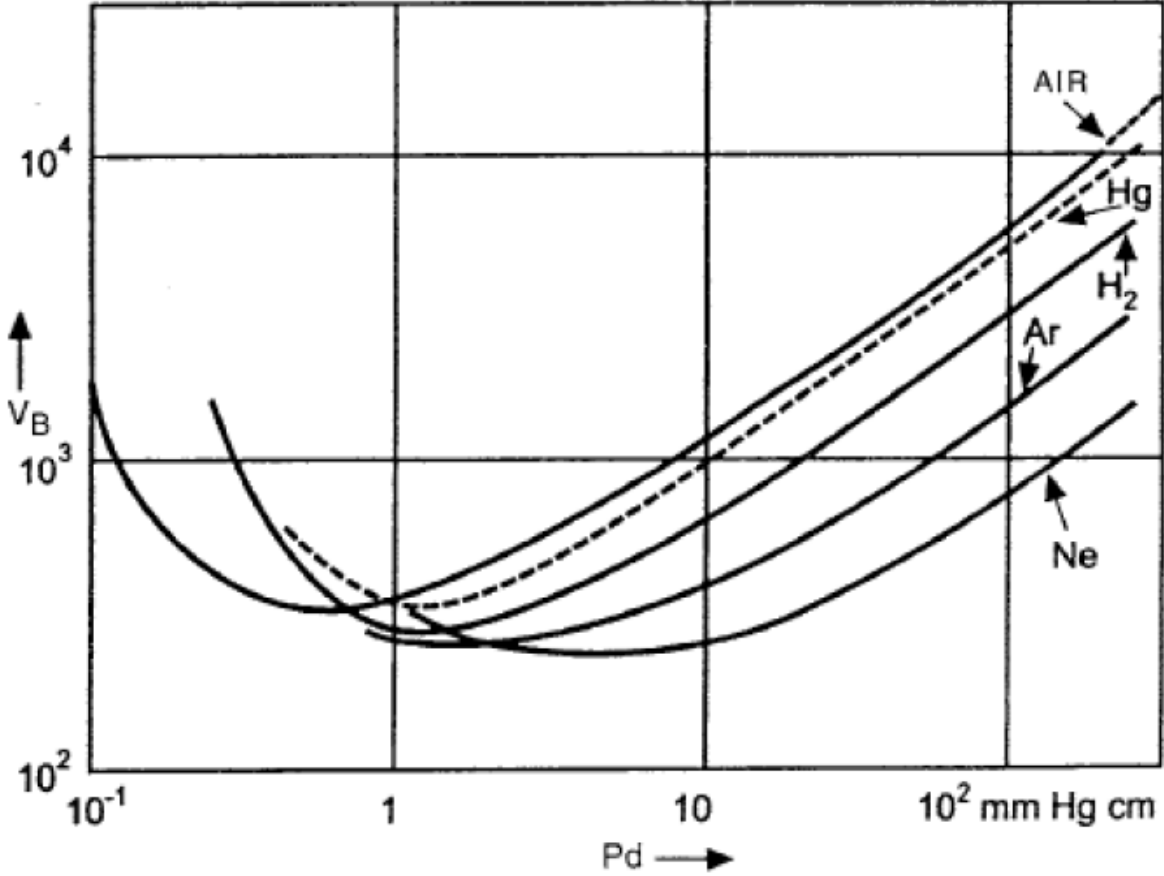


Figure 5: Paschen curve for a number of gases.

A typical sputtering configuration presents a fixed distance between the electrodes. Looking at the Paschen curve it is possible to note the existence of a minimum voltage to

maintain the discharge and two ends at very high potential. This phenomenon can be explained considering what happens in the two ends: at low values of pressure, there are few gas atoms for the electron-gas collisions and the secondary electron yield is too low to sustain the discharge. On the other hand, at high pressures, there are a lot of collisions, and the electrons mean free path is too short to acquire enough energy and the gas ionization is quenched. Similar considerations can be done for the cathode-anode distance d . Therefore, at either extreme of the Paschen curve, the ion generation rates are low and high voltages are required to sustain the discharge. In between, at typically a few hundred to a thousand volts, the discharge is self-sustaining.

The plasma discharge that occurs between two electrodes is well described from the I-V characteristic curve. The characteristic I-V curve describes how the current change in function of the variation of the difference of potential applied on two parallel plate at fixed distance in vacuum. Analyzing the graph reported in Figure 6 we can identify four specific zones:

1. The first part of the graph presents a very small current initially flowing through the electrodes due to the small number of ions generated in the system. With charge multiplication, the current increases rapidly, but the voltage remains quite constant (Zone 1: Townsend discharge).
2. When electrons produce enough ions to regenerate the same number of initial electrons, the discharge becomes self-sustaining. At this point the voltage drops accompanied by a sharp rise in current and normal glow occurs (Breakdown Voltage). Immediately after the breakdown the plasma shape on the cathode is not uniform but concentrated near the edges or at other surface irregularities. Increasing the power, the plasma increases its shape (the current increase while the voltage remains constant) until the cathode is completely covered (Zone 2: Normal discharge).
3. A further increase in power results in both voltage and cathode current increasing. This zone represents the operative domain for sputtering and other discharge processes such as plasma etching (Zone 3: Abnormal discharge).

- Increasing the power, the cathode can not dissipate the heat anymore. Now, thermionic emission of electrons exceeds the secondary-electron emissions and high current with low-voltage arcs propagate on the cathode (Zone 4: Arc discharge).

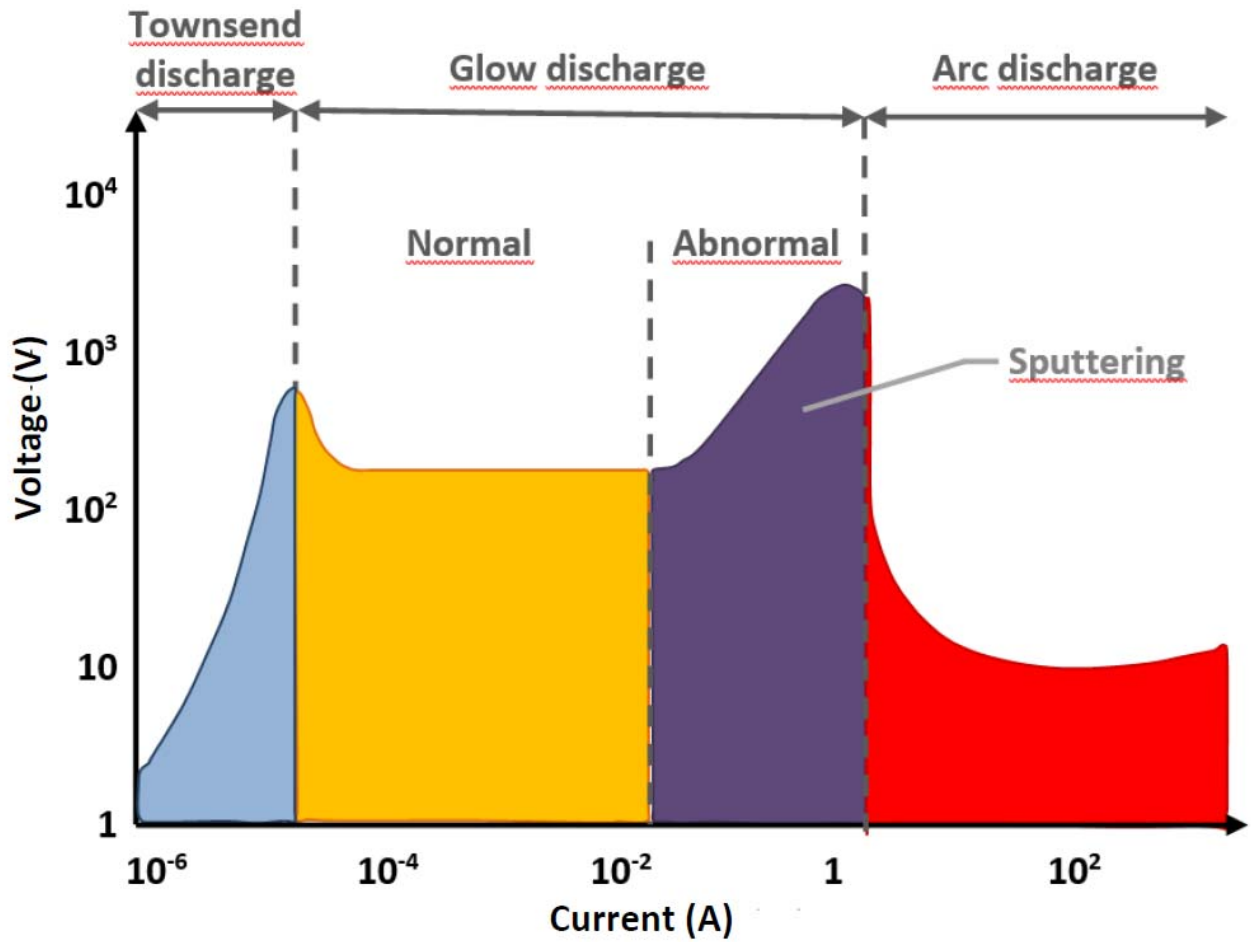


Figure 6: Characteristic I-V curve of an electrical discharge in vacuum⁸.

Chapter 3: Physical Vapour Deposition (PVD) Process

Physical vapour deposition (PVD) is a well-known technology that is widely used for the deposition of thin films regarding many demands, namely tribological behavior improvement, optical enhancement, visual/esthetic upgrading, and many other fields, with a wide range of applications already being perfectly established. The term “physical vapour deposition” appeared only in the 60s. At that time, the evolution of vacuum coating processes was needed, which was carried out through the development of well-known technologies, such as sputtering, vacuum, plasma technology, magnetic fields, gas chemistry, thermal evaporation and power sources control, as described in detail in Powell’s book⁹. In the last decades, the development of PVD deposition technologies has been focused essentially on the coating of tools, considering the strong evolution of the computer numerical control (CNC) machining processes, since new machining approaches have arisen. PVD technique is a thin film deposition process in which the coating grows on the substrate atom by atom. PVD entails the atomization or vaporization of material from a solid source, usually called target. Thin films usually have layers with thicknesses as thin as some atomic layers to films with several microns. This process causes a change in the properties of the surface and the transition zone between the substrate and the deposited material. On the other hand, the properties of the films can also be affected by the properties of the substrate. The atomic deposition process can be made in a vacuum, gaseous, plasma, or electrolytic environment. Moreover, the vacuum environment in the deposition chamber will reduce the gaseous contamination in the deposition process to a very low level¹⁰.

PVD is an atomistic deposition process in which there is a physical discharge of atoms or molecules and condensation and nucleation of these atoms onto a substrate through a vacuum or low pressure gaseous or plasma environment. Plasma or ions are usually the constituents of the vapour phase. Sometimes, the reactive gas can be introduced to the vapour during the deposition process and this is called reactive deposition. The atoms or molecules are conveyed in the form of a vapour via a vacuum or low pressure gaseous or plasma environment to the surface of the substrate for condensation to take place. Commonly, PVD processes are used to deposit thin films with thickness in the range of a few nanometers to a thousands of nanometers. The flexibility and adaptability of PVD to the market demands led to the development and the improvement of techniques for the various processes and thus multiple variants have arisen, some of them presented in Figure 7. These techniques are constantly evolving and continue to be inspiration source for many studies and developments. Sputtering (or cathodic spraying) and Evaporation are the most commonly used PVD methods for thin film deposition.

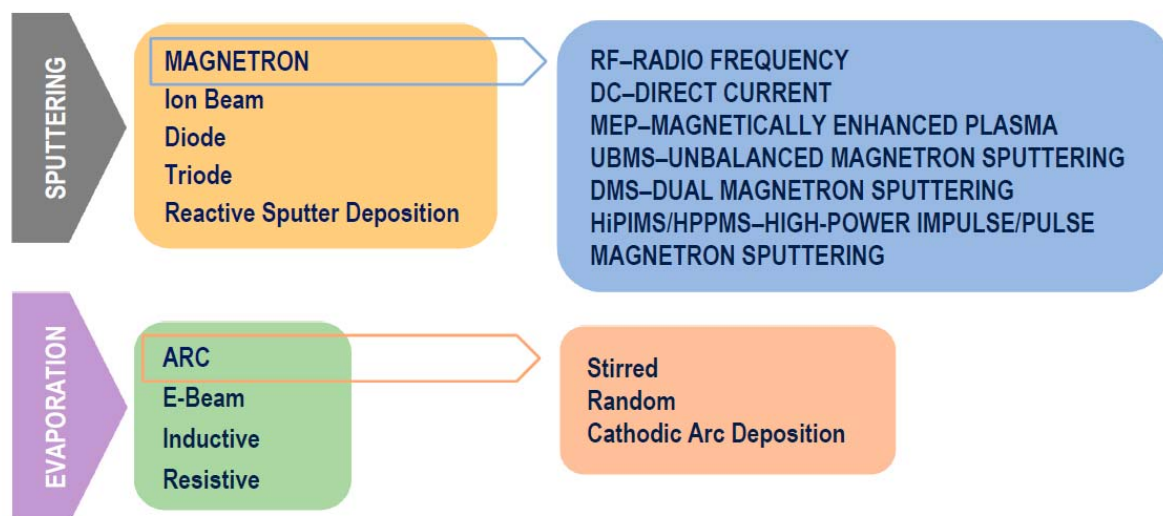


Figure 7: current physical vapour deposition (PVD) techniques for advanced coatings¹¹.

3.1 Magnetron sputtering Sources

Speaking about sputtering, we can simply consider two electrodes in vacuum (with a partial pressure of argon) powered with an opposite potential. This kind of sputtering, that represents the simpler process, is named diode sputtering. During the diode sputtering process, a target (cathode) plate is bombarded by energetic ions generated in a glow discharge plasma in front of the target. The bombardment process causes the removal (sputtering) of target atoms, forming a vapour, which may then condense on all the cold surfaces of the vacuum chamber and substrate, as a thin layer. The secondary electrons are emitted from the target surface as a result of the ion bombardment and they play an important role in maintaining the plasma discharge, in fact without secondary electrons the discharge is limited to the free electrons and the cathode current density can not reach a value sufficient for the sputtering phenomenon. The diode sputtering process has been developed for many years and different materials have been successfully deposited using this technique. However, this process was limited by low deposition rates, low ionization rate of the plasma, and high substrate heating effects due to the electrons bombardment. These limitations have been overcome by the development of magnetron sputtering. In the magnetron sources, a magnetic field configured parallel to the target surface can constrain secondary electron motion to the vicinity of the target, increasing the ionization probability of the argon gas. The magnets are arranged in special configuration, where one magnet pole is positioned at the central axis of the target and the second magnet pole (opposite to the previous) forming a ring around the outer edge of the target. This configuration, where all the magnetic lines born and die on the surface of the cathode, traps the electrons in specific zones of the cathode surface named plasma racetracks. The increased ionization efficiency of a magnetron results in a dense plasma near the target region. This leads to increased ion bombardment of the target, giving higher sputtering rates and, therefore, higher deposition rates at the substrate. In addition, the increased ionization efficiency achieved in the magnetron mode allows the discharge to be maintained at lower operating pressures (typically, $\sim 10^{-3}$ mbar, compared to $\sim 10^{-2}$ mbar) and lower operating voltages (typically, ~ 500 V, compared to $\sim 2-3$ kV of the diode sputtering) than it is possible in diode sputtering mode.



Figure 8: plasma of a magnetron sputtering rectangular source¹².

The magnetron sputtering sources present opposite magnets arranged in specific configuration to confine the plasma near the cathode surface, moreover the intensity of the magnetic field of the single magnets is fundamental to identify the typology of magnetron source used. The magnetrons can be divided in different types of sources as represented in Figure 9, in function of the difference in intensity between the inner and outer magnets.

We can classify them in:

1. Balanced

2. Unbalanced first type
3. Unbalanced second type

The difference in performance between the two types of magnetron is very significant. In a balanced magnetron the plasma is strongly confined to the target region. A region of dense plasma typically extends some 60 mm from the target surface. Films grown on substrates positioned within this region are subjected to concurrent ion bombardment, which strongly influences the structure and properties of the coating. Substrates placed outside this region, however, will lie in an area of low plasma density. Consequently, the ion current drawn at the substrate (typically $< 1 \text{ mA/cm}^2$) is generally insufficient to modify the structure of the thin film. The energy of the bombarding ions can be increased by increasing the negative bias applied to the substrate. However, this can introduce defects in the film structure, and it increases the residual film stress. Obviously, this effect is detrimental for the thin film properties. Thus, it is difficult to deposit fully dense films on large, or complex components using conventional magnetrons¹³. To Grow dense films without introducing excessive intrinsic stresses a high flux ($> 2 \text{ mA/cm}^2$) of relatively energy ($< 100 \text{ eV}$) ions is generally preferred¹⁴ as reported in literature. These conditions can be reached easily, working with magnetron sources in unbalanced configuration of second type.

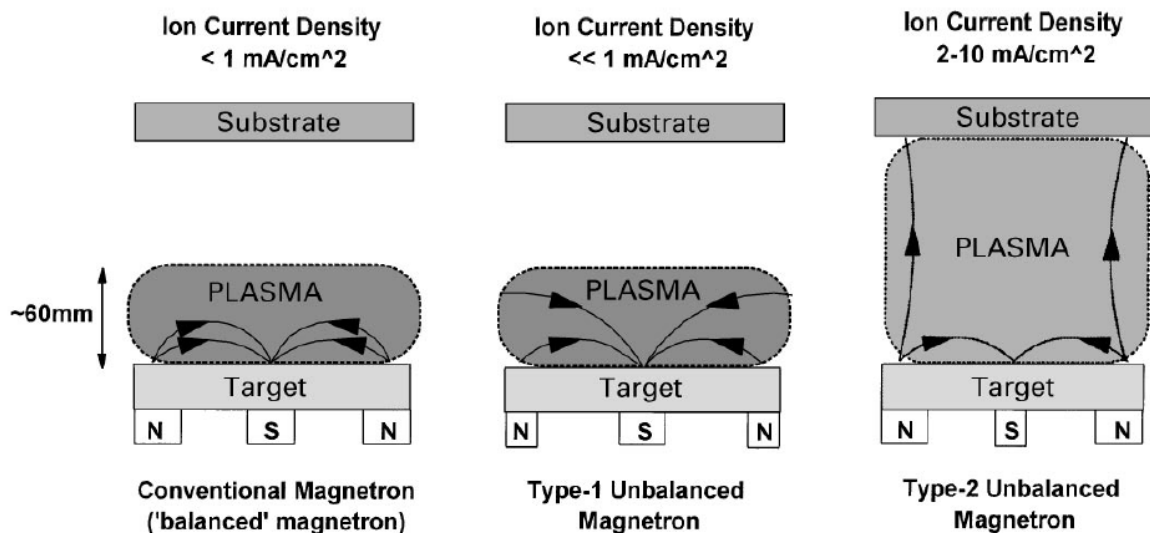


Figure 9: Schematic representation of the plasma confinement observed in balanced and unbalanced magnetrons¹⁵.

In an unbalanced magnetron sputtering system, either the central magnet or the outer magnets are stronger than other, so there are magnetic lines that extend into outer space. Electrons in a magnetron follow magnetic field lines, so when there are these unclosed lines, electrons which follow them get lost from target vicinity. When the central magnet is stronger (unbalanced of the first type) the electrons get lost from plasma radially, while in case when the outer magnets are stronger (unbalanced of the second type), there are electrons that end up close to the substrate. This last configuration leads to ionization events close to the substrate, so there is some ion bombardment of the substrate. Window and Savvides¹⁶ found that the ion flux on the substrate for a type II can be as high as the flux of sputtered atoms (or even up to 10 times higher), while for a Type I magnetron it is only 0.025 % of the atom flux. The second type unbalanced magnetron moves the plasma to substrate driving a higher number of electrons and consequently ions (electrostatically attracted) on the surface of the sample. This effect provides additional heating of the substrate, which assists the deposition process and facilitates the chemical reaction ¹⁷ e.g. nitridation or carbonization during the reactive sputtering deposition.

Until now the unbalanced magnetron sputtering sources are described only qualitatively focusing the attention just on the high difference of magnitude between the internal and the external magnet pack. Nowadays the magnets cover a wide range of possible magnetic fields and for this reason the magnets combinations in an unbalanced setup is quite large. A quantitative measurement of the grade of unbalancing of the magnetron sputtering source was proposed from Brown and Bellido-Gonzalez of Gencoa¹⁸. They introduced a coefficient g that is related with the magnetic field component perpendicular to the cathode surface (B_z) and the radius of the target (R_T) as indicated in the following equation:

$$g = \frac{B_z}{R_T} \qquad \text{Equation 4}$$

According to the value obtained it is possible to establish what is the level of unbalancing of the magnetron sputtering source consulting the Table 7.

TABLE 7: TYPES OF BALANCED AND UNBALANCED MAGNETRONS AS CLASSIFIED BY GENCOA¹⁸.

Type	Group Description	g coefficient
I	Extremely balanced	$g \geq 2,00$
II	Very balanced	$1,75 \leq g < 2,00$
III	Medium balanced	$1,50 \leq g < 1,75$
IV	Unbalanced	$1,25 \leq g < 1,50$
V	Very unbalanced	$1,00 \leq g < 1,25$
VI	Extremely unbalanced	$g < 1,00$

Following back to the magnetic field, it is introduced into the magnetron sputtering source in order to confine electrons close to the target surface, so that they are not able to escape the target vicinity and increase the ionization probability, but it has been shown by Goree and Sheridan¹⁹ that the magnetic field should not be too strong. With the increase of $B_{max} r$ (which is a maximum value of MF component that is tangential to the target) the average number of ionizations per electron was growing until at some point it reached the saturation. The point at which the average number of ionizations is saturated is when for most of electrons all the energy is lost during the collisions in plasma. After that point the increase of magnetic field strength will lead to higher confinement of electrons which, in its turn, will only make the erosion profile smaller, but will not lead to more ionizations. Goree and Sheridan found a dimensionless parameter β and showed that the saturation begins when β is higher than 15 as reported in Figure 10.

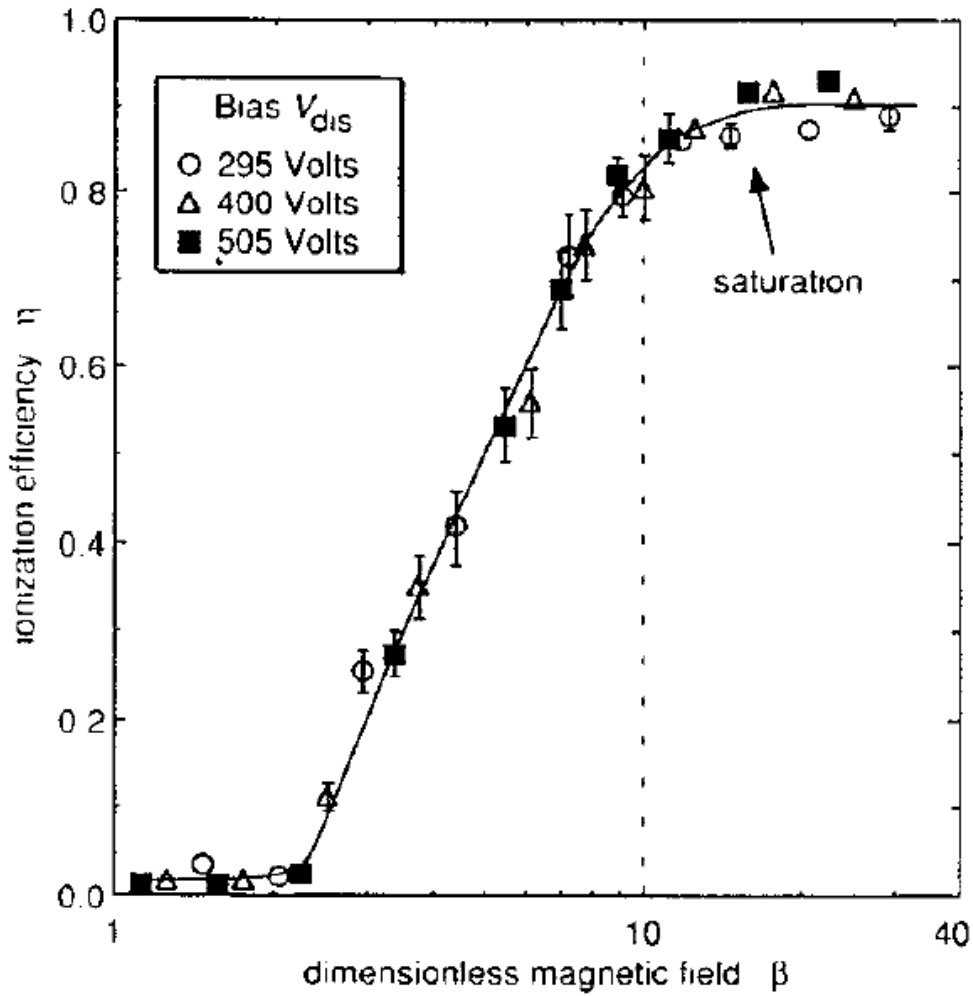


Figure 10: dependence of the ionization efficiency η on the dimensionless parameter β ¹⁹.

The dimensionless parameter β introduced from Goree and Sheridan¹⁹ is calculated as follows:

$$\beta = \sqrt{\frac{e_c}{2m_e} \frac{a}{\sqrt{U_c}} B_r^{max}} \quad \text{Equation 5}$$

Where e_c is the elementary charge, m_e is the mass of electron, a is the radius of maximum erosion (the radius of the racetrack), U_c is the cathode potential (i.e. discharge voltage), and $B_{r_{max}}$ is the maximum of the radial component of the magnetic field on the surface of the cathode. A typical value of B_{max} for a 3 inches magnetron sputtering source stays between 300G and 600G, and from Equation 5 for bigger radii of the racetrack the magnetic field should be weaker.

3.2 Reactive Magnetron Sputtering

Magnetron sputtering can be applied to deposit pure metals or to create metal compounds with nitrogen oxygen or carbon. The compound thin film coatings could be sputtered either by using a compound target directly, or by introducing a reactive gas along with the working gas into the chamber. However, controlling the stoichiometry and microstructure of the resultant thin film is very challenging due to the instability of the plasma. This instability in plasma stems from a hysteresis behavior revealed when certain parameters such as nitrogen partial pressure, plasma power and current are modified. This phenomenon is commonly explained in literature by the sputtering yield difference between compound and metal. In Figure 11 this effect can be observed where the processing curves for plasma intensity as a function of DC power in the TiN reactive sputtering has been plotted and compared with the non-reactive Ti sputtering with only pure argon.

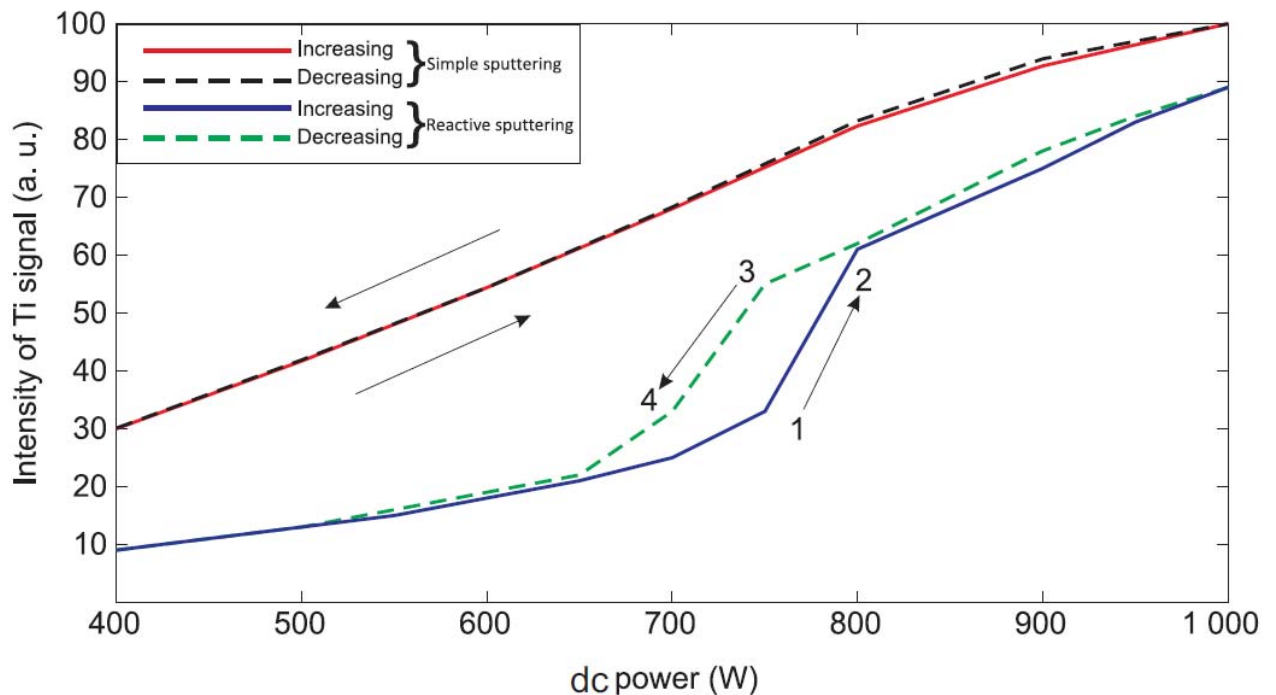


Figure 11: plasma intensity of Ti signal versus plasma dc power²⁰.

As it can be observed there is no significant increase in Ti signal until point 1. This indicates that almost all nitrogen in the chamber is consumed to form a TiN layer on the target surface. The target is said to become poisoned at this point. Since the sputtering yield of TiN is less than pure titanium the deposition rate is in its minimum state. As the plasma,

power increases the Ti signal increases abruptly to point 2. Here the target operates in metallic mode where the built-up TiN layer (on the cathode) is eroded by higher power plasma leading to sputter titanium nitride on the substrate. As the power decreases to point 3 the TiN layer gradually is formed on the target until it reaches to point 4 where the target returns to poisoned mode. The same hysteresis curve appears varying the reactive gas flow rate increased stepwise while the other parameters as current and argon pressure are kept constant. Similar curves are obtained during the reactive deposition of oxides or carbides starting from a pure metal target. The hysteresis curve influences the stoichiometry of the coating (i.e. color, hardness and other physical-chemical properties) and the reproducibility of the deposition as reported in Figure 12. In fact, maintaining fixed the argon and nitrogen fluxes and varying the magnetron current, the color of the obtained coating changes considerably. For this reason, the possibility to reduce the hysteresis area produces an advantage for the control of the coating properties, reducing the instability of the plasma processes. As evidenced from Larsson²¹ the hysteresis area is function of the pumping speed (see Figure 13) and the correct choice of the pumping speed, determine the stability of the plasma condition during the reactive magnetron depositions, guaranteeing the reproducibility of the coating processes.

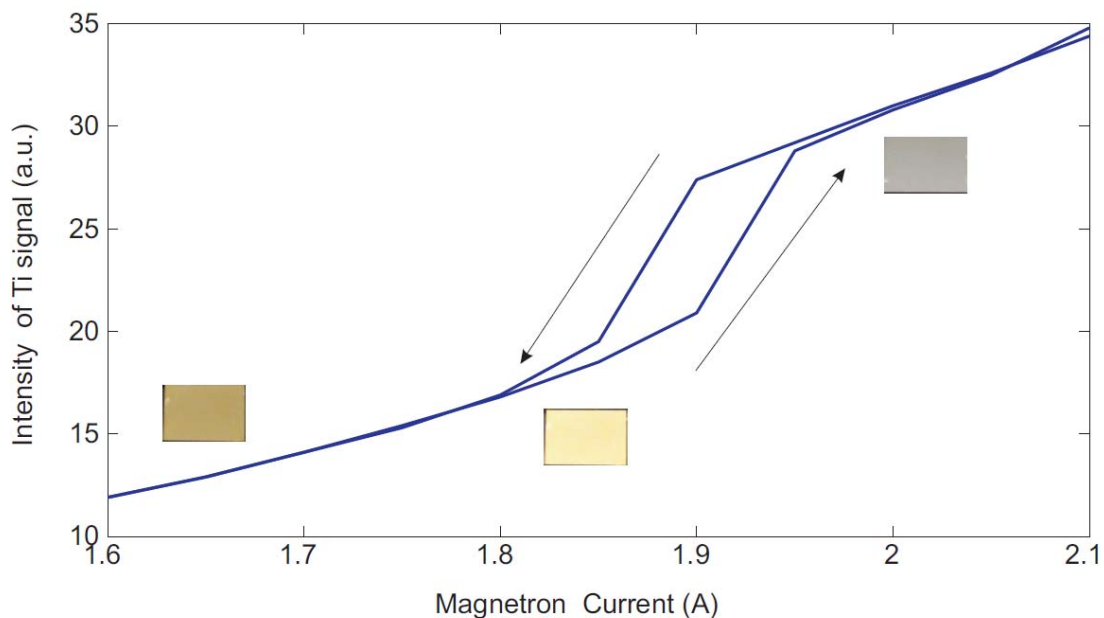


Figure 12: colour variation of TiN film at different magnetron currents (brown means excess of nitrogen, yellow is the stoichiometric concentration of TiN, grey represents a coating poor of nitrogen)²⁰.

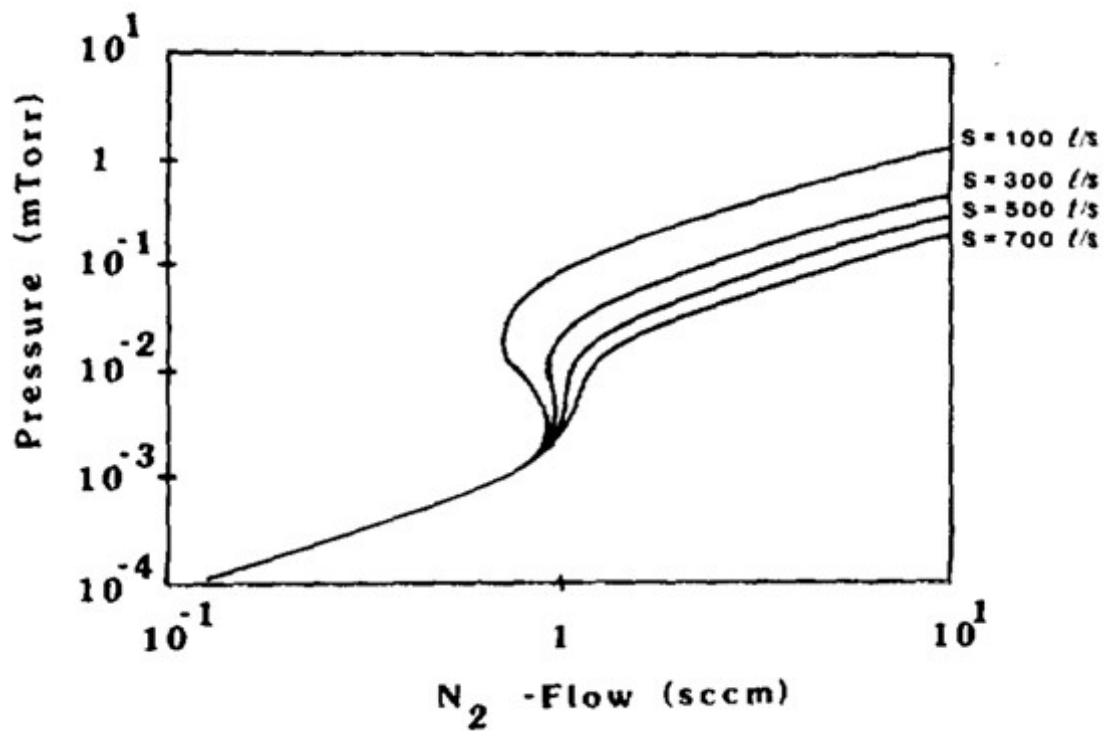


Figure 13: calculated curves for the partial pressure vs mass flow for the reactive gas, with different pumping speeds²¹.

3.3 Cathodic Vacuum Arc Sources

The cathodic vacuum arc is a high-current electrical discharge in which current is conducted by a plasma largely consisting of material ionized emitted from the cathode. This plasma can subsequently condense on internal parts of the vacuum chamber and on substrates placed in the coating apparatus. In the modern Industry vacuum arc deposition devices were developed in the former USSR in the 1970s²² and in the last decades vacuum arc deposition is considered the best technology for the deposition of hard coatings on cutting tools. A natural concentration of current in a small area (cathode spot) which randomly moves or directed by a magnetic field across the cathode surface produces jets of fully ionized and often multiply ionized vapor of the cathode material (essentially metals), while most of the power in the arc is dissipated at the anode²³.

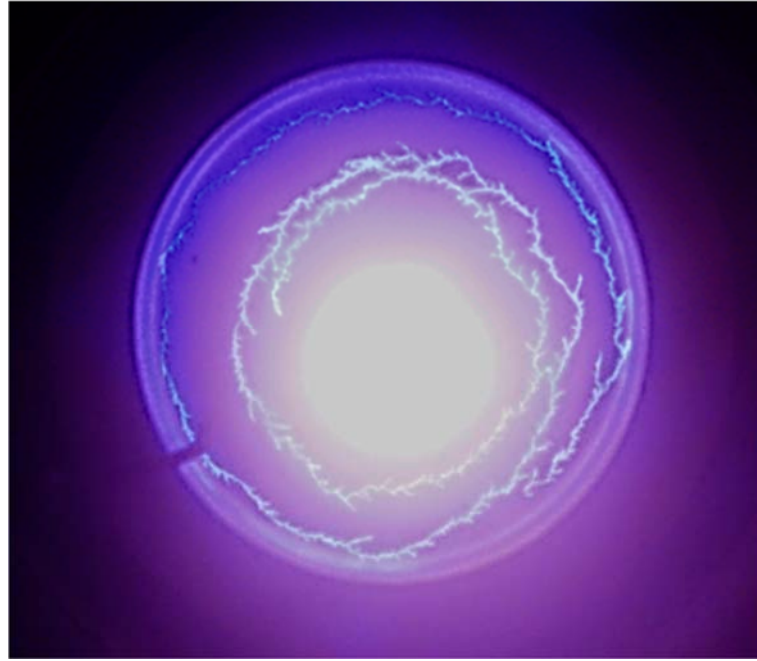


Figure 14: cathodic arc spot motion²⁴.

The electron emission processes distinguish the arc from other forms of discharges such as the glow. In the glow discharge, in fact, the secondary electron emission processes depend on the bombardment of the cathode by the ions present in the plasma (electron density: 10^{16} m^{-3})²⁵ or photons. These electrons need a high voltage to be accelerated and to reach enough energy to produce an ionization cascade capable to sustain the discharge. In the arc discharge the secondary electrons are emitted by the simultaneous effect of thermionic and field emission known as TF emission (electron density: 10^{19} - 10^{20} m^{-3})²⁶. These electrons are immediately accelerated by a local electric field, colliding with the evaporated metal ions, exciting them, and ionizing them, forming a denser plasma respect to the glow discharge with very high working current (from tens to hundreds of Amperes) and low voltage (tens of Volts). The vacuum arc does not require any background gas to operate producing ions and secondary electrons that self-sustain the discharge, but it can operate in a reactive partial atmosphere producing reactive coatings. The arc discharge, on the cathode surface, is confined in one or more small areas named cathode spots that move fast and random over all the cathode body. The number of these spots N_{cs} is proportional to the process current I , i.e. $N_{cs} = I / I_s$, where I_s is a characteristic cathode spot current which depends on the material of it is made. The current spot can cover a range from $\sim 0.4 \text{ A}$ for

very volatile cathode materials (e.g., Hg) to 300 A for very refractory materials (e.g., W)²⁷. The cathode spots motion, however, is influenced by the presence of a magnetic field. An ordered motion is observed primarily in the “retrograde” – $\mathbf{I} \times \mathbf{B}$ direction due to the magnitude of the magnetic field and secondly following the “acute angle rule”: if the magnetic-field lines cut the cathode surface obliquely, the cathode spots drift in the direction of the opening of the acute angle between the magnetic-field line and its projection on the cathode surface²³. The cathode spot is concentrated in a small area (few micrometers) and all the current passing through the electrodes is concentrated in this area. The heat produced for the joule effect in the cathodic spot region is extremely high to be exchanged, i.e., significantly exceeding the atmospheric pressure boiling temperature, even though the bulk temperature of the cathode might be close to room temperature. The consequence is an intense evaporation of the cathodic spot surface producing a large amount of metal ions directed approximately normal to the cathode surface. Moreover, due to the high temperature reached in the spot zone the metal forming the cathode is melted and sprayed away as metal droplets (macroparticles) as showed in Figure 16. Usually, the droplets are expelled at low angle close to the cathode plane, as reported in Figure 15, which could be deleterious in some applications if the right countermeasures are not applied (i.e. magnetic filters or high bias Voltage).

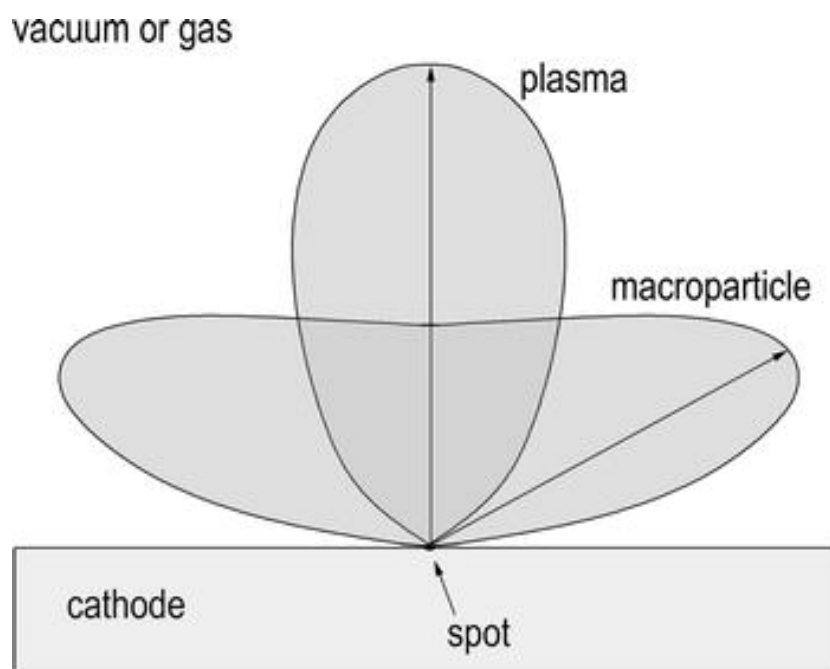


Figure 15: macroparticles emmision at low angle²⁸.

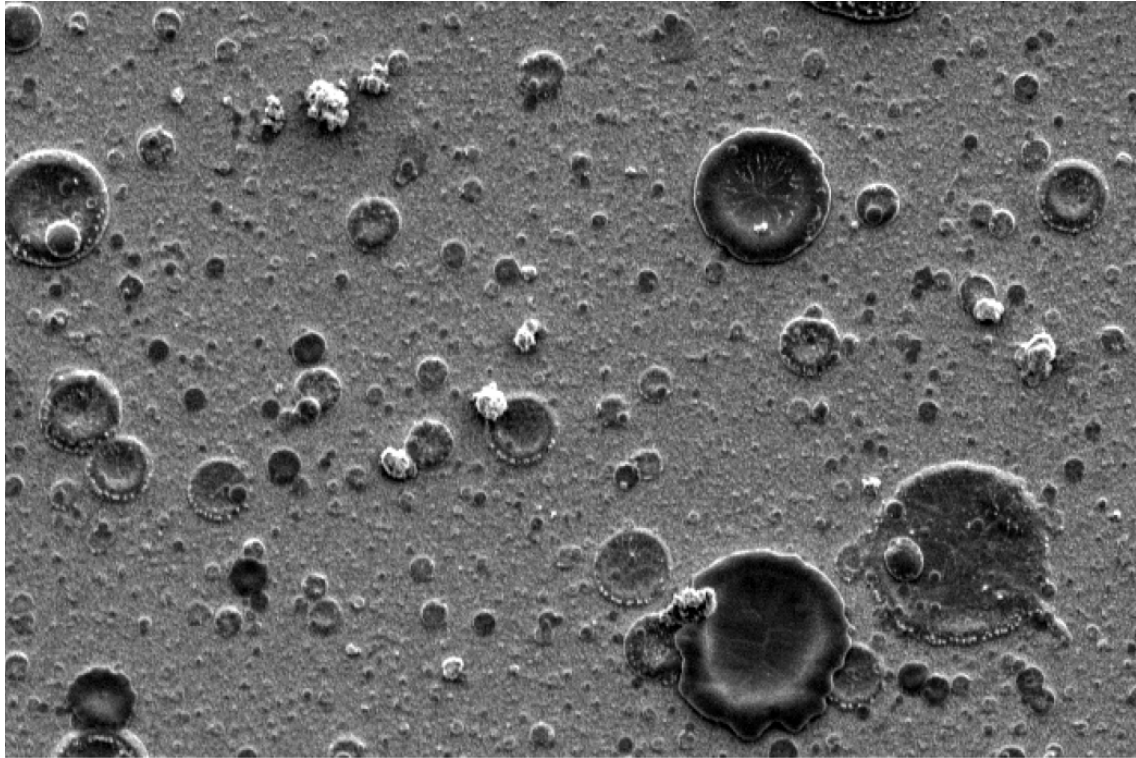


Figure 16: Cu macroparticles (~20 μ m diameter) on the surface of a copper thin film²⁹.

The macroparticles are cluster not charged and their adhesion on the substrate in most of the cases is poor and the consequence is the detaching from the coating, leaving a pinhole of its dimensions. This effect can be appreciated in Figure 17

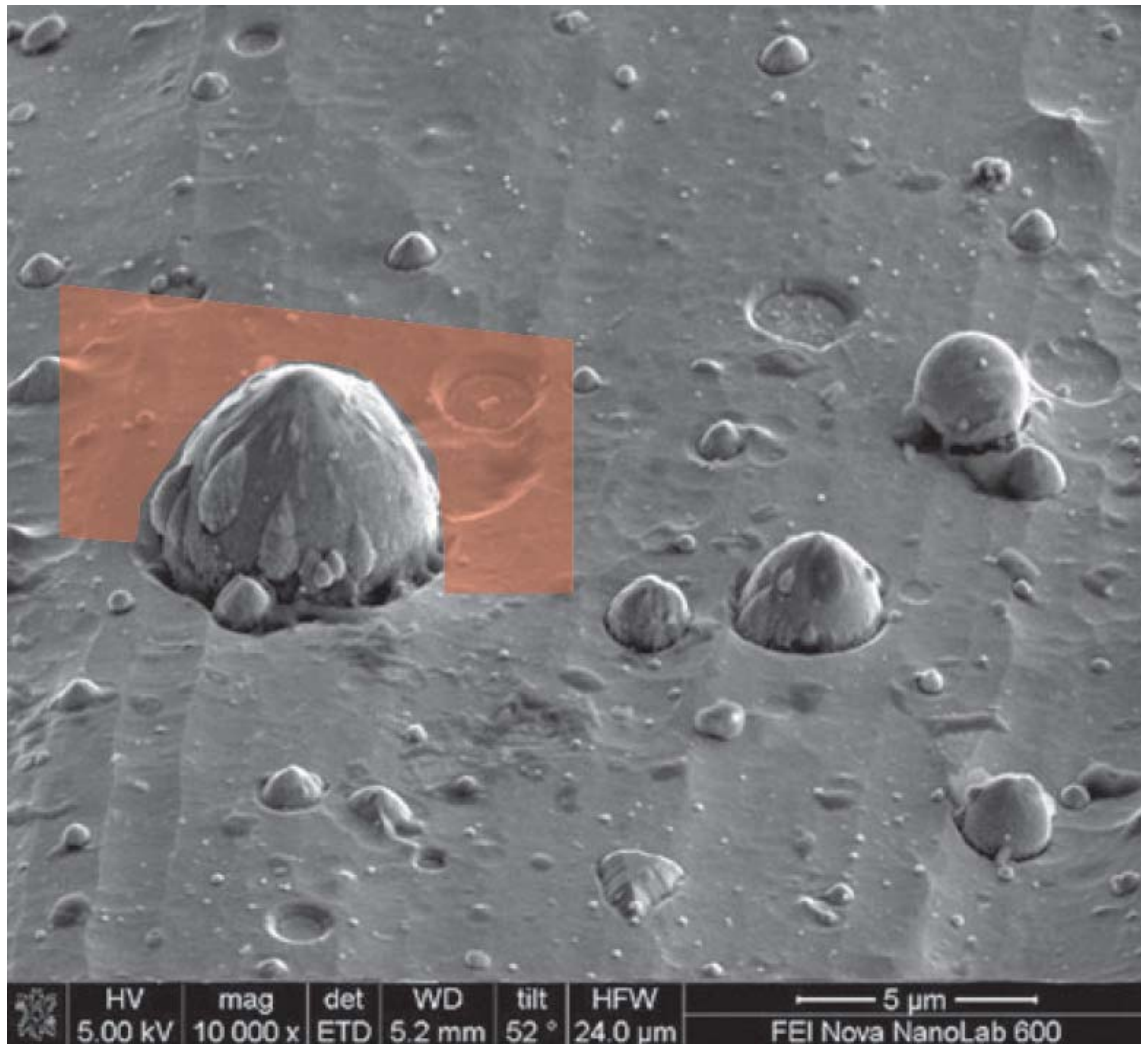


Figure 17: tilted view of the droplet selected for FIB section and TEM lamella preparation³⁰.

The macroparticles are an intrinsic effect of the cathodic vacuum arc discharge. They can be reduced acting on the cooling of the cathode (i.e. increasing the heat dissipation of the source), pulsing the DC current applied to the cathode (i.e. reducing the heating of the source) or filtering the plasma. This last choice is the most effective one, because it is the only configuration in which the sample does not see the cathodic vacuum arc source and the macroparticles can not arrive to the substrate. The filters are usually magnetic where exactly the magnetic field drives the plasma in a specific shape tube as reported in Figure 18 purifying it from the unwanted macroparticles. The magnetic field drives the electrons present in the plasma and the ions follow the electron due to their electrostatic attraction, while the macroparticles (neutrals) follow their original direction.

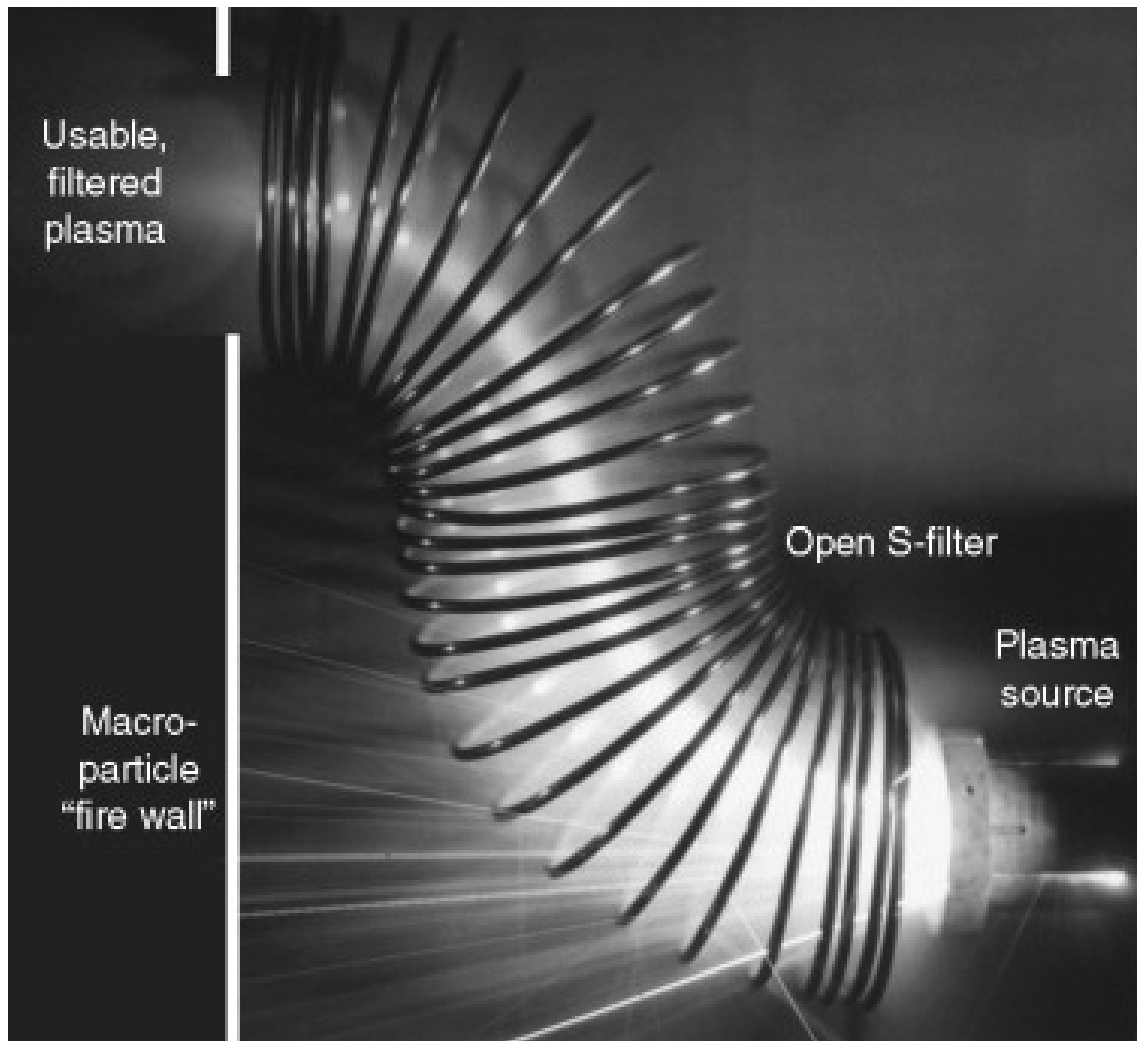


Figure 18: S-filter for cathodic vacuum arc source³¹.

3.4 Thin Film growth

The thin film growth, as well as the nucleation mode, determines many film properties such as: film density, surface area, surface morphology, and grain size. Some important aspects of the thin film growth are:

- ❖ surface roughness;
- ❖ surface temperature³²;
- ❖ adatom surface mobility;
- ❖ geometrical shadowing effects (angle-of-incidence effects);

- ❖ reaction and mass transport during deposition, such as segregation effects and void agglomeration;

Surface morphologies may vary from very smooth (e.g. glass surface) to very rough. Generally, as the film grows, the surface roughness increases, because some features or crystallographic planes grow faster than others¹⁰. Atomically deposited films generally exhibit a unique growth morphology, that look like logs or plates aligned and piled together and called a columnar morphology. This morphology develops due to geometrical effects and it is found whether the material is crystalline or amorphous. Generally, the columns are not single crystal grains but amorphous or polycrystalline. Energy of the adatom on the surface can modify the film structure from columnar morphology to a denser morphology or with larger grains. The film morphology can be described by a structure zone diagram (SZD), introduced in 1969 by Movchan and Demchishin³³ for very thick films growth by evaporation, where only the effect of the homologous temperature T_h taken into account.

$$T_h = \frac{T}{T_m} \qquad \text{Equation 6}$$

Where T_m is the material melting point. The concept of an SZD evolved over the years as PVD technology expanded from evaporation to sputtering first, and later to ion beam assisted deposition, HIPIMS, etc. To describe better the SZD for the magnetron sputtering technique, Thornton introduces also the dependence on pressure. This SZD has become a classic and is reproduced in many textbooks on PVD.

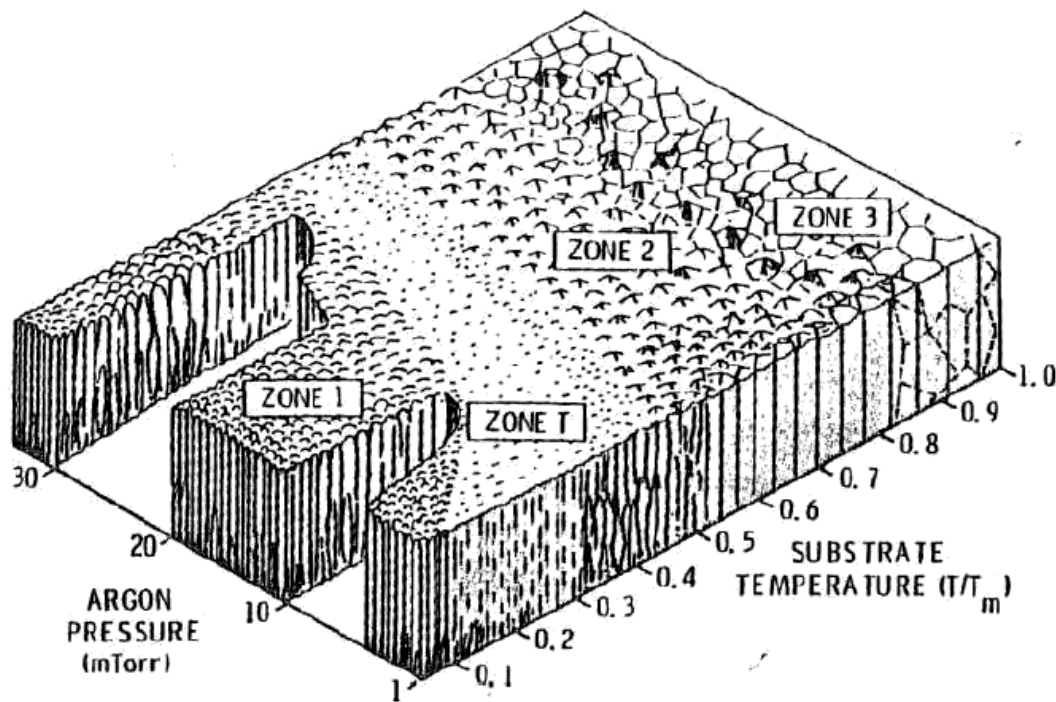


Figure 19: Structure zone diagram (SZD) proposed by Thornton. Substrate temperature and process pressure influence the film morphology³².

Temperature influences the adatom mobility. Increasing T_h bulk diffusion and recrystallization are possible and drastically change the film structure. The sputtering pressure influences the kinetic effects of particle impingement on film growth. At low pressure, the collision between sputtered particles and gas atoms are almost quenched. Sputtered atoms typically have several eV of kinetic energy, which is enough for the adatom rearrangement process on the surface. On the other side, at high pressure, the sputtered atoms suffer collisions with the process gas before arriving at the growth surface, and their distribution function is shifted to much lower energies. In Figure 19 the original Thornton SZD is reported.

In 2010, in order to develop an SZD that is as universal as feasible, Anders³⁴ proposed to extend and modify the Thornton SZD by maintaining the number of process axes but generalizing their meaning. The changes are the following:

the linear T_h axis is replaced with a generalized temperature, T^* , which includes the homologous temperature plus a temperature shift caused by the potential energy of particles arriving on the surface;

the linear pressure axis is replaced with a logarithmic axis for a normalized energy, E^* , describing displacement and heating effects caused by the kinetic energy of bombarding particles;

the unlabeled z-axis is replaced with a net film thickness, t^* , which will allow us to maintain the familiar qualitative illustration of film structure while indicating thickness reduction by densification and sputtering; it also includes i.e. ion etching as “negative thickness”.

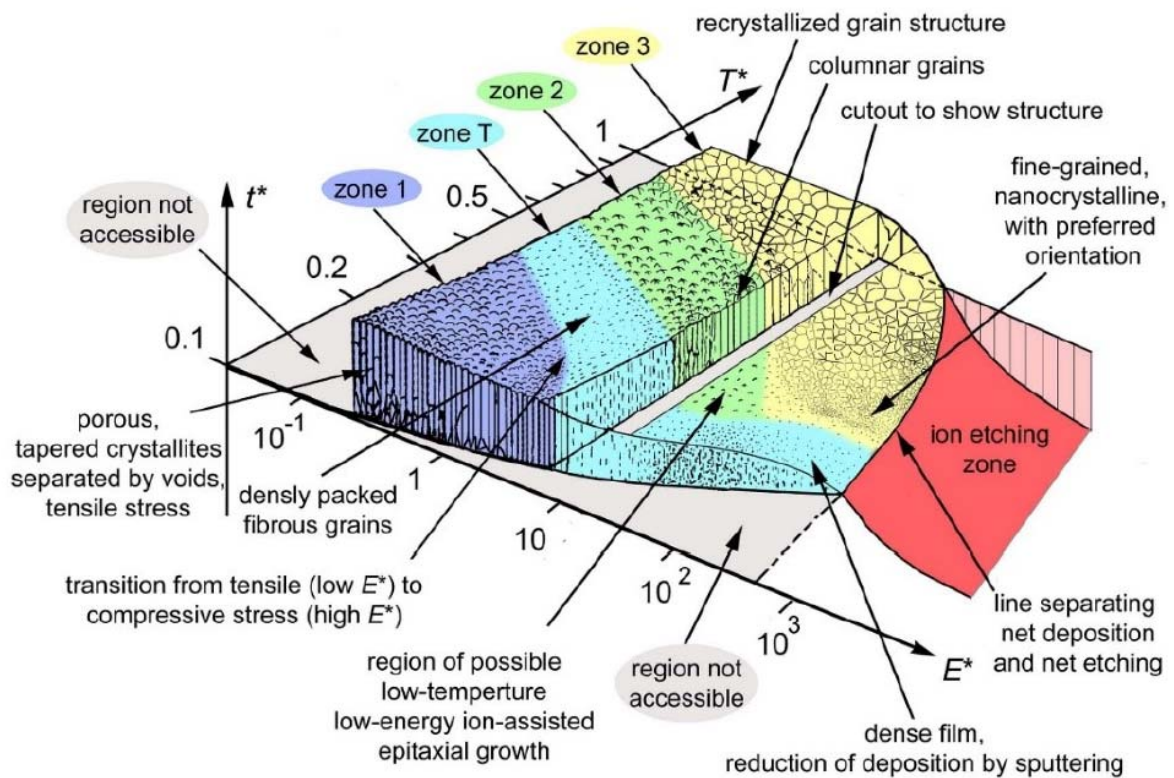


Figure 20: Structure zone diagram (SZD) proposed by Anders in 2010²⁴.

The SZD proposed by Anders is visible in Figure 21 and from both diagrams four different film structures can be identified:

ZONE 1: characterized by a fine-grained structure of textured and fibrous grains, pointing in the direction of the arriving vapor flux. The morphology is caused by the low mobility of the adatoms that produce a continued nucleation of grain.

ZONE T: a dense fibrous structure with a smooth, highly reflective surface. Diffusion is “remarkable”, but grain boundary diffusion is strongly limited. Ionic bombardment of the growing film can move the morphology from zone 1 to zone T.

ZONE 2: surface diffusion sets in, leading to uniform columnar grains.

ZONE 3: dense films with large grains, drive by bulk diffusion and recrystallization.

Chapter 4: Instrumentation

In this chapter the instrumentation used during the experimental part of the work of thesis is described. This part is fundamental for the reproducibility of the experiences and to cross check the data obtained and includes different sections: the PVD system used for the coatings production, the analytic instrumentation for the thin film characterization and the PVD sources used for the experimental coating depositions.

4.1 PVD System Prototypes

The hard coatings produced in this work of thesis has been deposited using two different PVD system prototypes located in the Material Science and Technology for Nuclear Physics Service at the National Laboratories of Legnaro. These two prototypes differ for the PVD technology (i.e. magnetron sputtering and cathodic vacuum arc) and the design of the vacuum system.



Figure 21: the PVD system prototypes located in the Material Science and Technology for Nuclear Physics Service at the National Laboratories of Legnaro. On the left the four chambers system dedicated to the magnetron sputtering and on the right the prototype dedicated to the cathodic arc deposition.

The four chambers PVD prototype presents a single pumping system (composed of one turbomolecular pump TMU071 Pfeiffer of 70 l/s and dry scroll PTS03001UNIV

Varian/Agilent pump of 15 m³/h) and four different chambers for the coating depositions (as reported in the scheme of Figure 22) For this thesis only one of the four chambers was used for the deposition of TiN and TiCN coatings. The benefit of the design of this prototype is the simultaneously vacuuming of the four chambers, once reached the desired base pressure each single chamber can be used maintaining the others in steady state. In the case of multiple PVD processes this design guarantees an effective time reduction, because the base pressure is reached with a single vacuum procedure for the four different coating deposition zones. The magnetron sputtering source used for the hard coating depositions is a homemade source with a planar cathode of two inches diameter and magnets fixed out of the water-cooling circuit. The vacuum chambers are cylinders made of stainless steel AISI 304, (the used one is 200 mm high and 300 mm wide), water cooled and sealed with conflat flanges.

The control unit of the PVD prototype is a National Instruments PLC, where the pumping systems and vacuum valves are controlled, while the power supply and the process gas sources (Ar, N₂, CH₄ extra pure 99,9999%) are governed separately. The control software developed during previous works is semi-automatic and it gives the possibility to monitor the baking temperature of the system. Moreover, it is implemented a safety control, for the back streaming protection of the system: after a blackout the system stays in idles state in order to avoid any kind of wrong procedure, causing a back streaming of the oil present in the primary pump (if the actual dry pump is substituted with a rotary vane pump). The standard base vacuum pressure without baking out the chamber walls is in the order of 10⁻⁶ mbar.

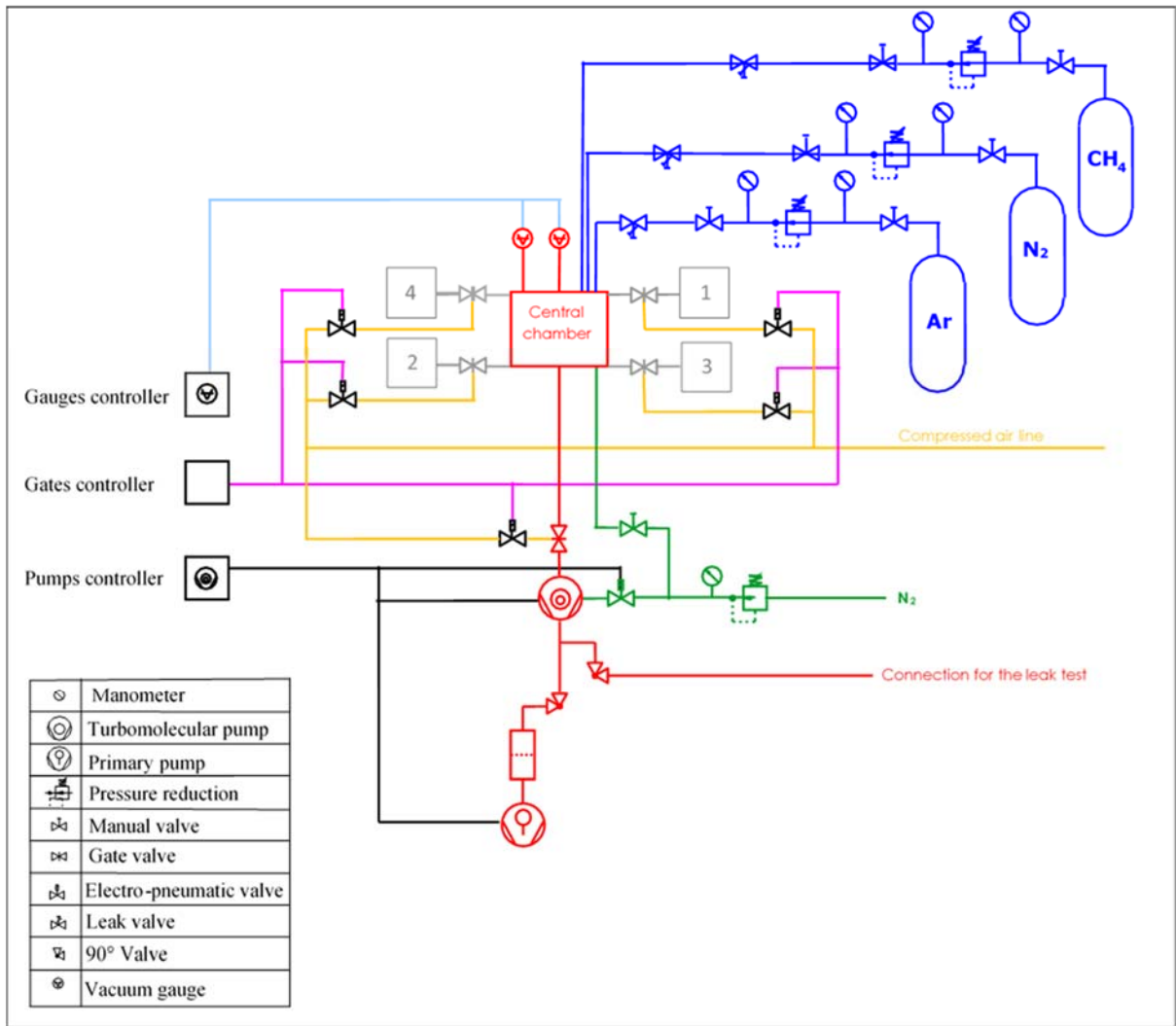


Figure 22: four chambers PVD Prototype vacuum scheme.

The arc deposition PVD prototype presents a single pumping system (composed of one turbomolecular pump TMU261P Pfeiffer of 230 l/s and dry scroll PTS03001UNIV Varian/Agilent pump of 15 m³/h) and a single vacuum chamber (as reported in) for the depositions of TiN, TiCN, TiAlCN, CrCN coatings. The cathodic vacuum arc source used for the hard coating depositions was a commercial source (GPA with a planar cathode of 80 mm diameter). The vacuum chamber is a cylinder made of stainless steel AISI 304 (490 mm high and 390 mm wide) and water cooled. The base vacuum pressure without baking out the chamber walls is in the order of 10⁻⁶ mbar.

The control unit of the PVD prototype is a Siemens PLC (Simatic HMI), with which the pumping systems, vacuum valves and arc power supply are controlled, while the process gas sources (Ar, N₂, CH₄ extra pure 99,9999%) are governed separately. The control

software, completely developed during this work is semi-automatic presents a safety control for the back streaming protection of the system: after a blackout the system stays in idles state in order to avoid any kind of wrong procedure, causing a back streaming of the oil present in the primary pump (if the actual dry pump is substituted with a rotary vane pump).

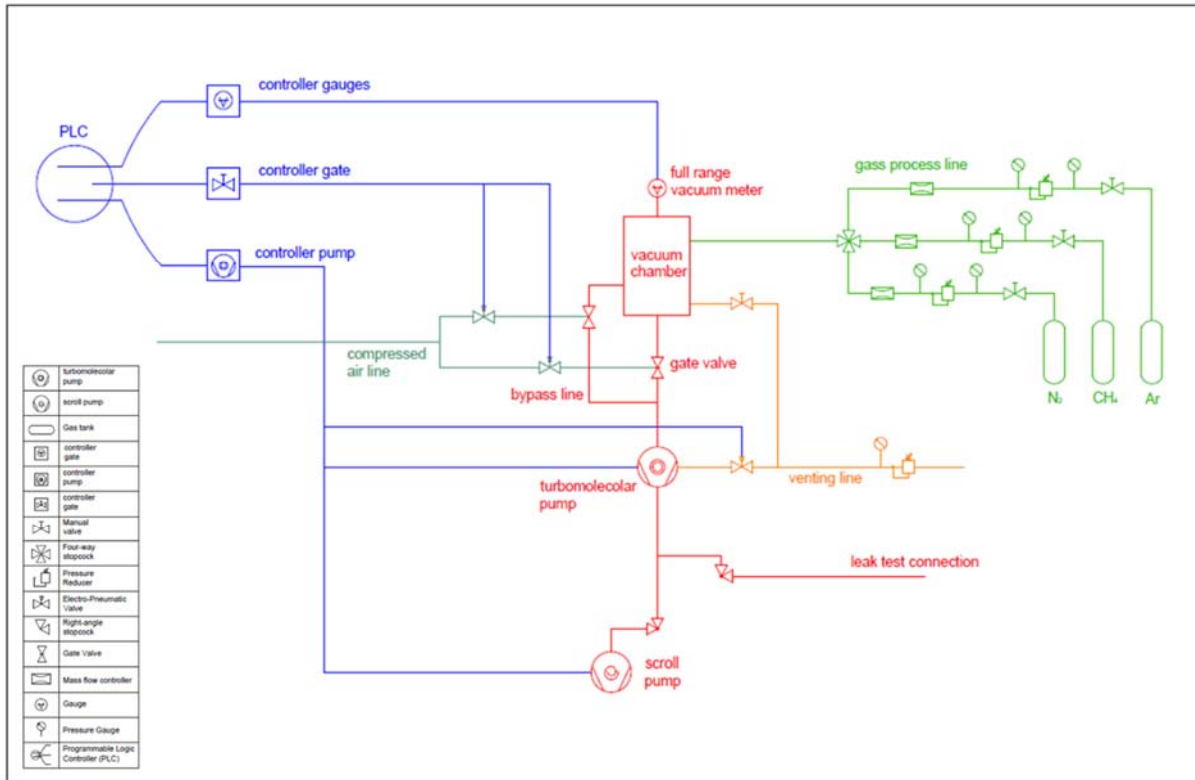


Figure 23: cathodic vacuum arc PVD Prototype vacuum scheme.

4.2 SEM and EDS microanalysis

The Scanning Electron Microscopy (SEM Philips model XL30) is used for the acquisition of the micrography of the coating surfaces, while the energy dispersion spectroscopy (EDS Bruker Quantax/SVE6) performs the elementary analysis on the coatings of this thesis. The microscope uses the secondary electrons produced from the primary electron bombardment of the specimen surface. The primary electrons are produced for thermal emission of a tungsten filament, once accelerated through the electron gun column they reach a difference of potential in the range of 2-30kV. The EDS microanalysis is a Bruker XFlash 410-M (active window of 10 mm², resolution 129 eV, count over 150000 cps, peltier cooling) that can discriminate the X-photons produced from the impingement of the primary electrons on the specimen surface. The energy of the X photons produced is

characteristic of the element from which it is generated, giving the quantitative analysis (relative abundance) of the single element or contaminant with an error of 5%.



Figure 24: SEM Philips XL30 and EDS Bruker XFlash 410-M.

4.3 X-Ray Diffractometer

The diffractometer used for the acquisition of the XRD spectra (X-Ray Diffraction) is a X'Pert Philips/PANalytical for powder analysis. The XRD can identify a phase of crystalline material and can provide informations on unit cell dimensions, crystal plane distance, which give precise data about the material composition and the variation respect to the compound stoichiometry. The spectra can be acquired with parallel plate collimator in a grazing angle configuration (incident beam fixed at 2° and moving the detector) or with a programmable receiving slit (PRS) in a gonio configuration (moving the beam and the detector). The right choice of the analysis configuration is related to the intensity of the

spectra peaks obtained. Usually operating in gonio configuration if the background noise due to the substrate is too high a grazing angle configuration is preferred. This set up increases the signal from the thin film respect to the signal of the substrate, increasing the quality of the analysis. The software used for the peak and material identification is the HighScore Plus ver. 4.5 PANalytical, which includes a wide library of all possible compounds and elements previously analyzed.



Figure 25: X'Pert Philips/PANalytical X-Ray Diffractometer.

4.4 Cathodic Vacuum Arc source

The cathodic vacuum arc source used for the experimental part and mounted on the noncommercial physical vapor deposition system described in this thesis is a commercial

arc produced by the GPA PlasmaApplikation mbH (Figure 26). The source mount a 90 mm diameter planar cathode 17 mm thick, fixed on the copper baseplate screwing a stainless-steel ring. The cathode is easily interchangeable and suitable for different target material. The thermal connection between the target and the copper base plate is guaranteed by a flexible carbon disc 1 mm thick. The plasma discharge is ignited acting on the electro pneumatic trigger (mounting a molybdenum tip, see Figure 27 Figure 28) that touching the cathode surface creates the arc spot. The process current suitable for the GPA source is in the range 50-100 A. The source must be water-cooled during the arc discharge to prevent the overheating of the cathode and magnets (used to drive the cathode spots). The connection 24V, indicated in Figure 27, is fundamental to avoid the melting of the trigger tip, in fact, it is directly connected with a high power resistance in order to reduce the current passing through the tip during the discharge ignition.



Figure 26: GPA cathodic vacuum arc³⁵.

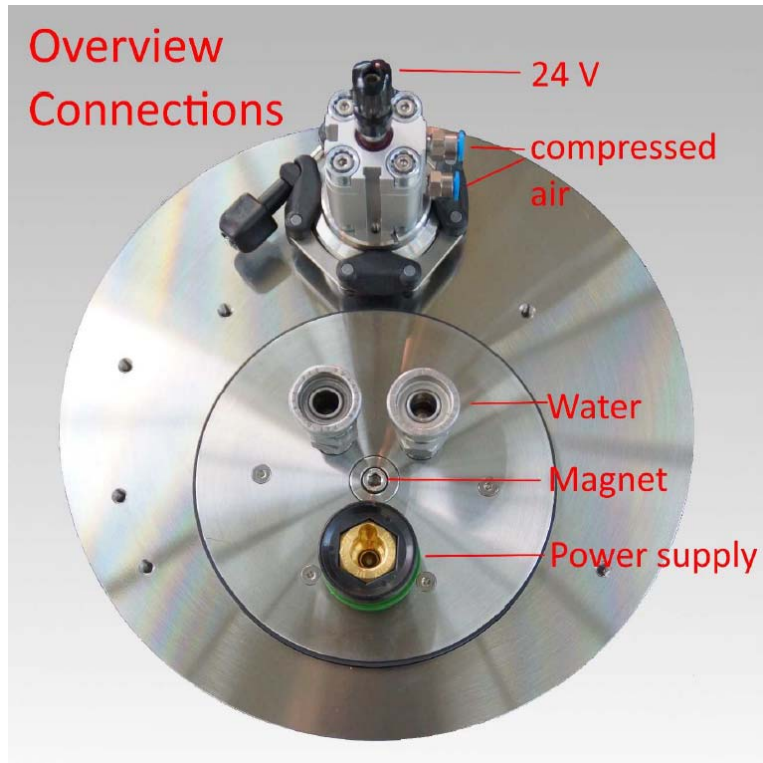


Figure 27: connections of the CVA source³⁵.

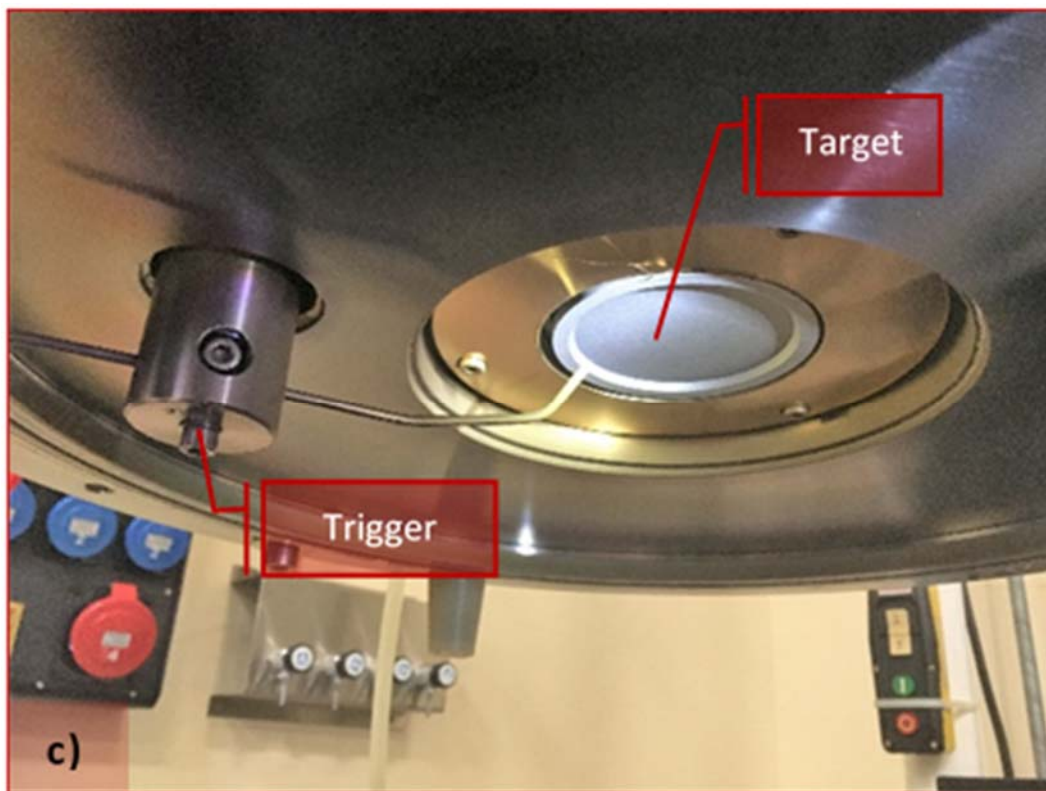


Figure 28: cathode and trigger from a vacuum side view.

4.5 Magnetron Sputtering Source

The magnetron sputtering source used for the experimental part of the thesis is a homemade magnetron. The source mounts a 2 inches diameter planar cathode 5 mm thick. The cathode is easily interchangeable and suitable for different target material. The thermal connection between the target and the copper base plate is guaranteed by a thin layer of silver paste. The process power suitable for the magnetron sputtering source is maximum 2 kW in DC configuration. The source must be water-cooled during the plasma discharge to prevent damages of the Viton O-rings and NdFeB magnets (maximum temperature of 80°C). These magnets are positioned out of the water-cooling circuit, in order to prevent the oxidation and their consequent embrittlement as reported in Figure 29. The magnetron sputtering presents an electrode powered with negative potential (cathode) of hundreds of Volts and a second electrode grounded (anode). The two components are electrically isolated using a fiberglass flange as indicated in the following figure.

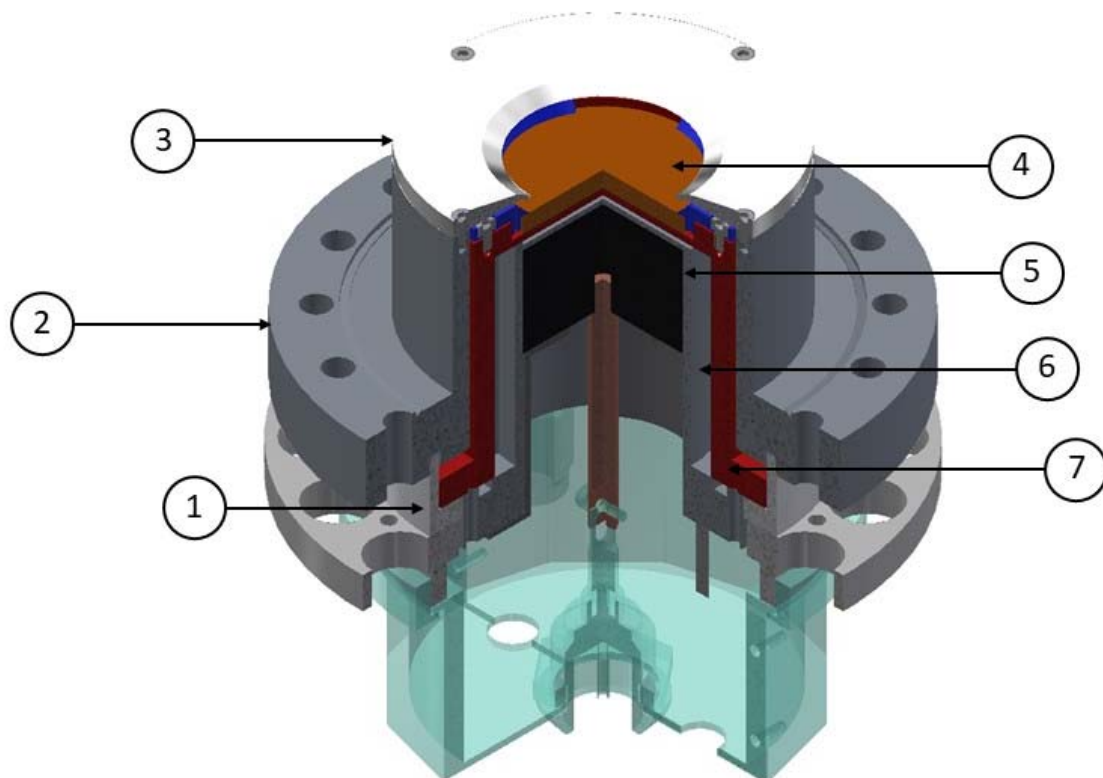


Figure 29: detailed view of the magnetron sputtering source: 1 insulating flange, 2 ground flange, 3 ground shield, 4 target, 5 magnet pack, 6 water cooling circuit, 7 cathode body.

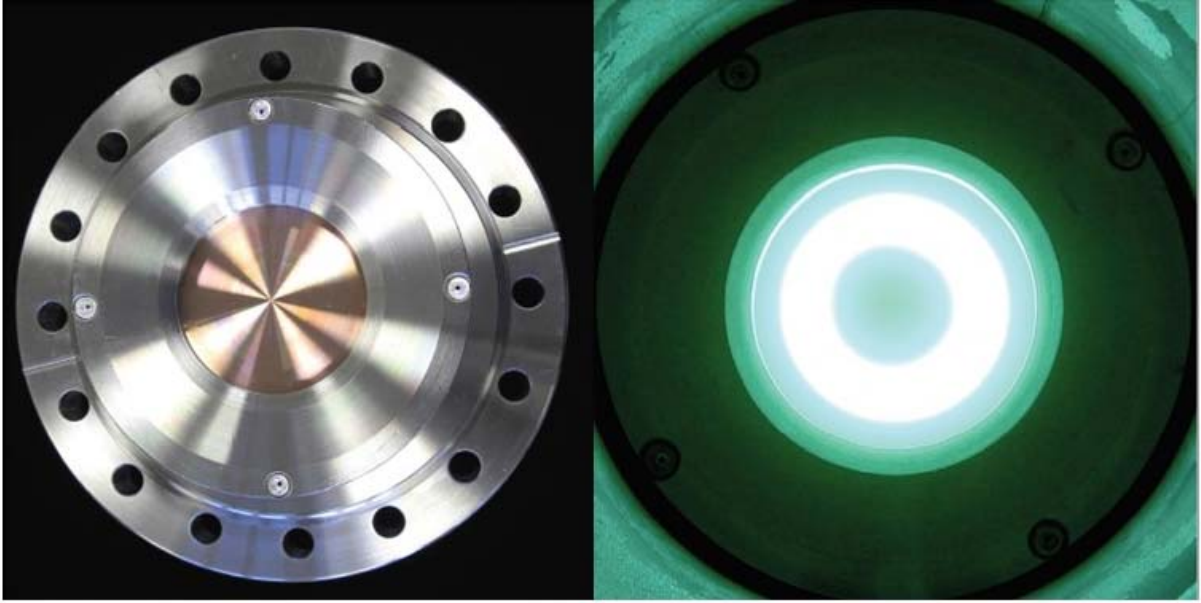


Figure 30: 2 inches magnetron sputtering source (left top view, right plasma view).

Chapter 5: Hard coatings deposited via Magnetron sputtering

This chapter reports the influence of the process parameters on the stoichiometry and on the structure of the coatings deposited with the magnetron sputtering techniques. In particular, the attention is focused on the process temperature and on the fluxes of the gases used for the deposition. Two different hard materials are deposited and characterized: the titanium nitride (TiN) and the titanium carbonitride (TiCN).

5.1 TiN Magnetron sputtering coatings

The first part of the research activity of this work of thesis is focused on the determination of the right process parameters for the thin film deposition of titanium nitride. The magnetron sputtering source used for the thin film deposition is a homemade 2 inches planar cathode 5 mm thick of Ti 99,99%. All the test coatings are realized depositing the thin films (2 μm thick) on quartz substrates previously cleaned in specific chemical bath and starting from a base vacuum pressure lower than $9 \cdot 10^{-6}$ mbar. The distance between the cathode and the substrate is maintained fixed at 5 cm. It is well known that reactive sputtering regime presents a hysteresis curve of which the first branch (increasing the reactive gas flux) is reported in the experimental plot of Figure 31. The data reported has been acquired varying the flux of the reactive gas N_2 and maintaining fixed the flux of the inert gas Ar and the power (1 kW) applied to the sputtering source. Plotting the voltage versus the N_2 flux variation, we can notice the jump of voltage in correspondence of the interval from 9 to 15 sccm of N_2 that separate the metal deposition (Ti) from the poisoned deposition (TiN_{1+x}). As reported in literature to obtain the TiN coating with the highest hardness performances the thin film has to be under stoichiometric in N_2 content (TiN_{1-x}) and this corresponds to choose the flux in the jump interval of the curve or immediately before.

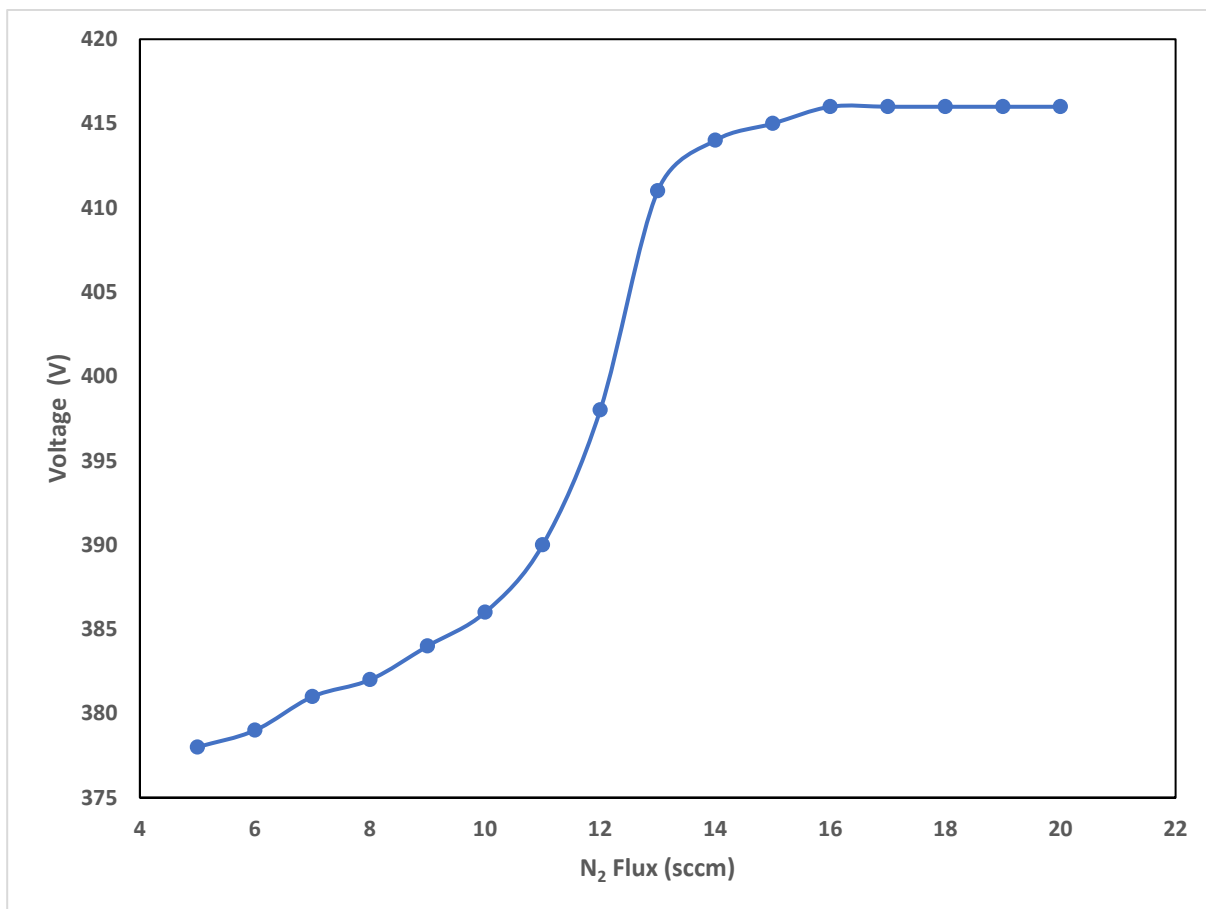


Figure 31: experimental curve Voltage versus N₂ flux (25 sccm Ar and 1kW power).

According to the literature, depending on the flux of nitrogen the color of the thin film changes from metallic grey to gold (TiN under stoichiometric) and then to brown (TiN_{1+x} over stoichiometric). The coatings obtained during the experiments reported in Table 8, were realized maintaining fixed the power at 1 kW and the argon flux at 25 sccm, while the flux of nitrogen was changed in each deposition. The coatings present colors from metallic grey (metal deposition) to dark brown (poisoned deposition), however the yellow characteristic of the TiN film can not be reached in all these tests. Moreover, in Table 8 it is indicated the atomic abundance of nitrogen and titanium obtained with EDS analysis. They show that the right elements ratio for the under stoichiometric TiN is reached during the test TiN 06. Unfortunately, the color of the coating is not the yellow characteristic of the TiN researched, but the elements abundance is the right one, this fact suggests that something else is needed to obtain our goal.

TABLE 8: TITANIUM NITRIDE THIN FILM DEPOSITION WITH FIXED ARGON FLUX AND VARYING THE NITROGEN FLUX.

<i>Sample n°</i>	<i>Ar (sccm)</i>	<i>N₂ (sccm)</i>	<i>Power (kW)</i>	<i>Color</i>	<i>N %</i>	<i>Ti%</i>
<i>TiN 01</i>	<i>25</i>	<i>20</i>	<i>1</i>	<i>Brown</i>	<i>83,42</i>	<i>16,58</i>
<i>TiN 02</i>	<i>25</i>	<i>10</i>	<i>1</i>	<i>Brown</i>	<i>43,71</i>	<i>59,29</i>
<i>TiN 03</i>	<i>25</i>	<i>12</i>	<i>1</i>	<i>Brown</i>	<i>69,08</i>	<i>30,92</i>
<i>TiN 04</i>	<i>25</i>	<i>15</i>	<i>1</i>	<i>Brown</i>	<i>70,15</i>	<i>29,85</i>
<i>TiN 05</i>	<i>25</i>	<i>11</i>	<i>1</i>	<i>Brown</i>	<i>64,49</i>	<i>35,51</i>
<i>TiN 06</i>	<i>25</i>	<i>7</i>	<i>1</i>	<i>Brown/gold</i>	<i>48,42</i>	<i>51,58</i>
<i>TiN 07</i>	<i>25</i>	<i>6</i>	<i>1</i>	<i>Metal grey</i>	<i>0</i>	<i>100</i>
<i>TiN 08</i>	<i>25</i>	<i>5</i>	<i>1</i>	<i>Metal grey</i>	<i>0</i>	<i>100</i>

In order to crosscheck the results obtained with EDS, the X-Ray Diffraction analysis has been chosen. From the X-Ray Diffraction spectrum (see Figure 32), it is possible to extrapolate the lattice parameter of the material deposited and the peak position of the most intense peak (crystallographic plane 111). To calculate the lattice parameter (α) of titanium nitride are needed the angle of the most intense peak ($2\theta^\circ$) and d-spacing (distance between two subsequent crystal planes). The stoichiometric TiN has $d_{111}=2,44738 \text{ \AA}$, and the most intense peak is the TiN (111) where 2θ is $36,689^\circ$. For materials with cubic lattice arrangement the formula used to determine α is:

$$\alpha = d_{hkl} \cdot \sqrt{(h^2 + k^2 + l^2)} \quad \text{Equation 7}$$

Observing the graphs reported in Figure 33 (where the lattice parameter is plotted versus the variation of N₂ flux) and Figure 34 (where the peak position is plotted in function

of the amount of N_2), the lattice parameter and the peak position for the thin film deposited during the experiment TiN 06 are the closest to the stoichiometric TiN. Moreover, increasing the nitrogen flux the distance from the ideal angle and lattice constant increases. This confirms the data obtained from the EDS analysis and suggests that the coating TiN 06 has the right amount of nitrogen and titanium, while the depositions with higher nitrogen flux presented an excess of N atoms. An explanation to the fact that the composition is right but not the color and not the crystallographic values could arrive from the consideration that the nitrogen in the thin film is in the correct proportion (EDS analysis), but it is not completely reacted with the titanium atoms (N_2 gas molecules or atoms entrapped in the material). In fact, supposing that the deposition is not enough energetic to complete the chemical reaction, the right coloration of the thin film can not be reached.

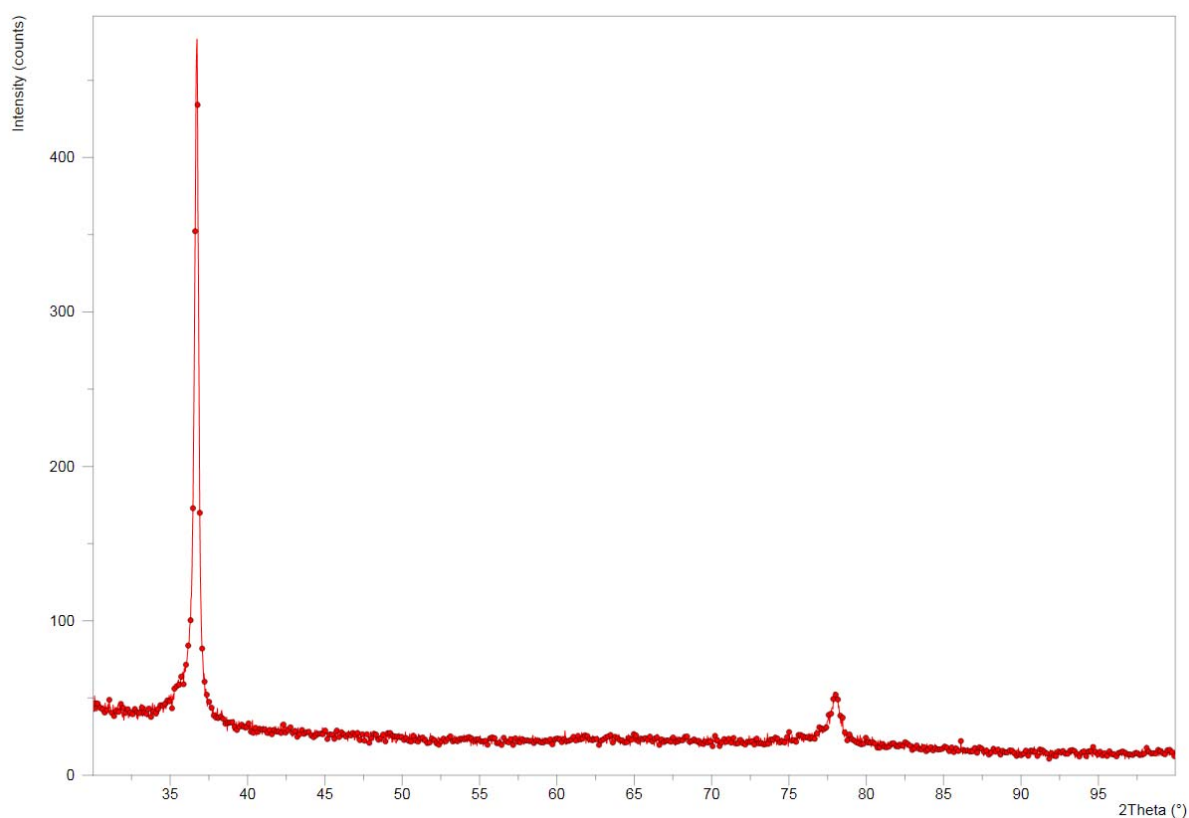


Figure 32: XRD spectrum of sample TiN_06

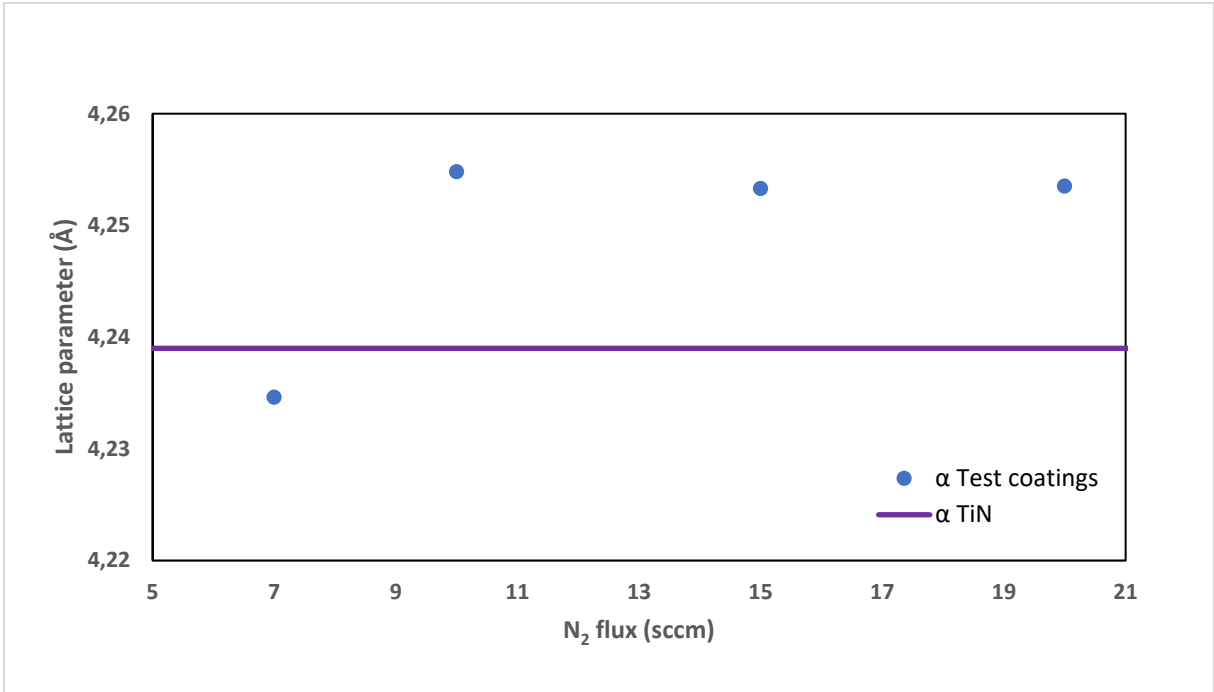


Figure 33: lattice parameter versus N₂ flux.

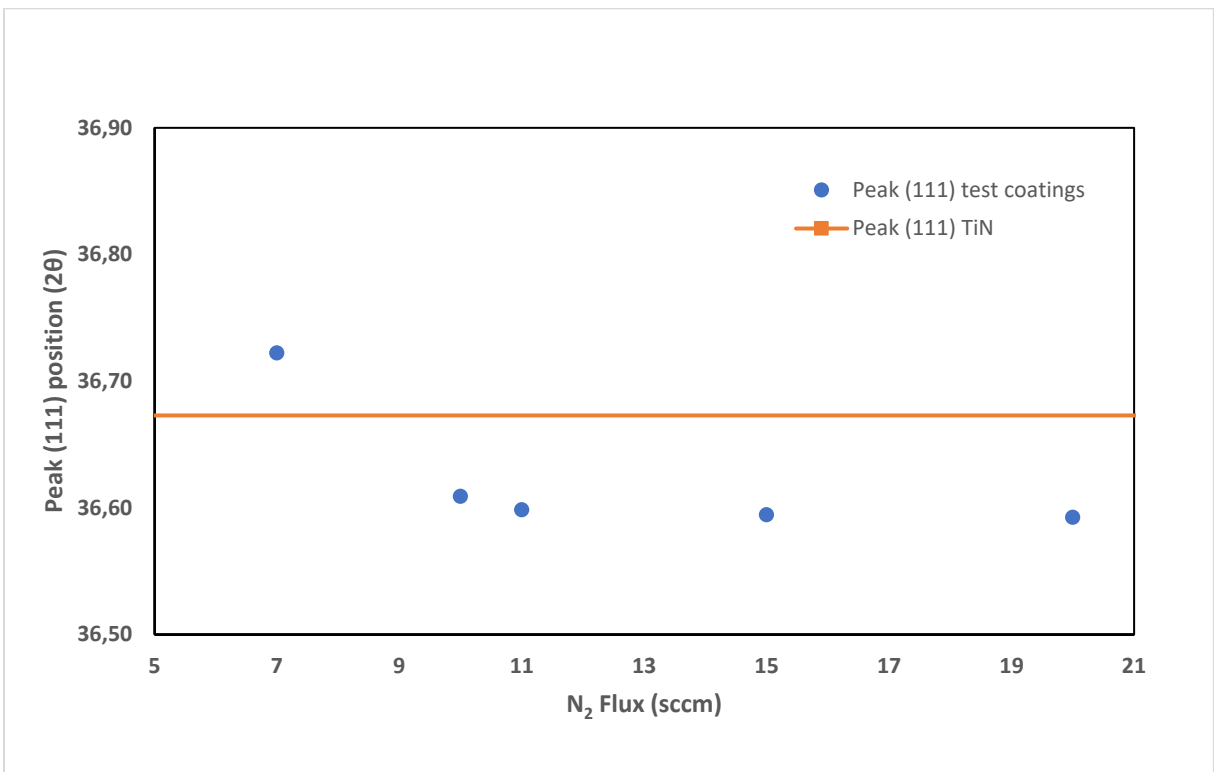


Figure 34: TiN (111) peak position versus N₂ flux.

Another way to crosscheck the data obtained from the EDS is to quantify the nitrogen content of the thin film starting again from the XRD data and relating the lattice constant obtained for the thin film coatings with the lattice parameter of stoichiometric TiN ($\alpha_{\text{TiN}} = 4,239 \text{ \AA}$). In fact, from the experimental value of the lattice constant α (TiNx), it is possible to calculate x, by the relation introduced from Nagakura³⁶:

$$\alpha(\text{TiNx}) = 4,1925 + 0,0467 x \quad \text{Equation 8}$$

Obtained x it is easy to understand if the coating produced is under, over or with the right stoichiometry of the material researched. The results obtained for several depositions at the same applied power of 1 kW and with the same Argon flow of 25 sccm are reported in the following table.

TABLE 9: EVALUATION OF THE N ABUNDANCE IN THE THIN FILM.

<i>Sample n°</i>	<i>N₂ (sccm)</i>	<i>Color</i>	<i>α (TiNx) (Å)</i>	<i>x (TiNx)</i>
<i>TiN 01</i>	<i>20</i>	<i>Brown</i>	<i>4,2548</i>	<i>1,33</i>
<i>TiN 02</i>	<i>10</i>	<i>Brown</i>	<i>4,2533</i>	<i>1,30</i>
<i>TiN 04</i>	<i>15</i>	<i>Brown</i>	<i>4,2546</i>	<i>1,33</i>
<i>TiN 05</i>	<i>11</i>	<i>Brown</i>	<i>4,2535</i>	<i>1,31</i>
<i>TiN 06</i>	<i>7</i>	<i>Brown/gold</i>	<i>4,2346</i>	<i>0,90</i>
<i>TiN 07</i>	<i>6</i>	<i>Metal grey</i>	<i>4,1014</i>	<i>-1,95</i>
<i>TiN 08</i>	<i>5</i>	<i>Metal grey</i>	<i>4,0883</i>	<i>-2,23</i>

Again, for the coating TiN 06 the x value calculated is the closest to the stoichiometry, while increasing or decreasing the flux relatively to the TiN 06 flux the coating obtained is metallic or sensibly over stoichiometric. This result confirms that it is necessary to increase the energy of the deposition during the coating grow. To verify this hypothesis a new series of coatings has been realized (increasing the energy deposition = increasing the process temperature), the sample holder was substituted with a new one, which was able to increase the substrate temperature during the deposition process. The new

sample holder is constituted of an IR lamp heater irradiating an Inconel plate of 2 inches diameter where the substrates are placed. To obtain a reference temperature for the following thermal treatments the deposition TiN 06 has been repeated monitoring the temperature, and it has been verified that the temperature never overcame 100°C. For this reason, the gases fluxes and process power are fixed, while the temperature is varied from 200 °C to 350 °C.

TABLE 10: N CONTENT IN FUNCTION OF THE TEMPERATURE VARIATION (EDS ANALYSIS).

<i>Sample n°</i>	<i>N₂ (sccm)</i>	<i>Temperature(°C)</i>	<i>Color</i>	<i>N %</i>	<i>Ti%</i>
<i>TiN_11</i>	<i>7</i>	<i>200</i>	<i>Goldish</i>	<i>47,50</i>	<i>53,50</i>
<i>TiN_12</i>	<i>7</i>	<i>250</i>	<i>Goldish</i>	<i>47,98</i>	<i>55,02</i>
<i>TiN_13</i>	<i>7</i>	<i>350</i>	<i>Brown</i>	<i>62,76</i>	<i>37,24</i>
<i>TiN_23</i>	<i>7</i>	<i>300</i>	<i>Yellow</i>	<i>48,38</i>	<i>51,62</i>

TABLE 11: N CONTENT IN FUNCTION OF THE TEMPERATURE VARIATION (NAGAKURA EQUATION).

<i>Sample n°</i>	<i>N₂ (sccm)</i>	<i>Temperature (°C)</i>	<i>aTiNx (Å)</i>	<i>x (TiN_x)</i>
<i>TiN_11</i>	<i>7</i>	<i>200</i>	<i>4,2348</i>	<i>0,90</i>
<i>TiN_12</i>	<i>7</i>	<i>250</i>	<i>4,2351</i>	<i>0,91</i>
<i>TiN_13</i>	<i>7</i>	<i>350</i>	<i>4,2528</i>	<i>1,29</i>
<i>TiN_23</i>	<i>7</i>	<i>300</i>	<i>4,2371</i>	<i>0,96</i>



Figure 35: TiN_23 fixed on the sample holder.

As reported in Table 10 increasing the temperature from 200 °C to 300°C the amount of N atoms measured is almost constant considering the error of 5% in the EDS measurement, increasing the temperature to 350 °C the N content is considerably augmented. This result could be explained with the velocity of nitridation reaction: until 300°C the velocity reaction is enough to maintain the coatings near to the TiN stoichiometry while at 350°C the reaction velocity is too high, and an excess of nitrogen is entrapped in the coating. This means that at the actual conditions, described by the actual process parameters (gas fluxes, DC power, distance source-sample, etc.) the process temperature presents an interval (200-300°C) where it is possible to grow a stoichiometric TiN, while overcoming this range the coating results over stoichiometric, fact confirmed from the color of the samples acquired with the treatments. In Table 11 is reported the x (TiN_x) value in function of the variation temperature (from 200 °C to 350 °C), the results is extremely important, in fact if from the EDS analysis the N content results constant, the x (TiN_x) increases increasing the process temperature and the sample TiN 23 is the closest to the stoichiometric TiN. This means that

the difference in the results is probably due to the techniques of analysis. Different techniques can give different information on the coating analyzed and crosscheck the results obtained. The XRD techniques is related to the diffraction of crystalline planes, while the EDS depends on the X-photons emitted from the superficial element excited with the electrons of the SEM. For these reasons the EDS signal depends on all the elements present in the surface of the coating, while the XRD signal arrives only from the crystalline elements and not from the amorphous (background). The N₂ gas entrapped in the coating is not crystalline (background contribution), but can be detected from EDS, causing two different results of the same sample. Increasing the temperature (the energy deposition) the nitrogen reacts with titanium atoms forming the TiN lattice, reducing in this way the N₂ molecule entrapped in the material (background contribution), fact confirmed from the spectra reported in Figure 36.

Another interesting observation on sample TiN 23 arrives from the topographic analysis of the coating surface. Pointing the attention on the TiN 23 micrography reported in Figure 37 it is clear that the atoms on the surface are arranged in clusters with a tridimensional shape. This surface is characteristic of the TiN 23 coating and it is not present in the other coatings tested. This means that this surface structure can be obtained only when the coating has a composition near to the TiN stoichiometry.

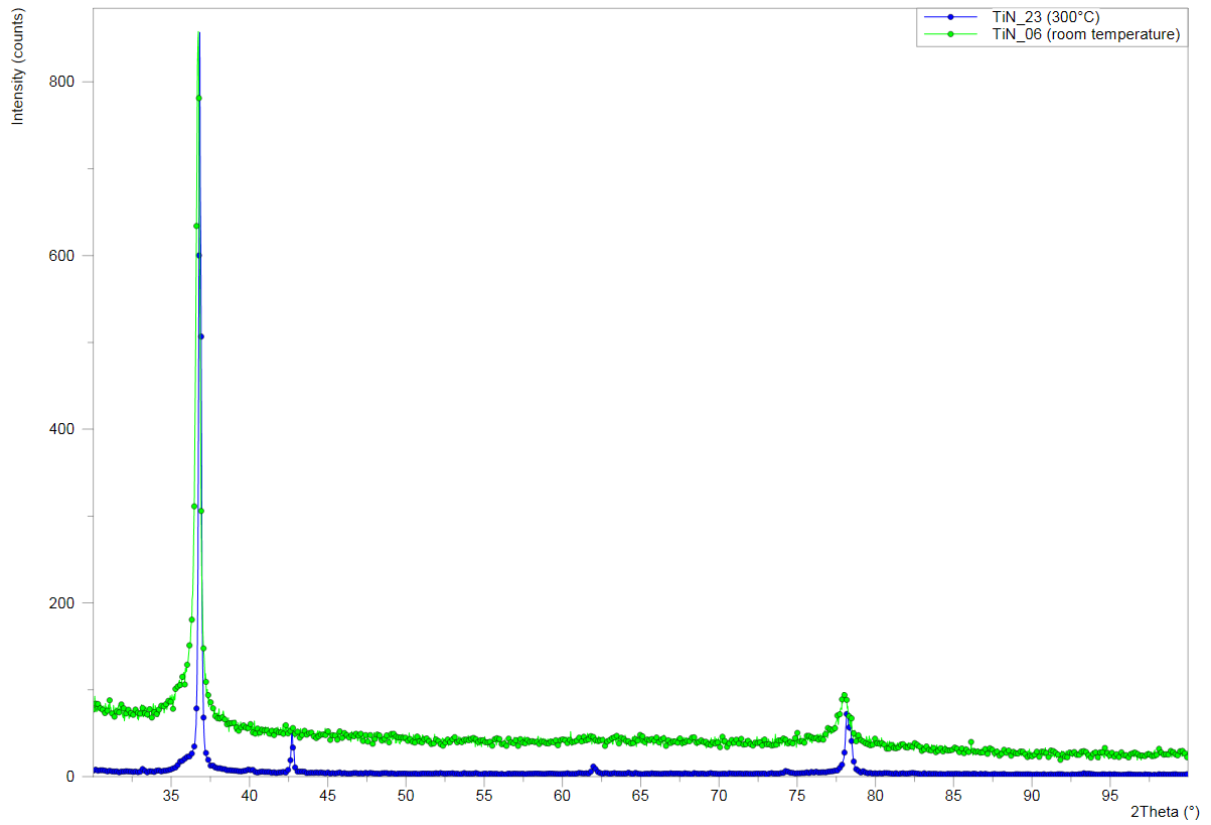


Figure 36: XRD spectra of TiN coatings in function of the process temperature variation.

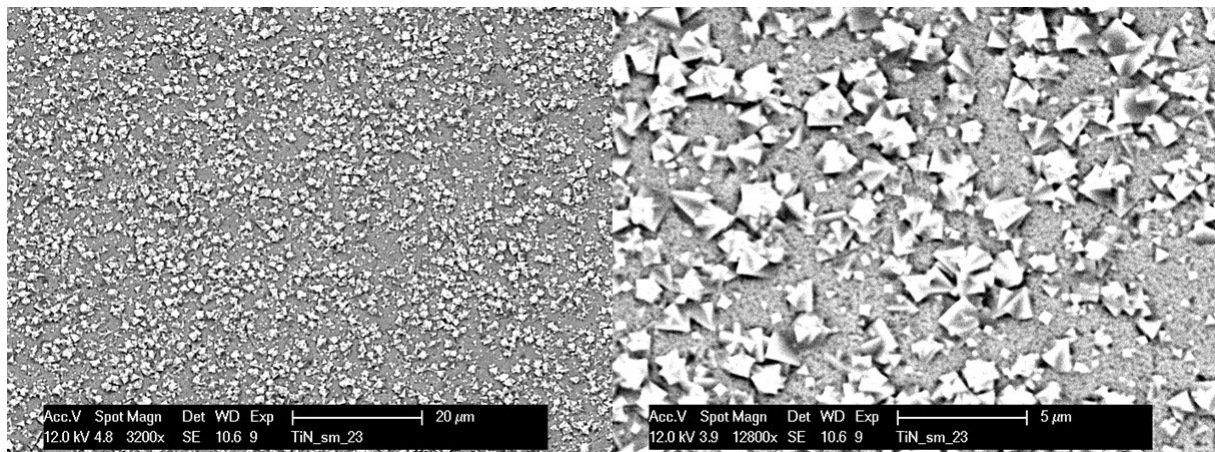


Figure 37: SEM micrography of TiN 23 coating at different magnifications.

5.2 TiCN Magnetron sputtering coatings

Subsequently to the TiN depositions the research activity of this work of thesis has been focused on the determination of the right process parameters for the thin film deposition of titanium carbonitride. The magnetron sputtering source used for the thin film deposition is a homemade 2 inches planar cathode 5 mm thick of Ti 99,99%. All the test coatings are realized depositing the thin films (2 μm thick) on quartz substrates previously cleaned in specific chemical bath and starting from a base vacuum pressure lower than $9 \cdot 10^{-6}$ mbar. The distance between the cathode and the substrate is maintained fixed at 5 cm. The data reported were acquired maintaining fixed the power (1 kW) applied to the sputtering source and varying the fluxes of the process gases (Ar, N₂ and CH₄) and the treatment temperature. Titanium carbonitride depositions are held in the same chamber used for the TiN coatings. The TiCN coatings can be realized playing with the concentration of three elements, increasing the complexity of reaction respect to the TiN thin film production. From the literature it is well known that the TiCN can present different colours (black to brown) that correspond to different contents of the constituent elements. In particular, the black coatings are produced when carbon presents the highest relative abundance of reactive gas (near the TiC composition) and brown when nitrogen is the most abundant (near the TiN composition). Following the knowhow acquired from the previous experiments, where the temperature is a fundamental parameter to bring additional energy to the species and to obtain the right stoichiometry, the choice is to start with a process temperature of 200 °C and then increase it until the identification of the right element composition. Moreover, the fluxes ratio of the process gases is another important variable to consider. The experiments reported in Table 12 present different colours and composition and relating these results with the temperature and fluxes it is possible to resume the coating deposition behaviour. In fact, pointing the attention on the composition, it is immediate to notice that the high carbon composition is never reached (CH₄ flux too low), while the brown and red colours are reached in the experiment from TiCN 06 to TiCN 10. The dark grey coating are thin films in which the carbon and nitrogen have not reacted completely with titanium, due to their lower process temperature, while increasing the temperature the amount of carbon and nitrogen increases maintaining the other process parameter fixed (samples TiCN 06 to TiCN 10) and the brown and red colours are obtained. This means that the process temperature is

the fundamental parameter to obtain the complete reaction of the species involved and a minimum of temperature is required.

TABLE 12: PROCESS PARAMETERS OF TiCN MGN COATINGS.

<i>Sample n°</i>	<i>Ar (sccm)</i>	<i>CH₄ (sccm)</i>	<i>N₂ (sccm)</i>	<i>Temp (°C)</i>	<i>Color</i>	<i>Ti%</i>	<i>C%</i>	<i>N%</i>
<i>TiCN 02</i>	<i>13</i>	<i>6,5</i>	<i>4</i>	<i>200</i>	<i>Dark grey</i>	<i>17,69</i>	<i>36,88</i>	<i>45,43</i>
<i>TiCN 03</i>	<i>13</i>	<i>6,5</i>	<i>3</i>	<i>200</i>	<i>Dark grey</i>	<i>24,57</i>	<i>39,34</i>	<i>36,09</i>
<i>TiCN 04</i>	<i>13</i>	<i>4</i>	<i>3</i>	<i>300</i>	<i>Dark grey</i>	<i>34,8</i>	<i>26,17</i>	<i>39,02</i>
<i>TiCN 06</i>	<i>17</i>	<i>4</i>	<i>3</i>	<i>430</i>	<i>Brown</i>	<i>25,49</i>	<i>27,22</i>	<i>47,29</i>
<i>TiCN 09</i>	<i>17</i>	<i>4</i>	<i>3</i>	<i>400</i>	<i>Brown</i>	<i>37,13</i>	<i>22,34</i>	<i>40,53</i>
<i>TiCN 10</i>	<i>17</i>	<i>4</i>	<i>3</i>	<i>350</i>	<i>Brown</i>	<i>42,36</i>	<i>21,85</i>	<i>35,79</i>

Observing the SEM micrography reported Figure 38 and Figure 39 it is immediately visible that the coatings have different surface morphology. The film of the TiCN 09 deposition shows the surface full of small round tridimensional clusters of carbonitrides. On the other hand, the film of TiCN 10 shows a surface arrangement similar to the titanium nitride previously studied with a pyramid-shape clusters. These results suggest that these films have different typologies of nucleation and the structures resulted will present different behavior versus the wear rate analysis.

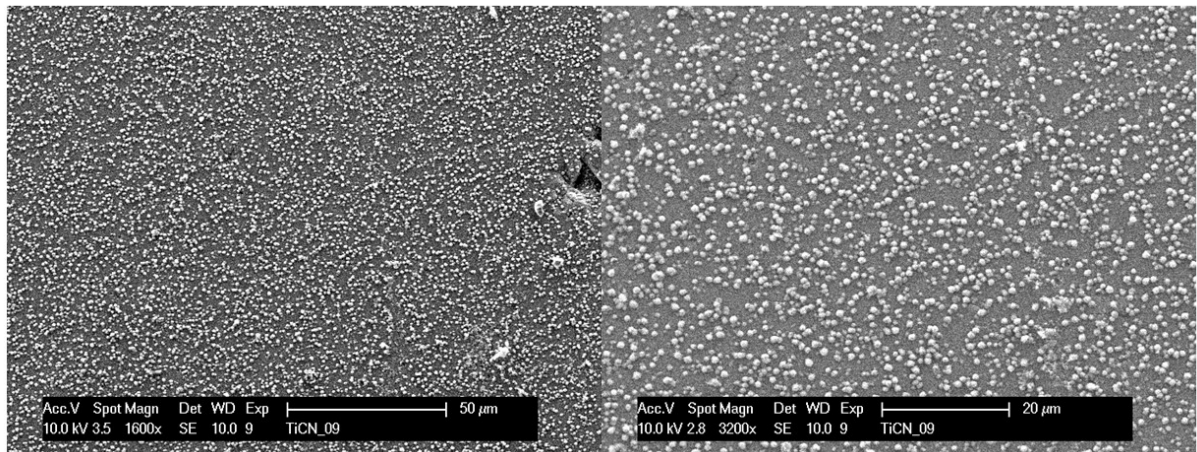


Figure 38: SEM micrography of TiCN_09 coating at different magnifications.

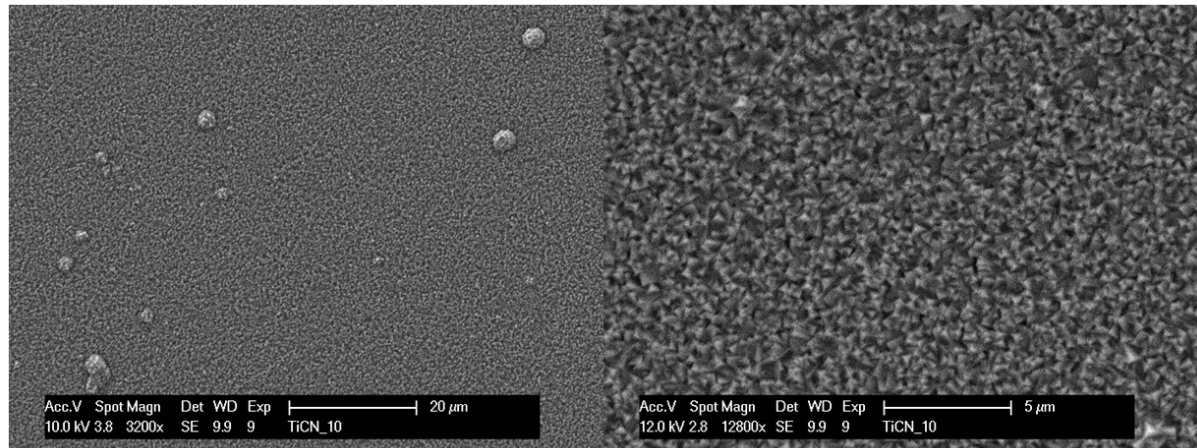


Figure 39: SEM micrography of TiCN_10 coating at different magnifications.

The XRD analysis verify the presence of TiCN crystal lattice with the chemical composition of $TiC_{0.3}N_{0.7}$, according to the stoichiometry researched. The $TiC_{0.3}N_{0.7}$ presents a cubic structure with two predominant peaks (111) at 36,47 2Theta and (022) at 42,36 2Theta. The diffractograms reported in Figure 40 show a difference in the orientation between the TiCN 09 and TiCN 10 coatings: TiCN 09 presents a preferential growing direction forming 111 crystal planes, while the TiCN 10 grows preferentially along 022 direction, explaining the two different surfaces analyzed with SEM micrography.

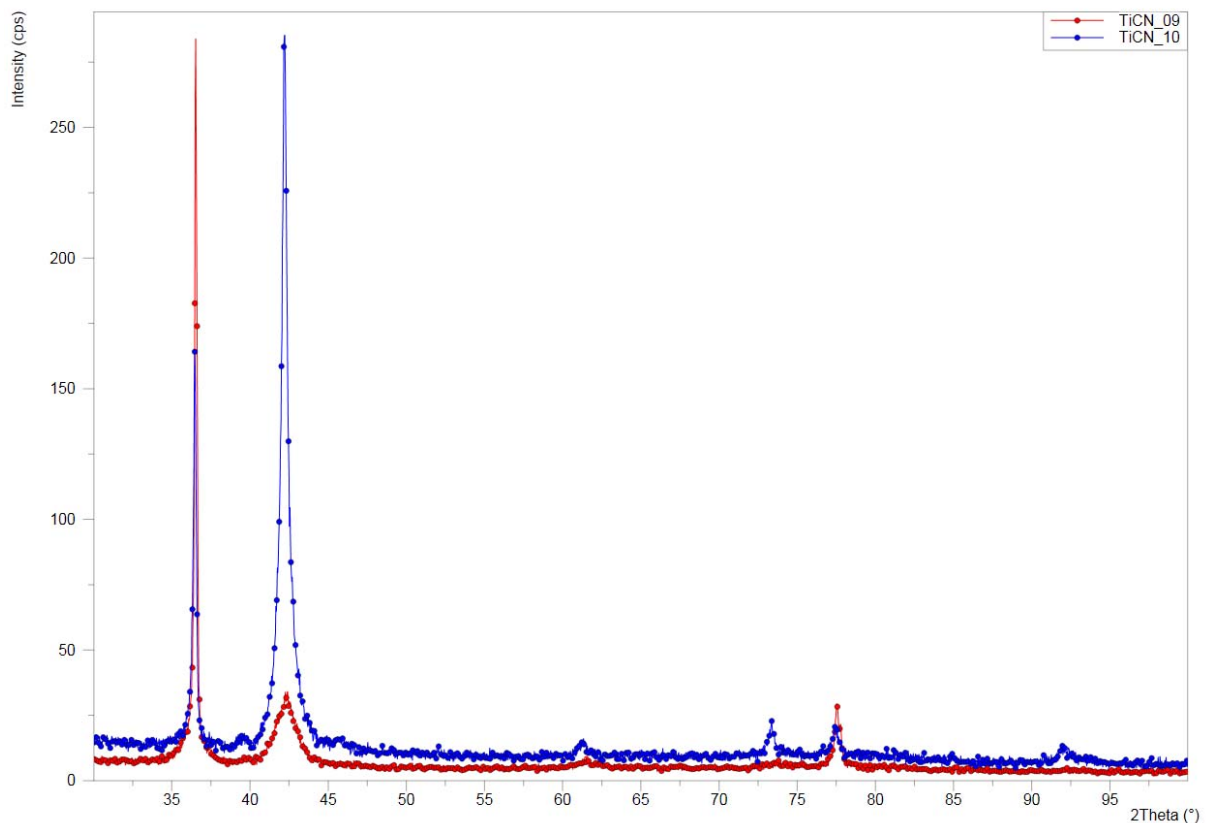


Figure 40: XRD spectra of TiCN coatings showing a different preferential growing orientation (TiCN 09 and TiCN 10).

5.3 Conclusions of Magnetron sputtering coatings

The magnetron sputtering techniques showed the possibility to deposit hard materials as TiN and TiCN. Obviously, the process parameters are fundamental to obtain the coating with the physical properties desired. Our goal for this part of the research is the identification of the coatings deposited via magnetron sputtering that can improve the lifetime of the lamination rolls made of tungsten carbide. For this reason four planar samples of tungsten carbide are deposited, respectively two of them with TiN and two with TiCN, as reported in Table 13, that will be subsequently evaluated from the point of view of their wear rate.

TABLE 13: MAGNETRON SPUTTERING DEPOSITION PARAMETERS AND SUBSTRATE MATERIALS.

<i>Deposition Parameters</i>	<i>Substrate material</i>
<i>TiN 22</i>	<i>EC10F</i>
<i>TiN 23</i>	<i>EC10F</i>
<i>TiCN 09</i>	<i>EC10F</i>
<i>TiCN 10</i>	<i>EC10F</i>

Chapter 6: Hard coatings deposited via Cathodic Vacuum Arc (CVA)

This chapter reports the influence of the process parameters on the stoichiometry and on the structure of the coatings deposited with the cathodic vacuum arc techniques. In particular, the attention is focused on the process temperature, on the fluxes of the gases used for the deposition and on the bias applied to the substrate. Three different hard materials are deposited and characterized: the titanium nitride (TiN), the titanium carbonitride (TiCN) and the chromium carbonitride (CrCN).

6.1 TiN Cathodic Vacuum Arc Coatings

To compare the physical properties (for example wear rate) of the hard coatings obtained with different deposition techniques, in this work of thesis the research activity has been focused on the determination of the right process parameters for the thin film deposition of titanium nitride via cathodic vacuum arc technique. The CVA source used for the thin film deposition is a commercial GPA source 80 mm diameter planar cathode 10 mm thick of Ti 99,99%. All the test coatings are realized depositing the thin films (2 μm thick) on quartz substrates previously cleaned in specific chemical bath and starting from a base vacuum pressure lower than $9 \cdot 10^{-6}$ mbar. The distance between the cathode and the substrate is maintained fixed at 15 cm. The CVA technique is more energetic than magnetron sputtering, in fact, as reported in the Table 14, the TiN coatings realized reach the yellow color without thermal treatments. In this part of the thesis it is analyzed the influence of the bias (negative potential applied to the sample to accelerate the plasma ions impacting on the surface) usually applied to reduce the amount of macroparticles on the coating and to densify the coating structure.

TABLE 14: PROCESS PARAMETERS OF TiN CVA DEPOSITIONS.

<i>Sample n°</i>	<i>Arc current (A)</i>	<i>N₂ (sccm)</i>	<i>Bias (V)</i>	<i>Color</i>	<i>Ti%</i>	<i>N%</i>
<i>TiN CVA 03</i>	<i>80</i>	<i>35</i>	<i>0</i>	<i>Yellow</i>	<i>37,64</i>	<i>62,36</i>
<i>TiN CVA 06</i>	<i>80</i>	<i>35</i>	<i>-30</i>	<i>Yellow</i>	<i>46,06</i>	<i>53,94</i>
<i>TiN CVA 07</i>	<i>80</i>	<i>35</i>	<i>-30</i>	<i>Yellow</i>	<i>46,14</i>	<i>53,86</i>
<i>TiN CVA 08</i>	<i>80</i>	<i>35</i>	<i>-100</i>	<i>Yellow</i>	<i>54,78</i>	<i>45,22</i>
<i>TiN CVA 09</i>	<i>80</i>	<i>35</i>	<i>-100</i>	<i>Yellow</i>	<i>52,39</i>	<i>47,61</i>

As reported in Table 14, the bias increases the Ti content, due to higher attraction of the Ti ions produced from the cathode. Moreover, reaching -100 V the DC bias effect is positive from the point of view of macroparticles reduction, but it is dramatically negative for the stress induced on the coatings structure. In fact, the SEM micrography reported in Figure 41 shows the presence of superficial cracks, due to the stress produced from the high plasma energy. The residual stress is confirmed from the XRD analysis (where it is evidenced the increase of the amorphous contribution at higher voltage).

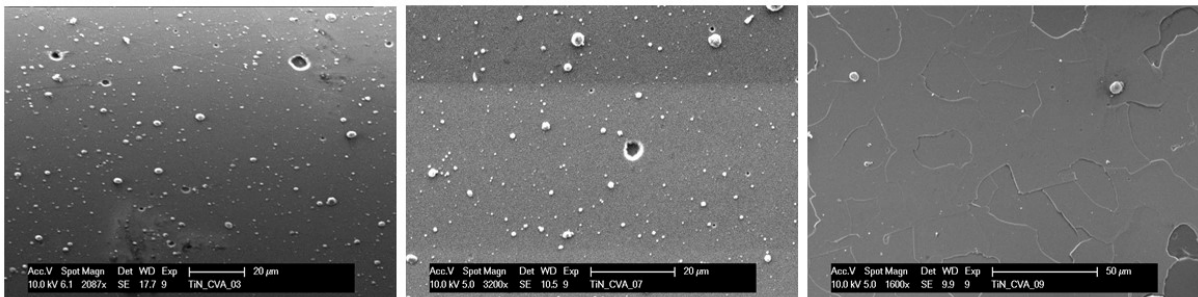


Figure 41: SEM micrography of TiN CVA coatings for different DC bias applied (0 V, -30 V, -100 V).

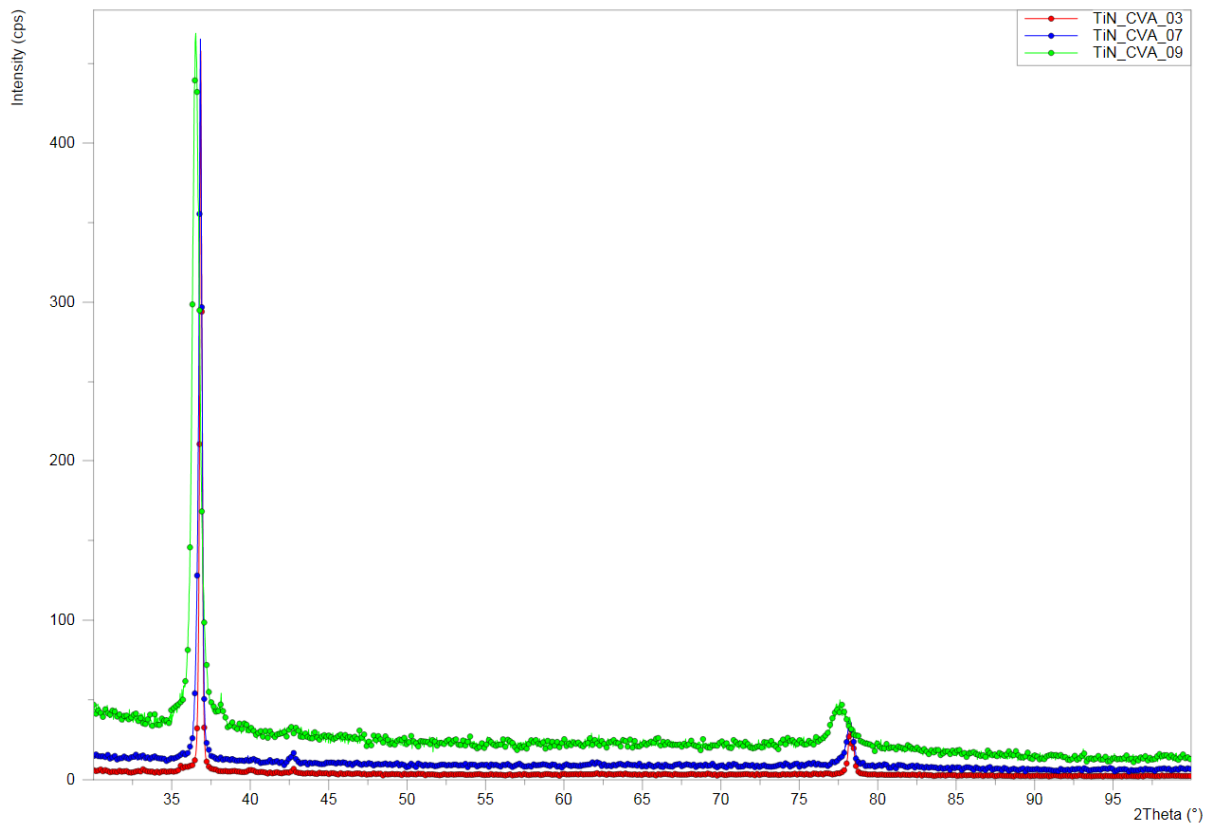


Figure 42: TiN XRD spectra in function of the DC bias applied.

6.2 TiCN Cathodic Vacuum Arc Coatings

The second run of CVA depositions has been focused on the determination of the right process parameters for the thin film deposition of titanium carbon nitride. The CVA source used for the thin film deposition is the same source utilized for TiN depositions: 90 mm diameter planar cathode 17 mm thick of Ti 99,99%. All the test coatings are realized depositing the thin films (2 μm thick) on quartz substrates previously cleaned for vacuum applications and starting from a base pressure lower than $9 \cdot 10^{-6}$ mbar. From the experiments tabulated immediately after, it is possible to affirm the proportion of the atoms in coating material depends on the treatment temperature and on the gas flux ratio. In particular, the formation of the carbonitrides starts with a temperature above 380 °C.

TABLE 15: PROCESS PARAMETERS OF TiCN CVA COATINGS.

<i>Sample n°</i>	<i>CH₄ (sccm)</i>	<i>N₂ (sccm)</i>	<i>Color</i>	<i>Temperature (°C)</i>	<i>Ti%</i>	<i>C%</i>	<i>N%</i>
<i>TiCN CVA 01</i>	<i>3</i>	<i>35</i>	<i>Yellow</i>	<i>-</i>	<i>48,92</i>	<i>3,84</i>	<i>47,25</i>
<i>TiCN CVA 02</i>	<i>5</i>	<i>35</i>	<i>Yellow</i>	<i>-</i>	<i>55,36</i>	<i>3,41</i>	<i>41,24</i>
<i>TiCN CVA 03</i>	<i>5</i>	<i>35</i>	<i>Yellow</i>	<i>-</i>	<i>49,28</i>	<i>4,00</i>	<i>46,72</i>
<i>TiCN CVA 04</i>	<i>10</i>	<i>35</i>	<i>Yellow</i>	<i>-</i>	<i>51,20</i>	<i>6,97</i>	<i>41,83</i>
<i>TiCN CVA 05</i>	<i>15</i>	<i>15</i>	<i>Grey</i>	<i>-</i>	<i>57,43</i>	<i>23,07</i>	<i>19,49</i>
<i>TiCN CVA 06</i>	<i>10</i>	<i>35</i>	<i>Brown/yellow</i>	<i>380</i>	<i>49,62</i>	<i>8,86</i>	<i>41,52</i>
<i>TiCN CVA 07</i>	<i>15</i>	<i>15</i>	<i>Yellow/grey</i>	<i>395</i>	<i>65,95</i>	<i>17,84</i>	<i>16,22</i>
<i>TiCN CVA 09</i>	<i>10</i>	<i>35</i>	<i>Brown</i>	<i>400</i>	<i>55,46</i>	<i>6,48</i>	<i>38,06</i>

From the X-Ray spectra of samples TiCN_04, TiCN_06 and TiCN_09 it is observed that the temperature to obtain a hard coating with a crystalline structure is 400°C. In fact, for a lower temperature the amorphous contribution indicated from the background level of the XRD spectra is much higher.

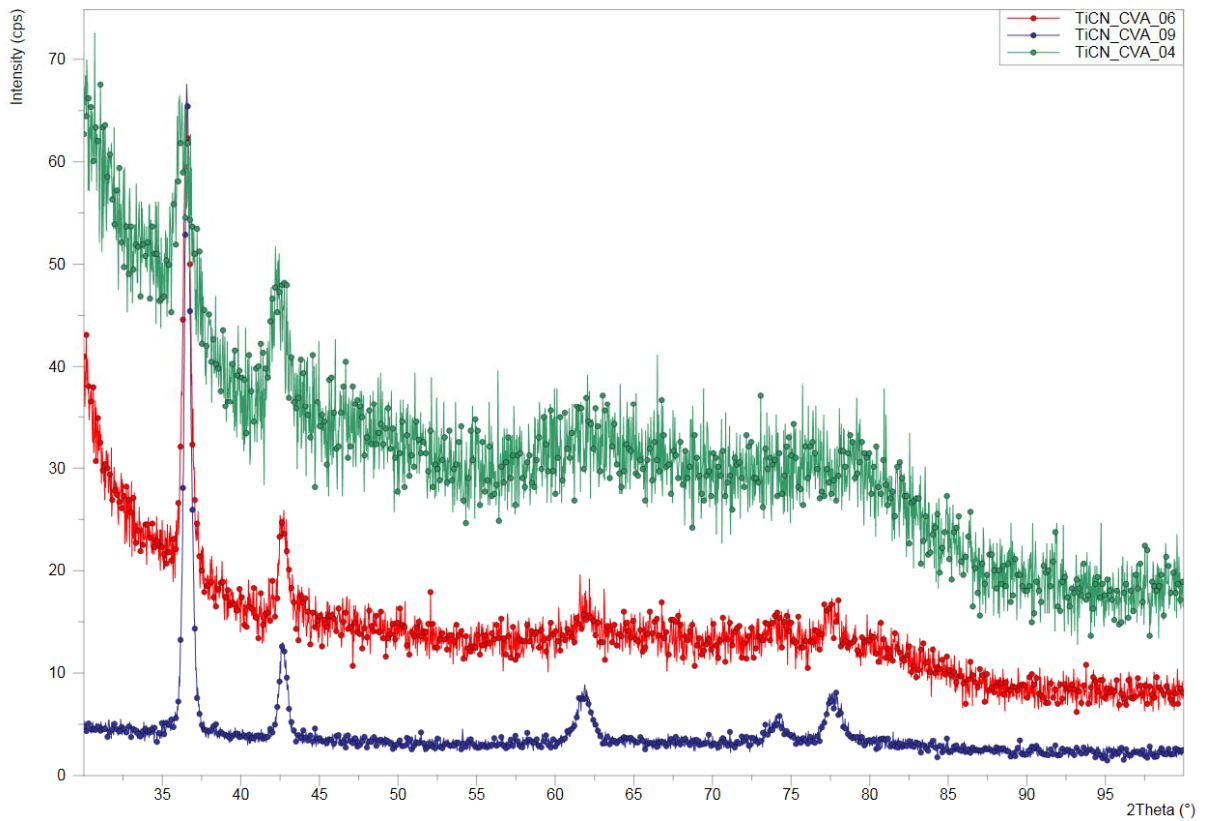


Figure 43: XRD spectra of TiCN coatings in function of the process temperature.

The SEM micrography reported in Figure 44 shows a coating surface completely different from the one obtained with magnetron sputtering: in this case, the thin film grows as island, as evidenced at higher magnification, and presents the unavoidable macroparticles.

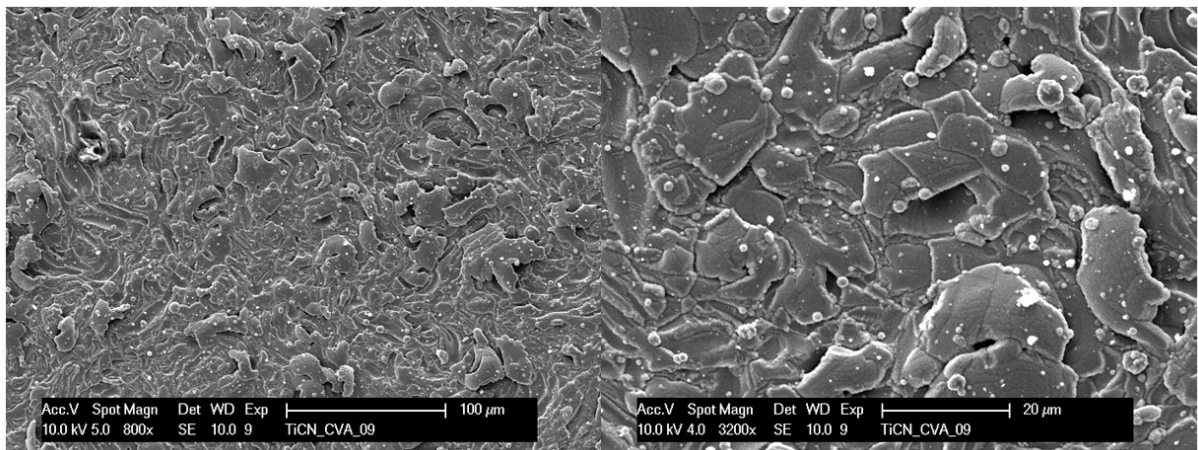


Figure 44: SEM micrography of TiCN CVA 09 coating at different magnifications.

6.3 CrCN Cathodic Vacuum Arc Coatings

The last run of CVA depositions has been focused on the determination of the right process parameters for the thin film deposition of chromium carbon nitride. The CVA source used for the thin film deposition is the same source utilized for TiN and TiCN depositions with a Cr 99,95% target of 90 mm diameter and 17 mm thick. All the test coatings are realized depositing the thin films (2 μm thick) on quartz substrates previously cleaned for vacuum applications and starting from a base pressure lower than $9 \cdot 10^{-6}$ mbar. As reported in Table 16, the composition of the coating is dependent of the fluxes ratio of the reactive gases and the temperature needed to obtain the coating is not very high (at least 150 °C).

TABLE 16: PROCESS PARAMETERS OF CrCN CVA COATINGS.

<i>Sample n°</i>	<i>CH₄ (sccm)</i>	<i>N₂ (sccm)</i>	<i>Color</i>	<i>Temperature (°C)</i>	<i>Cr%</i>	<i>C%</i>	<i>N%</i>
<i>CrCN CVA 01</i>	<i>10</i>	<i>35</i>	<i>Grey</i>	<i>300</i>	<i>63,76</i>	<i>5,33</i>	<i>44,56</i>
<i>CrCN CVA 02</i>	<i>15</i>	<i>25</i>	<i>Grey</i>	<i>250</i>	<i>53,01</i>	<i>20,40</i>	<i>26,59</i>
<i>CrCN CVA 03</i>	<i>15</i>	<i>15</i>	<i>Grey</i>	<i>150</i>	<i>40,90</i>	<i>18,90</i>	<i>40,20</i>
<i>CrCN CVA 04</i>	<i>10</i>	<i>20</i>	<i>Grey</i>	<i>150</i>	<i>50,03</i>	<i>26,70</i>	<i>23,27</i>
<i>CrCN CVA 05</i>	<i>15</i>	<i>30</i>	<i>Grey</i>	<i>150</i>	<i>43,14</i>	<i>29,81</i>	<i>27,05</i>

Moreover, from the observation of the XRD spectra reported in Figure 45 it is possible to verify that the temperature is not fundamental for the coating production. In fact, the peak (200) of CrCN located at $44,89^\circ 2\theta$ is not influenced from the temperature treatment but from the fluxes ratio for the reactive gases used to create the coating as evidenced from the crystal structure of sample CrCN CVA 05. The cubic crystal structure of sample CrCN CVA 05 deposited at 150 °C shows the absence of the amorphous contribution (symptom of a not complete reaction of Cr with the reactive gases) respect to the other coatings analyzed. Concluding the right fraction of reactive gases is fundamental to obtain a cubic CrCN completely crystalline and with a preferential plane growing along (200) direction.

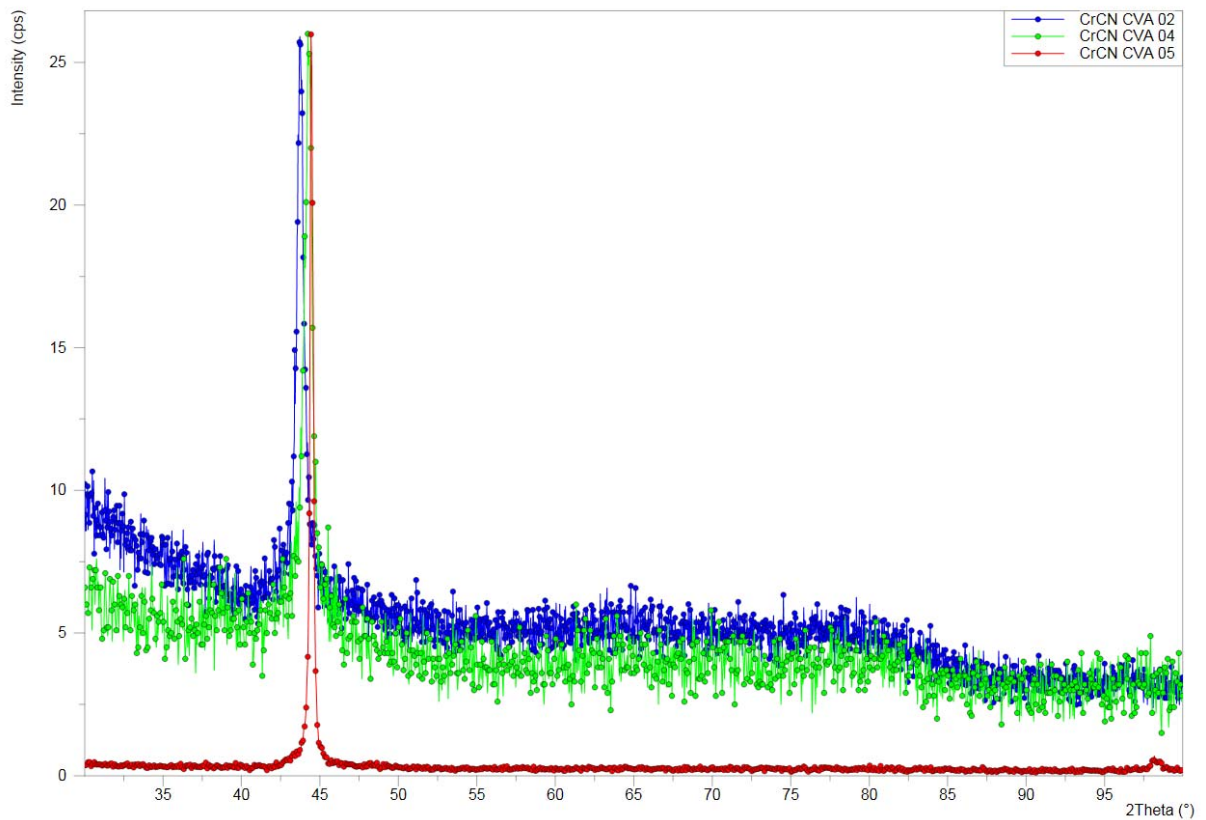


Figure 45: XRD spectra of CrCN coatings in function of the process temperature and reactive gases ratio.

The SEM analysis reported in Figure 46 shows that the coating surface of CrCN CVA 05 is particularly smooth in respect to the TiCN coatings suggesting a different behavior from the point of view of the wear rate estimation.

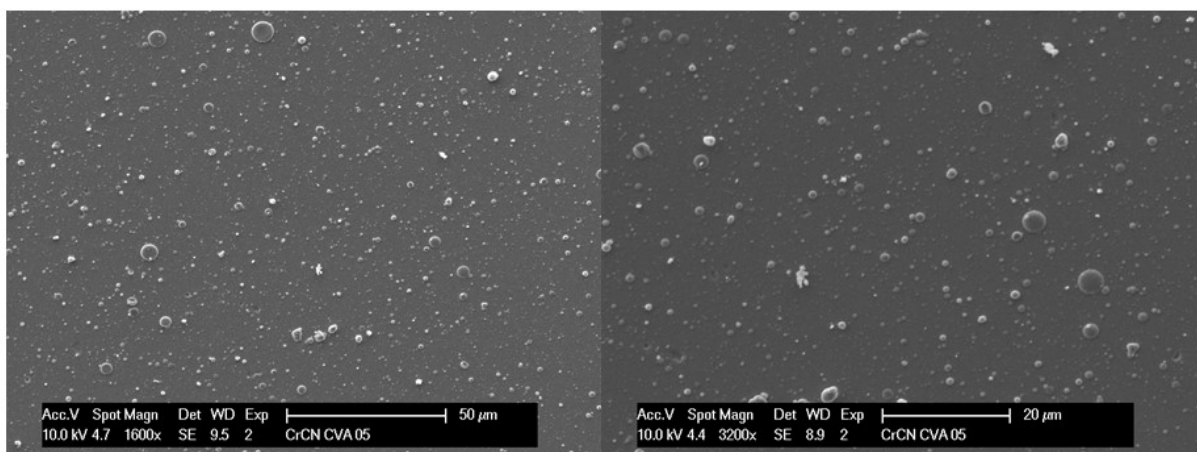


Figure 46: SEM micrography of CrCN CVA 05 coating at different magnifications.

6.4 Conclusion of Cathodic Vacuum Arc Coatings

The cathodic vacuum arc techniques showed the possibility to deposit hard materials as TiN and TiCN and CrCN. Obviously, the process parameters are fundamentals to obtain the coating with the physical properties desired. As for magnetron sputtering coatings, the goal of the research is the identification of the coatings deposited, in this case via cathodic vacuum arc that can improve the lifetime of the lamination rolls made of tungsten carbide. For this reason, three planar samples of tungsten carbide are deposited , respectively with TiN, TiCN and CrCN as reported in Table 17, that will be subsequently evaluated from the point of view of their wear rate.

TABLE 17: CATHODIC VACUUM ARC DEPOSITION PARAMETERS AND SUBSTRATE MATERIALS.

<i>Deposition Parameters</i>	<i>Substrate material</i>
<i>TiN CVA 07</i>	<i>EC11M</i>
<i>TiCN CVA 09</i>	<i>EC10F</i>
<i>CrCN CVA 05</i>	<i>EC10F</i>

Chapter 7: Wear Rate Evaluation of the PVD coatings.

The wear rate evaluation is the laboratory test that confirms if the coatings improve or not the lifetime of the tungsten carbide wire rolls. This analysis is realized from an external laboratory under the commission of Eurolls company. This laboratory has got all the infrastructures (in this case a tribometer Bruker CETR UMT-3) to evaluate the wear rate of the coatings deposited on the tungsten carbide rolls and it is located at the polytechnic department of engineering and architecture of Udine University. The wear rate test chosen is the balls on flat test (reported in Figure 47), a standard for the physical property analyzed³⁷⁻³⁹. The ball on flat is also the system that simulates with the higher approximation the real interaction of the wire with the rolls surface in the industrial environment. The wear rate test configuration consists in a ball of alumina maintained fixed in its position and pressed against the surface of the sample with a force of 80 N, in a Hertzian motion along its axis perpendicular to the force applied. The parameters adopted for the wear rate tests are reported in the following table:

TABLE 18: WEAR RATE TEST PARAMETERS.

<i>Wear Rate Test Parameters</i>	<i>Values</i>
<i>Force applied</i>	<i>80 N</i>
<i>Temperature test</i>	<i>25 °C</i>
<i>Frequency</i>	<i>10 Hz</i>
<i>Stroke Length</i>	<i>10 mm</i>
<i>Time</i>	<i>1 h</i>

Considering all the data reported in Table 18, the equation^{37,39} chosen to evaluate the wear rate of the different substrates and coatings analyzed is:

$$K = \frac{V}{F \cdot S} \left[\frac{\text{mm}^3}{\text{N} \cdot \text{m}} \right] \tag{Equation 9}$$

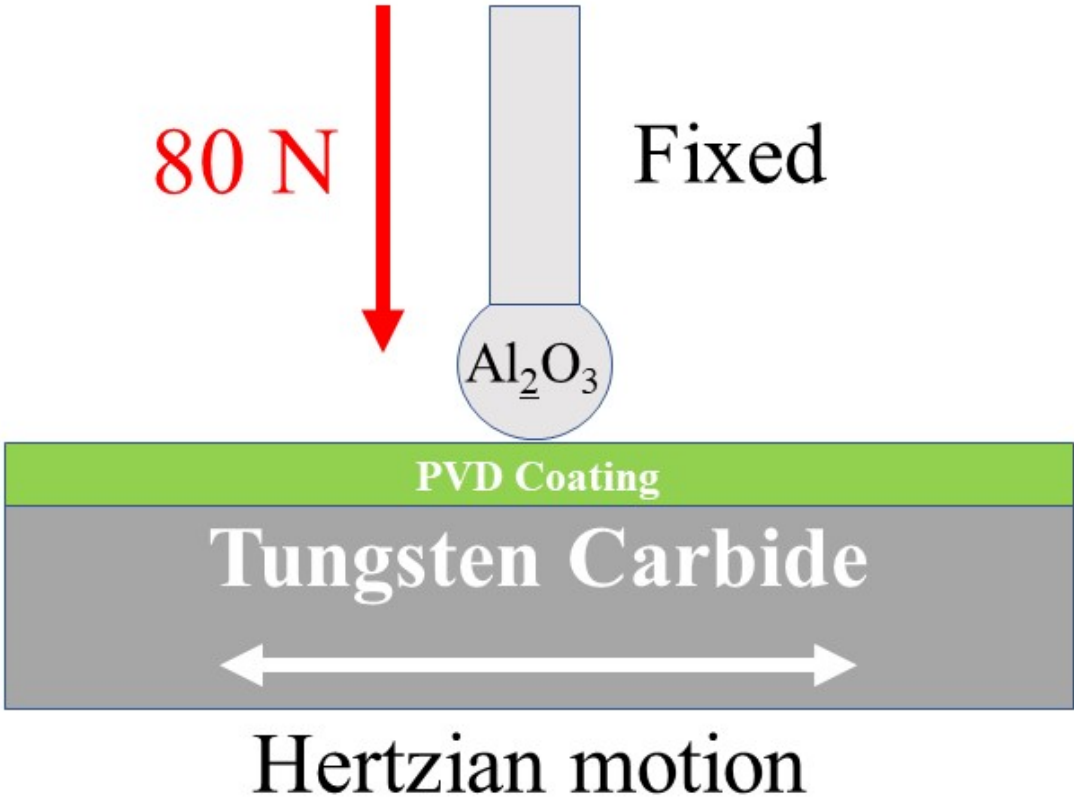


Figure 47: ball on flat configuration for the wear rate evaluation.

The results obtained from the wear rate tests are reported in the bar chart of Figure 48. The graph reports the wear rate of different blank materials (the grey bars), of which the composition is not reported for Eurolls confidentiality, but it is enough to know that different tungsten carbide samples have different content of cobalt. It is immediate to observe that the wear rates of the blank substrates increase with the relative abundance of cobalt (EC10F is the blank substrate with the lowest wear rate, while EC16F presents the highest value). In the graph it is also reported the wear rate of different coatings materials deposited with the cathodic vacuum arc techniques (green bars) and with magnetron sputtering techniques (red bars). The wear rates of the WC sample coated with a thin film of 2 microns produced with

the cathodic vacuum arc and magnetron sputtering technique not always are lower than the blank substrates. This demonstrates that only a specific hard coating deposited with PVD techniques can improve the lifetime of the WC rolls. The samples deposited by MGN sputtering techniques always present the wear rate higher than the one deposited by the cathodic vacuum arc, this means that the wear rate is dependent not only on the material deposited but also on the quality of the coating. The thin films deposited with cathodic vacuum arc are always denser than the magnetron sputtering ones, due to the higher energy of the process. Moreover, the coatings deposited with magnetron sputtering present different values of wear rate and this can be explained with the different coating structure. In fact, the sample TiN 23 and TiCN 10 have from SEM analysis an analogous surface topography consisting of tridimensional structures similar to pyramids, as reported in Figure 37 and Figure 39. These results confirm that the coating structures is fundamental to obtain the performance researched. Furthermore, the values of the wear rate estimated for these samples are closer to the ones obtained with cathodic vacuum arc.

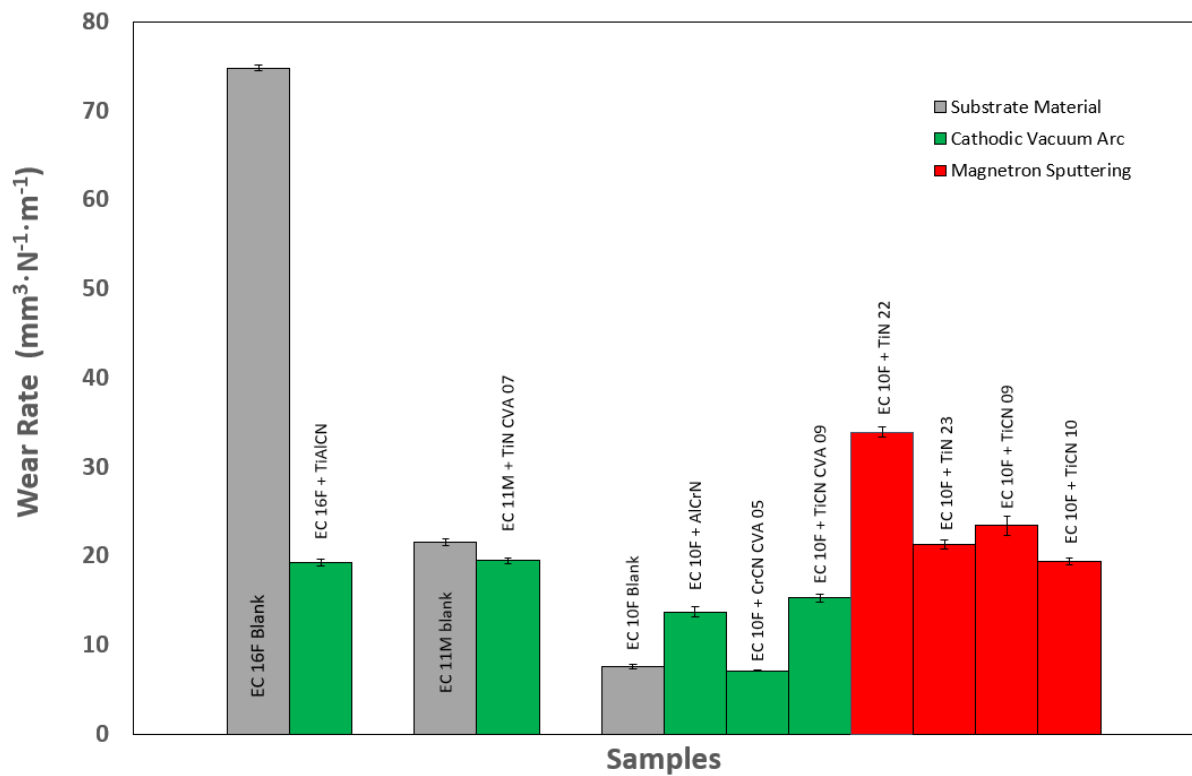


Figure 48: wear rate measurements of different WC blank substrates, coating materials and deposition techniques.

7.1 Conclusions of the Wear Rate Evaluation.

The results obtained from the wear rate tests are significant to determine the right coating to apply on the tungsten carbide wire rolls. The materials and the technology used to deposit the thin film, significantly modify the response of the wear rate test, independently from the blank base material on which the coatings are deposited. The highest performance is obtained from the sample coated with a hard material via cathodic vacuum arc technique (CrCN on EC10F) with a measured wear rate of $7,14 \text{ mm}^3 \cdot \text{N} \cdot \text{m}^{-1}$. The magnetron sputtering thin films measured on EC10F do not improve the wear rate of the base material, but they could be applied on softer materials as EC11M and EC16F to increase the lifetime or to create coatings with complex multilayer structures (as CVA plus MGN) already foreseen for further researches.

Chapter 8: Magnetron sputtering Source Design

The design of the magnetron sputtering source is one of the challenges of this work of thesis. The coating high of the system previously established in 600 mm determines the length of the planar source, while the wide one is chosen in order to confine the deposition only in the frontal part of the rotating carousel (sample holder). The source developed is a rectangular magnetron sputtering with a planar cathode 600 mm length and 130 mm width.

The magnetron sputtering source is 3D (three dimensional) designed by the Autodesk Inventor software and its axonometric view is reported in Figure 49.

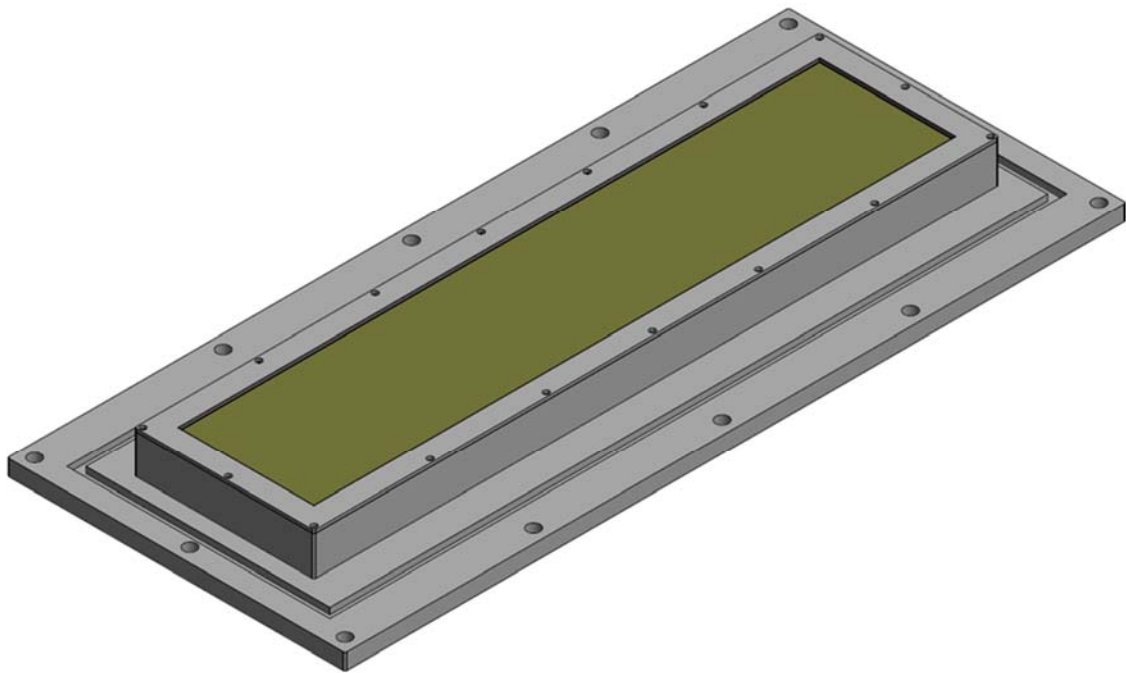


Figure 49: axonometric view of the magnetron sputtering source developed.

To better understand the design of the magnetron sputtering source we have to focus the attention on the abnormal glow discharge, where currents in the order of Amperes, and voltages in the order of hundreds, are necessary to maintain the plasma discharge (see Figure 6). These differences of potential are allowed decoupling the cathode (negative potential of

hundreds of Volts) from the coating chamber walls (grounded) connected with the ground shield of the magnetron source. This is immediately notable observing the cross section of the magnetron sputtering source reported in Figure 50, where in blue is indicated the ground shield potential and in red the cathode potential, divided interposing a Teflon insulator 1 cm thick colored in white. The distance between the cathode and the ground shield is always around 1 mm, to prevent the undesirable plasma ignition in these regions. The cathode body is made of OFHC copper while the grounded shield is in stainless steel 304.

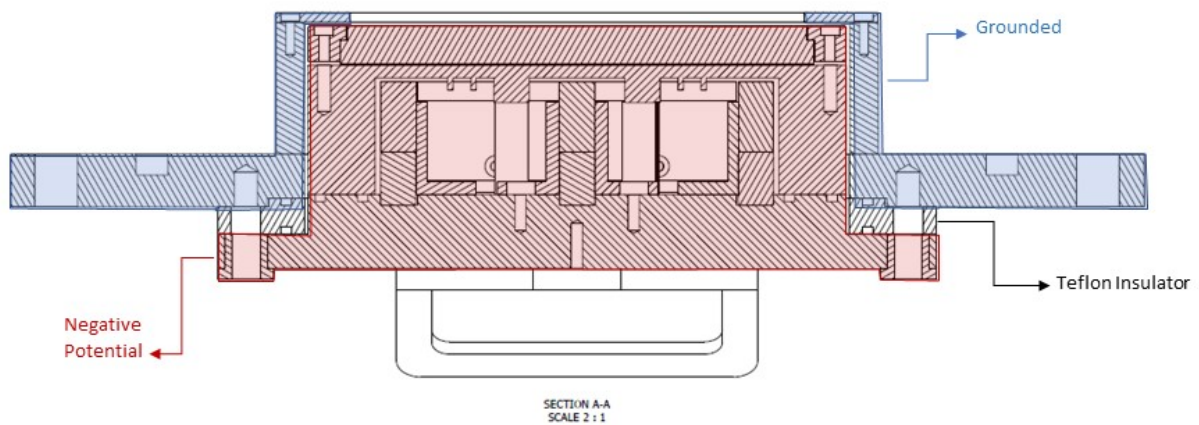


Figure 50: cross section of the magnetron sputtering source evidencing the potentials applied.

A fundamental part of the design of the MGN source is the magnet pack configuration. For this magnetron sputtering source the choice fell back in a configuration with an external rectangular array and a linear internal array of magnets (as reported in Figure 51) with opposite polarization, in order to close the magnetic lines on the cathode surface and to use the maximum possible area of the target. The working temperature for the magnets chosen for this MGN source is maximum 80 °C. For this reason the cathode must be water cooled immersing the magnets in a water flux as indicated in the cross section of Figure 52.

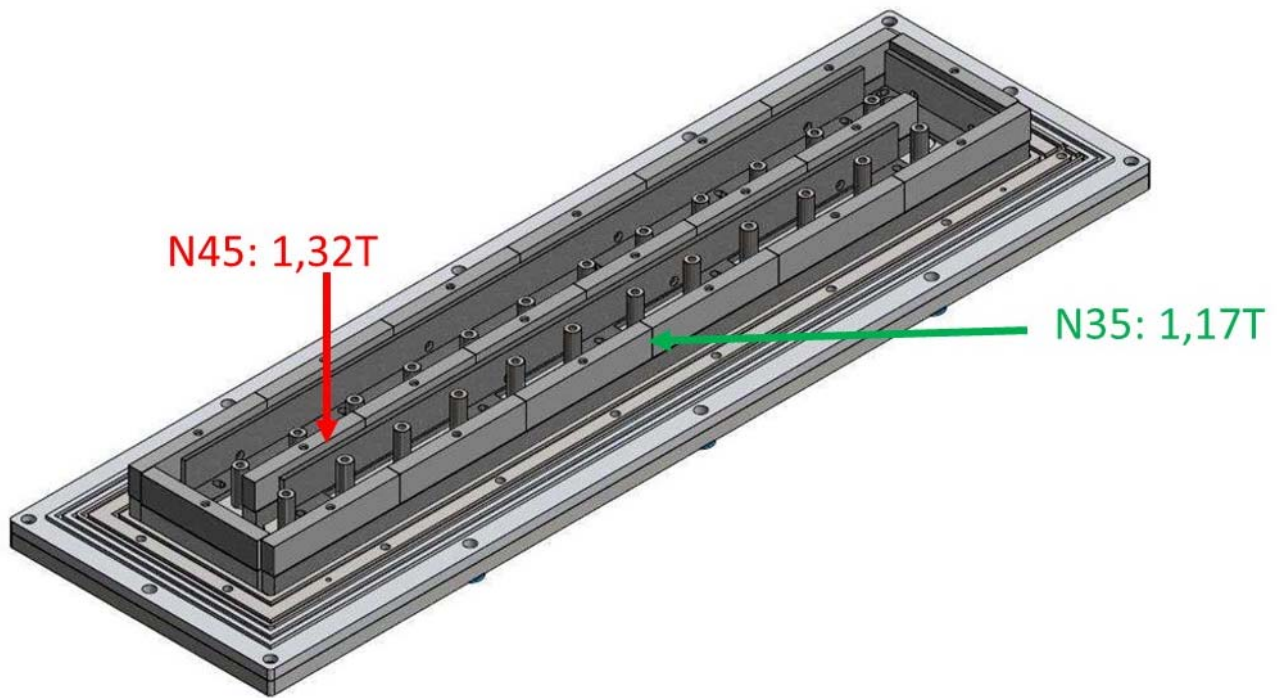


Figure 51: magnet pack configuration (external array N45, internal array N35).

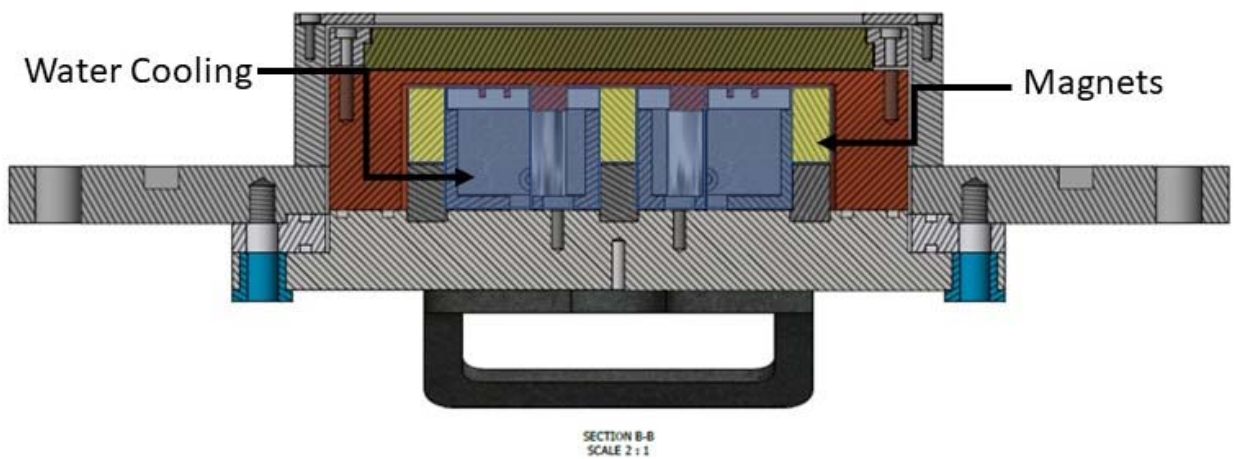


Figure 52: cross section of MGN source evidencing the water-cooling circuit and the magnets arrays.

One of the goals of the 3D design of the magnetron sputtering source is the production of an unbalanced magnetron source. For this reason, the choice of the magnets with the right magnetic field plays a fundamental role. To determine the right magnetic field a 2D FEM (two-dimensional finite element method) simulation is set up importing a section of the 3D CAD (Computer-Aided Design) drawing realized with Inventor. Once imported the 2D CAD section in the FEMM software version 4.2 the materials constituting the source, the magnetic field intensity and polarizations are associated to the specific components of the drawing. The magnets chosen for the simulations reported in Figure 53 are the N35 (1,17 T) for the external magnet pack and N45 (1,32 T) for the internal array. The boundary conditions for these simulations (where the magnetic field is considered tending to infinite) are indicated from the blue concentric lines.

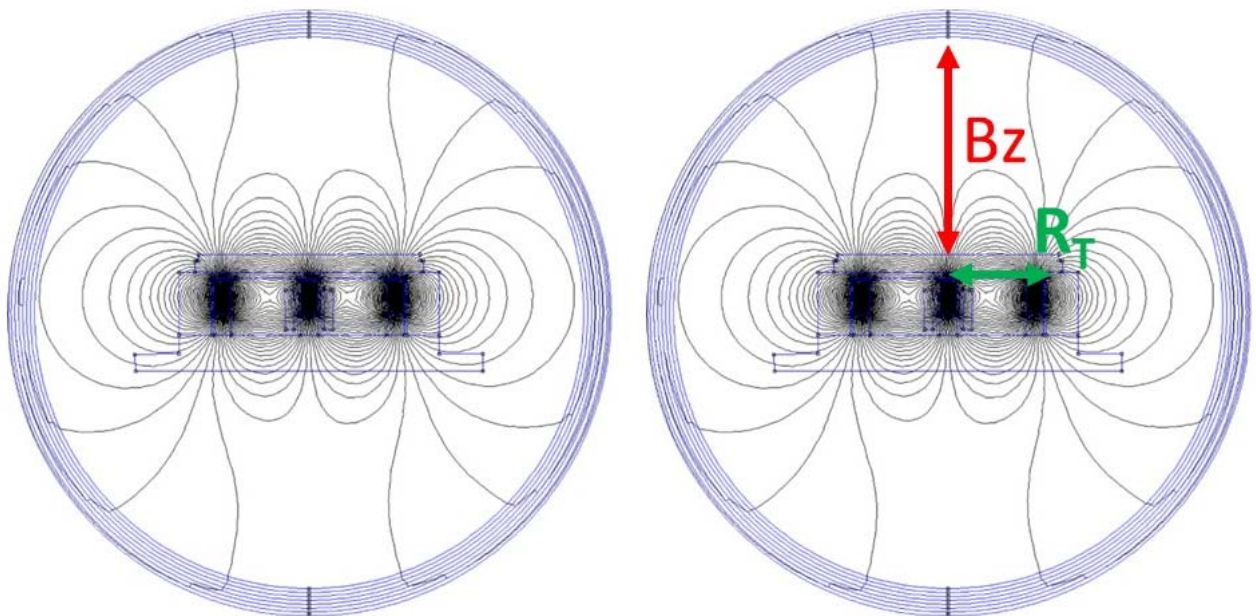


Figure 53: FEM simulation with N35 external magnet array and N45 inertnal magnet array.

With the equation: $g = \frac{B_z}{R_T}$ introduced from Gencoa it is possible to estimate the level of unbalancing of the magnetron sputtering sources, dividing the distance from the cathode surface at which B_z is equal to zero by the radius of the target. The magnetic field component B_z extrapolated from the 2D simulation of Figure 53 can be plotted in function of the distance from the cathode surface obtaining the graph reported in Figure 54. For this configuration the distance at which the B_z is equal to zero corresponds to 80 mm and diving by the radius of the target (65 mm) the result is a very unbalanced magnetron sputtering source ($g = 1,23$).

Moreover, focusing the attention of the radial component of the magnetic field on the surface of the cathode (reported in Figure 55) as introduced from Goree and Sheridan¹⁹: for a 3 inches cathode the B_r should stay in the range between 300 G and 600 G, to maximize the ionization rate of the plasma. At higher magnetic field the only effect is a reduction of the racetrack. The dimensions of the cathode developed in the PhD work are comparable with a 3 inches cathode and, as it can be verified the radial component of the magnetic field reaches maximum 500 G. This data verifies, also from this side, the correct choice of the magnet pack design.

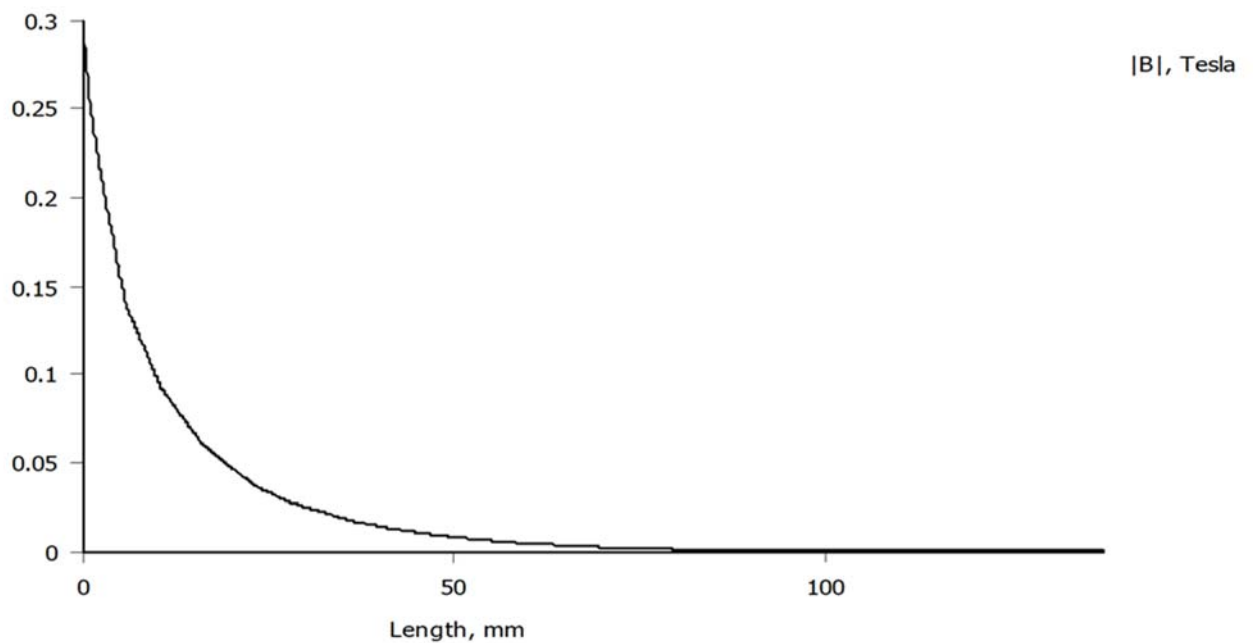


Figure 54: magnetic field component B_z in function of the distance from the cathode surface.

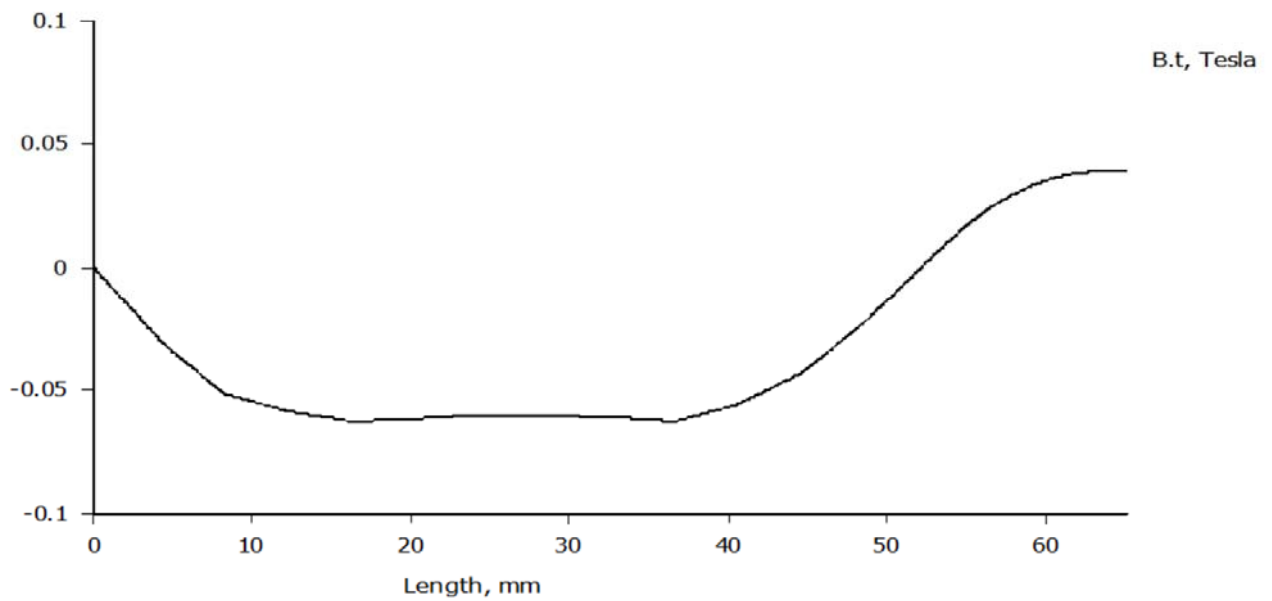


Figure 55: magnetic field component Br in function of the distance from the centre of the cathode.

The magnetron sputtering source is also a vacuum component of the Physical Vapour Deposition system. This means that the MGN source has a part which is exposed to atmospheric pressure and one exposed to the vacuum. The component has, then, to resist to a difference of pressure at least of 1 bar, condition analyzed with another finite element simulation. In this case the simulation is set up utilizing the simulation section predisposed in Autodesk Inventor imposing a difference of pressure of 1 bar between the atmospheric side and the vacuum side of the component (see Figure 56), the material of the cathode body (copper) and the constraints where the cathode is fixed to the external flange and then imposing blocked this surface (see Figure 57). The result of the simulation is reported in Figure 58 indicating the safety factor of the simulation. The value of the safety factor is the ratio between the maximum allowed stress and the equivalent stress (Von Mises) when the simulation is analyzing the yield strength, if the safety factor is less than 1 it means that a permanent deformation is present and the component cannot be accepted. The value obtained for the “vacuum simulation” of the cathode body is minimum 2,87, then no permanent deformation is present on the magnetron sputtering source.

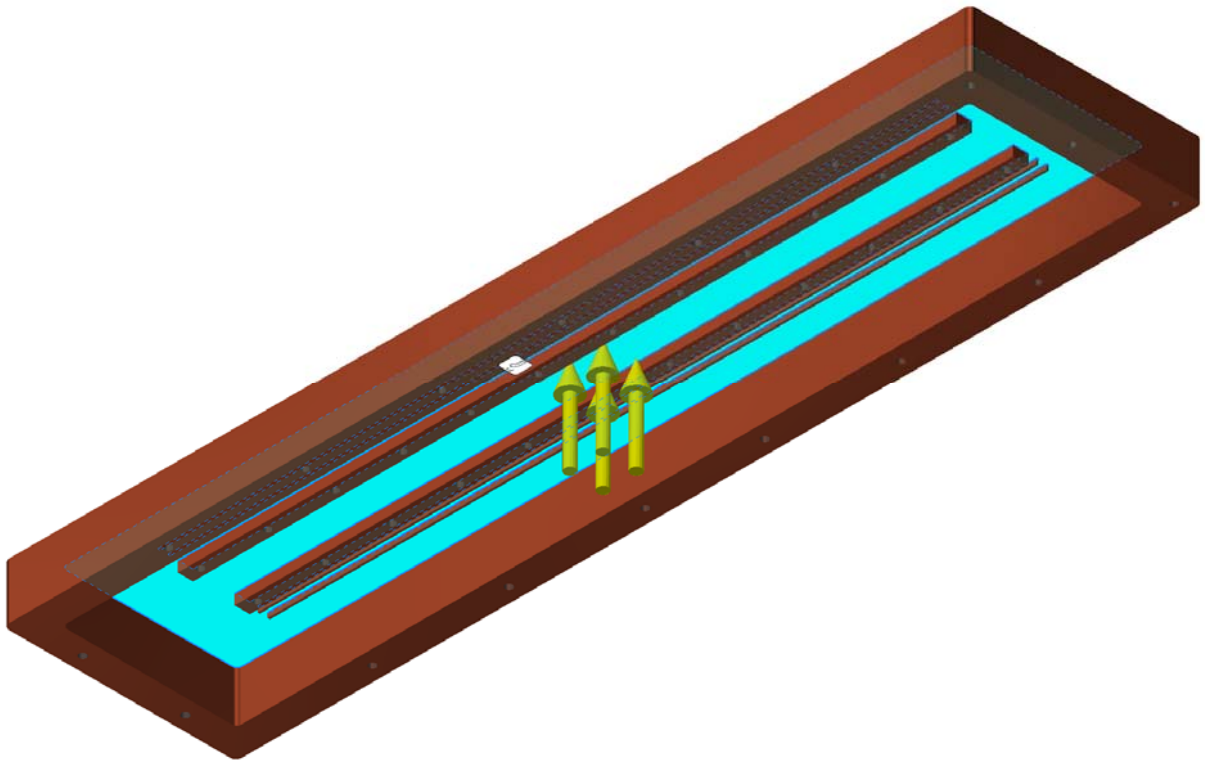


Figure 56: FEM simulation set up imposing a difference of pressure of 1 bar between the atmospheric and vacuum side of the cathode body.

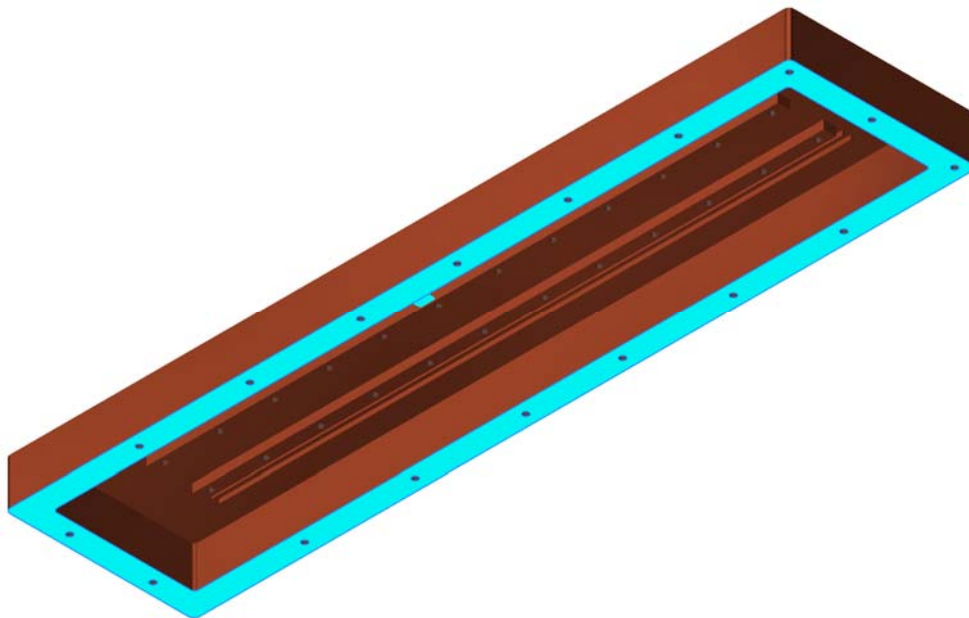


Figure 57: FEM simulation set up imposing the constraints where the cathode is fixed to the external flange.

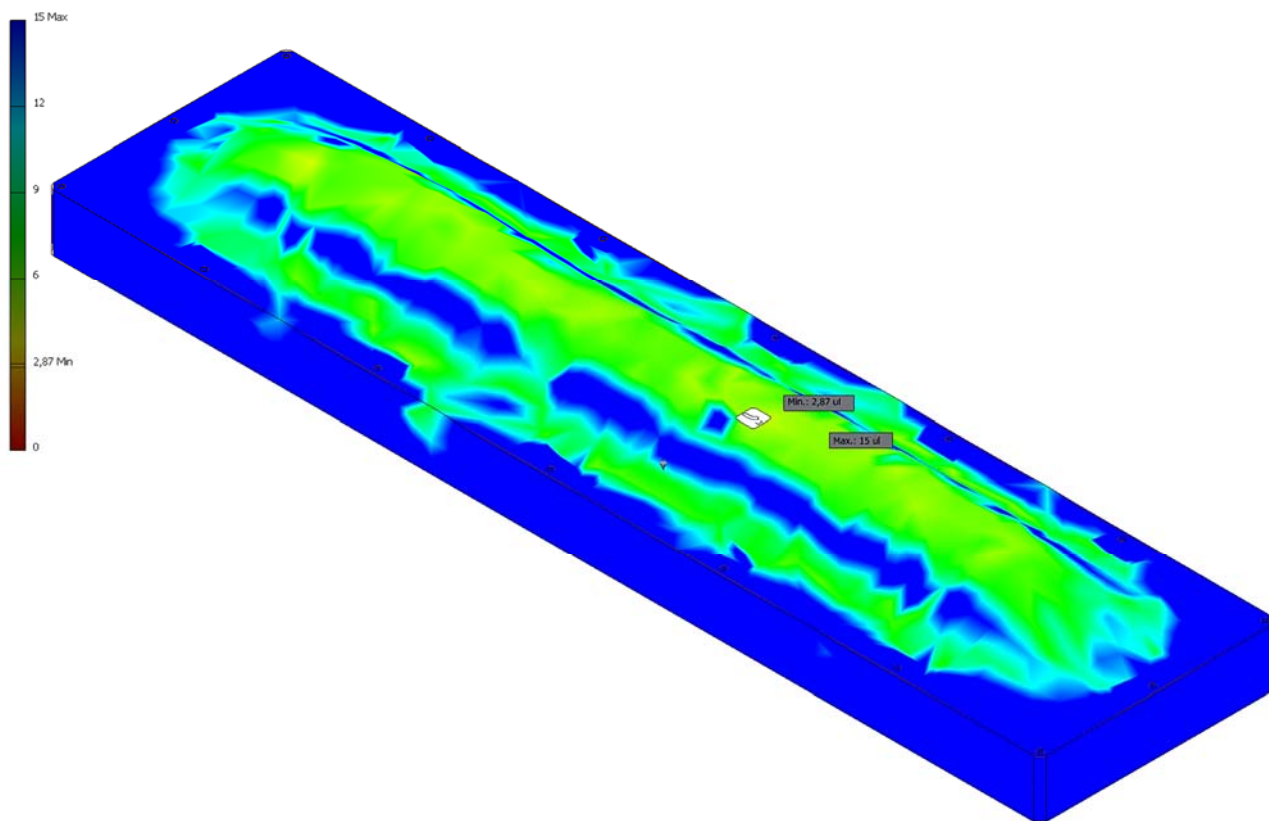


Figure 58: FEM results for the vacuum pressure simulation reported as safety factor.

Due to the presence of the magnet packs the cathode must be water-cooled, this means that the MGN source has a part exposed to the eater circuit pressure and one exposed to the vacuum. The component has, then, to resist to a difference of pressure at least of 4 bar, condition analyzed again with a finite element simulation. In this case, the simulation is set up imposing a difference of pressure of 4 bar between the water cooling side and the vacuum side of the component (see Figure 59) , as before the material of the cathode body (copper) and the constrains where the cathode is fixed to the external flange and then imposing blocked this surface (see Figure 57). The result of the simulation is reported in Figure 60 indicating the safety factor of the simulation: the value obtained for the “water cooling pressure simulation” of the cathode body is minimum 0,72, then with this configuration a permanent deformation is present on the magnetron sputtering source. This result makes necessary a stiffening of the magnetron source structure, reached adding a series of spacers (in aluminum 6061 to avoid the generation of any kind of magnetic interference on the

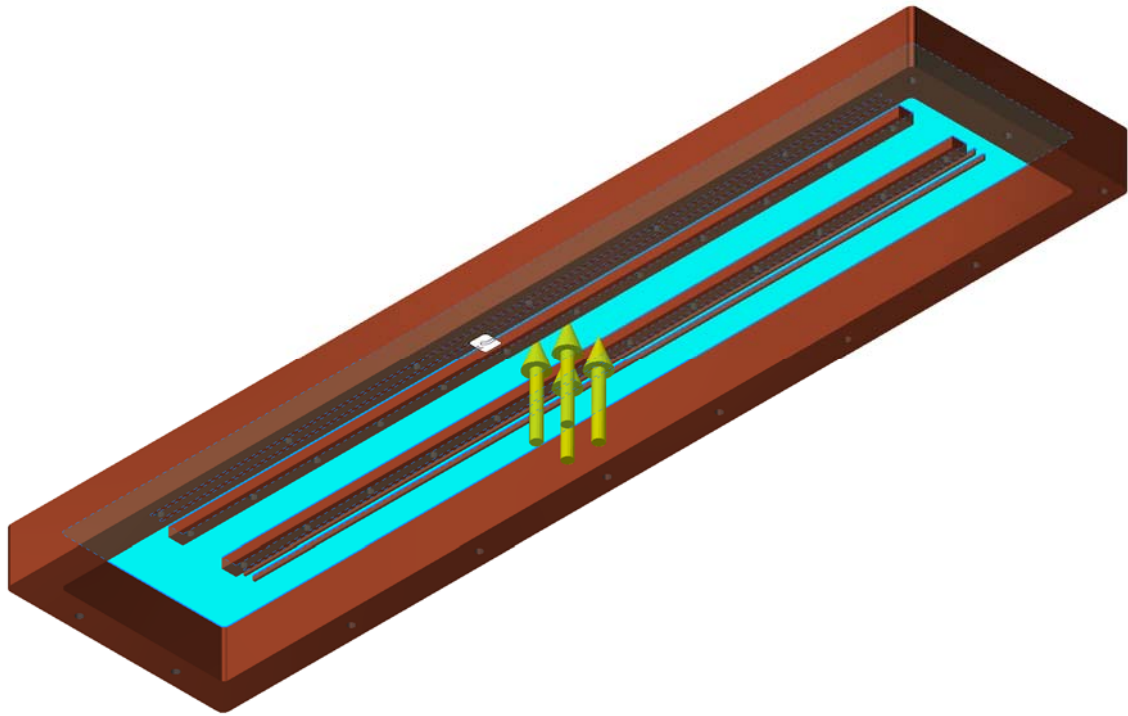


Figure 59: FEM simulation set up imposing a difference of pressure of 4 bar between the water-cooled side and the vacuum side of the cathode body.

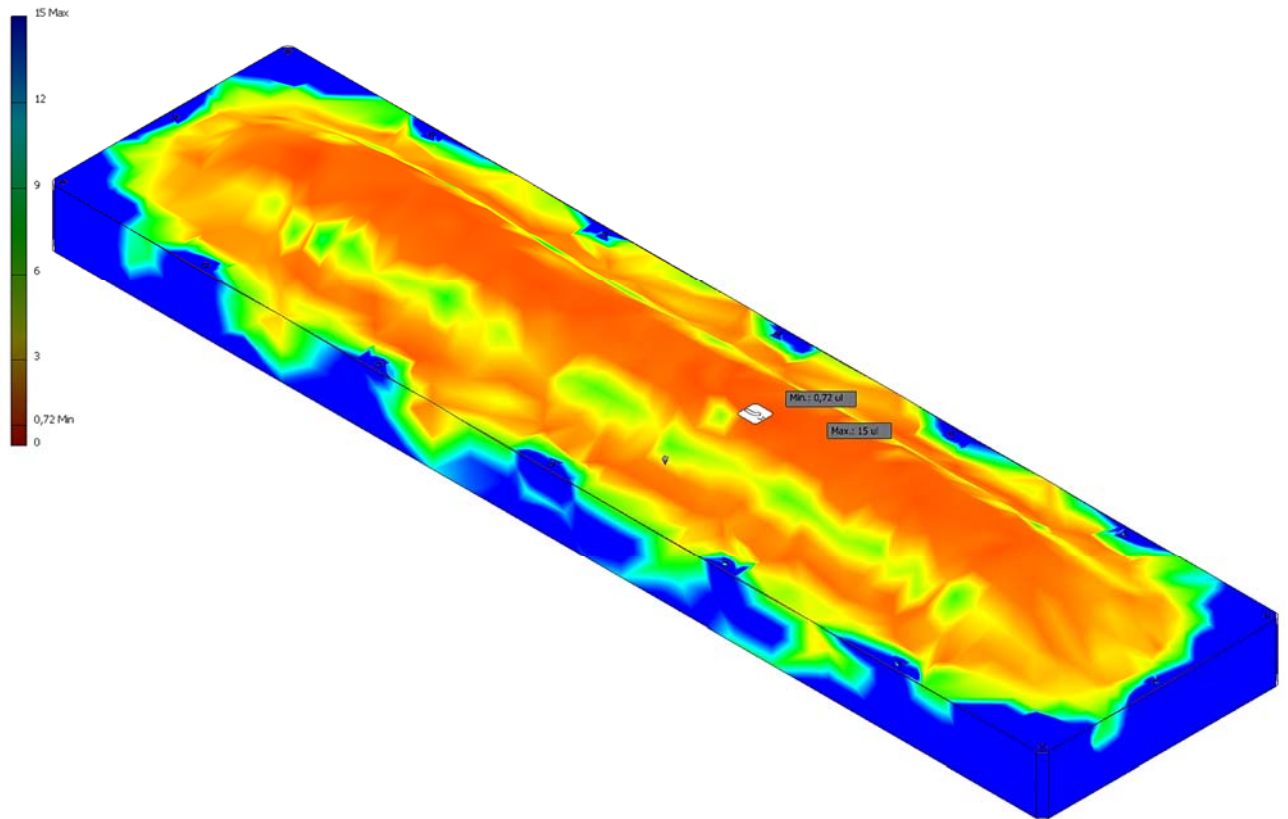


Figure 60: FEM results for the water-cooling pressure simulation reported as safety factor.

magnetic field lines produced by the magnet packs), in order to fix the uniformly the surface of the cathode body with the external flange (see Figure 61). This addition of spacers modifies the setup of the FEM simulation, in fact, now it is necessary to impose fixed the parts directly connected with the spacers, as reported in Figure 62.

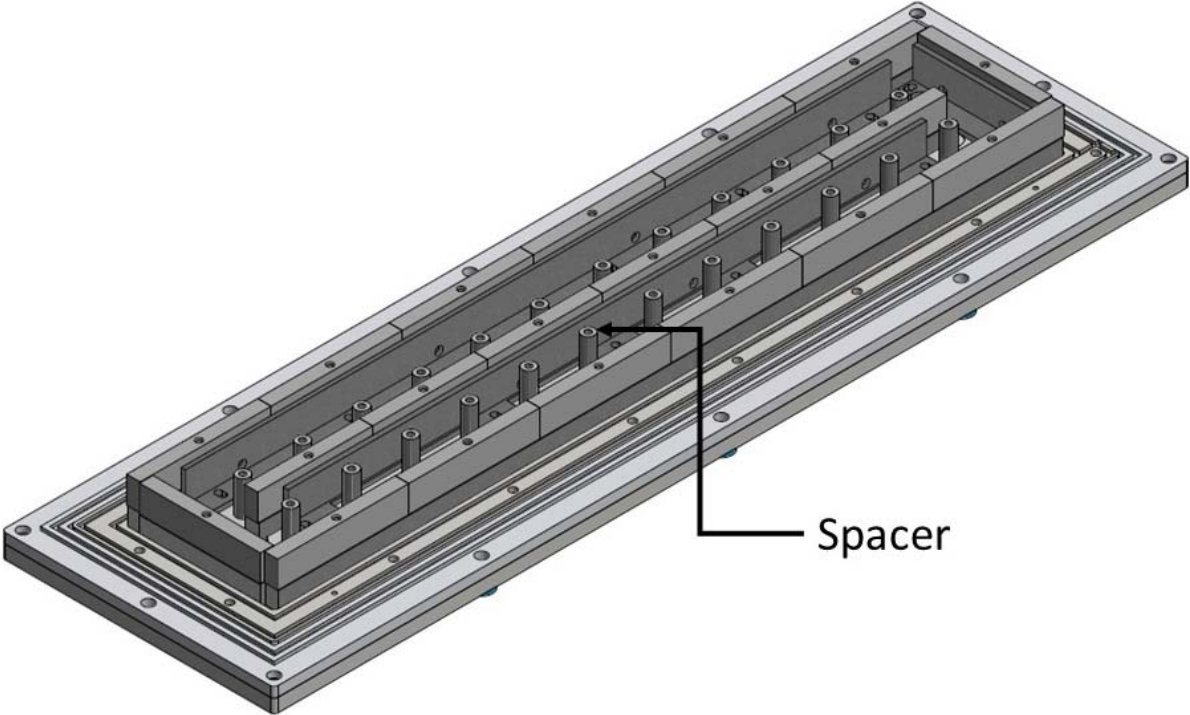


Figure 61: detailed view of the spacers connected to the cathode body.

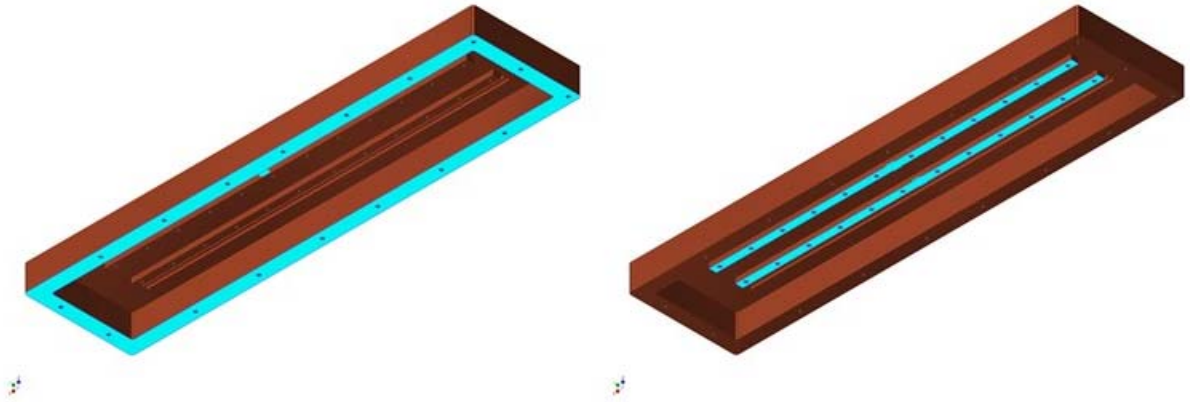


Figure 62: detailed view of the constrains imposed in the simulation with the addition of the spacers.

The result of the simulation reported as safety factor in Figure 63 shows how the addition of the spacers improve significantly the stiffness of the MGN source structure. The minimum value of the safety factor obtained from the simulation is 4,17 (see Figure 63) obtaining a component completely safe for the final application.

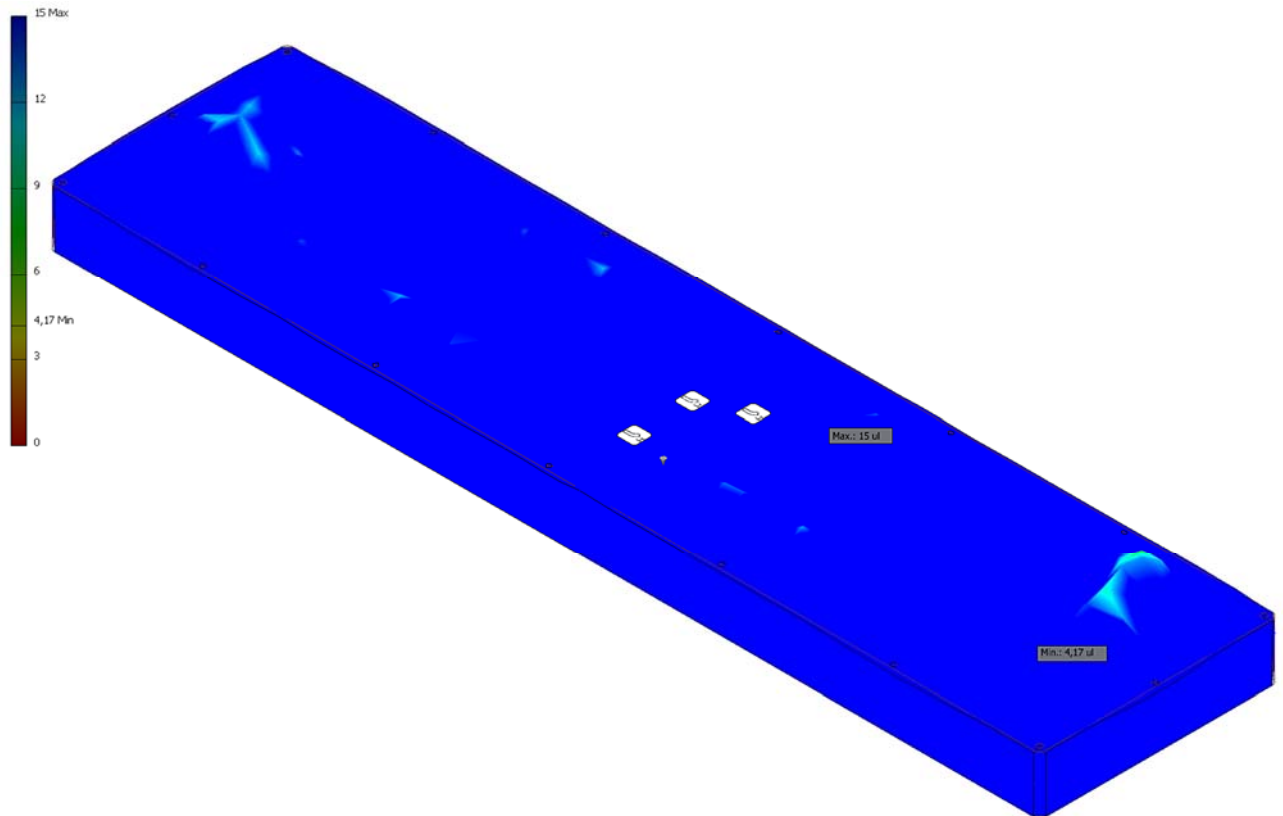


Figure 63: FEM simulation result, after the addition of spacers, reported as safety factor.

8.1 Conclusions of the Magnetron Sputtering Source Design.

The results obtained with the 3D CAD have reached the goal of the research, that corresponds to the realization of the custom magnetron sputtering source to apply to the final industrial system. The magnetron sputtering source obtained is very unbalanced, properties fundamental to work in reactive configuration, in fact the reaction is more efficient

transporting the plasma close to the substrate surface. The magnetron structure also presents a good safety factor obtained from FEM simulations, fundamental result to obtain the green light for the application of this component on the industrial machine. The magnetron sputtering developed during this PhD thesis and ready for the assembling on the PVD system is reported in Figure 64. The 2D drawings of the magnetron sputtering source described in this work are reported in the Annex of the thesis.



Figure 64: magnetron sputtering source ready for the assembling onto the industrial PVD system.

Chapter 9: Development of a non-commercial Physical Vapor Deposition System

This part of the work of thesis is dedicated to the characteristics of the physical vapor deposition system, developed for the coating of the tungsten carbide wire rolls. The system is designed to deposit thin films of hard materials (nitrides and carbonitrides of transition metals), using two different PVD techniques: the magnetron sputtering (completely developed in this work of thesis) and the cathodic vacuum arc (researched in the market and tested during the experimental part of the thesis). As indicated by the acronym of the coating techniques, the process happens under specific conditions, essentially under a partial pressure of specific reactive and non-reactive gases inside a process chamber with a total pressure lower than the atmosphere. The lowest pressure reachable is symptom of a cleaner process, in fact the lower the base pressure before the coating process, the lower the amount of contaminants present in the final thin film. For all these reasons, the system is essentially composed of three different units:

1. the vacuum system;
2. the deposition chamber and the sample holder;
3. The PVD sources and process power supplies;

These three units are controlled and monitored by a PLC (programmable control unit) Siemens, connected in turn with an UPS (uninterruptible power supply) to guarantee the safety of the PVD system during a blackout. In fact, a blackout sends an error message to the PLC that stops all the processes acting at this time and guides the system in an idle state.

9.1 The Vacuum system characteristics

The vacuum system of the PVD machine is designed to reach the base pressure lower than $1 \cdot 10^{-5}$ mbar, in the lowest time possible (lower is the pumping time lower is the total

process time), choosing the components with the best performances present in the market. The vacuum system can be divided in valves (VAT), pumping units (Edwards, reported in Figure 65) completely dry and nitrogen purged in order to avoid any kind of possible problems due to the use of CH₄ as process gas, vacuum meters (Edwards and MKS) and gas delivery system.

The valves are necessary to generate and control the vacuum inside the process chamber and the pumping line. They are fundamental to maintain the vacuum in steady state during for example a blackout and prevent a possible and dangerous venting of the whole system. Moreover, they maintain constant the total process pressure increasing or decreasing their aperture directly connected with the conductance of the line. In detail, the VAT valves mounted on the system are:

- ❖ n° 1 gate ISO 250 pneumatic valve series 12 aluminum body for the turbo pump;
- ❖ n° 2 gate ISO 100 pneumatic valves series 12 aluminum body for the by-pass line;
- ❖ n° 1 Butterfly ISO 100 motorized valve series 61.2 aluminum body for the modulation of the conductance along the by-pass pumping line;
- ❖ n° 1 angle ISO 40 pneumatic valve series 24 aluminum body for the pre vacuum of the turbomolecular pump;
- ❖ n°1 angle ISO 25 pneumatic valves series 24 aluminum body for the Penning vacuum meter protection;
- ❖ n°2 angle ISO 16 pneumatic valves series 24 for the capacitance vacuum meter protection and for the venting of the system.

The vacuum pumps are fundamental to generate the pressure state where the PVD process can be generated, and to maintain this regime also during the inlet of the process gases. The pumping units mounted on the PVD system are all dry pumps to prevent damages due to the CH₄ use, and they are composed of one primary pump booster to increase the pumping speed of the system until 10⁻³ mbar and a turbomolecular pump to reach base pressures lower than 1·10⁻⁵ mbar. In detail, the pumping units are:

- ❖ n° 1 primary dry pump multi claw model Drystar Edwards GV80 with a pumping speed of 80 mc/h and a final vacuum level lower than $1 \cdot 10^{-1}$ mbar;
- ❖ n°1 booster dry Roots model EH500 Edwards with a pumping speed of 500 mc/h and a final vacuum level lower than $3 \cdot 10^{-3}$ mbar;
- ❖ n°1 turbomolecular magnetic levitation pump model STP 2207 with a pumping speed of 2200 l/s and a final vacuum level lower than $1 \cdot 10^{-8}$ mbar.

The pumping unit presents a High Efficiency Particulate Air (HEPA) filter positioned immediately before the roots pump inserted in a black box as reported in Figure 65 to prevent any damage of the primary pumps during the first part of the vacuum process, when the regime is viscous and the powder can move along the pipe line. Moreover, at the beginning of the vacuum procedure the turbomolecular pump is bypassed with a parallel connection to the deposition chamber passing through the HEPA filter, to avoid that the powder can pass through the turbo pump and damage it.

During the vacuum process, the measure of the vacuum level is guaranteed by the Pirani gauge (low vacuum) and the penning gauge (high vacuum). During the coating process the penning vacuum meter is no more useful and the capacitive gauge is used. This fact is related to the presence of the plasma discharge that interacting with the penning gauge can false the pressure measurement, while the capacitance gage is indifferent to the presence of the plasma. In detail, the vacuum meters mounted on the system are:

- ❖ n° 2 Pirani gauges model APG100 Edwards (one in the process chamber and one between the roots and the turbo pump);
- ❖ n° 1 Penning gauge model AIM-X Edwards positioned in the process chamber;
- ❖ n° 1 Capacitance gauge model 627F MKS positioned in the process chamber.

The process gases used to ignite the plasma discharge are fed controlling the gas delivery system based on three thermal mass flow controllers for the three different process gases (Ar, N₂ and CH₄). In particular the mass flow meters are:

- ❖ n° 1 gas mass flow controller for Ar model GA50 MKS with a maximum flow rate of 500 sccm;

- ❖ n° 1 gas mass flow controller for N₂ model GA50 MKS with a maximum flow rate of 500 sccm;
- ❖ n° 1 gas mass flow controller for CH₄ mod. GA50 MKS with a maximum flow rate of 300 sccm.

The mass flow meters are connected all together in a single gas line (made of stainless steel AISI 316L electropolished internally) in order to mix the gases before entering the process chamber.

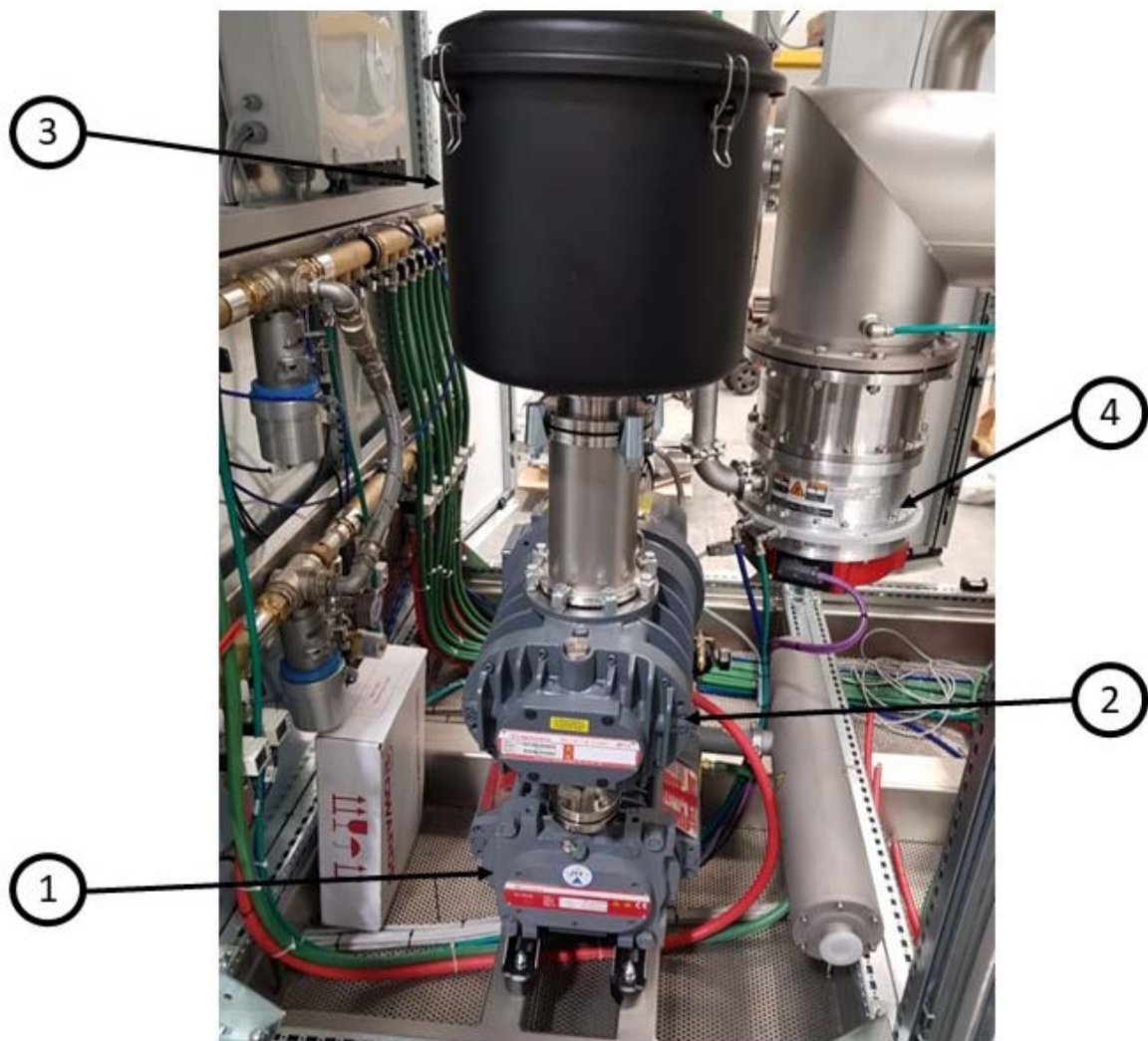


Figure 65: pumping unit composed of a screw pump 1, roots booster 2, HEPA filter 3 and turbomolecular pump 4.

9.2 The deposition chamber and the sample holder

The deposition chamber is the place where the deposition process happens, for this reason it must be water cooled to dissipate the heat generated from the PVD processes and from the heating elements (resistive heaters max 600 °C), present inside the chamber to degas the internal walls and to produce a thin film coating in temperature (as evidenced in the experimental part of the thesis the temperature is a fundamental parameter to achieve the right structure and composition). The deposition chamber is an octagon circumscribed to a circumference of diameter 800 mm and height 1050 mm, made of stainless steel AISI304 double walls (to guarantee the water cooling). A door with dimension 800 mm width and 1050 mm height is positioned on the front of the chamber to assure the charge and discharge of the sample holder. The sealings of the vacuum chamber and of the rest of the PVD system are made of Viton polymer.

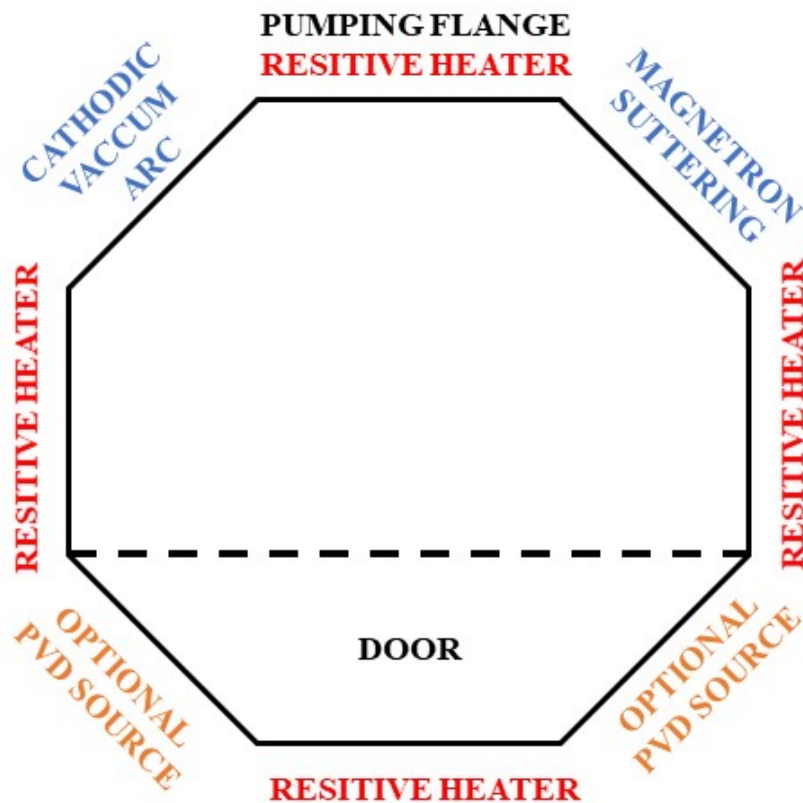


Figure 66: scheme of the component's distribution inside the deposition chamber.

The deposition chamber allocates two PVD technologies: the magnetron sputtering developed during the PhD work and three cathodic vacuum arcs (mounted vertically in a

single flange of the PVD system to cover 600 mm of coating high) from GPA company, deeply tested during the research of the hard coatings. The rest of the octagon's sides are occupied from four resistive heaters that can reach the maximum temperature of 600°C (reported in Figure 68), the pumping line flange and two more free flanges for future improvements of the PVD sources.

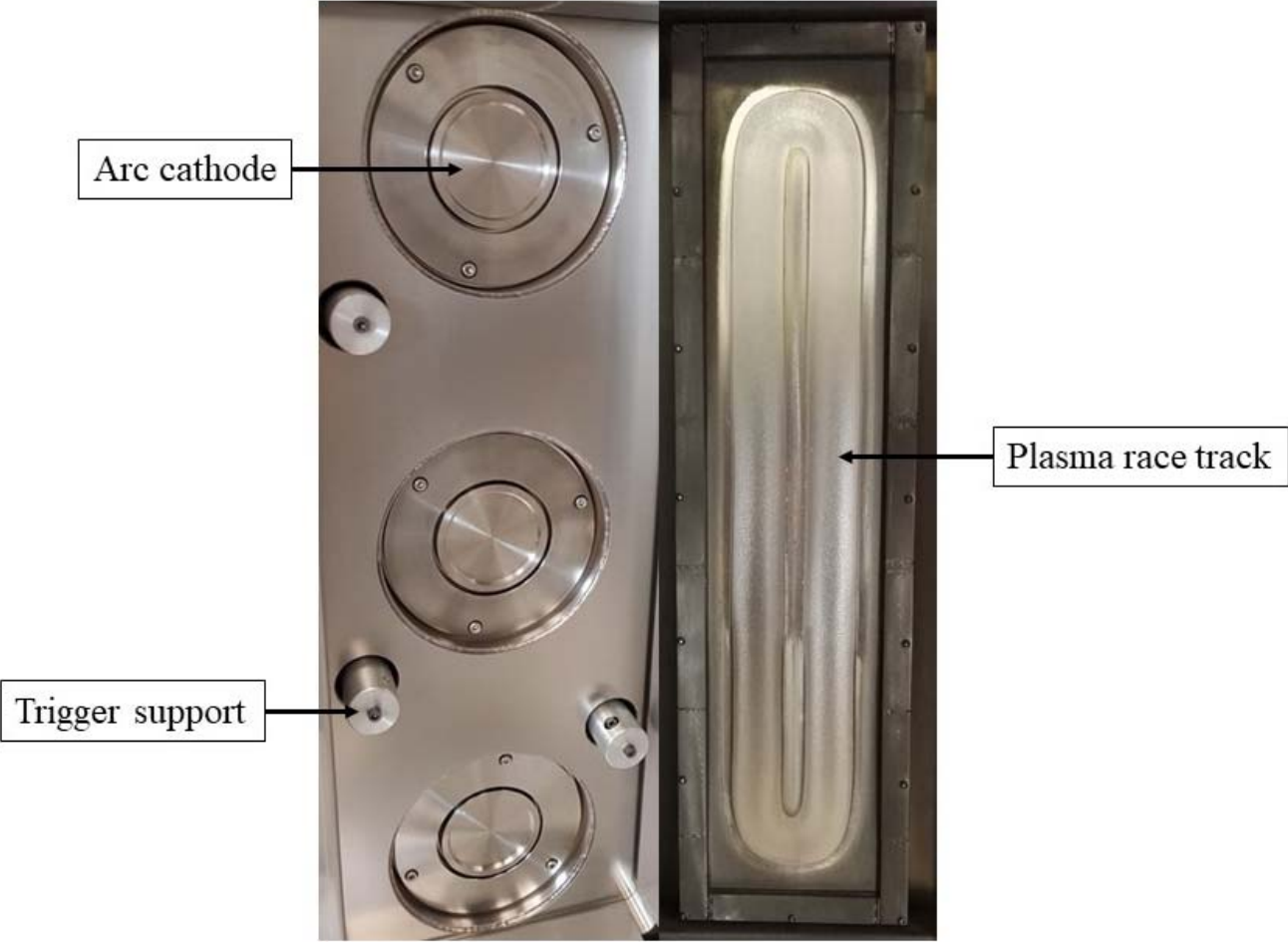


Figure 67: PVD sources mounted on the industrial system (on the left the arcs and on the right the magnetron).



Figure 68: detailed view of the resistive heater positioned in correspondence of the pumping flange.

Following are reported some 2D drawings of the chamber realized in collaboration with an external company VCS S.r.l., company expert in the design and production of industrial PVD systems.

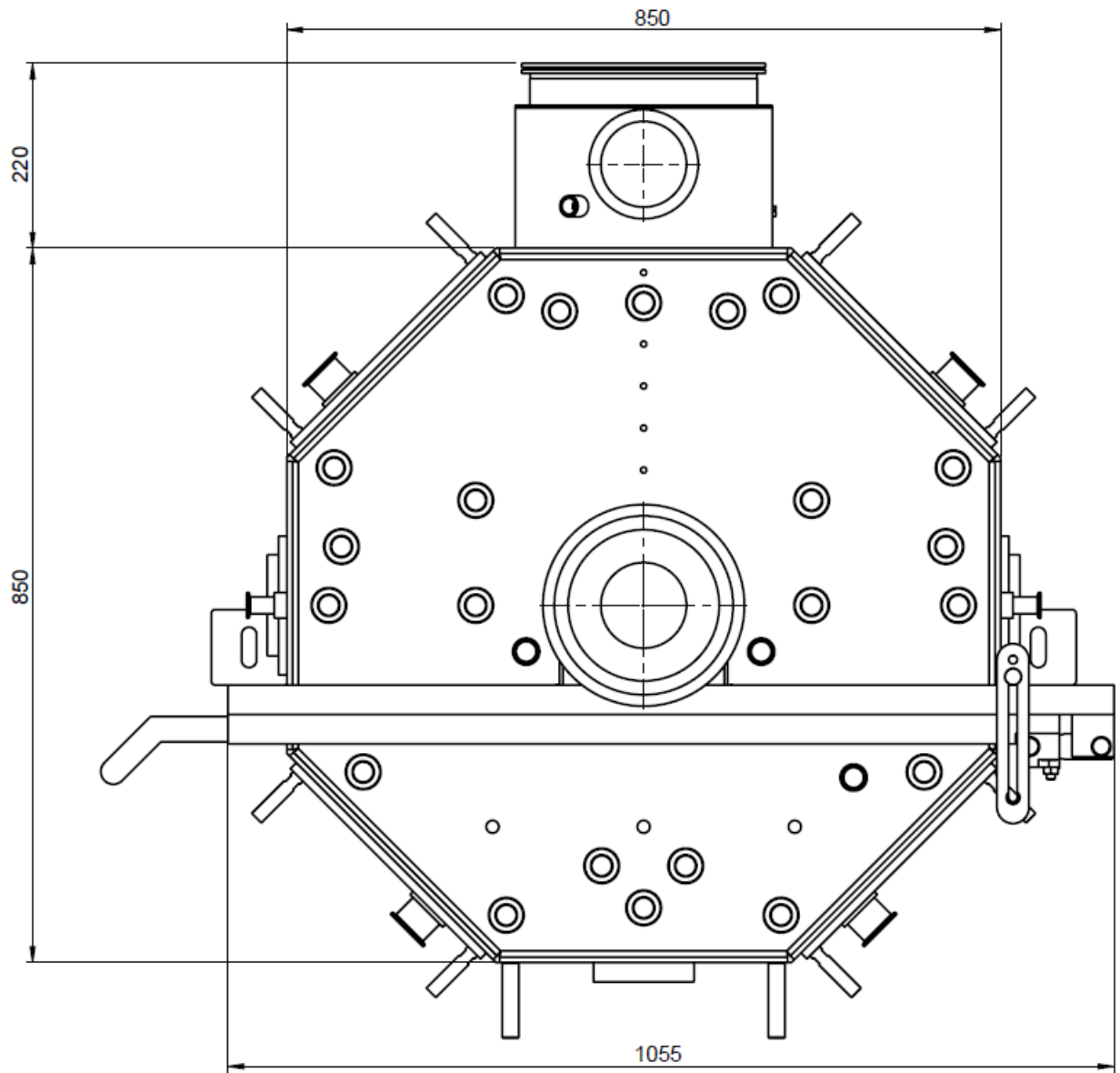


Figure 69: top view of the deposition chamber.

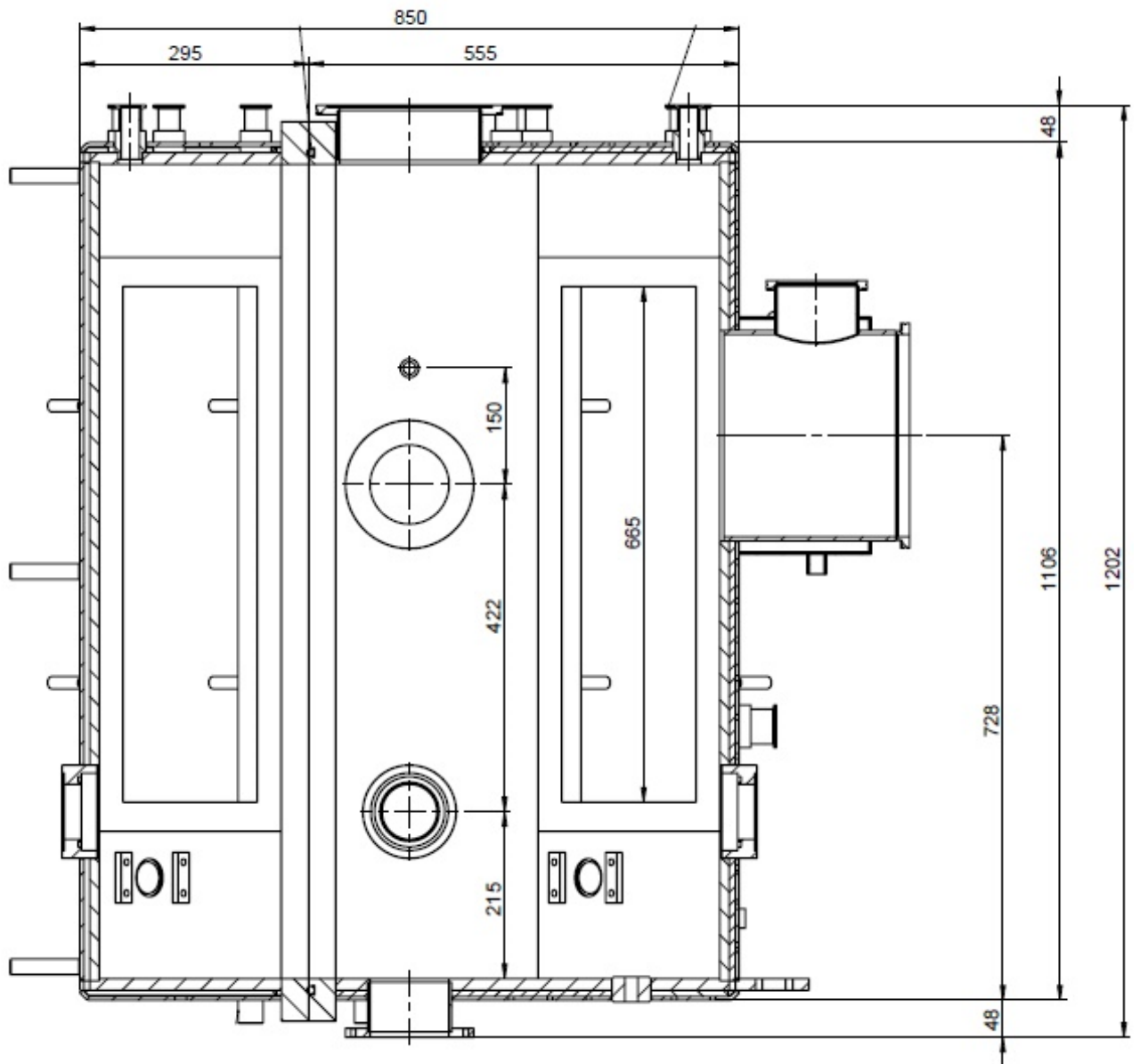


Figure 70: lateral view of the deposition chamber.

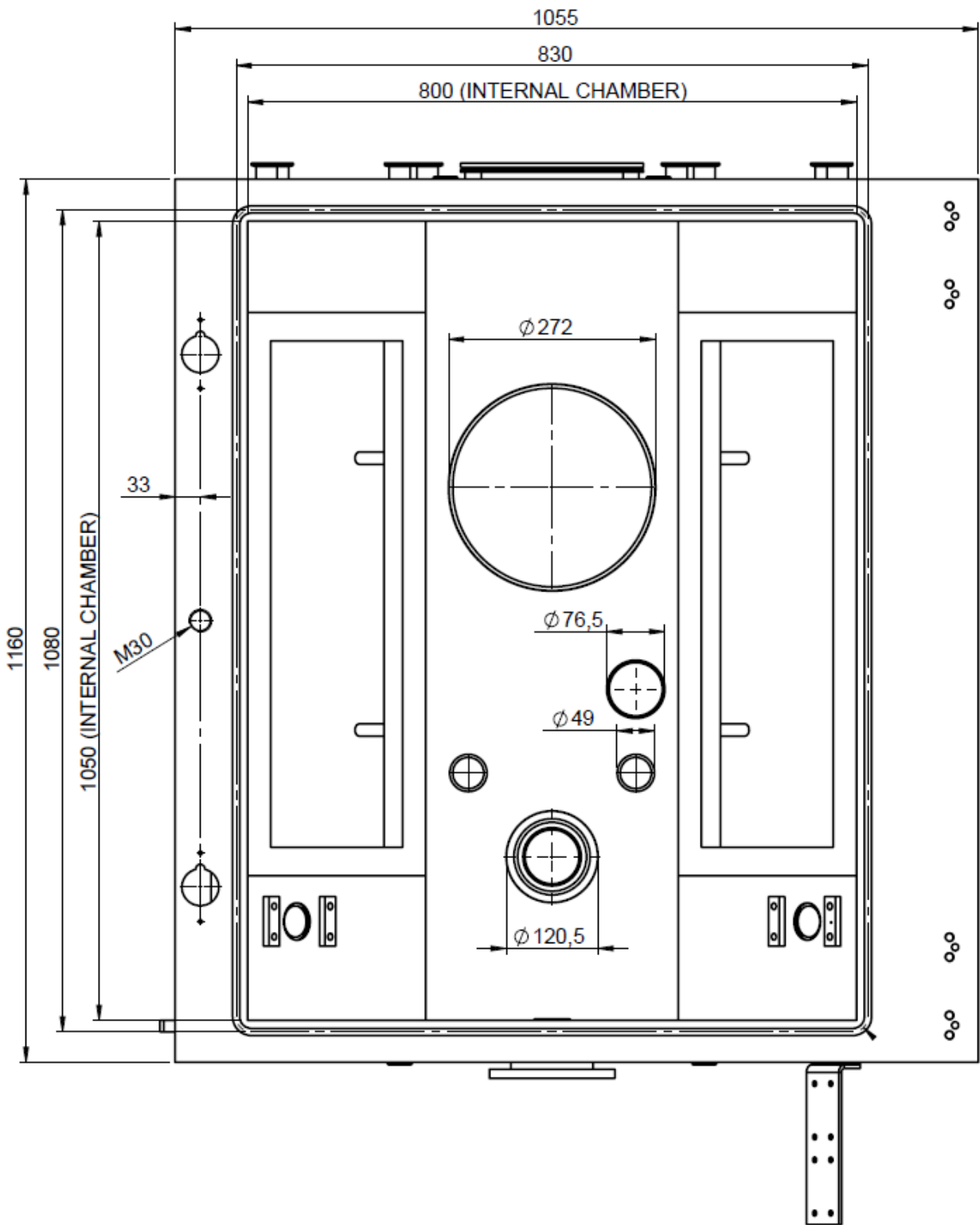


Figure 71: rear view of the deposition chamber.

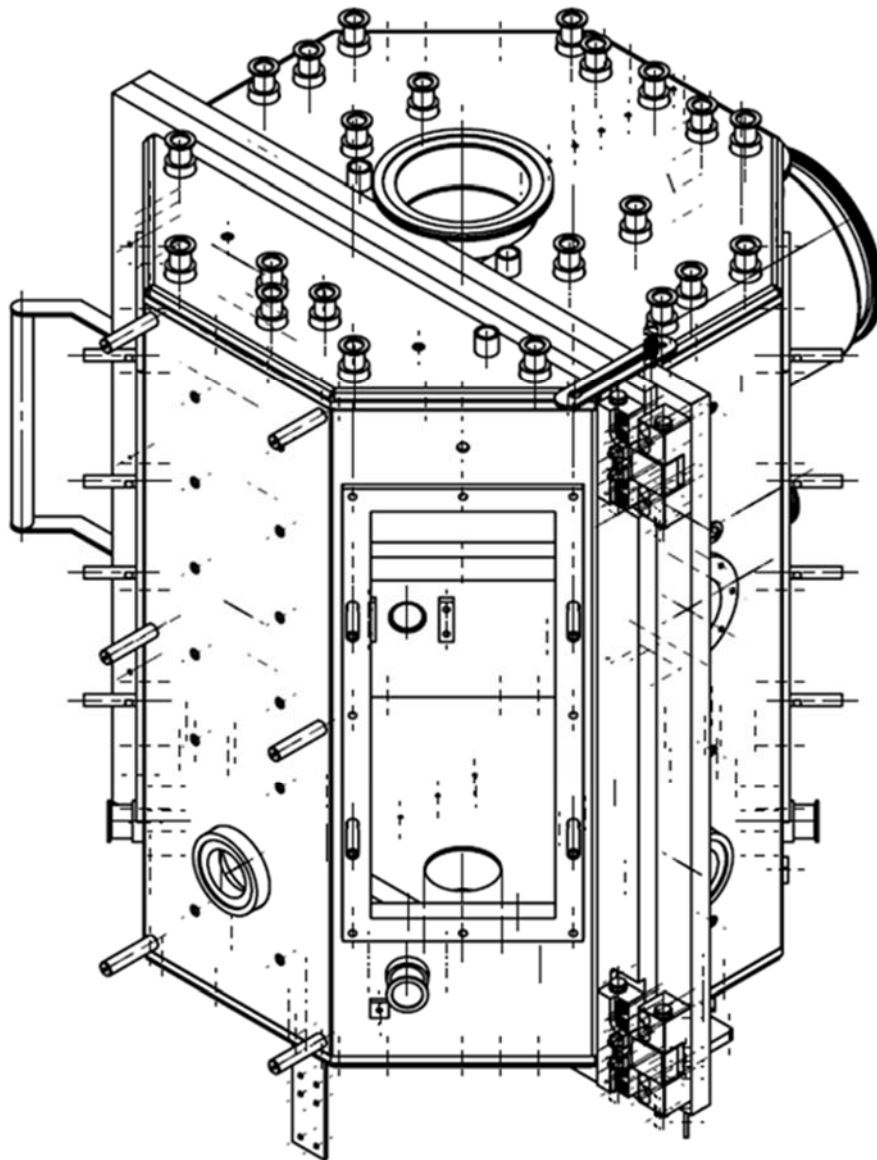


Figure 72: axonometric view of the deposition chamber.

The sample holder developed for the PVD system is realized to allocate wire rolls with specific dimensions (external diameter 90-150 mm and height 15 mm), representative of the gamma of tungsten carbide rolls mostly sold from the Eurolls company. The sample holder can rotate with a planetary motion (as reported in Figure 73), in order to uniform the thin film deposition on the whole surface of the rolls and must be insulated from the chamber, in order to power the pulsed Bias voltage on the substrates during the PVD depositions. The structure must support 1000 kg of charge weight and resist to a maximum temperature of 700 °C. the weight of the structure is dissipated on a stainless steel spheres positioned on the

base of the carousel as reported in Figure 74, they are of different diameter and are positioned alternately to avoid the stacking of the rotation. The materials used in the sample holder are stainless steel AISI 304, alumina and iron. The dimensions of the carousel are chosen in order to allocate the maximum number of rolls (coating high of 600 mm) previously described and to maintain a coating distance (distance between the source and the substrate) respectively for the rolls of 150 mm diameter: 150 mm for the arc depositions and 75 mm for the magnetron sputtering; and the rolls of 90 mm diameter: 195 mm for the arc depositions and 120 mm for the magnetron sputtering.

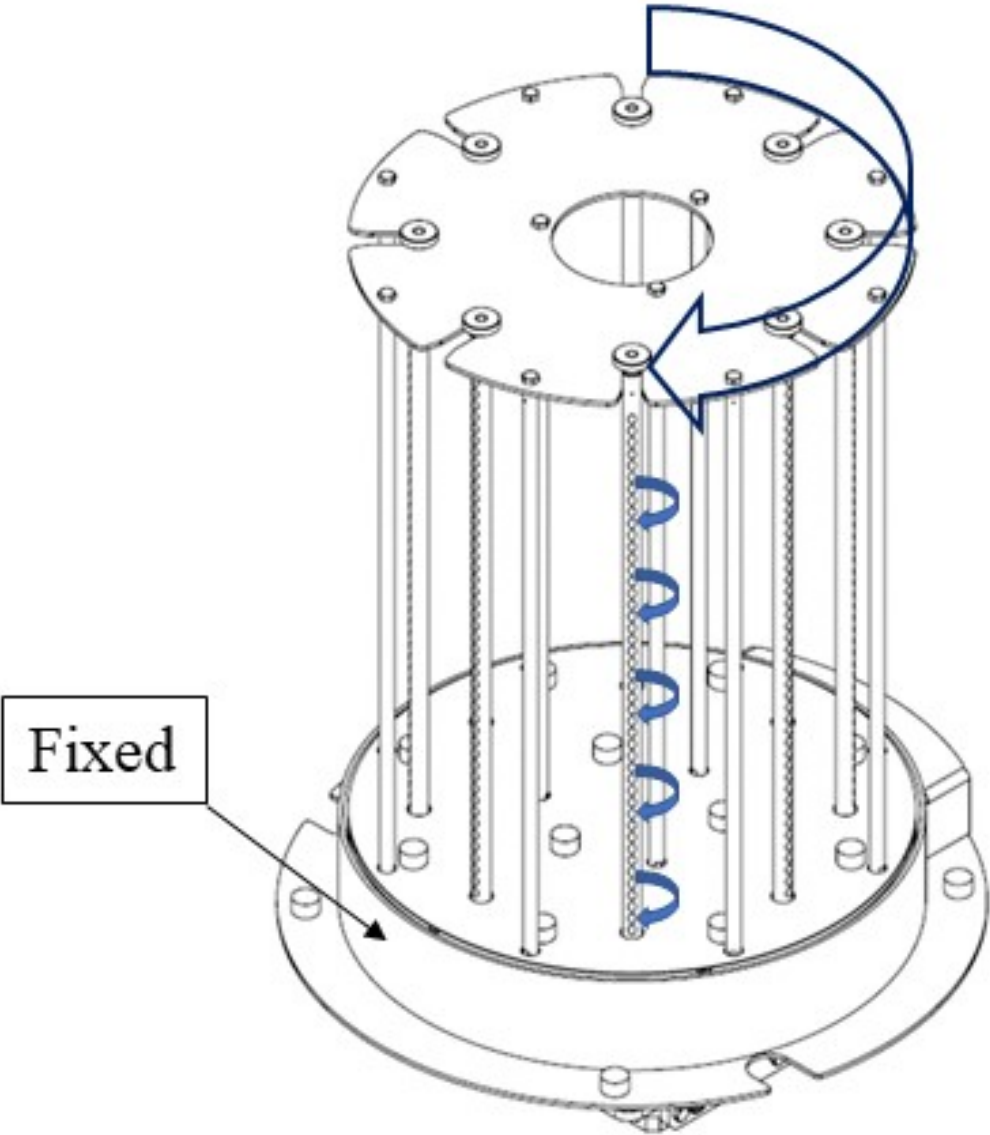


Figure 73: the sample holder evidencing the planetary motion.



Figure 74: the base of the sample holder evidencing the spheres used to dissipate the weight and maintain the rotation.

Following are reported some 2D drawings of the carousel:

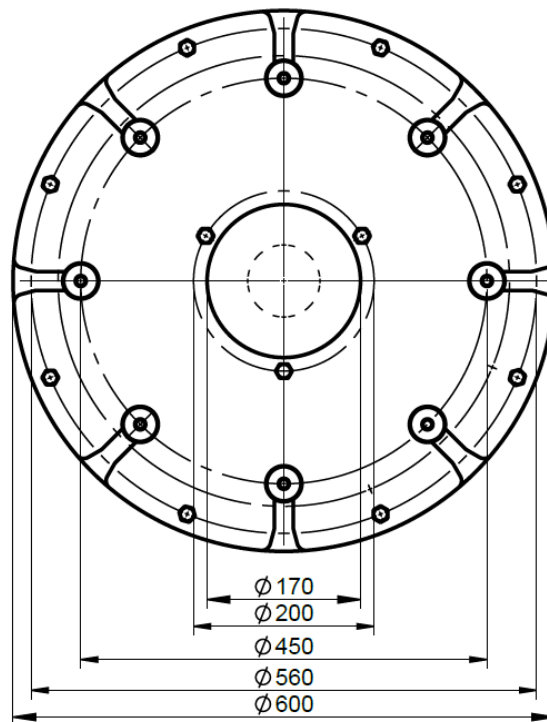


Figure 75: top view of the carousel.

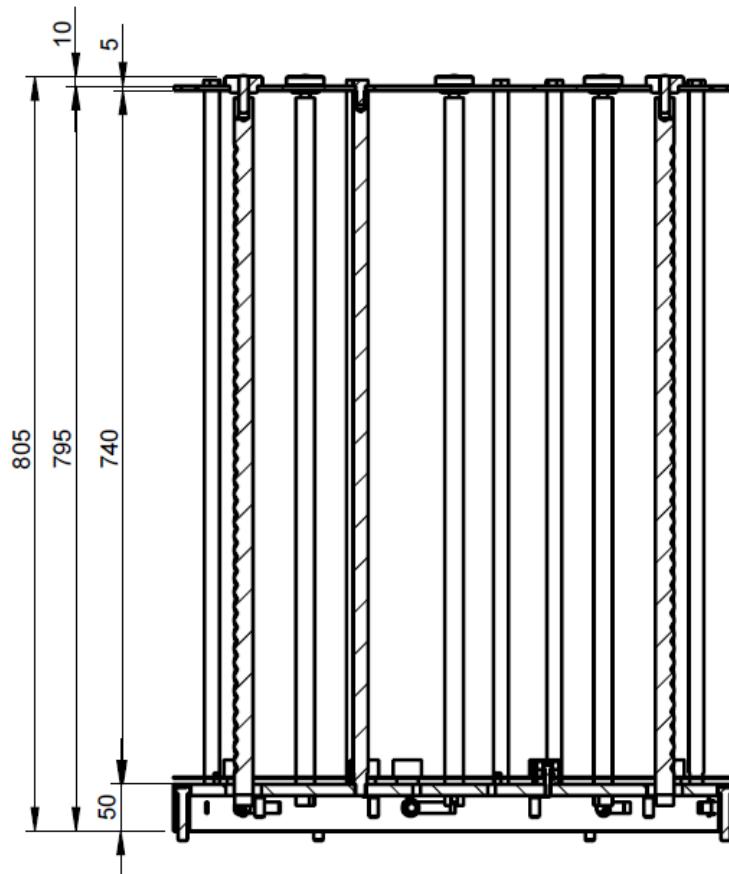


Figure 76: lateral view of the carousel.

9.3 The process power supplies.

The power supplies represent a fundamental choice for the design of a PVD system, in fact they are specific for the coatings that the system will produce. The present PVD machine allocates three different power supplies:

1. the cathodic vacuum arc power supply (one for each cathode), a direct current (DC) source with a current range (5-100A) and a voltage range (0-30V) model GPA PB100.
2. the magnetron sputtering DC power supply, operating in the range (0-30A) and (10-1000V) with an ignition voltage of 1500V (useful for poisoned targets), Pinnacle 12 kW model PNCL 12K 400 PFP KI P16 from Advanced Energy.

- the bias pulsed DC power supply, operating in the range (0-50A) and (10-1000V) with the frequency regulation in the medium range (1 to 30 kHz) (useful for the deposition of denser coatings and nonconductive materials), Solvix 15 kW medium frequency model Magix15k-BA-P-IGBT-30kHz-1000V-50A.

The operative ranges for the Pinnacle and the Solvix are reported in the following page.

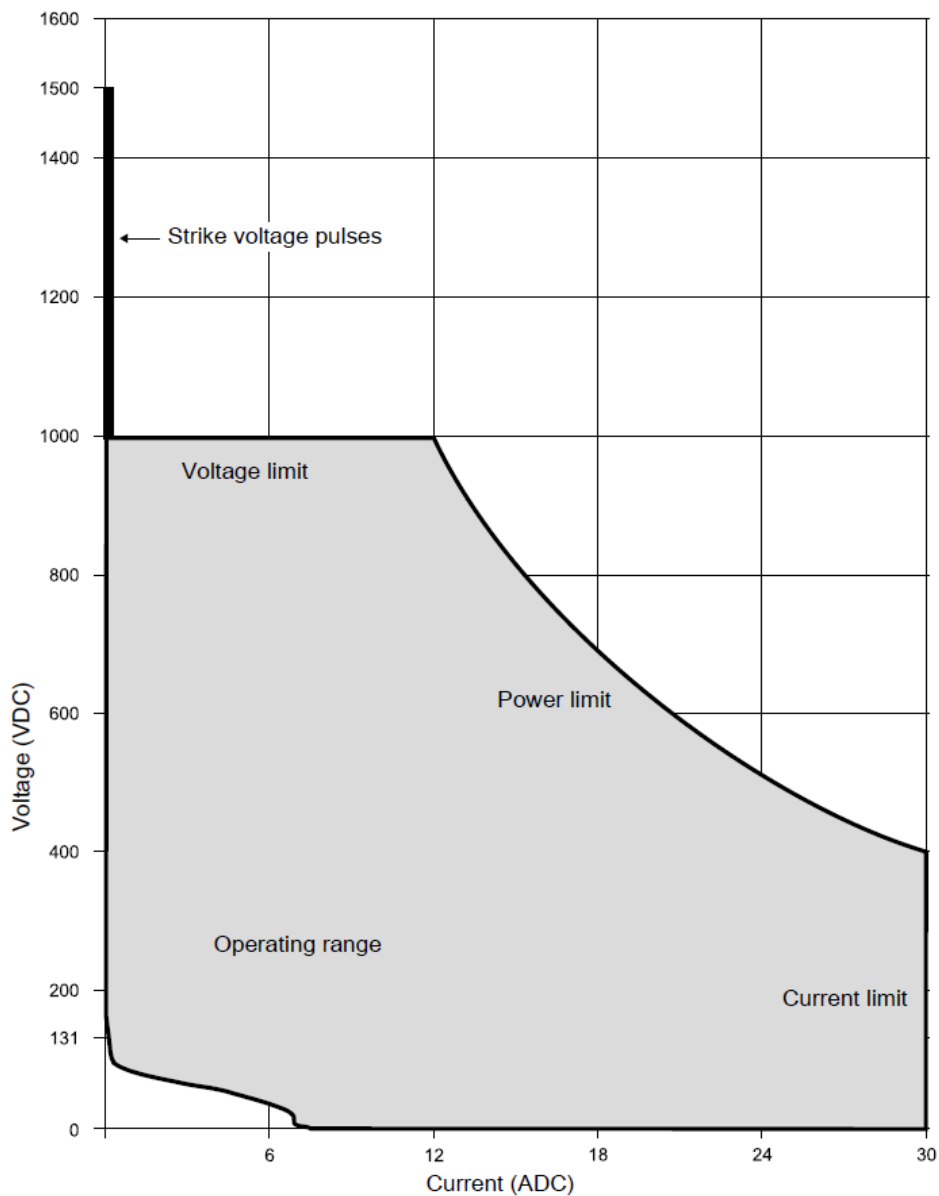


Figure 77: Pinnacle 12 kW operating range.

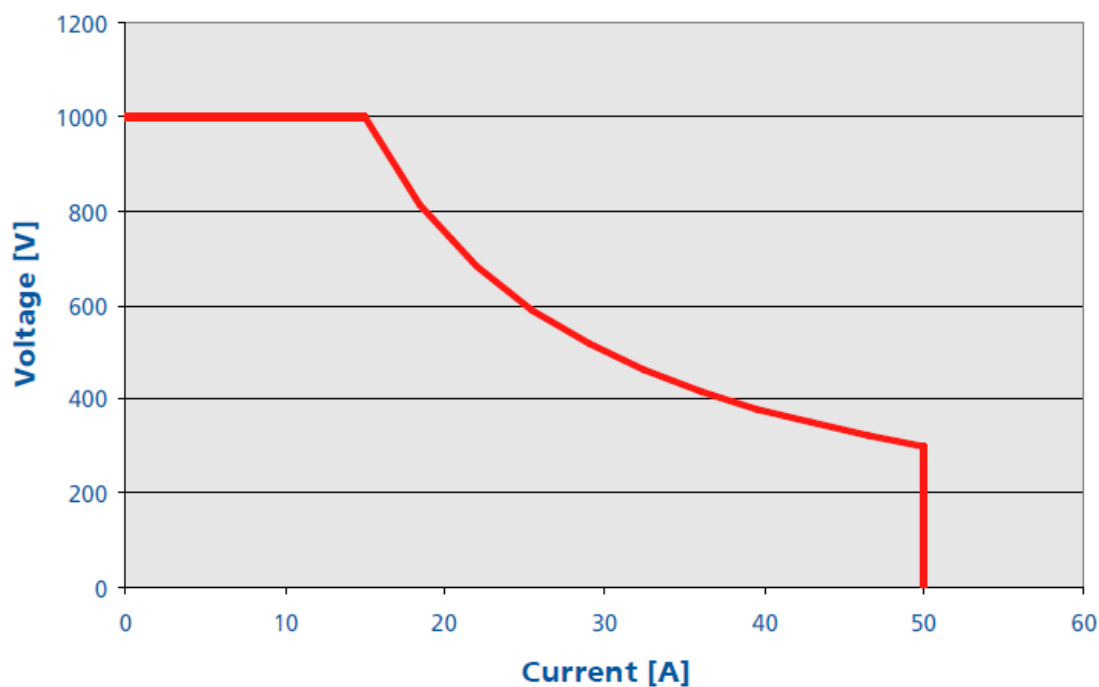


Figure 78: Magix15kW operating range.

9.4 Evaluation of the Outgassing rate of the PVD system

The fundamental property of the vacuum system is of course the amount of gas produced from all the internal components of the system exposed to the vacuum. This value can be experimentally evaluated, and it is named as the outgassing rate of the vacuum prototype. The outgassing rate is obviously fundamental, because it limits the base pressure reached during the vacuum process and from this it limits the purity of the thin film that will be grown on the sample. The outgassing rate depends on the materials adopted to build the vacuum system (for example zinc must be avoided) and on the history of the components used, it means the machining techniques of the component but also the cleaning procedures used before the definitive assembling. The cleaning protocol is essential in order to prepare the surface exposed to the vacuum but also to prevent the recontamination during the assembling. In fact, initially the vacuum components are cleaned in ultrasonic bath with specific soaps (in this case Rodadaclean from NGL), then rinsed in deionized water and

subsequently dried with a nitrogen flux (no with compressed air because it contains oil traces). Once prepared all the parts during the vacuum system assembling it is mandatory to take care of the possible contamination of the components due to the manipulation and on the dust present in the atmosphere. To prevent this undesirable effect the vacuum parts are manipulated with nitrile gloves and protected as possible with aluminum foils.

Once completed the assembling of the non-commercial PVD system the base pressure and the outgassing rate can be evaluated. The base pressure of the empty system (without the carousel) is measured after 24 h of pumping process, baking out the system at 500°C for 4 h and reaching the vacuum level of $2 \cdot 10^{-6}$ mbar. At this point it is possible to start the experimental evaluation of the degassing rate, that consists in plotting the pressure values in function of the time. Once the deposition chamber is separated from the pumping line, the pressure starts increasing (as reported in Figure 79) due to the gases produced from the internal walls of the vacuum chamber and no more evacuated.

Interpolating linearly the curve obtained it is possible to extrapolate the value of the outgassing rate, as reported from Chigiato⁴⁰, from the slope of the interpolation line as indicated in the following equation:

$$dP = \frac{k_B T}{V} Q dt$$

Equation 10

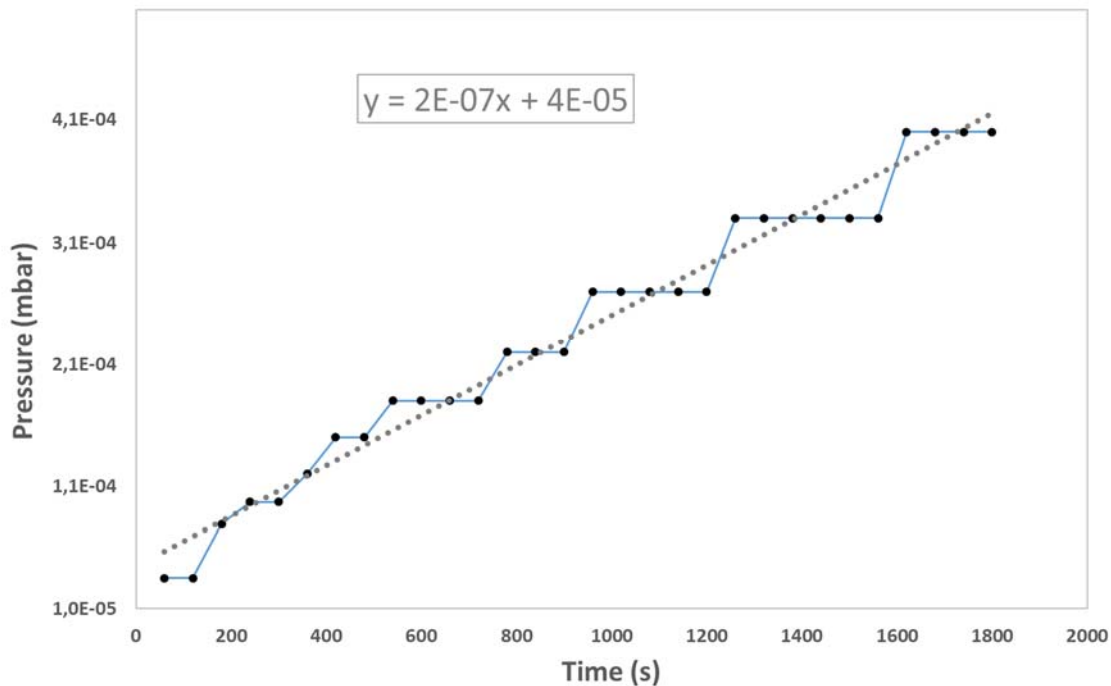


Figure 79: the chamber pressure variation in function of the time (without pumping).

Dividing this value in $[\text{mbar}\cdot\text{l}\cdot\text{s}^{-1}]$ by the internal surface of the chamber expressed in cm^2 , the result is total outgassing rate for unit of surface exposed expressed in $[\text{mbar}\cdot\text{l}\cdot\text{s}^{-1}\cdot\text{cm}^{-2}]$. The results of the experimental evaluation of the degassing rate for unit of surface is $6\cdot 10^{-12} \text{ mbar}\cdot\text{l}\cdot\text{s}^{-1}\cdot\text{cm}^{-2}$ coherent with the value of the baked stainless steel reported in literature⁴⁰, around $3\cdot 10^{-12} \text{ mbar}\cdot\text{l}\cdot\text{s}^{-1}\cdot\text{cm}^{-2}$. After this test it is possible to assure that all the components assembled are perfectly cleaned and that the assembling procedure are performed guaranteeing the requested cleanliness, moreover any kind of leakage is avoided.

9.5 Conclusions of the Development of a non-commercial Physical Vapor Deposition System

The development of the PVD system have reached and satisfied all the milestones imposed at the beginning of the project. The research and development of a new custom magnetron sputtering source extremely unbalanced of the second type, with a coating high of 600 mm, and a maximum working DC power of 12 kW (tested for few minutes with a titanium grade

2 cathode) represents one of the milestones satisfied from the work of thesis. The choice of the commercial cathodic vacuum arc sources, (after a long market research through the worldwide producers that offer homemade sources) tested during the hard coatings research, fully satisfied the possibility to guarantee the coating high of 600 mm and an easy substitution of the target due to their specific flange and cathode dimensions. These two technologies make the PVD system completely versatile from the point of view of the combination of coating materials and PVD techniques. The choice a levitation turbomolecular pump reduces at the minimum the maintenance due to the absence of the lubricated bearings, reducing the cost for the company, moreover, the dry primary pump and booster reduce the possible contamination due to the oil back streaming and failures due to the CH₄ use. Concluding the choice of the vacuum components, materials and the attention on the cleaning and manipulation determine the final base pressure of the PVD system ($2 \cdot 10^{-6}$ mbar) and its outgassing rate ($6 \cdot 10^{-12}$ mbar \cdot l \cdot s $^{-1}$ \cdot cm $^{-2}$) comparable to the backed stainless steel AISI 316 L, represent the fundamental condition to obtain coatings with the best performances. Following are reported a 3D rendering of the PVD machine realized during the development and a picture of the system at the Eurolls coating plant with different wire rolls deposited with TiN.

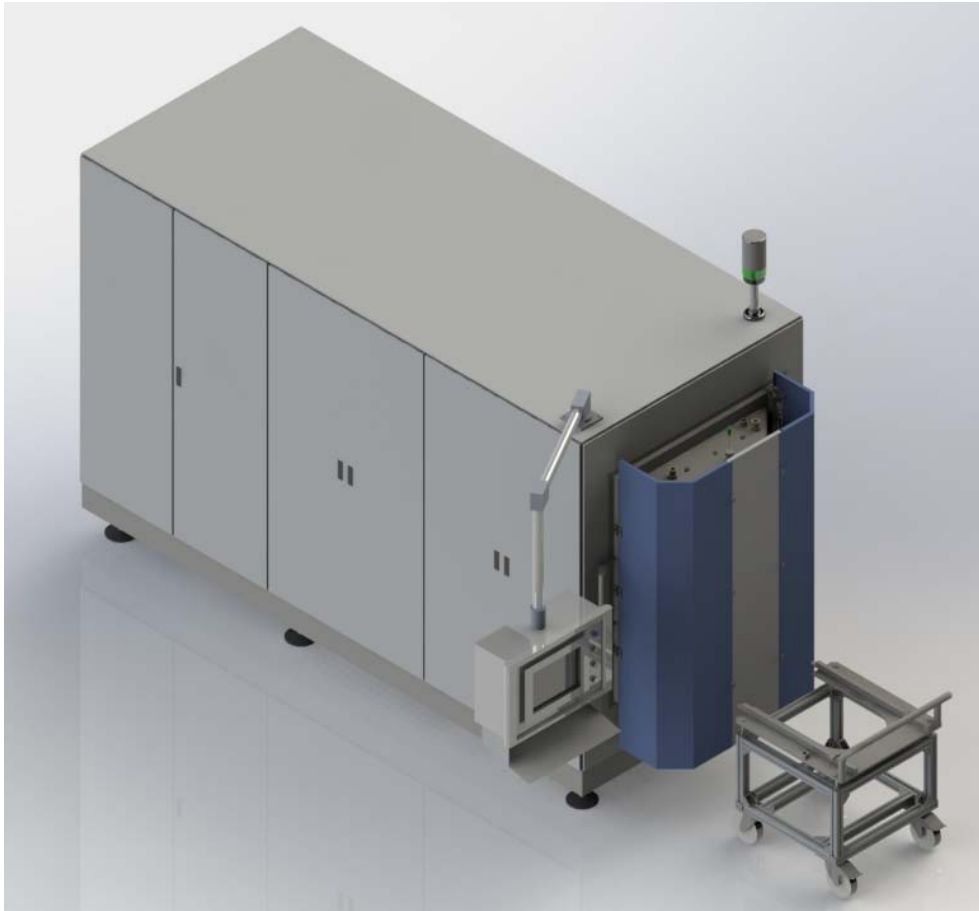


Figure 80: 3D rendering of the non-commercial PVD system.

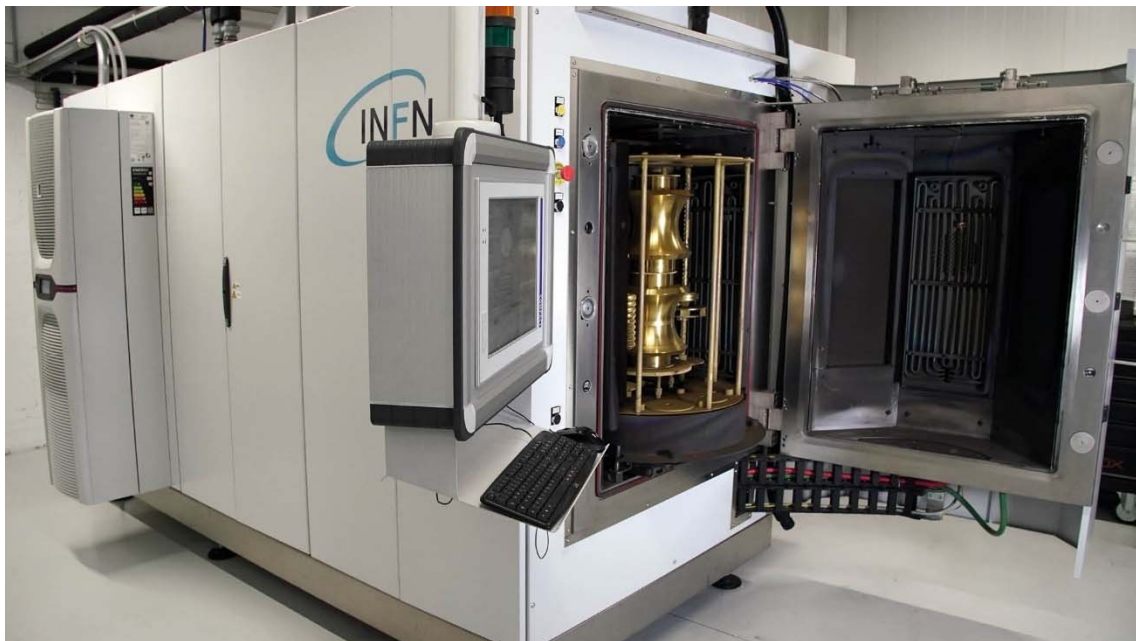


Figure 81: real view of the non-commercial PVD system with the carousel and rolls inserted in the deposition chamber⁴¹.

Conclusions

During this PhD work, various facets of the thin film hard coatings depositions and of the developments of a noncommercial PVD system have been addressed.

The magnetron sputtering techniques showed the possibility to deposit hard materials as TiN and TiCN, unfortunately on EC10F substrates they do not improve the wear rate of the base material, but they could be applied on softer materials as EC11M and EC16F to increase the lifetime, or to create coatings with complex multilayer structures made by CVA and MGN.

The cathodic vacuum arc techniques showed the possibility to deposit hard materials as TiN, TiCN and CrCN. The highest performance obtained from the ball on flat test, belongs to the EC10F sample coated with CrCN via cathodic vacuum arc, the measured wear rate is $7,14 \text{ mm}^3 \cdot \text{N} \cdot \text{m}^{-1}$.

The results of this work say that the lifetime of the roll coated with the hard material in the industrial environment cannot be improved only applying coatings with higher hardness. In fact, materials with higher hardness as TiCN (3260 HV) respect to CrCN (2300 HV), deposited on the same substrate (EC10F), present higher wear rate and lower lifetime. To improve the performance of the tungsten carbide wire rolls, it is mandatory to take into account the whole system coating-substrate and not only the single part separately.

This fact confirms the importance of the development of the versatile PVD system developed during this work: the combination of different technologies (cathodic arc and magnetron sputtering) and coating materials, enormously extend the range of achievable hard material that this machine can produce. The demonstration of the drive towards the continuous improvement, the noncommercial PVD system, completed during the PhD work and located in the coating plant of Eurolls, is continuously working in this direction.



Figure 82: wire rolls of different dimensions and shape deposited with TiN^{II}.



Figure 83: wire rolls deposited with TiCN^{II}.

Acknowledgments

I would like to spend some words to thank all the people that made possible to win this challenge. First of all, my half Andrea and my family that always encourage me in the difficulties and push me to get the result. I would like to thank all my colleagues of the Material Science and Technologies for Nuclear Physics Service at the National Laboratories of Legnaro for the support and with whose collaboration the research arrived to a formidable result, Giorgio, Silvia M., Cristian, Fabrizio, Alisa, Antonio, Eduard, Andrii, Vanessa, Luca, Nico, Paola and Silvia P.. The last two persons that I would like to thank are Prof. G. Fiorentini and Prof. V. Palmieri: remembering their words.

G. Fiorentini during the meeting with me and Palmieri in which I declared my desire to begin the PhD in physics said: *“Are you sure of this decision?”* and after my assent he continued with: *“I will support you and my door will always remain opened”*.

V. Palmieri after the first concourse for a fixed term contract for INFN to which I took part said: *“congratulation for the result obtained, now you only need a doctorate”*, Grazie Prof.!



List of Figures

FIGURE 1: TUNGSTEN CARBIDE WIRE ROLLS ¹	XI
FIGURE 2: WIRE ROLLING CASSETTES ²	XII
FIGURE 3: MICROHARDNESS OF CARBIDES, MIXED CARBIDES OR CARBONITRIDES AS A FUNCTION OF THE VALENCE ELECTRON CONCENTRATION ⁴	16
FIGURE 4: SCHEMATIC ILLUSTRATION OF THE STRUCTURE OF DIFFERENT TYPES OF COATING.	17
FIGURE 5: PASCHEN CURVE FOR A NUMBER OF GASES.	22
FIGURE 6: CHARACTERISTIC I-V CURVE OF AN ELECTRICAL DISCHARGE IN VACUUM ⁸	24
FIGURE 7: CURRENT PHYSICAL VAPOUR DEPOSITION (PVD) TECHNIQUES FOR ADVANCED COATINGS ¹¹	26
FIGURE 8: PLASMA OF A MAGNETRON SPUTTERING RECTANGULAR SOURCE ¹²	28
FIGURE 9: SCHEMATIC REPRESENTATION OF THE PLASMA CONFINEMENT OBSERVED IN BALANCED AND UNBALANCED MAGNETRONS ¹⁵	29
FIGURE 10: DEPENDENCE OF THE IONIZATION EFFICIENCY H ON THE DIMENSIONLESS PARAMETER B ¹⁹	32
FIGURE 11: PLASMA INTENSITY OF TI SIGNAL VERSUS PLASMA DC POWER ²⁰	33
FIGURE 12: COLOUR VARIATION OF TiN FILM AT DIFFERENT MAGNETRON CURRENTS (BROWN MEANS EXCESS OF NITROGEN, YELLOW IS THE STOICHIOMETRIC CONCENTRATION OF TiN, GREY REPRESENTS A COATING POOR OF NITROGEN) ²⁰	34
FIGURE 13: CALCULATED CURVES FOR THE PARTIAL PRESSURE VS MASS FLOW FOR THE REACTIVE GAS, WITH DIFFERENT PUMPING SPEEDS ²¹	35
FIGURE 14: CATHODIC ARC SPOT MOTION ²⁴	36
FIGURE 15: MACROPARTICLES EMISSION AT LOW ANGLE ²⁸	37
FIGURE 16: CU MACROPARTICLES (~20MM DIAMETER) ON THE SURFACE OF A COPPER THIN FILM ²⁹	38
FIGURE 17: TILTED VIEW OF THE DROPLET SELECTED FOR FIB SECTION AND TEM LAMELLA PREPARATION ³⁰	39
FIGURE 18: S-FILTER FOR CATHODIC VACUUM ARC SOURCE ³¹	40
FIGURE 19: STRUCTURE ZONE DIAGRAM (SZD) PROPOSED BY THORNTON. SUBSTRATE TEMPERATURE AND PROCESS PRESSURE INFLUENCE THE FILM MORPHOLOGY ³²	42
FIGURE 20: STRUCTURE ZONE DIAGRAM (SZD) PROPOSED BY ANDERS IN 2010 ³⁴	43
FIGURE 21: THE PVD SYSTEM PROTOTYPES LOCATED IN THE MATERIAL SCIENCE AND TECHNOLOGY FOR NUCLEAR PHYSICS SERVICE AT THE NATIONAL LABORATORIES OF LEGNARO. ON THE LEFT THE FOUR CHAMBERS SYSTEM DEDICATED TO THE MAGNETRON SPUTTERING AND ON THE RIGHT THE PROTOTYPE DEDICATED TO THE CATHODIC ARC DEPOSITION.	45
FIGURE 22: FOUR CHAMBERS PVD PROTOTYPE VACUUM SCHEME.	47
FIGURE 23: CATHODIC VACUUM ARC PVD PROTOTYPE VACUUM SCHEME.	48
FIGURE 24: SEM PHILIPS XL30 AND EDS BRUKER XFLASH 410-M.	49
FIGURE 25: X'PERT PHILIPS/PANALYTICAL X-RAY DIFFRACTOMETER.	50

FIGURE 26: GPA CATHODIC VACUUM ARC ³⁵ .	51
FIGURE 27: CONNECTIONS OF THE CVA SOURCE ³⁵ .	52
FIGURE 28: CATHODE AND TRIGGER FROM A VACUUM SIDE VIEW. .	52
FIGURE 29:DETAILED VIEW OF THE MAGNETRON SPUTTERING SOURCE: 1 INSULATING FALGE,2 GROUND FLANGE,3 GROUND SHIELD,4 TARGET,5 MAGNET PACK, ,6 WATER COOLING CIRCUIT, 7 CATHODE BODY. .	53
FIGURE 30: 2 INCHES MAGNETRON SPUTTERING SOURCE (LEFT TOP VIEW, RIGTH PLASMA VIEW). .	54
FIGURE 31: EXPERIMENTAL CURVE VOLTAGE VERSUS N ₂ FLUX (25 SCCM AR AND 1kW POWER). .	56
FIGURE 32: XRD SPECTRUM OF SAMPLE TiN_06.....	58
FIGURE 33: LATTICE PARAMETER VERSUS N ₂ FLUX. .	59
FIGURE 34: TiN (111) PEAK POSITION VERSUS N ₂ FLUX. .	59
FIGURE 35: TiN_23 FIXED ON THE SAMPLE HOLDER. .	62
FIGURE 36: XRD SPECTRA OF TiN COATINGS IN FUNCTION OF THE PROCESS TEMPERATURE VARIATION.	64
FIGURE 37: SEM MICROGRAPHY OF TiN 23 COATING AT DIFFERENT MAGNIFICATIONS.....	64
FIGURE 38: SEM MICROGRAPHY OF TiCN_09 COATING AT DIFFERENT MAGNIFICATIONS.	67
FIGURE 39: SEM MICROGRAPHY OF TiCN_10 COATING AT DIFFERENT MAGNIFICATIONS.	67
FIGURE 40: XRD SPECTRA OF TiCN COATINGS SHOWING A DIFFERENT PREFERENTIAL GROWING ORIENTATION (TiCN 09 AND TiCN 10).	68
FIGURE 41: SEM MICROGRAPHY OF TiN CVA COATINGS FOR DIFFERENT DC BIAS APPLIED (0 V,-30 V,-100 V).....	72
FIGURE 42: TiN XRD SPECTRA IN FUNCTION OF THE DC BIAS APPLIED.....	73
FIGURE 43: XRD SPECTRA OF TiCN COATINGS IN FUNCTION OF THE PROCESS TEMPERATURE.	75
FIGURE 44: SEM MICROGRAPHY OF TiCN CVA 09 COATING AT DIFFERENT MAGNIFICATIONS.	75
FIGURE 45: XRD SPECTRA OF CrCN COATINGS IN FUNCTION OF THE PROCESS TEMPERATURE AND REACTIVE GASES RATIO.	77
FIGURE 46: SEM MICROGRAPHY OF CrCN CVA 05 COATING AT DIFFERENT MAGNIFICATIONS.	77
FIGURE 47: BALL ON FLAT CONFIGURATION FOR THE WEAR RATE EVALUATION.....	80
FIGURE 48: WEAR RATE MEASUREMENTS OF DIFFERENT WC BLANK SUBSTRATES, COATING MATERIALS AND DEPOSITION TECHNIQUES.....	81
FIGURE 49: AXONOMETRIC VIEW OF THE MAGNETRON SPUTTERING SOURCE DEVELOPED.....	83
FIGURE 50: CROSS SECTION OF THE MAGNETRON SPUTTERING SOURCE EVIDENCING THE POTENTIALS APPLIED.	84
FIGURE 51: MAGNET PACK CONFIGURATION (EXTERNAL ARRAY N45, INTERNAL ARRAY N35).	85
FIGURE 52: CROSS SECTION OF MGN SOURCE EVIDENCING THE WATER-COOLING CIRCUIT AND THE MAGNETS ARRAYS.	85
FIGURE 53: FEM SIMULATION WITH N35 EXTERNAL MAGNET ARRAY AND N45 INERTNAL MAGNET ARRAY.	86
FIGURE 54: MAGNETIC FIELD COMPONENT Bz IN FUNCTION OF THE DISTANCE FROM THE CATHODE SURFACE.	87
FIGURE 55: MAGNETIC FIELD COMPONENT Br IN FUNCTION OF THE DISTANCE FROM THE CENTRE OF THE CATHODE.....	88
FIGURE 56: FEM SIMULATION SET UP IMPOSING A DIFFERENCE OF PRESSURE OF 1 BAR BETWEEN THE ATMOSPHERIC AND VACUUM SIDE OF THE CATHODE BODY.	89
FIGURE 57:FEM SIMULATION SET UP IMPOSING THE CONSTRAINS WHERE THE CATHODE IS FIXED TO THE EXTERNAL FLANGE.	89

FIGURE 58: FEM RESULTS FOR THE VACUUM PRESSURE SIMULATION REPORTED AS SAFETY FACTOR.....	90
FIGURE 59: FEM SIMULATION SET UP IMPOSING A DIFFERENCE OF PRESSURE OF 4 BAR BETWEEN THE WATER-COOLED SIDE AND THE VACUUM SIDE OF THE CATHODE BODY.	91
FIGURE 60: FEM RESULTS FOR THE WATER-COOLING PRESSURE SIMULATION REPORTED AS SAFETY FACTOR.	91
FIGURE 61: DETAILED VIEW OF THE SPACERS CONNECTED TO THE CATHODE BODY.	92
FIGURE 62: DETAILED VIEW OF THE CONSTRAINS IMPOSED IN THE SIMULATION WITH THE ADDITION OF THE SPACERS.	92
FIGURE 63: FEM SIMULATION RESULT, AFTER THE ADDITION OF SPACERS, REPORTED AS SAFETY FACTOR.	93
FIGURE 64: MAGNETRON SPUTTERING SOURCE READY FOR THE ASSEMBLING ONTO THE INDUSTRIAL PVD SYSTEM.....	94
FIGURE 65: PUMPING UNIT COMPOSED OF A SCREW PUMP 1, ROOTS BOOSTER 2, HEPA FILTER 3 AND TURBOMOLECULAR PUMP 4.	98
FIGURE 66: SCHEME OF THE COMPONENT'S DISTRIBUTION INSIDE THE DEPOSITION CHAMBER.....	99
FIGURE 67: PVD SOURCES MOUNTED ON THE INDUSTRIAL SYSTEM (ON THE LEFT THE ARCS AND ON THE RIGHT THE MAGNETRON).	100
FIGURE 68: DETAILED VIEW OF THE RESISTIVE HEATER POSITIONED IN CORRESPONDENCE OF THE PUMPING FLANGE.	101
FIGURE 69: TOP VIEW OF THE DEPOSITION CHAMBER.....	102
FIGURE 70: LATERAL VIEW OF THE DEPOSITION CHAMBER.....	103
FIGURE 71: REAR VIEW OF THE DEPOSITION CHAMBER.	104
FIGURE 72: AXONOMETRIC VIEW OF THE DEPOSITION CHAMBER.	105
FIGURE 73: THE SAMPLE HOLDER EVIDENCING THE PLANETARY MOTION.	106
FIGURE 74: THE BASE OF THE SAMPLE HOLDER EVIDENCING THE SPHERES USED TO DISSIPATE THE WEIGHT AND MAINTAIN THE ROTATION.	107
FIGURE 75: TOP VIEW OF THE CAROUSEL.....	107
FIGURE 76: LATERAL VIEW OF THE CAROUSEL.....	108
FIGURE 77: PINNACLE 12 kW OPERATING RANGE.	109
FIGURE 78: MAGIX15kW OPERATING RANGE.....	110
FIGURE 79: THE CHAMBER PRESSURE VARIATION IN FUNCTION OF THE TIME (WITHOUT PUMPING).	112
FIGURE 80: 3D RENDERING OF THE NON-COMMERCIAL PVD SYSTEM.	114
FIGURE 81: REAL VIEW OF THE NON-COMMERCIAL PVD SYSTEM WITH THE CAROUSEL AND ROLLS INSERTED IN THE DEPOSITION CHAMBER ⁴¹	114
FIGURE 82: WIRE ROLLS OF DIFFERENT DIMENSIONS AND SHAPE DEPOSITED WITH TIN ⁴¹	116
FIGURE 83: WIRE ROLLS DEPOSITED WITH TiCN ⁴¹	116

List of Tables

TABLE 1: CLASSIFICATION OF VARIOUS HARD MATERIALS IN FUNCTION OF THE CHEMICAL BOND ⁴	14
TABLE 2: PROPERTIES AND BEHAVIOR OF VARIOUS GROUPS OF HARD MATERIALS (M = METALLIC; C = COVALENT; I = IONIC) ⁵ . .	15
TABLE 3: CARBIDES, NITRIDES, OXIDES AND BORIDES EMPLOYED TO RESIST CORROSION AND WEAR ⁶	18
TABLE 4: PROPERTIES OF METALLIC HARD MATERIALS	19
TABLE 5: PROPERTIES OF COVALENT HARD MATERIALS	20
TABLE 6: PROPERTIES OF IONIC HARD MATERIALS	20
TABLE 7: TYPES OF BALANCED AND UNBALANCED MAGNETRONS AS CLASSIFIED BY GENCOA ¹⁸	31
TABLE 8: TITANIUM NITRIDE THIN FILM DEPOSITION WITH FIXED ARGON FLUX AND VARYING THE NITROGEN FLUX.	57
TABLE 9: EVALUATION OF THE N ABUNDANCE IN THE THIN FILM.	60
TABLE 10: N CONTENT IN FUNCTION OF THE TEMPERATURE VARIATION (EDS ANALYSIS).	61
TABLE 11: N CONTENT IN FUNCTION OF THE TEMPERATURE VARIATION (NAGAKURA EQUATION).	61
TABLE 12: PROCESS PARAMETERS OF TiCN MGN COATINGS.	66
TABLE 13: MAGNETRON SPUTTERING DEPOSITION PARAMETERS AND SUBSTRATE MATERIALS.	69
TABLE 14: PROCESS PARAMETERS OF TiN CVA DEPOSITIONS.	72
TABLE 15: PROCESS PARAMETERS OF TiCN CVA COATINGS.	74
TABLE 16: PROCESS PARAMETERS OF CrCN CVA COATINGS.....	76
TABLE 17: CATHODIC VACUUM ARC DEPOSITION PARAMETERS AND SUBSTRATE MATERIALS.	78
TABLE 18: WEAR RATE TEST PARAMETERS.	79

Bibliography

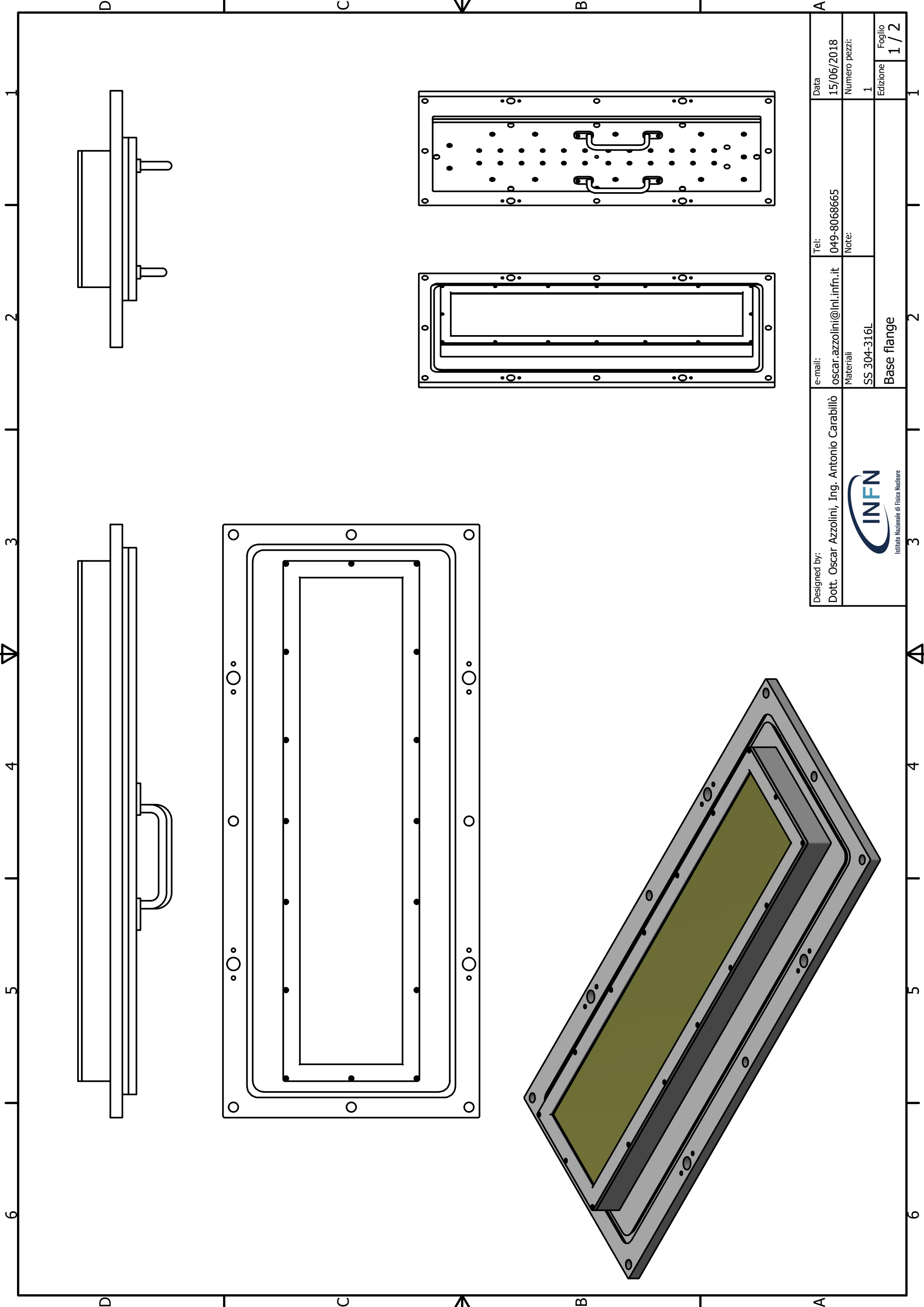
1. Tungsten Carbide Wire Rolls. eurolls.com/en/main/products/wire-products/item/27-wire-rolls/46-tungsten-carbide-wire-rolls.
2. Special Wire Microcassettes Type C. eurolls.com/en/main/products/wire-products/item/26-wire-rolling-cassettes/49-special-wire-microcassettes-type-c.
3. H. A. Sundquist, M. T. Kurkinen & E. H. Sirvio. *Met. Technol.* **10**, (1983) 130.
4. Holleck, H. Material selection for hard coatings. *J. Vac. Sci. Technol. Vac. Surf. Films* **4**, 2661–2669 (1986).
5. Subramanian, C. & Strafford, K. N. Review of multicomponent and multilayer coatings for tribological applications. *Wear* **165**, 85–95 (1993).
6. P. Vincenzini, K.N. Strafford, P. K. Datta and J. Gray. *Surface Engineering Practices: Processes, Fundamentals and Applications in Corrosion and Wear*, Ellis Horwood, Chichester. (1990).
7. *Materials Science of Thin Films*. (Elsevier, 2002). doi:10.1016/B978-0-12-524975-1.X5000-9.
8. Pira Cristian. Nb thick films in 6 GHz superconducting resonant cavities. (Università di Padova, 2018).
9. Powell, C.F.; Oxley, J.H.; Blocher, J.M. *Vapour Deposition*. (John Wiley & Sons, 1966).
10. Mattox, D. M. *Handbook of physical vapor deposition (PVD) processing*. (Elsevier, 2010).


11. Baptista, A., Silva, F., Porteiro, J., Míguez, J. & Pinto, G. Sputtering Physical Vapour Deposition (PVD) Coatings: A Critical Review on Process Improvement and Market Trend Demands. *Coatings* **8**, 402 (2018).
12. pvd-plating magnetron sputtering source. <http://www.pvd-plating.com/>.
13. Musil, J. & Kadlec, S. Reactive sputtering of TiN films at large substrate to target distances. *Vacuum* **40**, 435–444 (1990).
14. Adibi, F., Petrov, I., Greene, J. E., Hultman, L. & Sundgren, J. -E. Effects of high-flux low-energy (20–100 eV) ion irradiation during deposition on the microstructure and preferred orientation of Ti_{0.5}Al_{0.5}N alloys grown by ultra-high-vacuum reactive magnetron sputtering. *J. Appl. Phys.* **73**, 8580–8589 (1993).
15. Kelly, P. J. & Arnell, R. D. Magnetron sputtering: a review of recent developments and applications. *Vacuum* **56**, 159–172 (2000).
16. Savvides, N. & Window, B. Unbalanced magnetron ion-assisted deposition and property modification of thin films. *J. Vac. Sci. Technol.* **4**, 504–508 (1986).
17. Window, B. & Savvides, N. Charged Particle Fluxes from Planar Magnetron Sputtering Sources. *J. Vac. Sci. Technol. Vac. Surf. Films* **4**, 196–202 (1986).
18. Brown, R. & Bellido-Gonzalez, V. Comparison of balanced and unbalanced array designs. (2013).
19. Goree, J. & Sheridan, T. E. Magnetic field dependence of sputtering magnetron efficiency. *Appl. Phys. Lett.* **59**, 1052–1054 (1991).
20. Rafieian, D. Optimal Deposition Conditions of TiN Barrier Layers for the Growth of Vertically Aligned Carbon Nanofibers. 44.
21. Larsson, T., Blom, H., Nender, C. & Berg, S. A physical model for eliminating instabilities in reactive sputtering. 6.

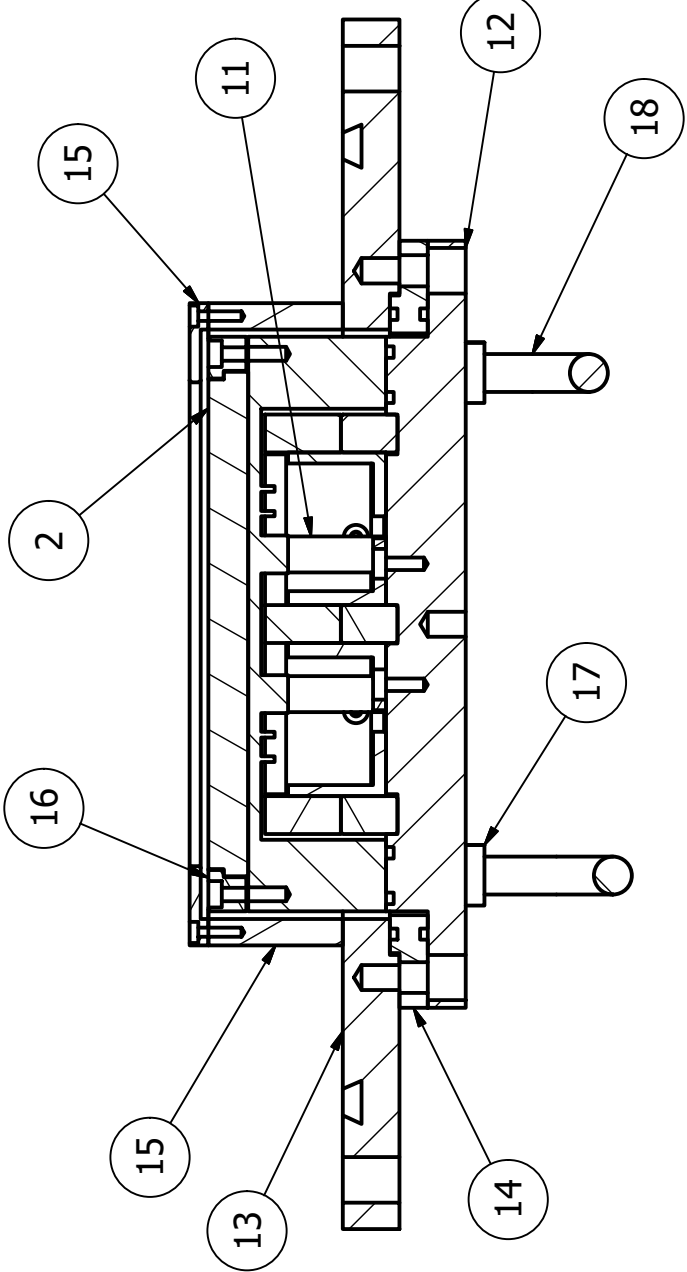
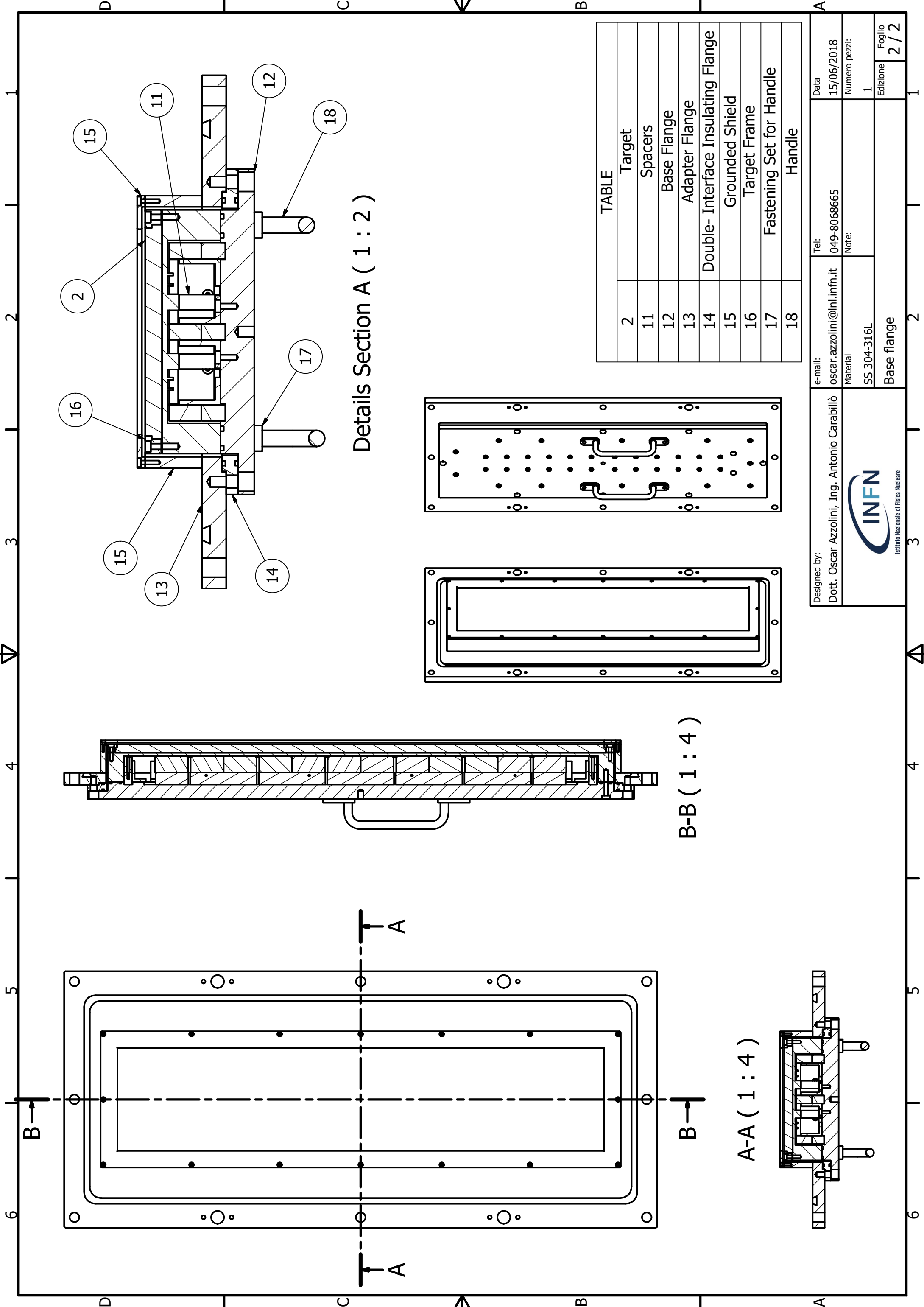
22. Aksenov, I. I., Belous, V. A., Strel'nitskij, V. E. & Aksyonov, D. S. PHYSICS OF RADIOTECHNOLOGY AND ION-PLASMA TECHNOLOGIES VACUUM-ARC EQUIPMENT AND COATING TECHNOLOGIES IN KIPT. 13.
23. Boxman, R. L. & Zhitomirsky, V. N. Vacuum arc deposition devices. *Rev. Sci. Instrum.* **77**, 021101 (2006).
24. Wang, S., Lin, Z., Qiao, H., Ba, D. & Zhu, L. Influence of a Scanning Radial Magnetic Field on Macroparticle Reduction of Arc Ion-Plated Films. *Coatings* **8**, 49 (2018).
25. Valente-Feliciano, A.-M. HiPIMS: a New Generation of Film Deposition Techniques for SRF Applications. **7** (2013).
26. WANG, Y., LI, C., SHI, J., WU, X. & DING, H. Measurement of electron density and electron temperature of a cascaded arc plasma using laser Thomson scattering compared to an optical emission spectroscopic approach. *Plasma Sci. Technol.* **19**, 115403 (2017).
27. Boxman, R. L., Sanders, D. M. & Martin, P. J. *Handbook of Vacuum Arc Science & Technology: Fundamentals and Applications*. (William Andrew, 1996).
28. Anders, A. Macroparticles. in *Cathodic Arcs: From Fractal Spots to Energetic Condensation* (ed. Anders, A.) 265–298 (Springer New York, 2008). doi:10.1007/978-0-387-79108-1_6.
29. Keppel, G., Ricca, F. D., Greggio, C. & Palmieri, V. Design and Setup of a Cathodic Arc Vapor Deposition Source. **3**.
30. Bemporad, E., Sebastiani, M., De Felicis, D., Mangione, V. & Carassiti, F. Focused ion beam and transmission electron microscopy as a powerful tool to understand localized corrosion phenomena. *Corros. Rev.* **29**, (2011).
31. Anders, A. Chapter 10 - Unfiltered and Filtered Cathodic Arc Deposition. in *Handbook of Deposition Technologies for Films and Coatings (Third Edition)* (ed. Martin, P. M.)

- 466–531 (William Andrew Publishing, 2010). doi:10.1016/B978-0-8155-2031-3.00010-7.
- 32.Thornton, J. A. & Hoffman, D. W. Stress-related effects in thin films. *Thin Solid Films* **171**, 5–31 (1989).
- 33.Movchan, B. A. & Demchishin, A. V. STRUCTURE AND PROPERTIES OF THICK CONDENSATES OF NICKEL, TITANIUM, TUNGSTEN, ALUMINUM OXIDES, AND ZIRCONIUM DIOXIDE IN VACUUM. *Fiz Met. Met.* **28** 653-60 Oct 1969 (1969).
- 34.Anders, A. A structure zone diagram including plasma-based deposition and ion etching. *Thin Solid Films* **518**, 4087–4090 (2010).
- 35.Home - GPA Ges. für PlasmaApplikation mbH. <http://www.plasmaapplikation.de/de/>.
- 36.Nagakura. Lattice parameter of the non-stoichiometric compound TiN,. *Appl Cryst* **8** 65 (1975).
- 37.Lekka, M. *et al.* Room and high temperature wear behaviour of Ni matrix micro- and nano-SiC composite electrodeposits. *Surf. Coat. Technol.* **206**, 3658–3665 (2012).
- 38.Marin, E. *et al.* Diffusive thermal treatments combined with PVD coatings for tribological protection of titanium alloys. *Mater. Des.* **89**, 314–322 (2016).
- 39.Lanzutti, A., Lekka, M., de Leitenburg, C. & Fedrizzi, L. Effect of pulse current on wear behavior of Ni matrix micro-and nano-SiC composite coatings at room and elevated temperature. *Tribol. Int.* **132**, 50–61 (2019).
- 40.Chiggiato, P. Materials and Properties IV Outgassing. *CERN Accel. Sch. CAS Vac. Part. Accel.* **47** (2017).
- 41.PVD | Eurolls. <http://www.eurolls.com/advanced-technologies/en/treatments/pvd>.

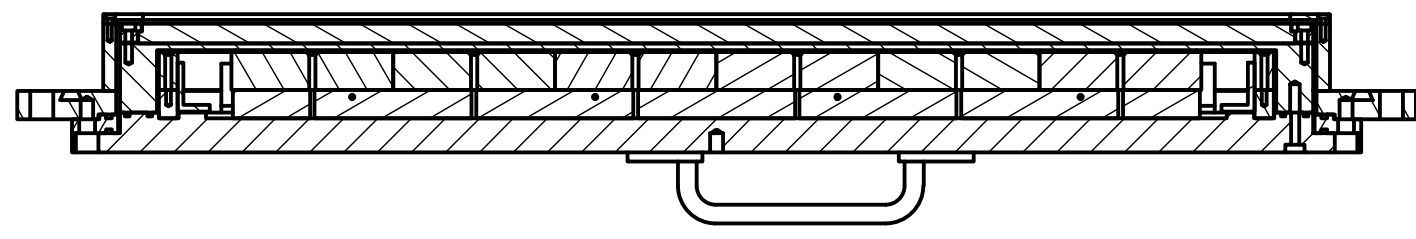
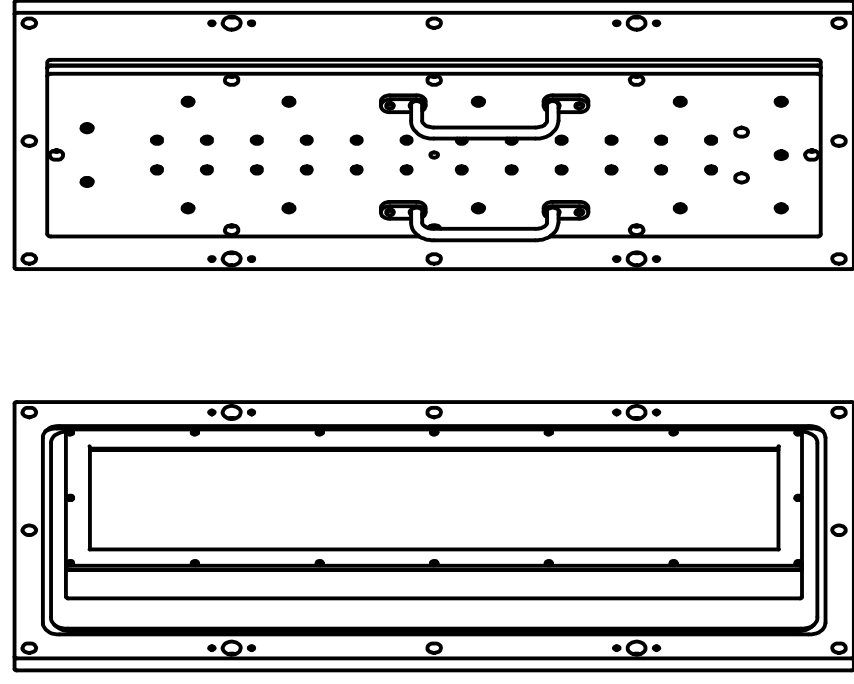
Thesis Annex



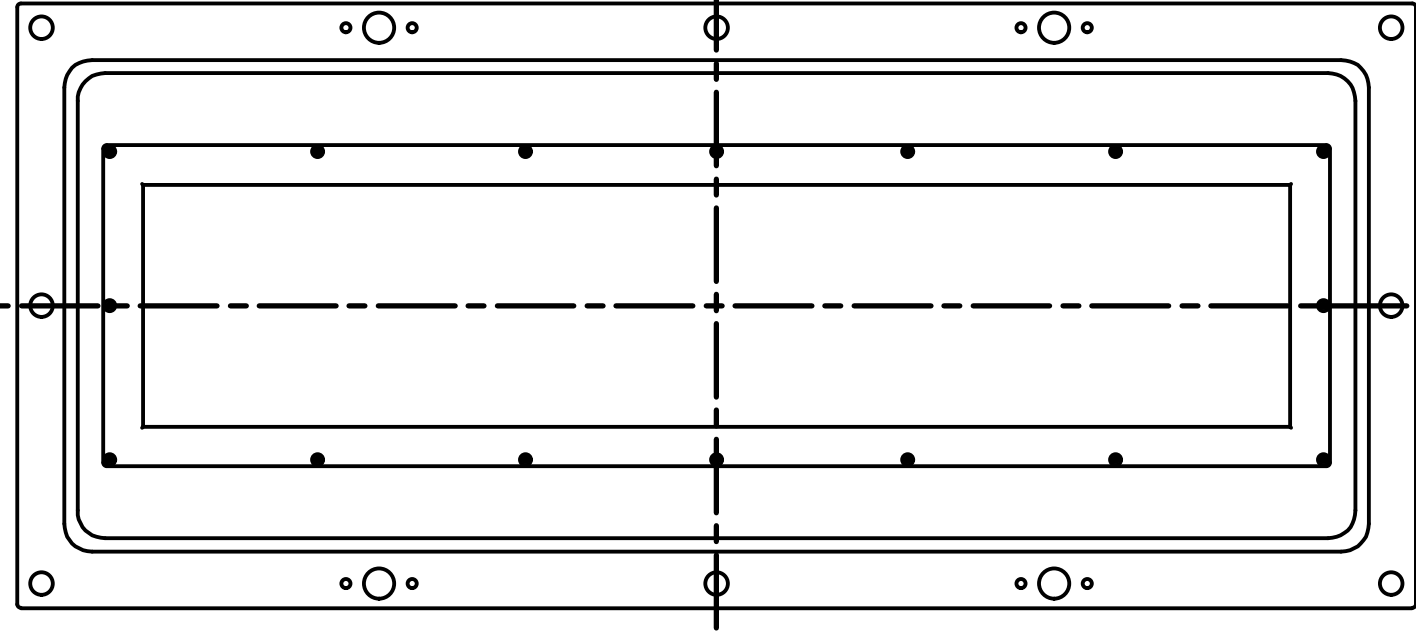
Designed by: Dott. Oscar Azzolini, Ing. Antonio Carabillò	e-mail: oscar.azzolini@lnl.infn.it	Tel: 049-8068665	Data 15/06/2018
 Istituto Nazionale di Fisica Nucleare	Materiali SS 304-316L	Note:	Numero pezzi: 1
	Base flange		Edizione 1 / 2



Details Section A (1 : 2)



B-B (1 : 4)



A-A (1 : 4)

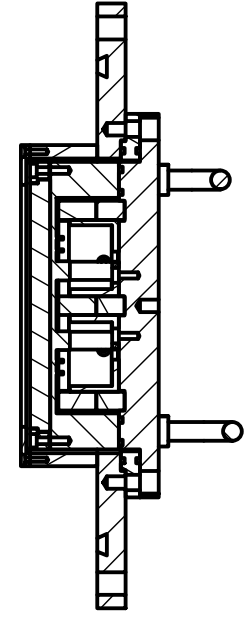
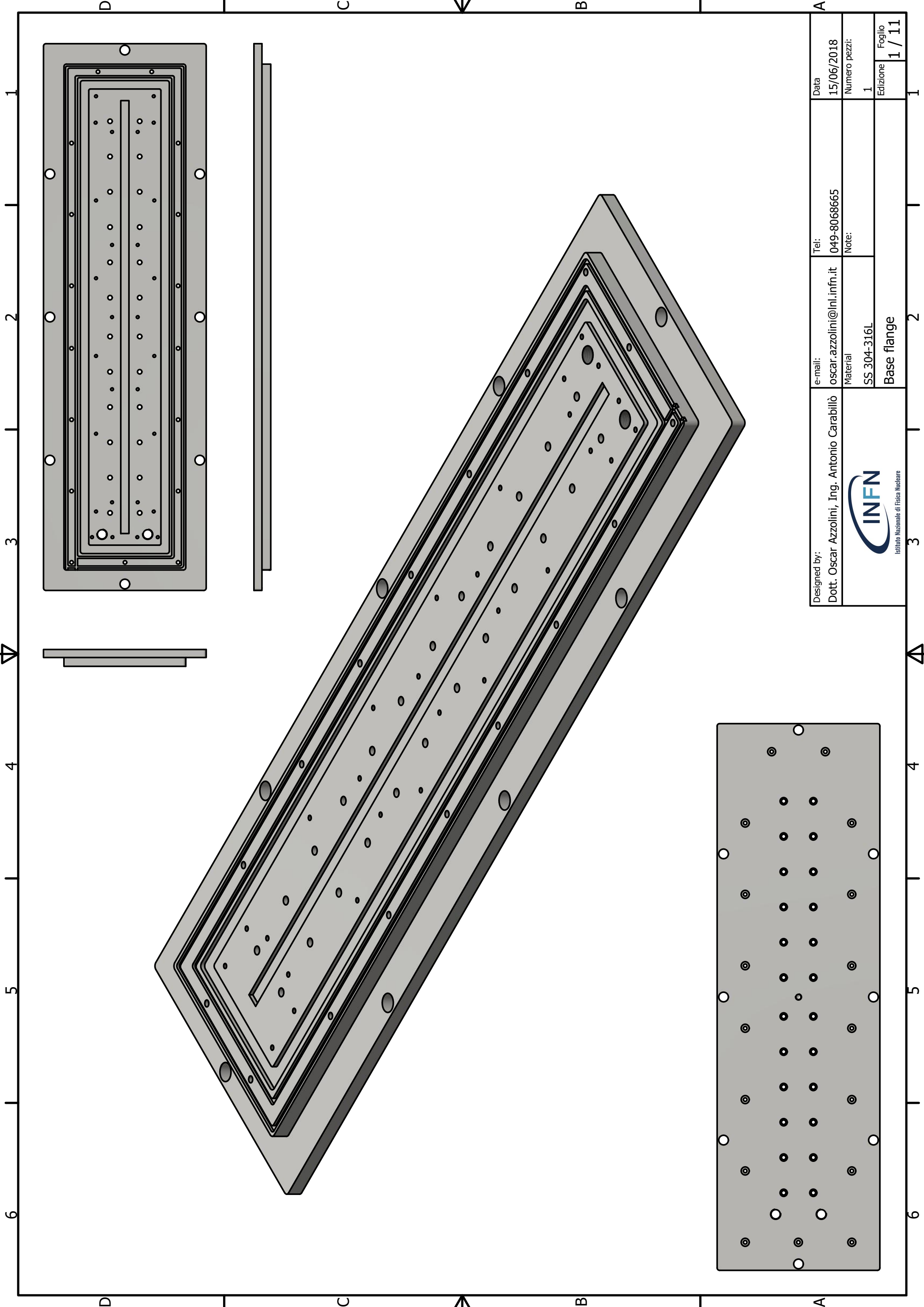



TABLE	
2	Target
11	Spacers
12	Base Flange
13	Adapter Flange
14	Double- Interface Insulating Flange
15	Grounded Shield
16	Target Frame
17	Fastening Set for Handle
18	Handle

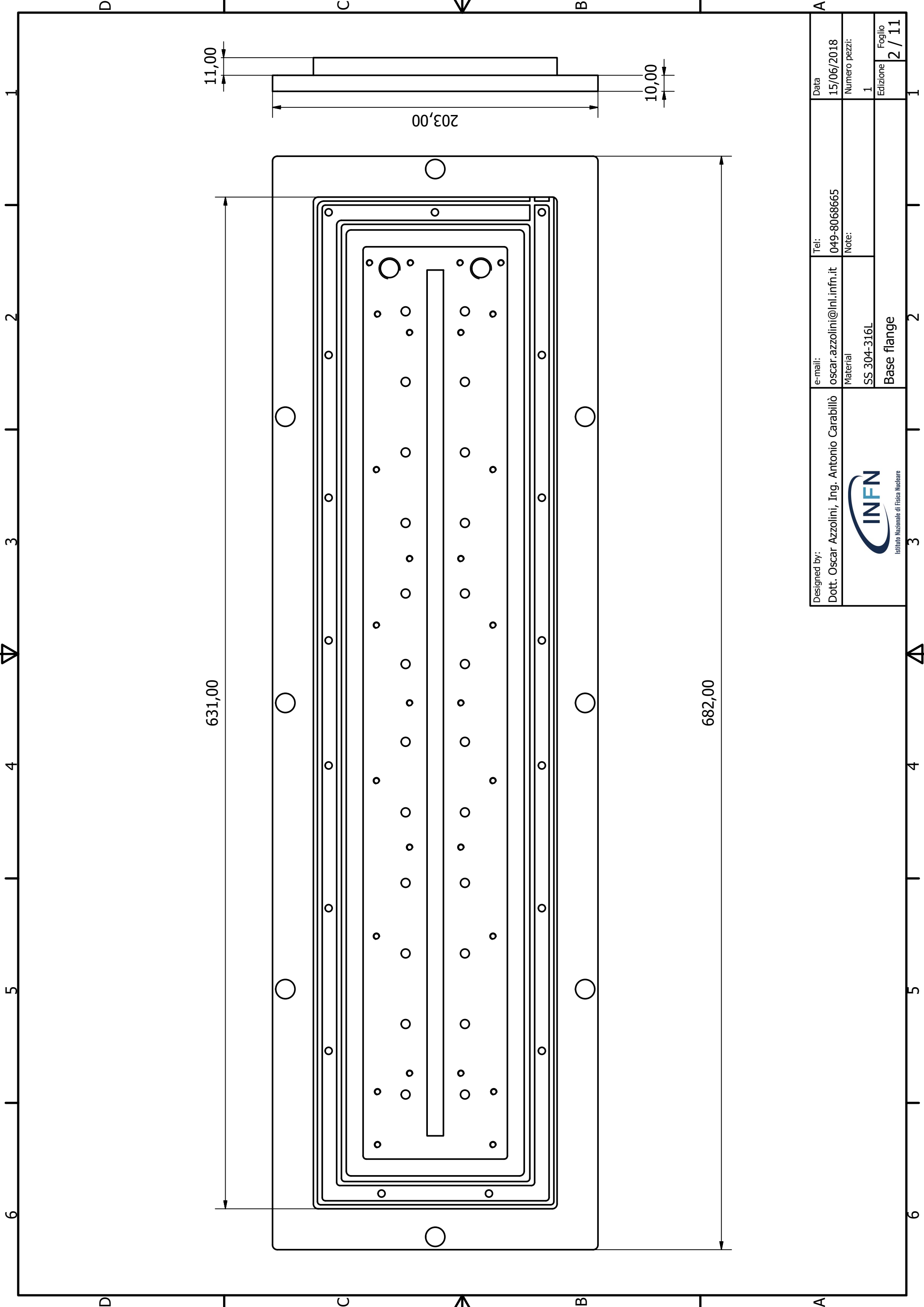
Designed by: Dott. Oscar Azzolini, Ing. Antonio Caraballo	e-mail: oscar.azzolini@lnl.infn.it	Tel: 049-8068665	Data 15/06/2018
	Material SS 304-316L	Note:	Numero pezzi: 1
Base flange			Edizione 2 / 2


INFN
Istituto Nazionale di Fisica Nucleare

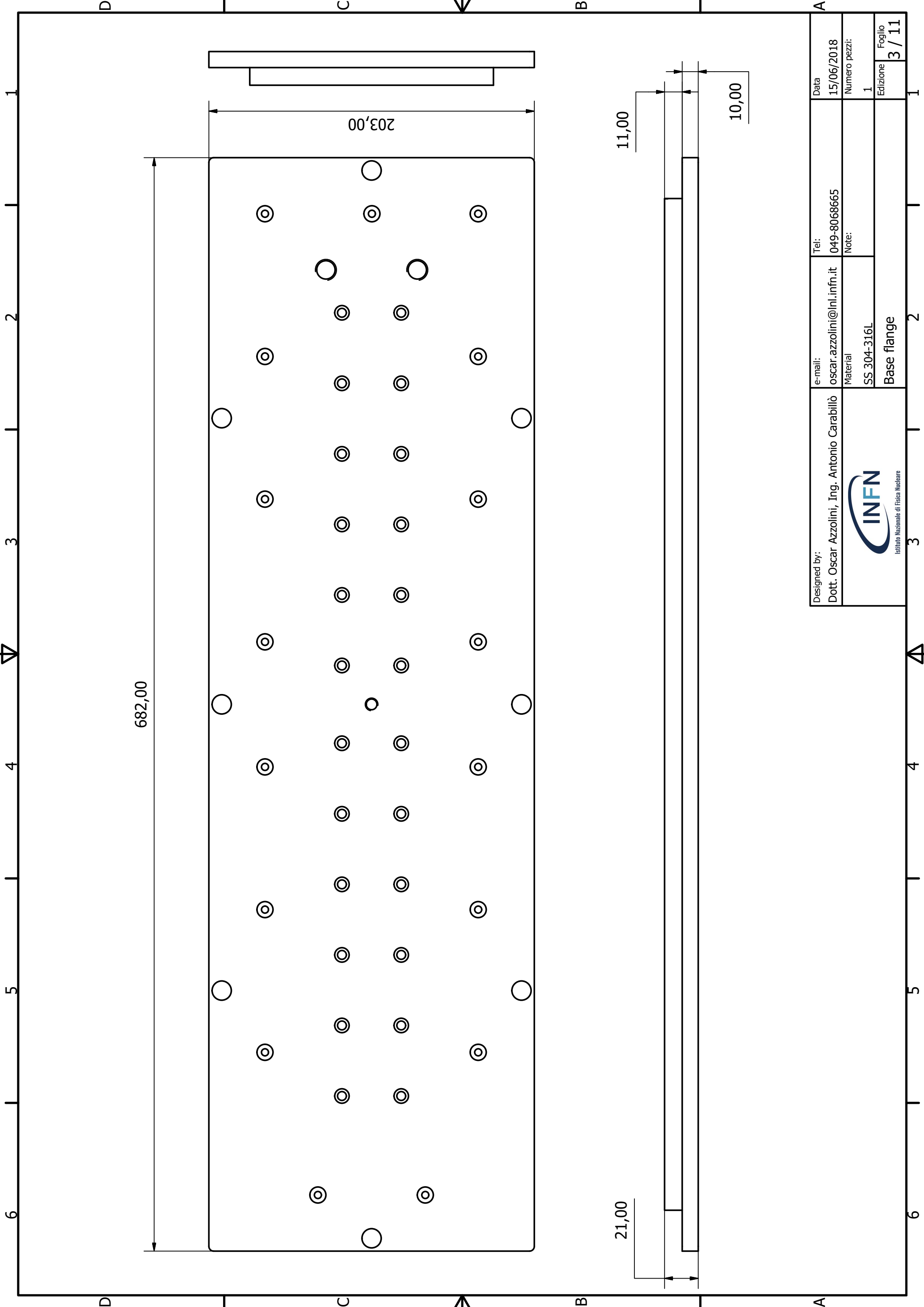
1
2
3
4
5
6




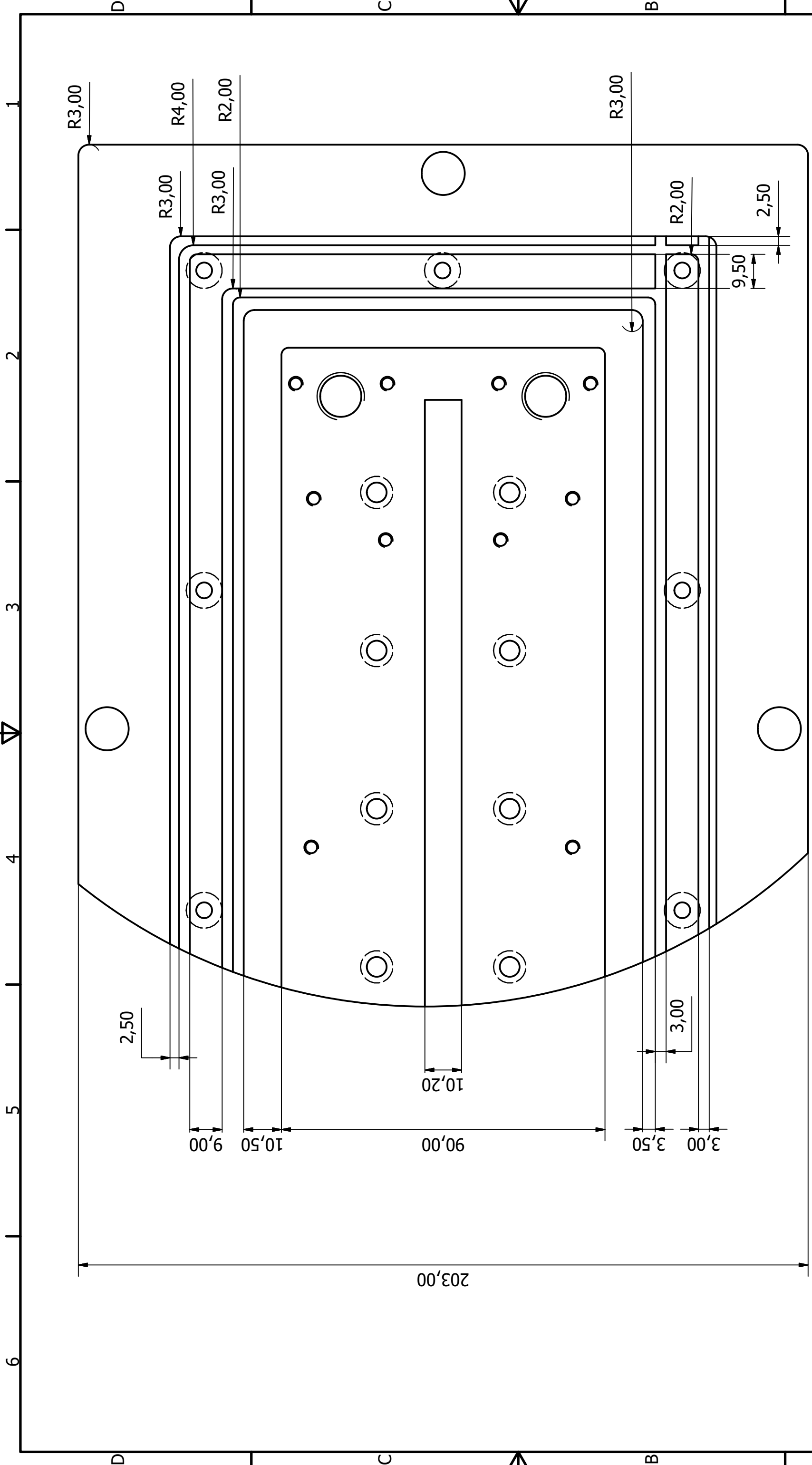
Designed by: Dott. Oscar Azzolini, Ing. Antonio Carabillò	e-mail: oscar.azzolini@lnl.infn.it	Tel: 049-8068665	Data 15/06/2018
 Istituto Nazionale di Fisica Nucleare	Material SS 304-316L	Note:	Numero pezzi: 1
	Base flange		Edizione 1 / 11




Designed by: Dott. Oscar Azzolini, Ing. Antonio Carabillò	e-mail: oscar.azzolini@lnl.infn.it	Tel: 049-8068665	Data 15/06/2018
	Material SS 304-316L	Note:	Numero pezzi: 1
 Istituto Nazionale di Fisica Nucleare			Edizione 1
Base flange			Foglio 2 / 11

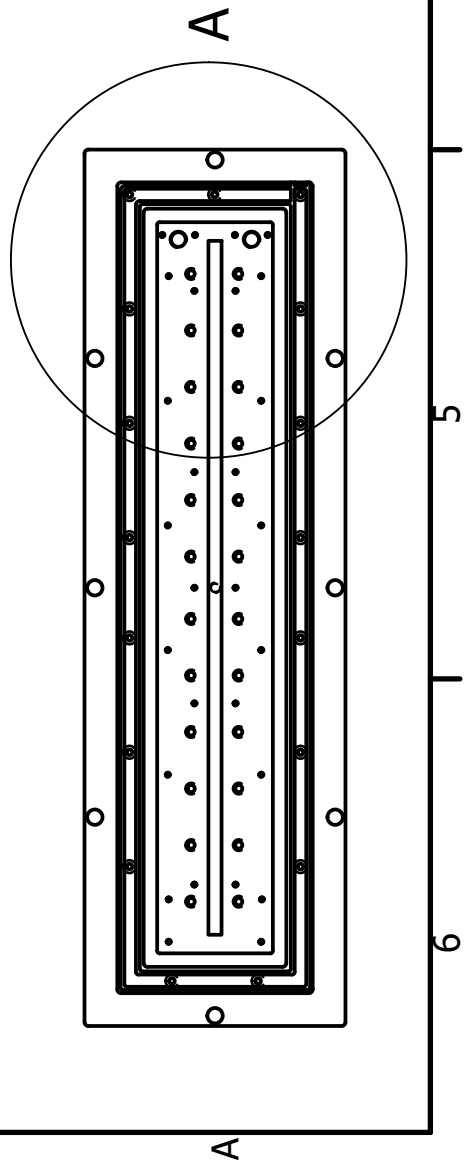


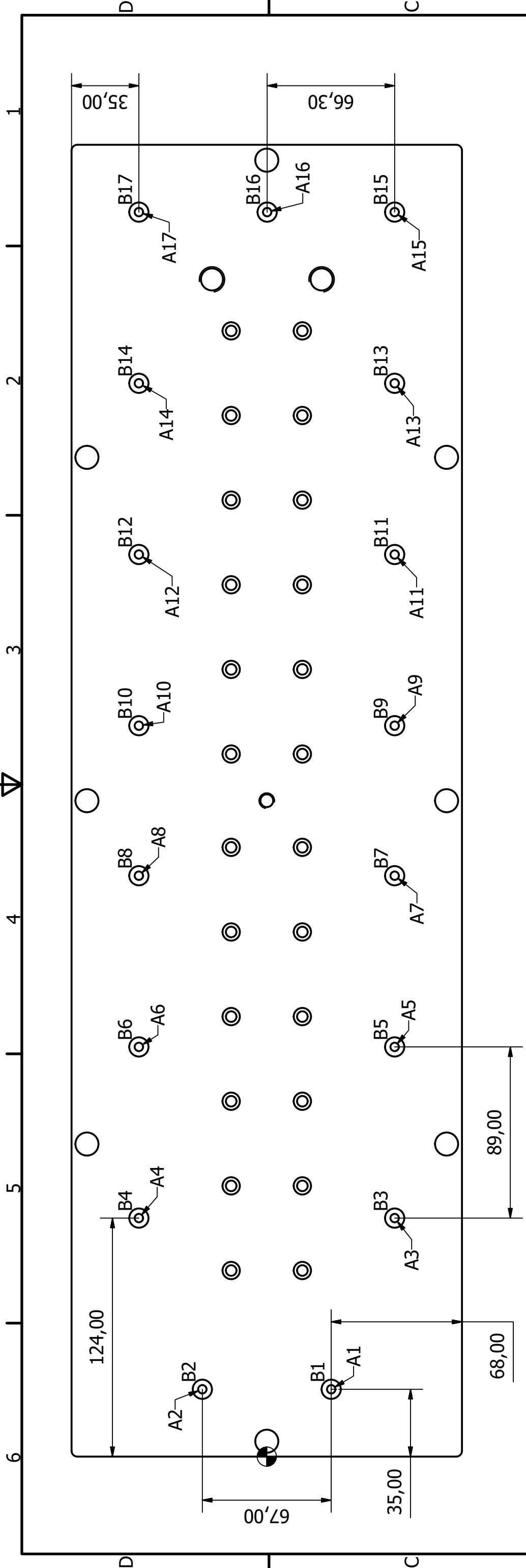
Designed by: Dott. Oscar Azzolini, Ing. Antonio Carabillò	e-mail: oscar.azzolini@lnl.infn.it	Tel: 049-8068665	Data 15/06/2018
	Material SS 304-316L	Note:	Numero pezzi: 1
 Istituto Nazionale di Fisica Nucleare			Edizione 3 / 11
			Foglio 3 / 11



A (1:1)

Designed by: Dott. Oscar Azzolini, Ing. Antonio Carabillò	e-mail: oscar.azzolini@lnl.infn.it	Tel: 049-8068665	Data 15/06/2018
 Istituto Nazionale di Fisica Nucleare	Material SS 304-316L	Note:	Numero pezzi: 1
	Base flange		Edizione 4 / 11





HOLE	QUOTA X	QUOTA Y	DESCRIPTION
A1	35,00	-33,50	Ø4,40 THRU
A2	35,00	33,50	Ø4,40 THRU
A3	124,00	-66,50	Ø4,40 THRU
A4	124,00	66,50	Ø4,40 THRU
A5	213,00	-66,50	Ø4,40 THRU
A6	213,00	66,50	Ø4,40 THRU
A7	302,00	-66,50	Ø4,40 THRU
A8	302,00	66,50	Ø4,40 THRU
A9	380,00	-66,50	Ø4,40 THRU
A10	380,00	66,50	Ø4,40 THRU
A11	469,00	-66,50	Ø4,40 THRU
A12	469,00	66,50	Ø4,40 THRU
A13	558,00	-66,50	Ø4,40 THRU
A14	558,00	66,50	Ø4,40 THRU
A15	647,00	-66,50	Ø4,40 THRU
A16	647,00	-0,20	Ø4,40 THRU
A17	647,00	66,50	Ø4,40 THRU

HOLE TABLE			
HOLE	QUOTA X	QUOTA Y	DESCRIPTION
B1	35,00	-33,50	Ø10,00 -4,00 DEEP
B2	35,00	33,50	Ø10,00 -4,00 DEEP
B3	124,00	-66,50	Ø10,00 -4,00 DEEP
B4	124,00	66,50	Ø10,00 -4,00 DEEP
B5	213,00	-66,50	Ø10,00 -4,00 DEEP
B6	213,00	66,50	Ø10,00 -4,00 DEEP
B7	302,00	-66,50	Ø10,00 -4,00 DEEP
B8	302,00	66,50	Ø10,00 -4,00 DEEP
B9	380,00	-66,50	Ø10,00 -4,00 DEEP

HOLE TABLE			
HOLE	QUOTA X	QUOTA Y	DESCRIPTION
B10	380,00	66,50	Ø10,00 -4,00 DEEP
B11	469,00	-66,50	Ø10,00 -4,00 DEEP
B12	469,00	66,50	Ø10,00 -4,00 DEEP
B13	558,00	-66,50	Ø10,00 -4,00 DEEP
B14	558,00	66,50	Ø10,00 -4,00 DEEP
B15	647,00	-66,50	Ø10,00 -4,00 DEEP
B16	647,00	-0,20	Ø10,00 -4,00 DEEP
B17	647,00	66,50	Ø10,00 -4,00 DEEP

Designed by: **Dott. Oscar Azzolini, Ing. Antonio Carabillò**

Tel: 049-8068665

e-mail: oscar.azzolini@lnl.infn.it

Material: SS 304-316L

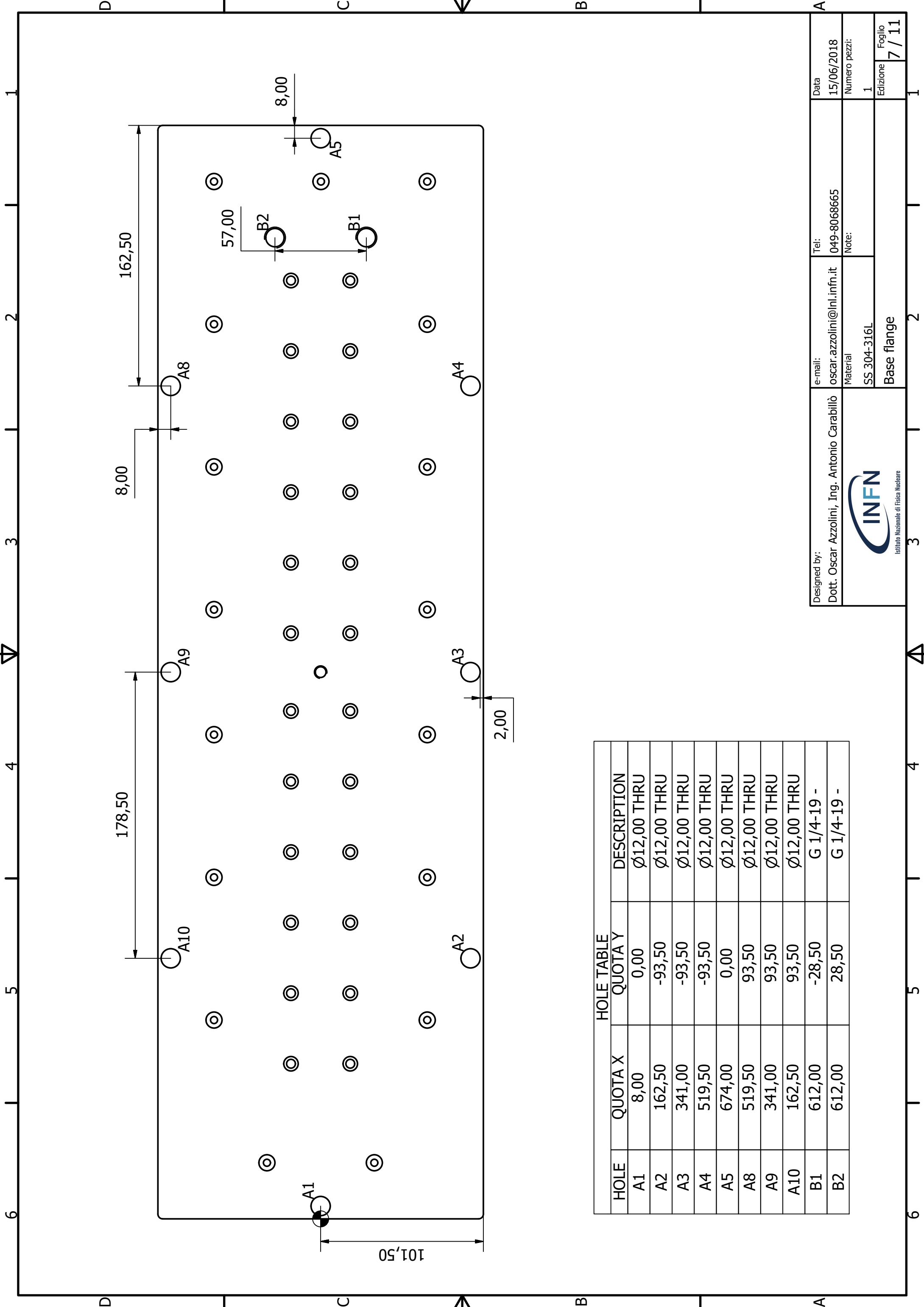
Base flange

Data: 15/06/2018

Numero pezzi: 1

Edizione: 1

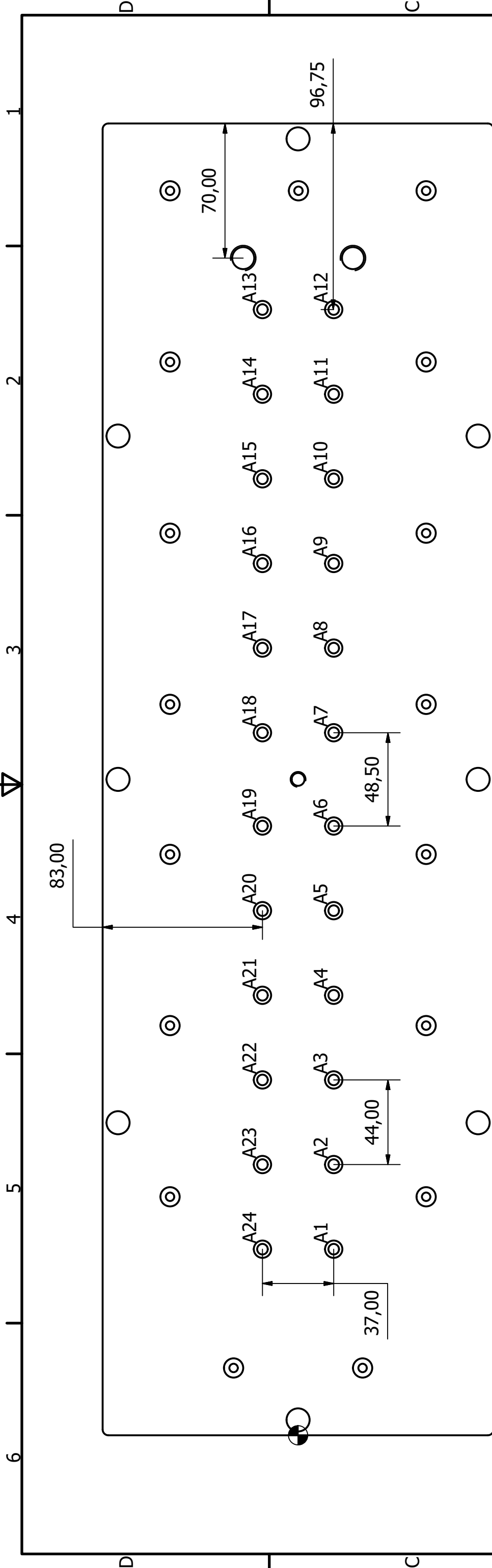
Foglio: 6 / 11



HOLE TABLE

HOLE	QUOTA X	QUOTA Y	DESCRIPTION
A1	8,00	0,00	Ø12,00 THRU
A2	162,50	-93,50	Ø12,00 THRU
A3	341,00	-93,50	Ø12,00 THRU
A4	519,50	-93,50	Ø12,00 THRU
A5	674,00	0,00	Ø12,00 THRU
A8	519,50	93,50	Ø12,00 THRU
A9	341,00	93,50	Ø12,00 THRU
A10	162,50	93,50	Ø12,00 THRU
B1	612,00	-28,50	G 1/4-19 -
B2	612,00	28,50	G 1/4-19 -

Designed by: Dott. Oscar Azzolini, Ing. Antonio Carabillò	e-mail:	Tel:	Data
	oscar.azzolini@lnl.infn.it	049-8068665	15/06/2018
	Material	Note:	Numero pezzi:
	SS 304-316L		1
 Istituto Nazionale di Fisica Nucleare			Edizione
Base flange			7 / 11



HOLE TABLE			
HOLE	QUOTA X	QUOTA Y	DESCRIPTION
A1	96,75	-18,50	Ø5,50 THRU └┘ Ø9,00
A2	140,75	-18,50	Ø5,50 THRU └┘ Ø9,00
A3	184,75	-18,50	Ø5,50 THRU └┘ Ø9,00
A4	228,75	-18,50	Ø5,50 THRU └┘ Ø9,00
A5	272,75	-18,50	Ø5,50 THRU └┘ Ø9,00
A6	316,75	-18,50	Ø5,50 THRU └┘ Ø9,00
A7	365,25	-18,50	Ø5,50 THRU └┘ Ø9,00
A8	409,25	-18,50	Ø5,50 THRU └┘ Ø9,00
A9	453,25	-18,50	Ø5,50 THRU └┘ Ø9,00
A10	497,25	-18,50	Ø5,50 THRU └┘ Ø9,00

HOLE TABLE			
HOLE	QUOTA X	QUOTA Y	DESCRIPTION
A11	541,25	-18,50	Ø5,50 THRU └┘ Ø9,00
A12	585,25	-18,50	Ø5,50 THRU └┘ Ø9,00
A13	585,25	18,50	Ø5,50 THRU └┘ Ø9,00
A14	541,25	18,50	Ø5,50 THRU └┘ Ø9,00
A15	497,25	18,50	Ø5,50 THRU └┘ Ø9,00
A16	453,25	18,50	Ø5,50 THRU └┘ Ø9,00
A17	409,25	18,50	Ø5,50 THRU └┘ Ø9,00
A18	365,25	18,50	Ø5,50 THRU └┘ Ø9,00

HOLE TABLE			
HOLE	QUOTA X	QUOTA Y	DESCRIPTION
A19	316,75	18,50	Ø5,50 THRU └┘ Ø9,00
A20	272,75	18,50	Ø5,50 THRU └┘ Ø9,00
A21	228,75	18,50	Ø5,50 THRU └┘ Ø9,00
A22	184,75	18,50	Ø5,50 THRU └┘ Ø9,00
A23	140,75	18,50	Ø5,50 THRU └┘ Ø9,00
A24	96,75	18,50	Ø5,50 THRU └┘ Ø9,00

Designed by:
Dott. Oscar Azzolini, Ing. Antonio Carabillò

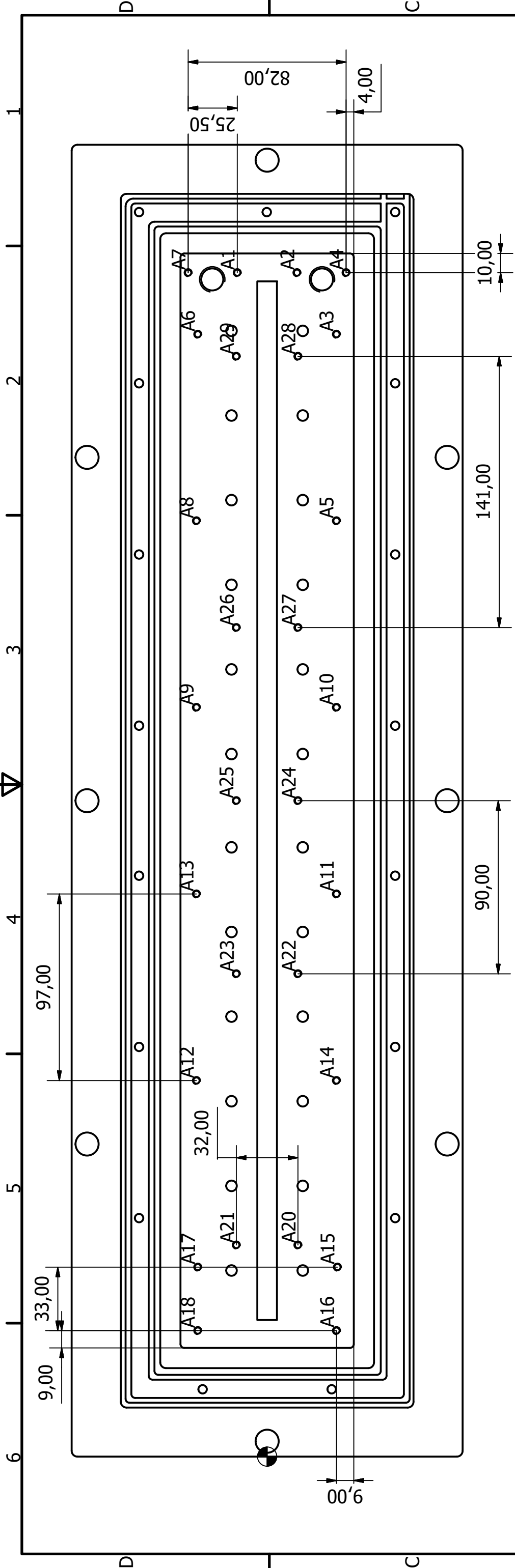
e-mail: oscar.azzolini@lnl.infn.it
Tel: 049-8068665

Material: SS 304-316L
Note:

Base flange

Data: 15/06/2018
Numero pezzi: 1

Edizione: 8 / 11
Foglio: 1



HOLE TABLE

HOLE	QUOTA X	QUOTA Y	DESCRIPTION
A1	615,50	15,50	M4x0.7 - 6H
A2	615,50	-15,50	M4x0.7 - 6H
A3	583,50	-36,00	M4x0.7 - 6H
A4	615,50	-41,00	M4x0.7 - 6H
A5	486,50	-36,00	M4x0.7 - 6H
A6	583,50	36,00	M4x0.7 - 6H
A7	615,50	41,00	M4x0.7 - 6H
A8	486,50	36,70	M4x0.7 - 6H
A9	389,50	36,70	M4x0.7 - 6H
A10	389,50	-36,00	M4x0.7 - 6H
A11	292,50	-36,00	M4x0.7 - 6H
A12	195,50	36,70	M4x0.7 - 6H
A13	292,50	36,70	M4x0.7 - 6H
A14	195,50	-36,00	M4x0.7 - 6H

HOLE TABLE

HOLE	QUOTA X	QUOTA Y	DESCRIPTION
A15	98,50	-36,50	M4x0.7 - 6H
A16	65,50	-36,00	M4x0.7 - 6H
A17	98,50	36,00	M4x0.7 - 6H
A18	65,50	36,00	M4x0.7 - 6H
A20	110,00	-16,00	M4x0.7 - 6H
A21	110,00	16,00	M4x0.7 - 6H
A22	251,00	-16,00	M4x0.7 - 6H
A23	251,00	16,00	M4x0.7 - 6H
A24	341,00	-16,00	M4x0.7 - 6H
A25	341,00	16,00	M4x0.7 - 6H
A26	431,00	16,00	M4x0.7 - 6H
A27	431,00	-16,00	M4x0.7 - 6H
A28	572,00	-16,00	M4x0.7 - 6H
A29	572,00	16,00	M4x0.7 - 6H

Designed by: **Dott. Oscar Azzolini, Ing. Antonio Carabillò**

Tel: **049-8068665**

e-mail: **oscar.azzolini@lnl.infn.it**

Material: **SS 304-316L**

Base flange

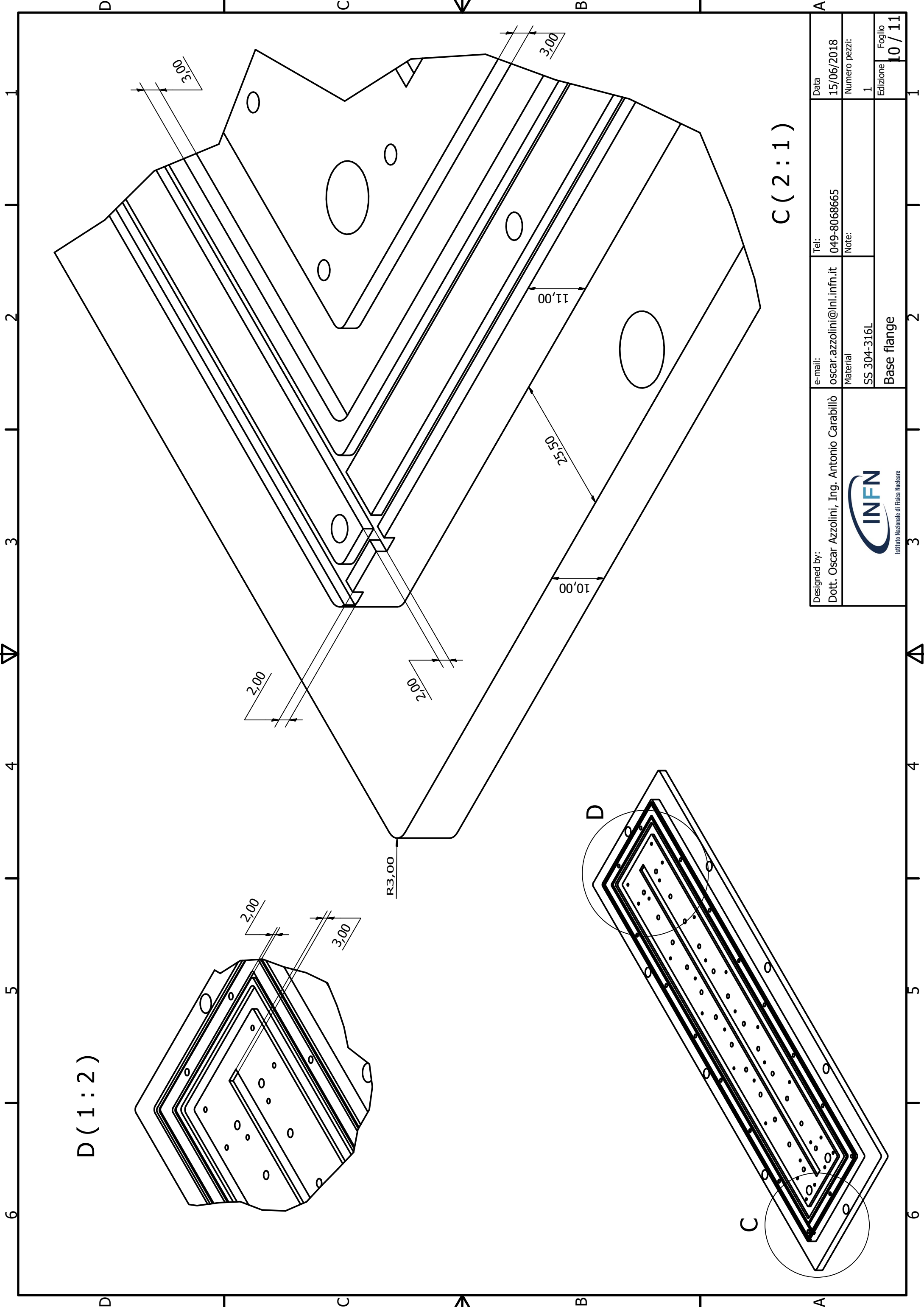
Data: **15/06/2018**

Numero pezzi: **1**

Edizione: **1**

Foglio: **9 / 11**

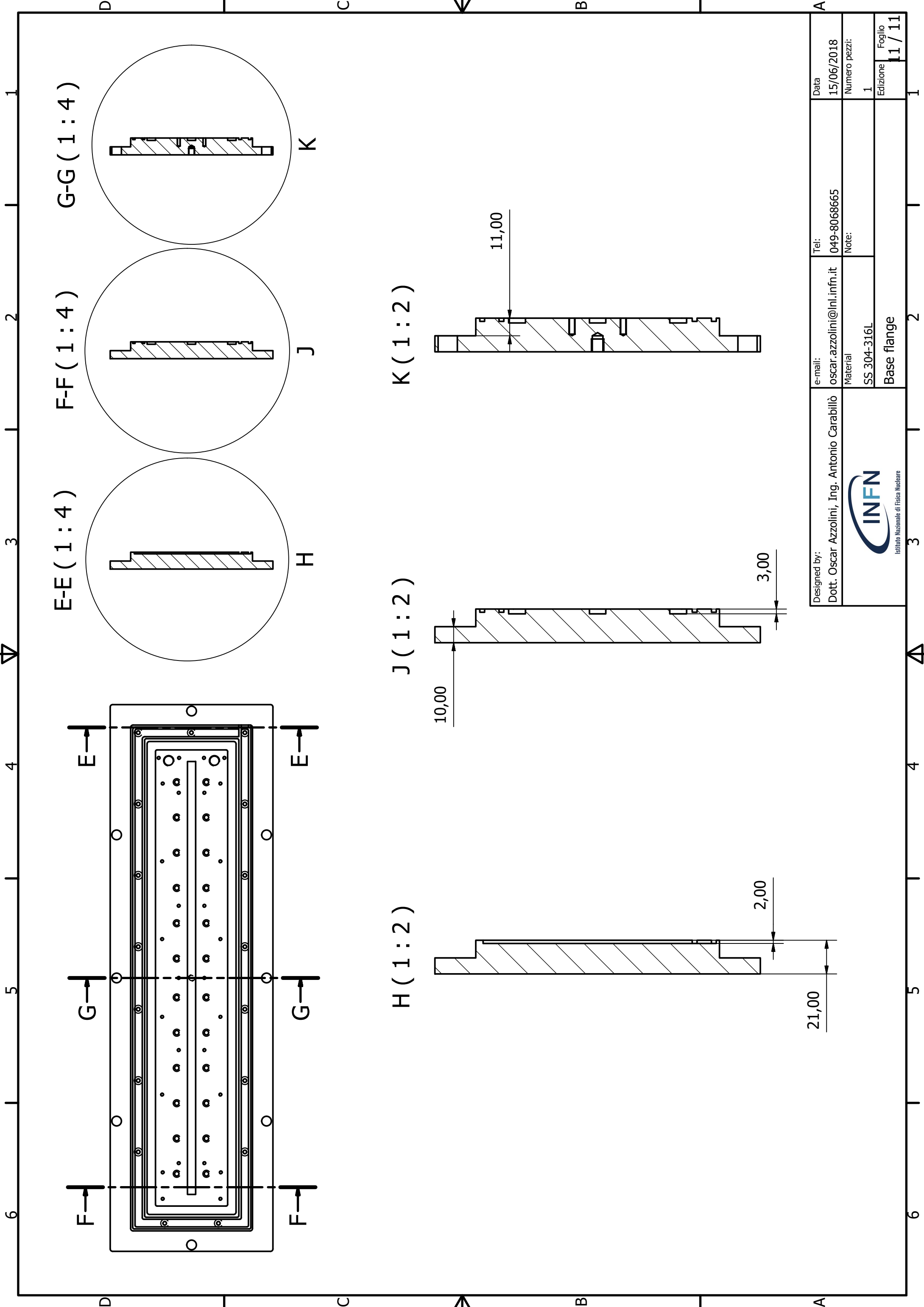




Designed by: Dott. Oscar Azzolini, Ing. Antonio Carabillò	e-mail: oscar.azzolini@lnl.infn.it	Tel: 049-8068665	Data 15/06/2018
 Istituto Nazionale di Fisica Nucleare	Material SS 304-316L	Note:	Numero pezzi: 1
	Base flange		Edizione 10 / 11

D (1:2)

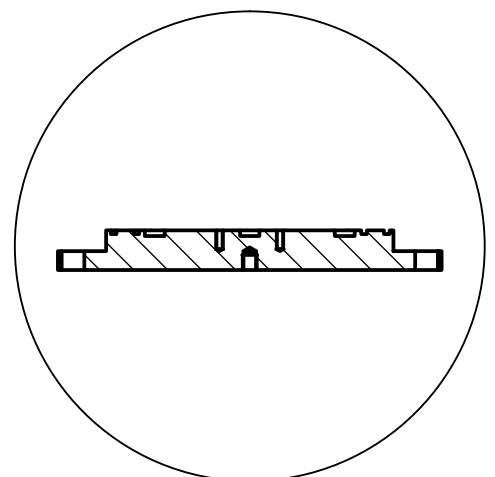
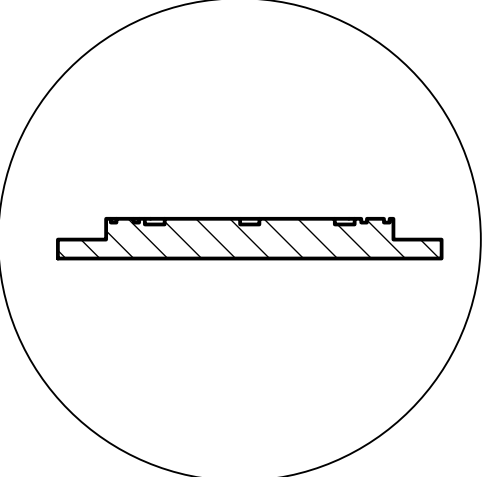
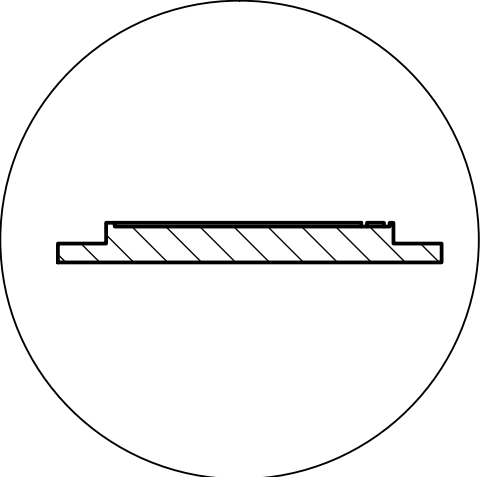
C (2:1)



E-E (1:4)

F-F (1:4)

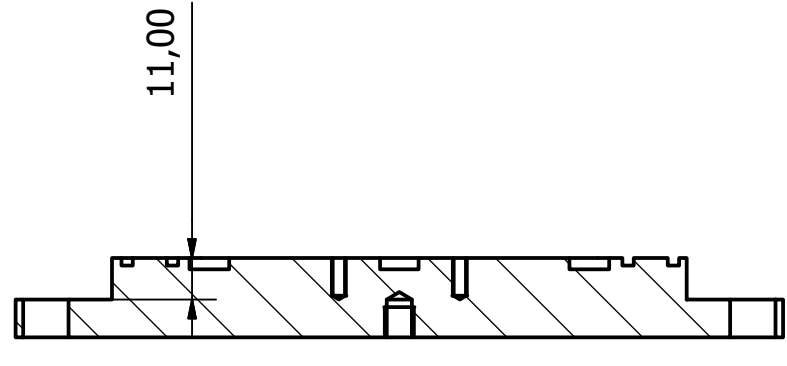
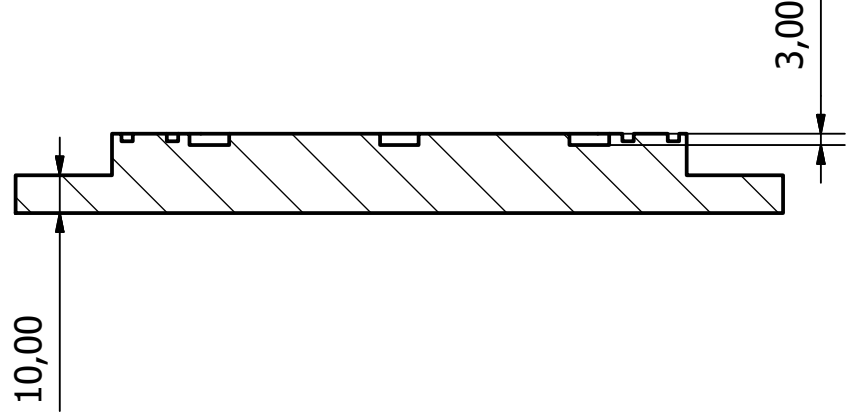
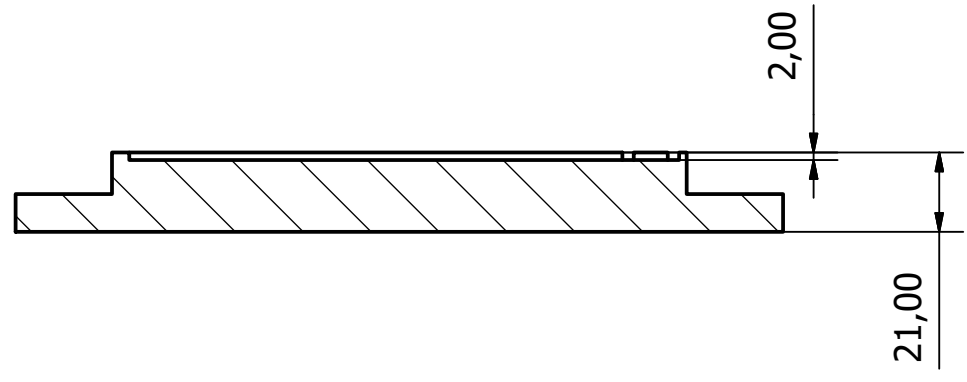
G-G (1:4)



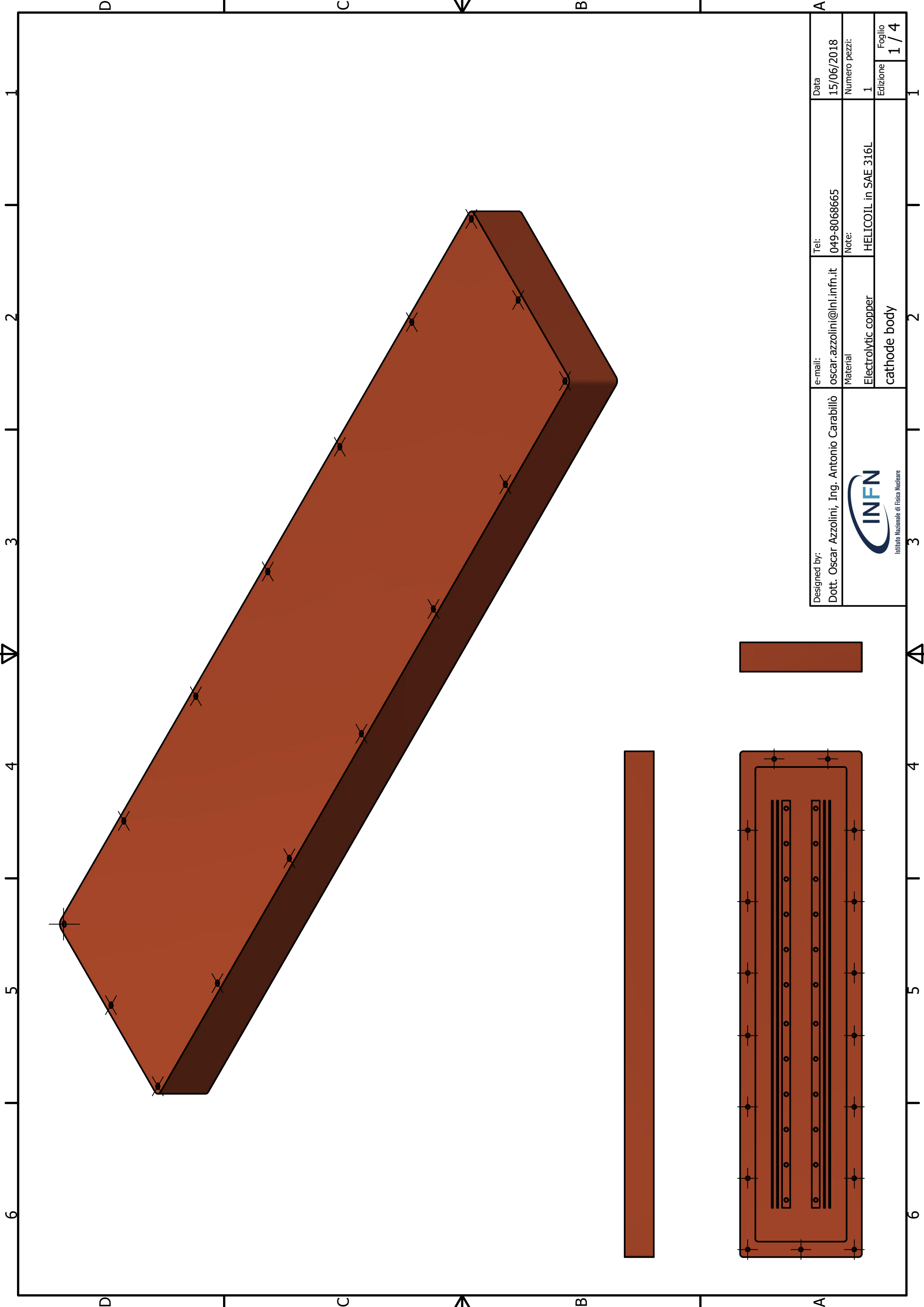
H (1:2)

J (1:2)

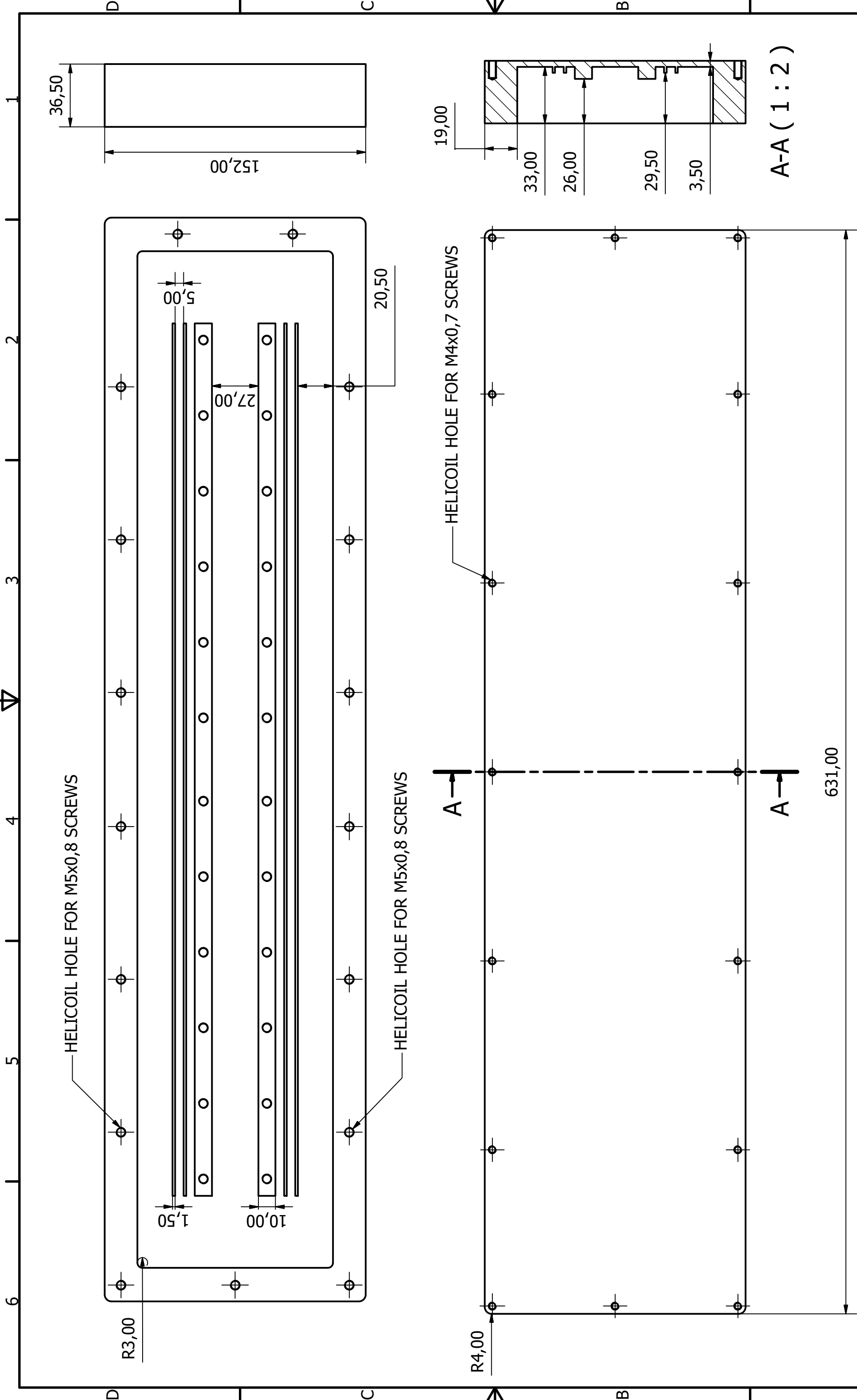
K (1:2)



Designed by: Dott. Oscar Azzolini, Ing. Antonio Carabillò		e-mail: oscar.azzolini@lnl.infn.it		Tel: 049-8068665		Data 15/06/2018	
 Istituto Nazionale di Fisica Nucleare		Material SS 304-316L		Note:		Numero pezzi: 1	
		Base flange		Edizione 1 / 1		Foglio 1 / 11	



Designed by: Dott. Oscar Azzolini, Ing. Antonio Carabillò	e-mail: oscar.azzolini@lnl.infn.it	Tel: 049-8068665	Data 15/06/2018
	Material Electrolytic copper	Note: HELICOIL in SAE 316L	Numero pezzi: 1
 Istituto Nazionale di Fisica Nucleare			Edizione 1 / 4



HELICOIL HOLE FOR M5x0,8 SCREWS

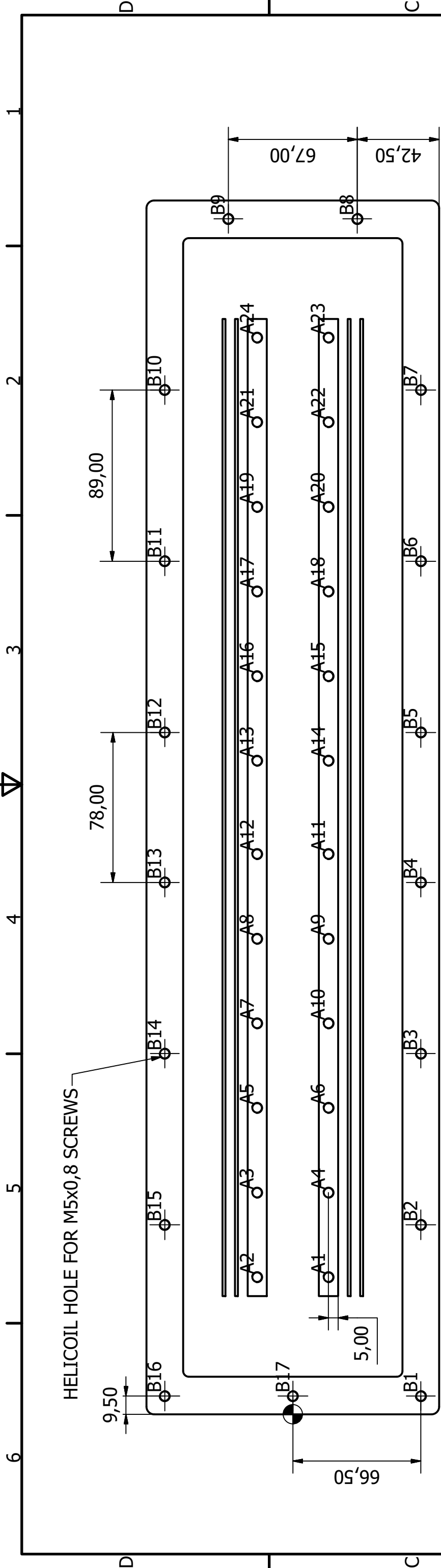
HELICOIL HOLE FOR M5x0,8 SCREWS

HELICOIL HOLE FOR M4x0,7 SCREWS

A-A (1:2)

NOTE:
All the holes are with HELICOIL in SAE 316L (316L stainless steel)

Designed by: Dott. Oscar Azzolini, Ing. Antonio Carabillò	e-mail: oscar.azzolini@lnl.infn.it	Tel: 049-8068665	Data 15/06/2018
 Istituto Nazionale di Fisica Nucleare	Material Electrolytic copper	Note: HELICOIL in SAE 316L	Numero pezzi: 1
	cathode body		Edizione 2 / 4



HELICOIL HOLE FOR M5x0,8 SCREWS

HOLE	QUOTA X	QUOTA Y	DESCRIPTION
B1	9,50	-66,50	M5.5x0.5 - 6H
B2	98,50	-66,50	M5.5x0.5 - 6H
B3	187,50	-66,50	M5.5x0.5 - 6H
B4	276,50	-66,50	M5.5x0.5 - 6H
B5	354,50	-66,50	M5.5x0.5 - 6H
B6	443,50	-66,50	M5.5x0.5 - 6H
B7	532,50	-66,50	M5.5x0.5 - 6H
B8	621,50	-33,50	M5.5x0.5 - 6H
B9	621,50	33,50	M5.5x0.5 - 6H
B10	532,50	66,50	M5.5x0.5 - 6H
B11	443,50	66,50	M5.5x0.5 - 6H
B12	354,50	66,50	M5.5x0.5 - 6H
B13	276,50	66,50	M5.5x0.5 - 6H
B14	187,50	66,50	M5.5x0.5 - 6H
B15	98,50	66,50	M5.5x0.5 - 6H
B16	9,50	66,50	M5.5x0.5 - 6H
B17	9,50	0,00	M5.5x0.5 - 6H

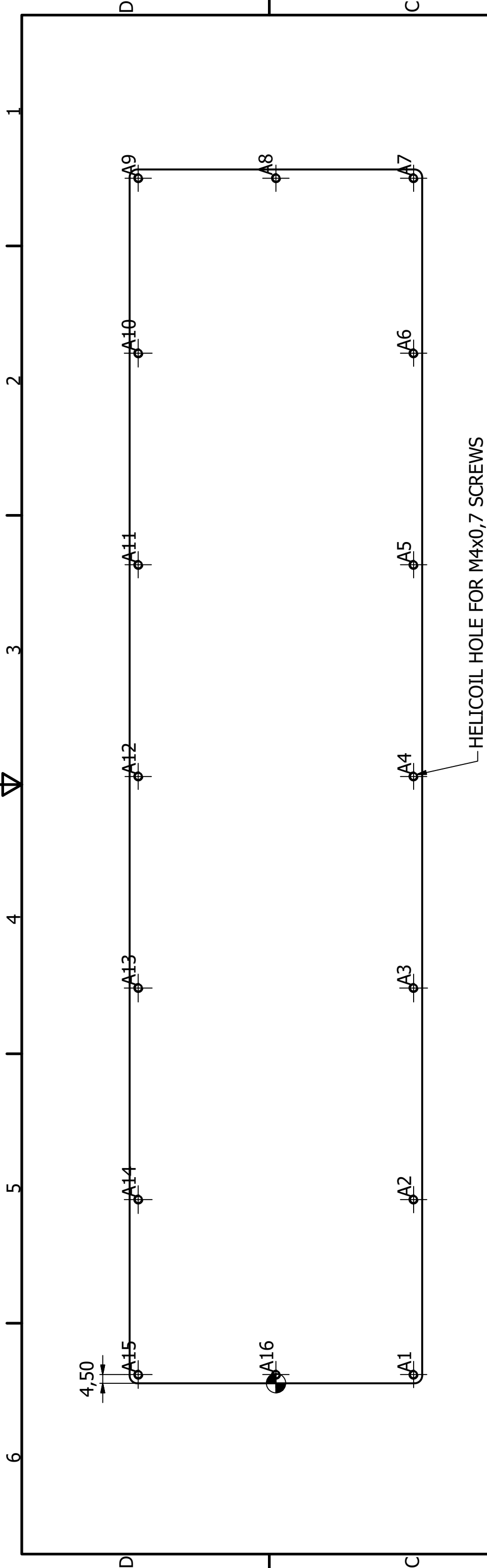
HOLE	XDIM	QUOTA Y	DESCRIPTION
A1	71,25	-18,50	M5.5x0.5 - 6H
A2	71,25	18,50	M5.5x0.5 - 6H
A3	115,25	18,50	M5.5x0.5 - 6H
A4	115,25	-18,50	M5.5x0.5 - 6H
A5	159,25	18,50	M5.5x0.5 - 6H
A6	159,25	-18,50	M5.5x0.5 - 6H
A7	203,25	18,50	M5.5x0.5 - 6H
A8	247,25	18,50	M5.5x0.5 - 6H
A9	247,25	-18,50	M5.5x0.5 - 6H
A10	203,25	-18,50	M5.5x0.5 - 6H
A11	291,25	-18,50	M5.5x0.5 - 6H
A12	291,25	18,50	M5.5x0.5 - 6H

HOLE	XDIM	QUOTA Y	DESCRIPTION
A13	339,75	18,50	M5.5x0.5 - 6H
A14	339,75	-18,50	M5.5x0.5 - 6H
A15	383,75	-18,50	M5.5x0.5 - 6H
A16	383,75	18,50	M5.5x0.5 - 6H
A17	427,75	18,50	M5.5x0.5 - 6H
A18	427,75	-18,50	M5.5x0.5 - 6H
A19	471,75	18,50	M5.5x0.5 - 6H
A20	471,75	-18,50	M5.5x0.5 - 6H
A21	515,75	18,50	M5.5x0.5 - 6H
A22	515,75	-18,50	M5.5x0.5 - 6H
A23	559,75	-18,50	M5.5x0.5 - 6H
A24	559,75	18,50	M5.5x0.5 - 6H

NOTE:

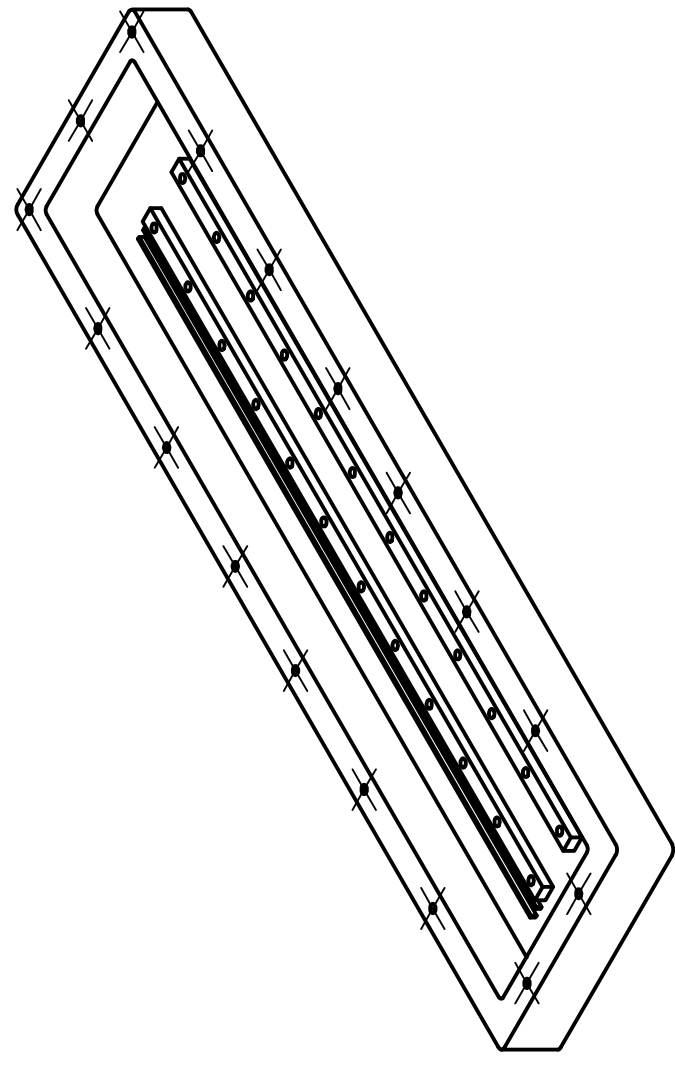
All the holes are with HELICOIL in SAE 316L (316L stainless steel).
The description in the table is indicative, make sure that helicoil holes are for M5x0,8 screws.

Designed by: Dott. Oscar Azzolini, Ing. Antonio Carabillò	e-mail: oscar.azzolini@lni.infn.it	Tel: 049-8068665	Data 15/06/2018
	Material Electrolytic copper	Note: HELICOIL in SAE 316L	Numero pezzi: 1
cathode body			Edizione 1
			Foglio 3 / 4




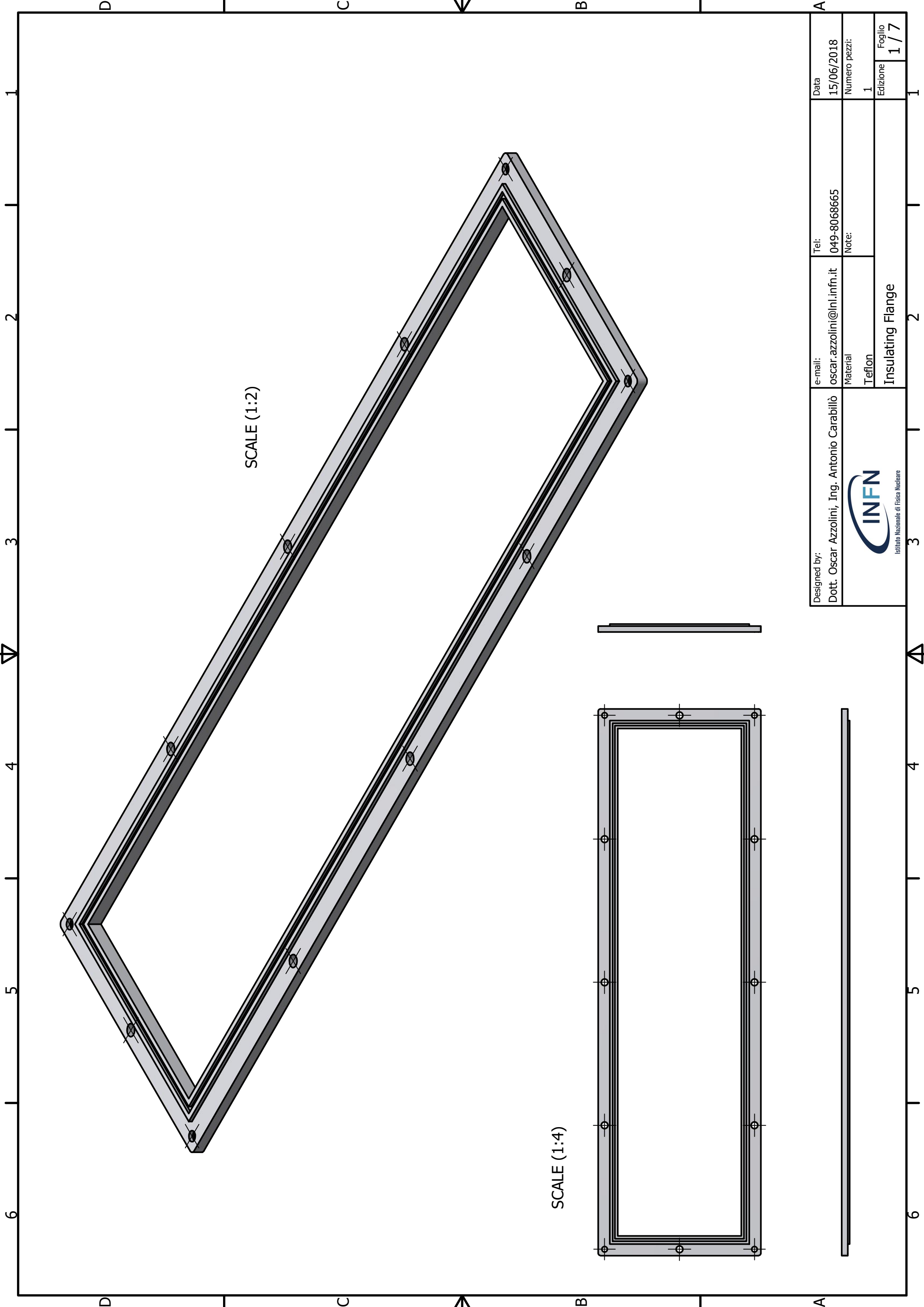
HOLE TABLE

HOLE	QUOTA X	QUOTA Y	DESCRIPTION
A1	4,50	-71,50	M4.5x0.75 - 6H
A2	95,50	-71,50	M4.5x0.75 - 6H
A3	205,50	-71,50	M4.5x0.75 - 6H
A4	315,50	-71,50	M4.5x0.75 - 6H
A5	425,50	-71,50	M4.5x0.75 - 6H
A6	535,50	-71,50	M4.5x0.75 - 6H
A7	626,50	-71,50	M4.5x0.75 - 6H
A8	626,50	0,00	M4.5x0.75 - 6H
A9	626,50	71,50	M4.5x0.75 - 6H
A10	535,50	71,50	M4.5x0.75 - 6H
A11	425,50	71,50	M4.5x0.75 - 6H
A12	315,50	71,50	M4.5x0.75 - 6H
A13	205,50	71,50	M4.5x0.75 - 6H
A14	95,50	71,50	M4.5x0.75 - 6H
A15	4,50	71,50	M4.5x0.75 - 6H
A16	4,50	0,00	M4.5x0.75 - 6H



NOTE:
 All the holes are with HELICOIL in SAE 316L (316L stainless steel).
 The description in the table is indicative, make sure that helicoil holes are for M4x0,7 screws.

Designed by: Dott. Oscar Azzolini, Ing. Antonio Carabillò	e-mail: oscar.azzolini@lnl.infn.it	Tel: 049-8068665	Data 15/06/2018
	Material Electrolytic copper	Note: HELICOIL in SAE 316L	Numero pezzi: 1
cathode body			Edizione 1
 Istituto Nazionale di Fisica Nucleare			Foglio 4 / 4

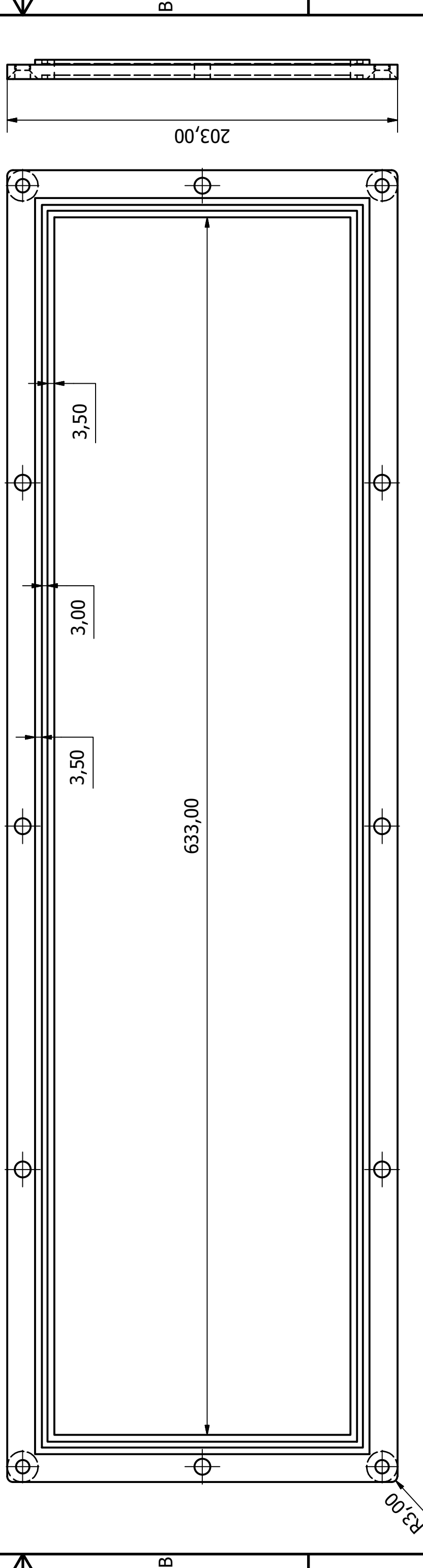
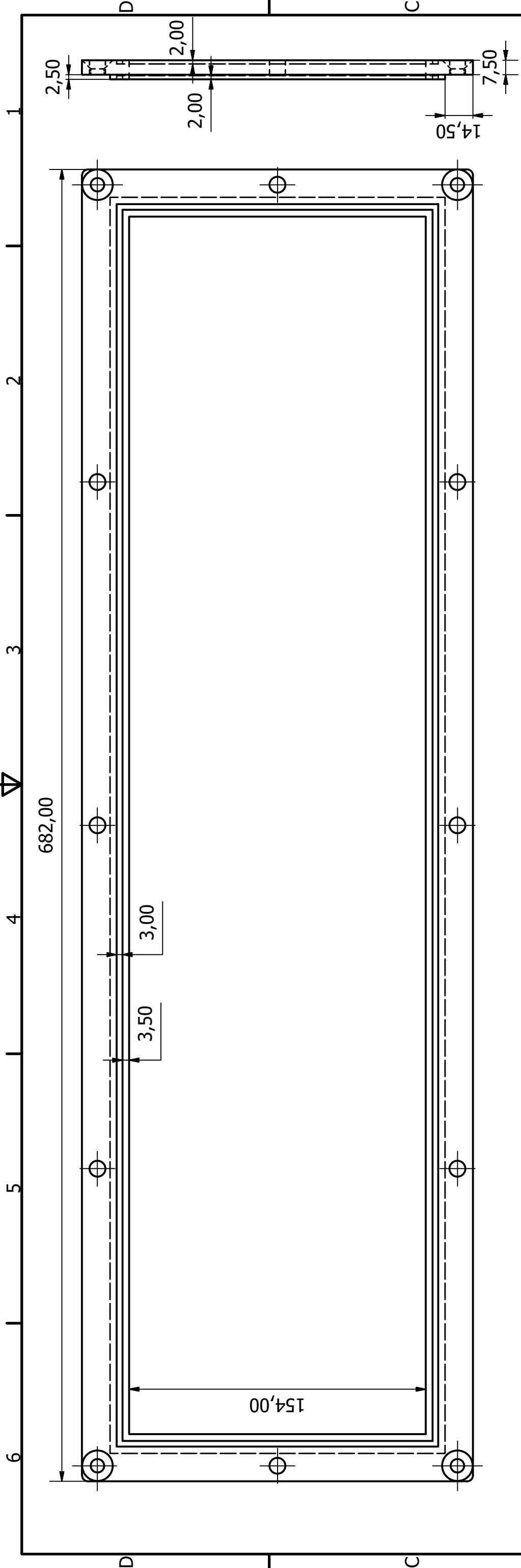


SCALE (1:2)


SCALE (1:4)

Designed by: Dott. Oscar Azzolini, Ing. Antonio Carabillò	e-mail: oscar.azzolini@lnl.infn.it	Tel: 049-8068665	Data 15/06/2018
	Material Teflon	Note:	Numero pezzi: 1
	Insulating Flange		Edizione 1 / 7

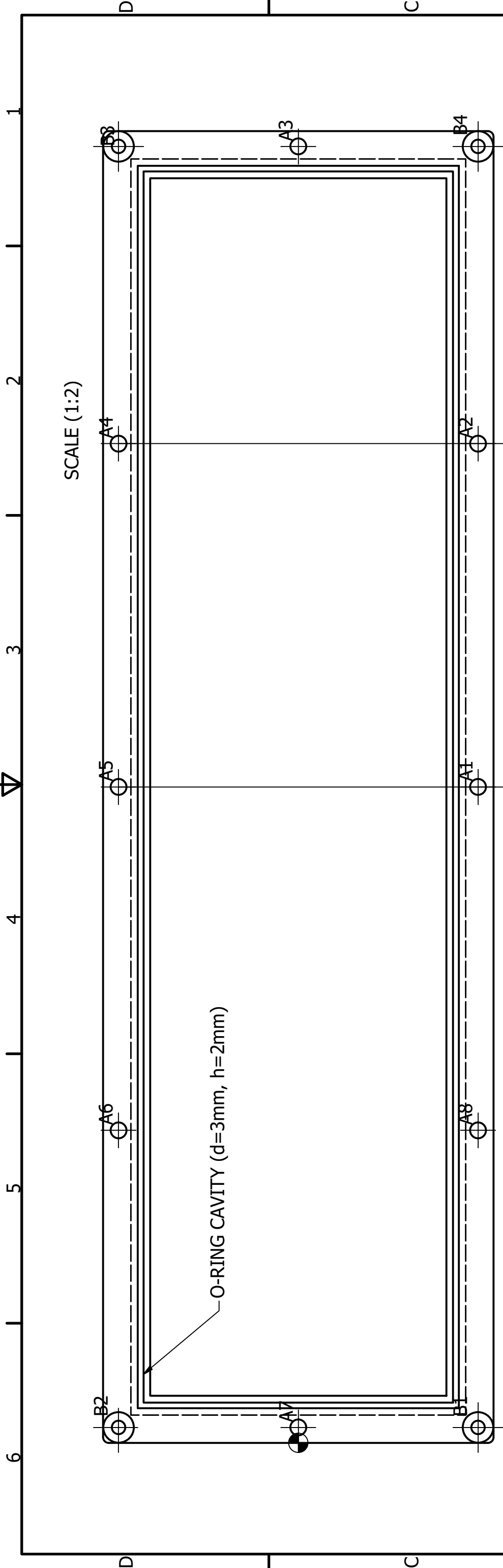




SCALE (1:2)

Designed by: Dott. Oscar Azzolini, Ing. Antonio Carabillò	e-mail: oscar.azzolini@lni.infn.it	Tel: 049-8068665	Data 15/06/2018
	Material Teflon	Note:	Numero pezzi: 1
 Istituto Nazionale di Fisica Nucleare			Edizione 1
			Foglio 2 / 7

Insulating Flange



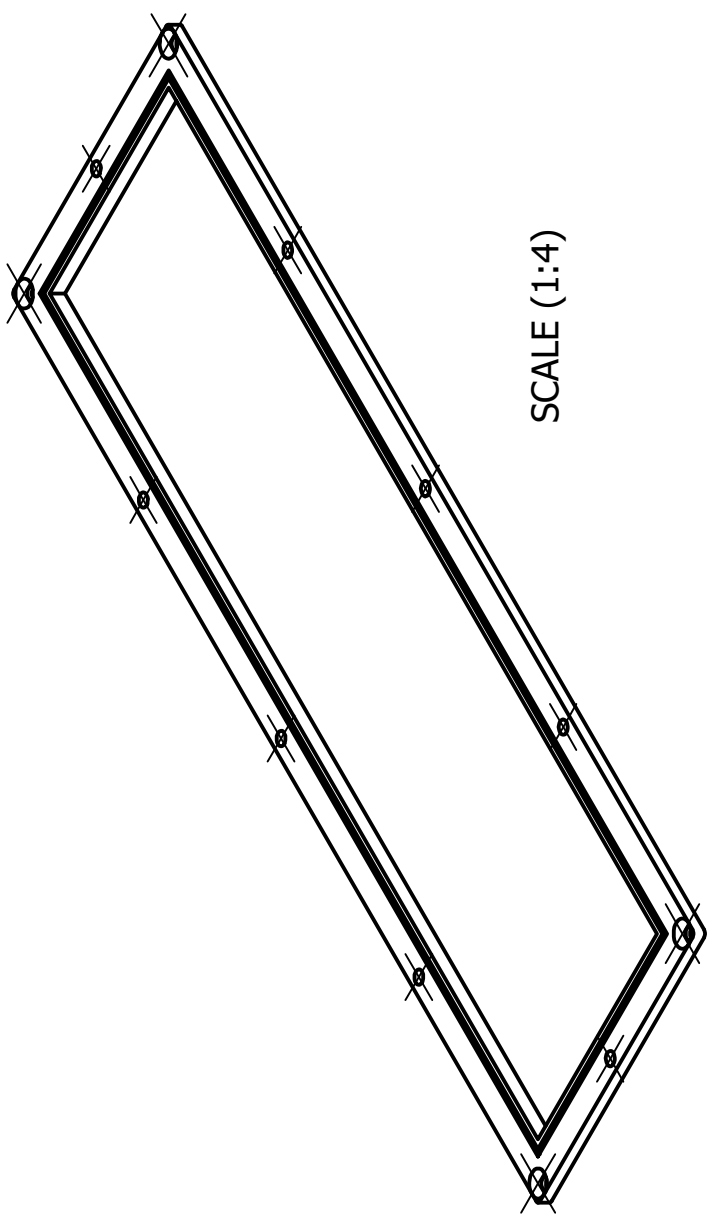
SCALE (1:2)

O-RING CAVITY (d=3mm, h=2mm)


178,50

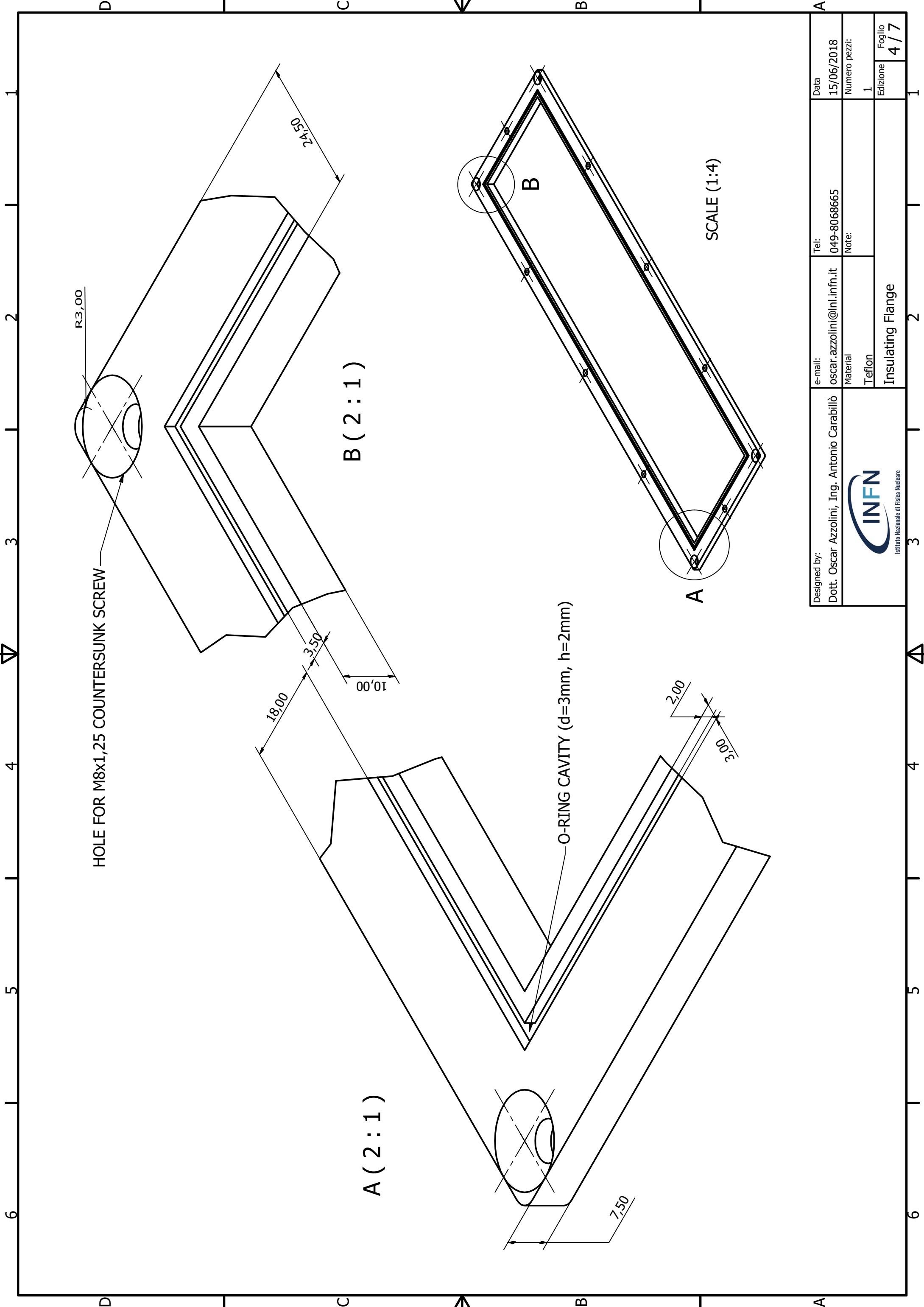
HOLE TABLE			
HOLE	QUOTA X	QUOTA Y	DESCRIPTION
A1	341,00	-93,50	Ø8,20 THRU
A2	519,50	-93,50	Ø8,20 THRU
A3	674,00	0,00	Ø8,20 THRU
A4	519,50	93,50	Ø8,20 THRU
A5	341,00	93,50	Ø8,20 THRU
A6	162,50	93,50	Ø8,20 THRU
A7	8,00	0,00	Ø8,20 THRU
A8	162,50	-93,50	Ø8,20 THRU


HOLE TABLE			
HOLE	QUOTA X	QUOTA Y	DESCRIPTION
B1	8,00	-93,50	∨ Ø7,00 THRU ∨ Ø16,00 X 90,00°
B2	8,00	93,50	∨ Ø7,00 THRU ∨ Ø16,00 X 90,00°
B3	674,00	93,50	∨ Ø7,00 THRU ∨ Ø16,00 X 90,00°
B4	674,00	-93,50	∨ Ø7,00 THRU ∨ Ø16,00 X 90,00°

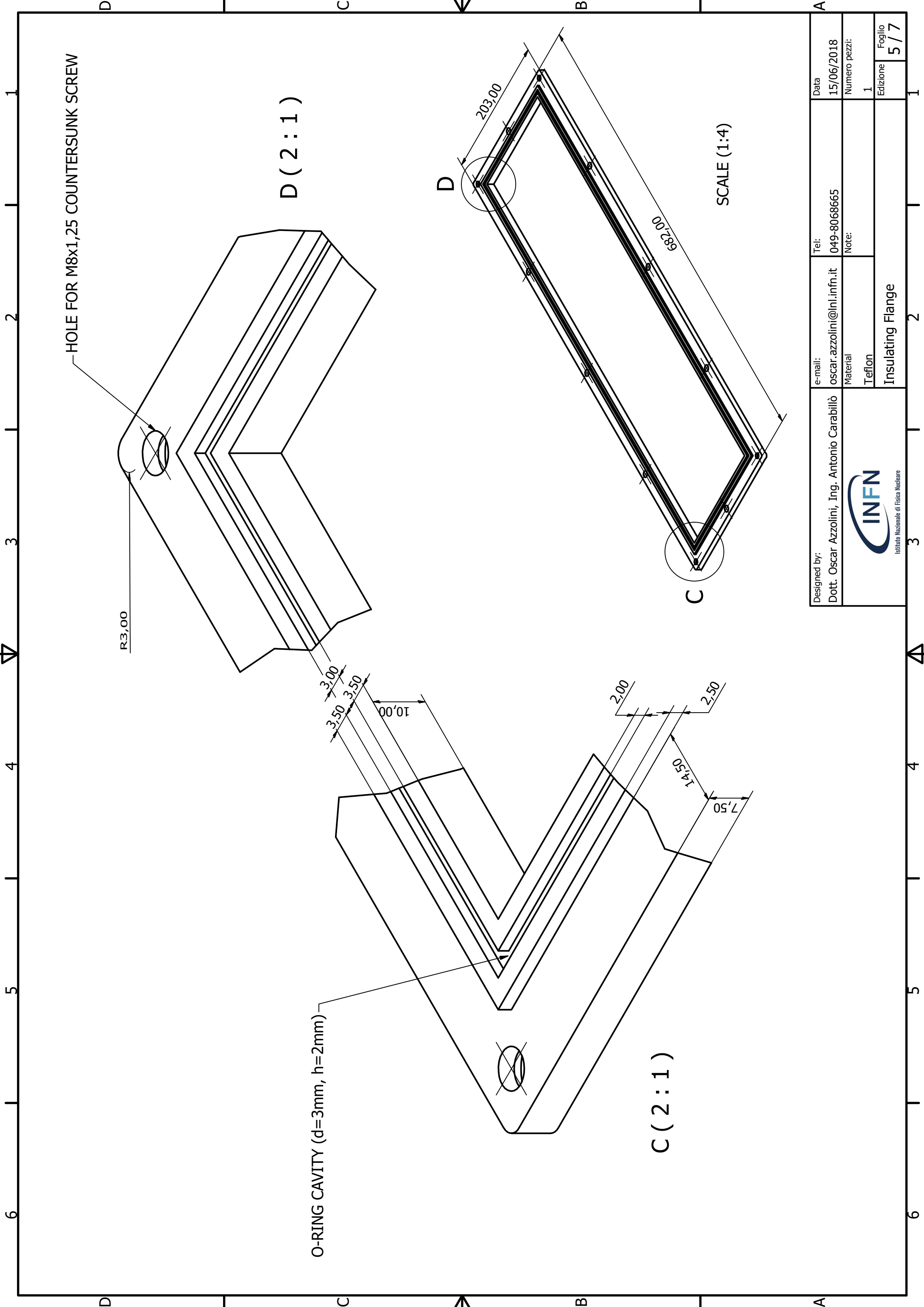


SCALE (1:4)

Designed by: Dott. Oscar Azzolini, Ing. Antonio Carabillò	e-mail:	Tel:	Data
	oscar.azzolini@lni.infn.it	049-8068665	15/06/2018
 Istituto Nazionale di Fisica Nucleare	Material	Note:	Numero pezzi:
	Teflon		1
Insulating Flange			Edizione
			3 / 7

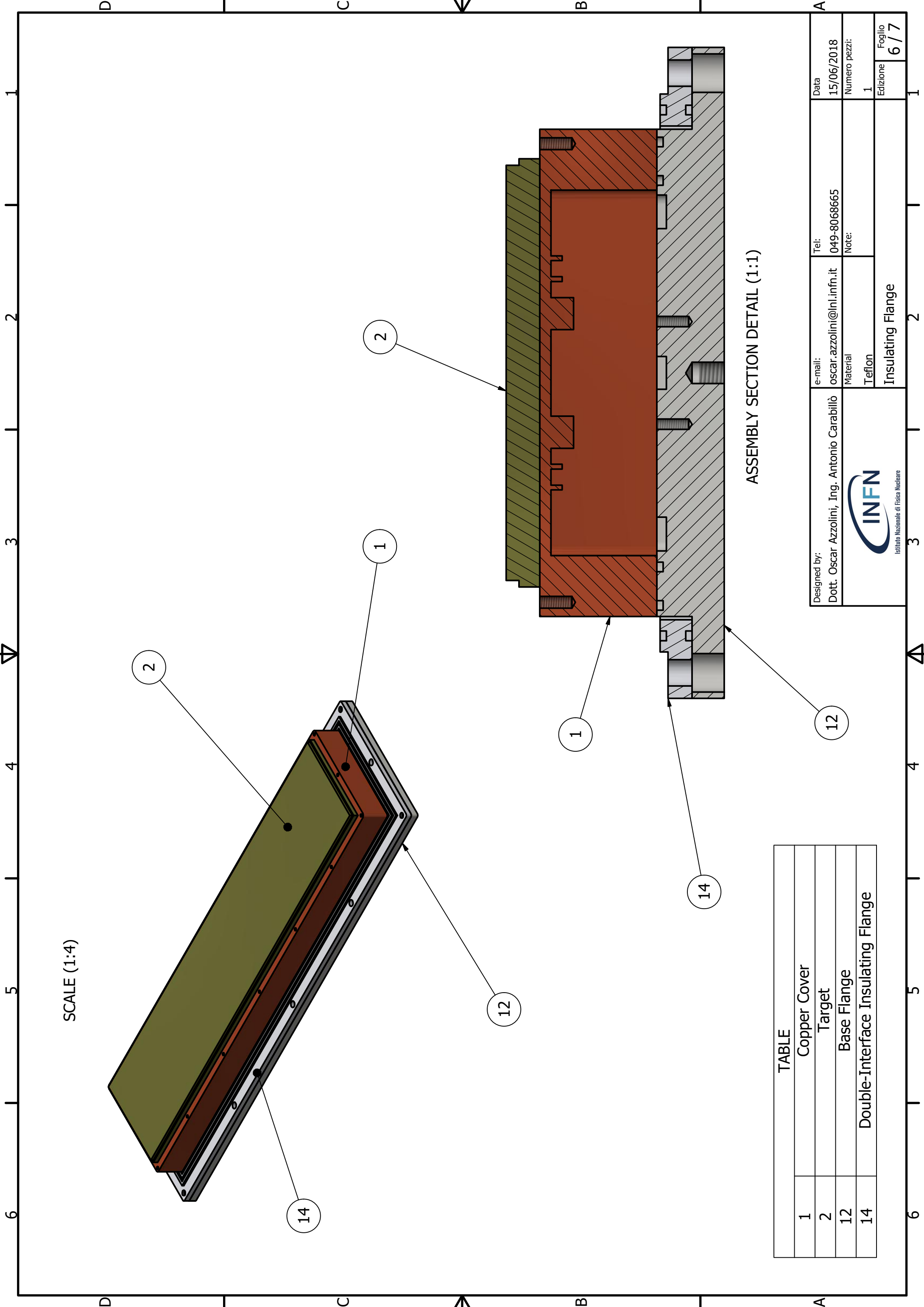


Designed by: Dott. Oscar Azzolini, Ing. Antonio Carabillò	e-mail: oscar.azzolini@lnl.infn.it	Tel: 049-8068665	Data 15/06/2018
	Material Teflon	Note:	Numero pezzi: 1
 Istituto Nazionale di Fisica Nucleare			Edizione 4 / 7



Designed by:	Dott. Oscar Azzolini, Ing. Antonio Carabillò	e-mail:	oscar.azzolini@lni.infn.it	Tel:	049-8068665	Data	15/06/2018
		Material	Teflon	Note:		Numero pezzi:	1
		Insulating Flange		Edizione	1	Foglio	5/7




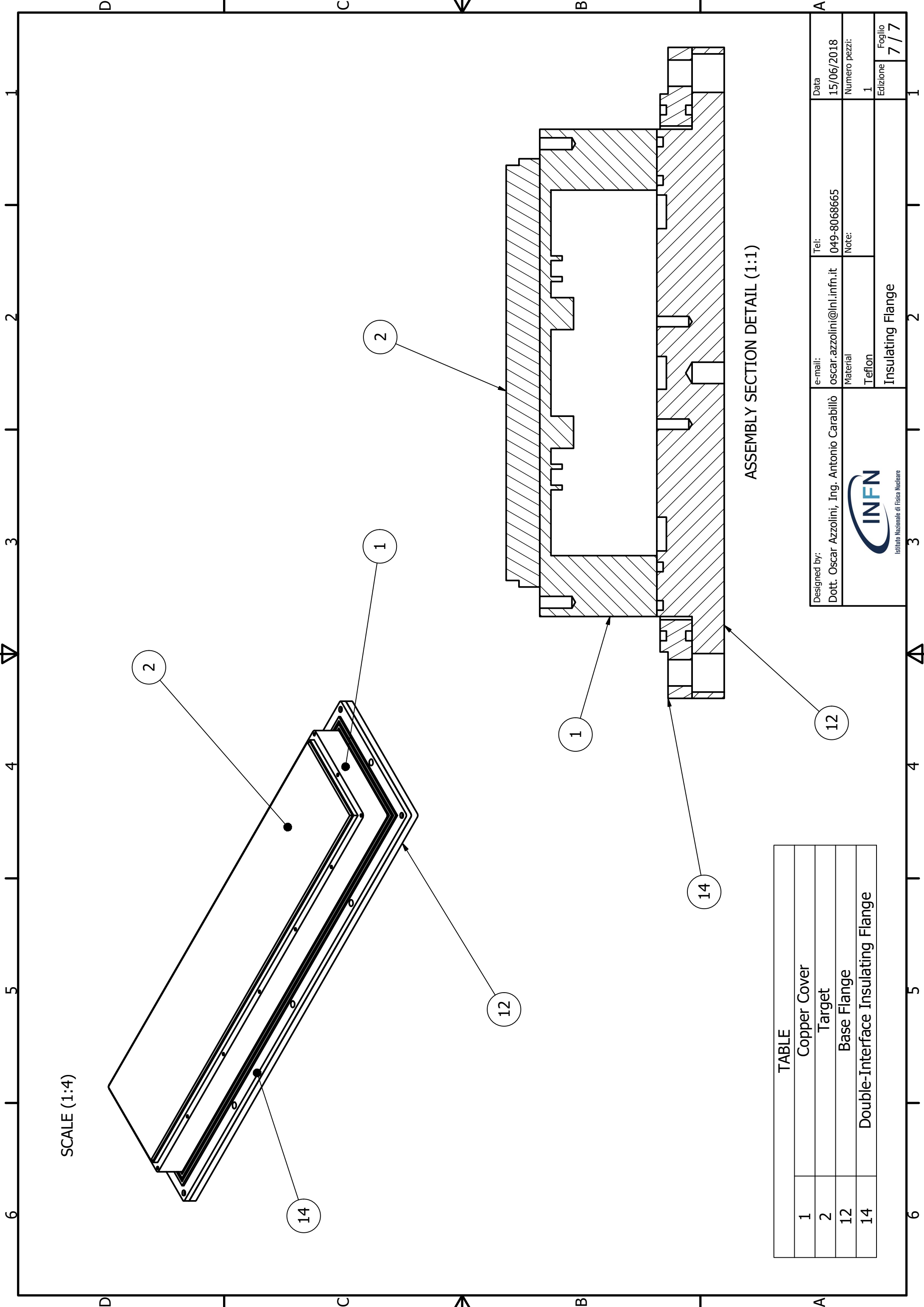


SCALE (1:4)

ASSEMBLY SECTION DETAIL (1:1)

TABLE	
1	Copper Cover
2	Target
12	Base Flange
14	Double-Interface Insulating Flange


Designed by: Dott. Oscar Azzolini, Ing. Antonio Carabillò  Istituto Nazionale di Fisica Nucleare	e-mail:	Tel:	Data
	oscar.azzolini@lnl.infn.it	049-8068665	15/06/2018
	Material	Note:	Numero pezzi:
Teflon		1	Edizione
Insulating Flange			Foglio
			6 / 7

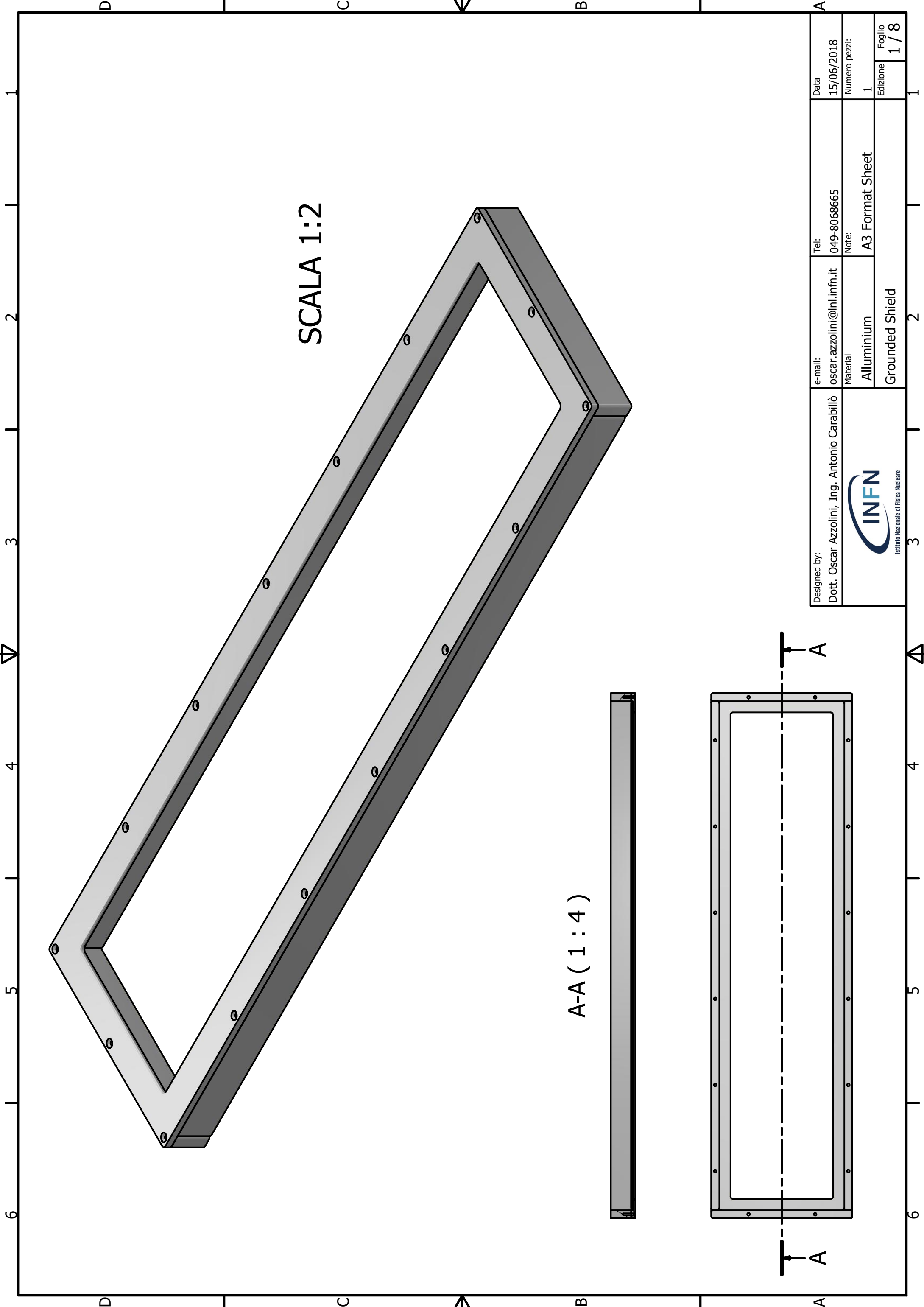


SCALE (1:4)

ASSEMBLY SECTION DETAIL (1:1)

TABLE	
1	Copper Cover
2	Target
12	Base Flange
14	Double-Interface Insulating Flange

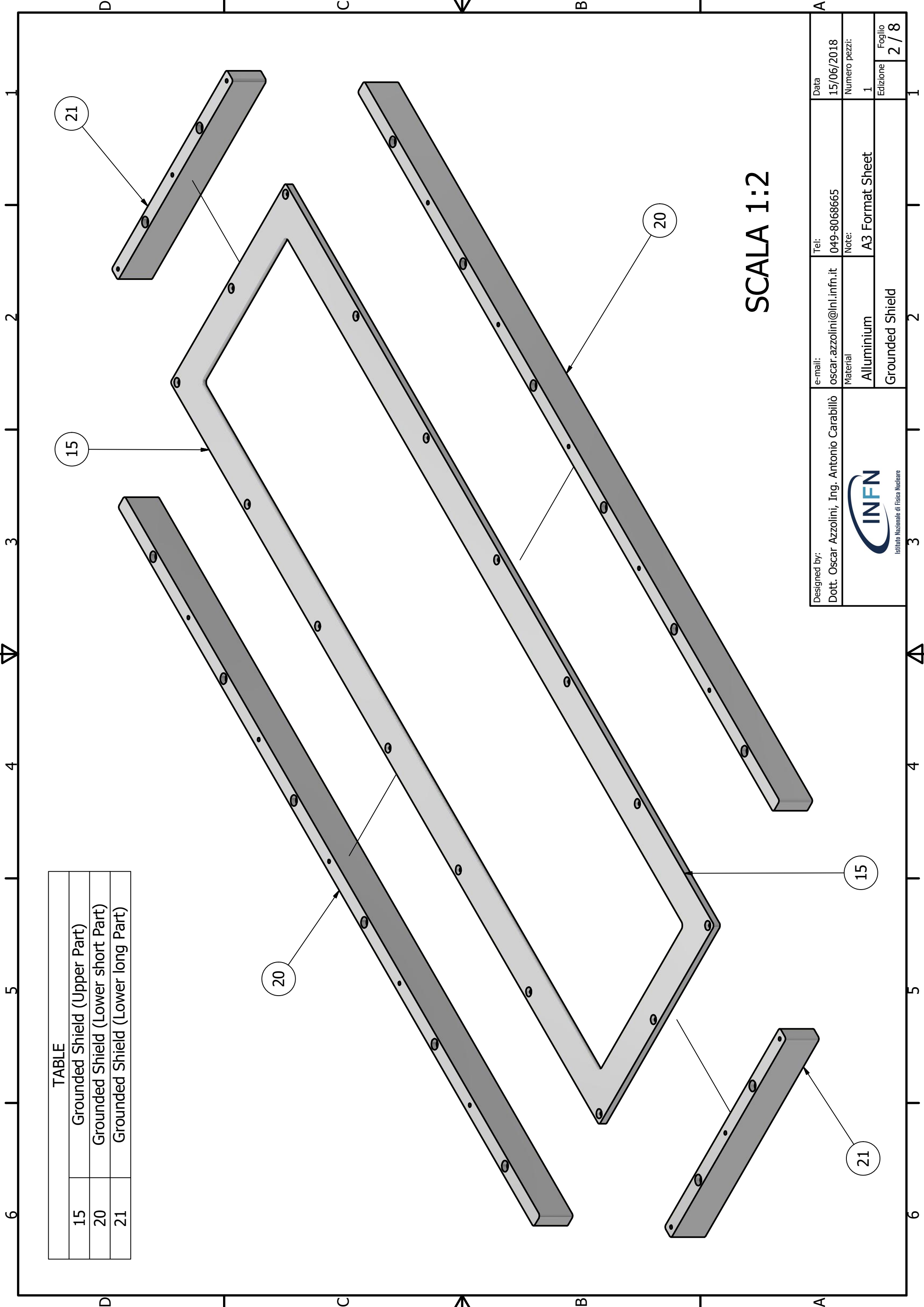
Designed by: Dott. Oscar Azzolini, Ing. Antonio Carabillò  Istituto Nazionale di Fisica Nucleare	e-mail:	oscar.azzolini@lni.infn.it	Tel:	049-8068665	Data	15/06/2018
	Material		Note:		Numero pezzi:	1
	Teflon				Edizione	7/7
	Insulating Flange					



SCALA 1:2


A-A (1 : 4)

Designed by: Dott. Oscar Azzolini, Ing. Antonio Carabillò	e-mail: oscar.azzolini@lnl.infn.it	Tel: 049-8068665	Data 15/06/2018
 Istituto Nazionale di Fisica Nucleare	Material Alluminium	Note: A3 Format Sheet	Numero pezzi: 1
	Grounded Shield		Edizione 1 / 8



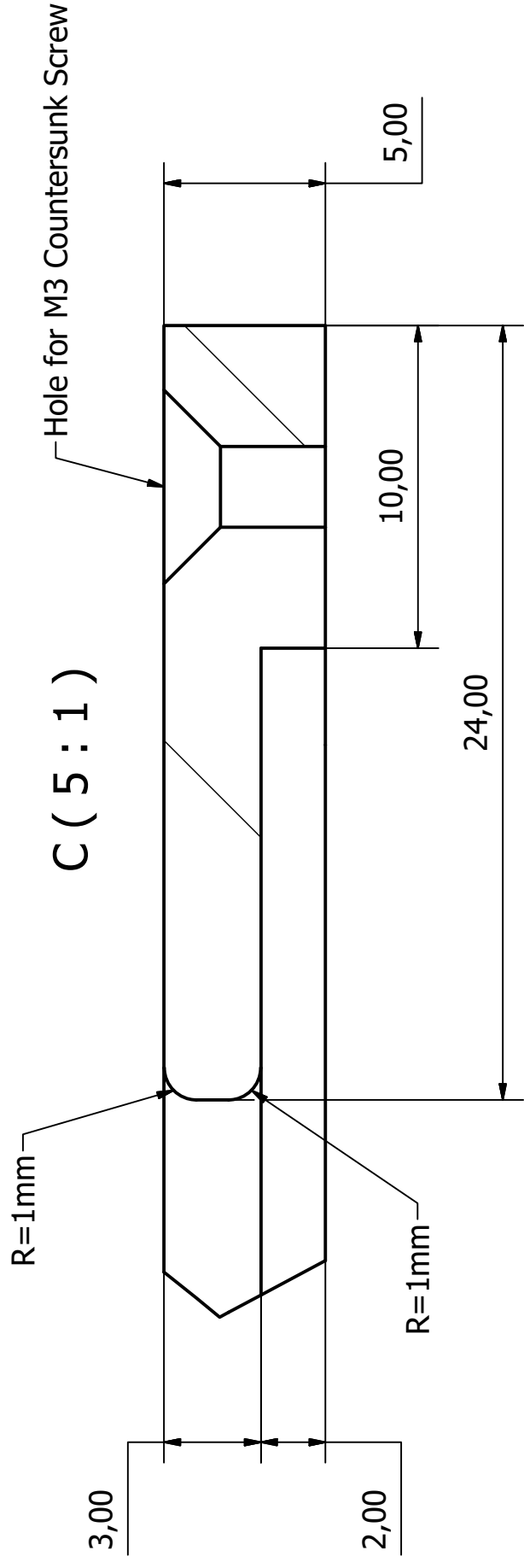
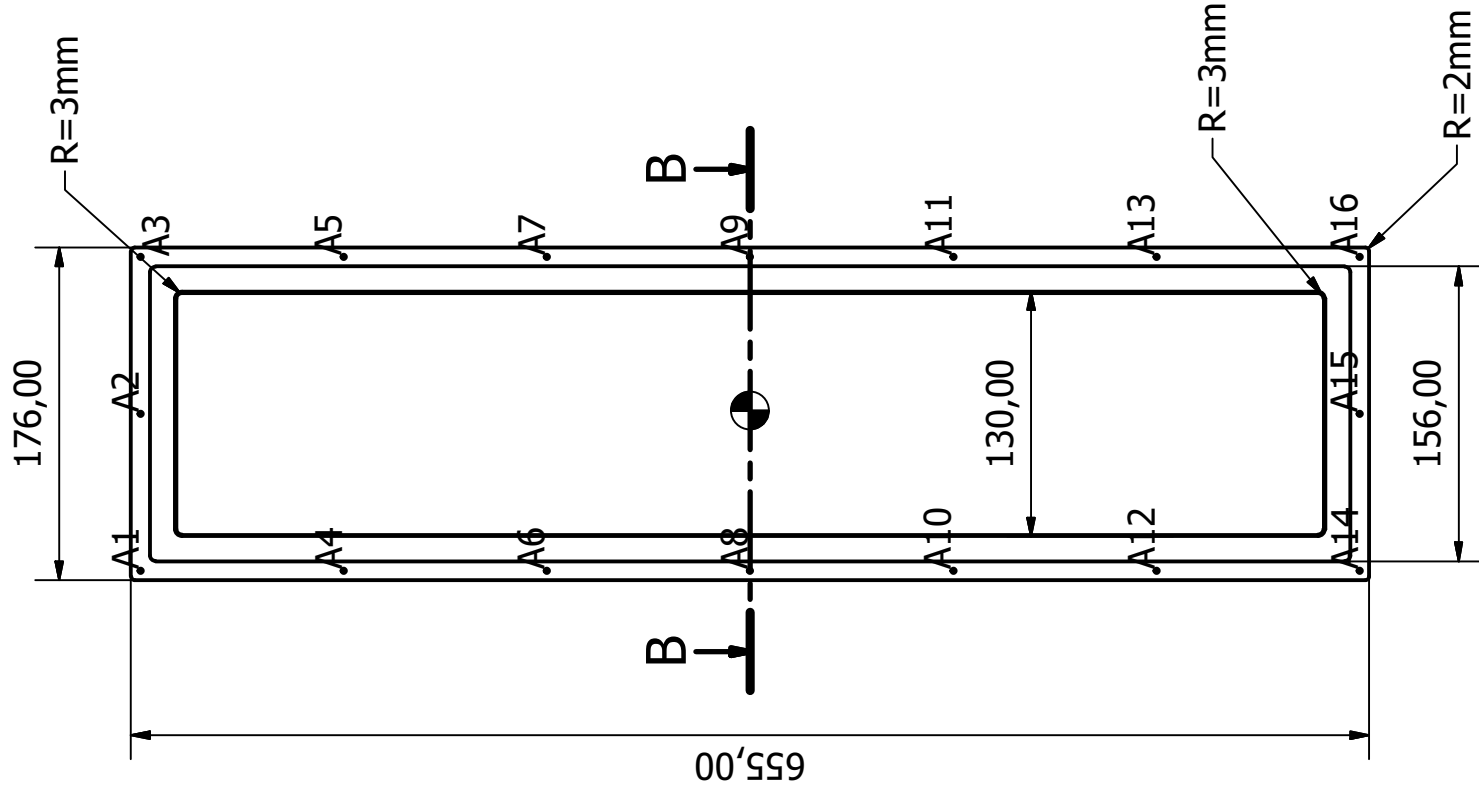
SCALA 1:2

TABLE	
15	Grounded Shield (Upper Part)
20	Grounded Shield (Lower short Part)
21	Grounded Shield (Lower long Part)

Designed by: Dott. Oscar Azzolini, Ing. Antonio Carabillò	e-mail: oscar.azzolini@lnl.infn.it	Tel: 049-8068665	Data 15/06/2018
	Material Alluminium	Note: A3 Format Sheet	Numero pezzi: 1
 Istituto Nazionale di Fisica Nucleare			Edizione 2 / 8
			Foglio 2 / 8

GROUNDING SHIELD (UPPER PART)

number of the part: 1



C (5 : 1)

Hole for M3 Countersunk Screw

HOLE TABLE			
HOLE	QUOTA X	QUOTA Y	HOLE DEPTH
A1	-84,77	322,50	5,00
A2	-1,77	322,50	5,00
A3	81,23	322,50	5,00
A4	-84,77	215,00	5,00
A5	81,23	215,00	5,00
A6	-84,77	107,50	5,00
A7	81,23	107,50	5,00
A8	-84,77	0,00	5,00

$\varnothing 2,50$ THRU
 $\sphericalangle \varnothing 6,00 \times 90,00^\circ$

HOLE TABLE			
HOLE	QUOTA X	QUOTA Y	HOLE DEPTH
A9	81,23	0,00	5,00
A10	-84,77	-107,50	5,00
A11	81,23	-107,50	5,00
A12	-84,77	-215,00	5,00
A13	81,23	-215,00	5,00
A14	-84,77	-322,50	5,00
A15	-1,77	-322,50	5,00
A16	81,23	-322,50	5,00

$\varnothing 2,50$ THRU
 $\sphericalangle \varnothing 6,00 \times 90,00^\circ$



B-B (1 : 4)

Designed by:
Dott. Oscar Azzolini, Ing. Antonio Carabillò



e-mail:
oscar.azzolini@lnl.infn.it

Material
Alluminium
Grounded Shield

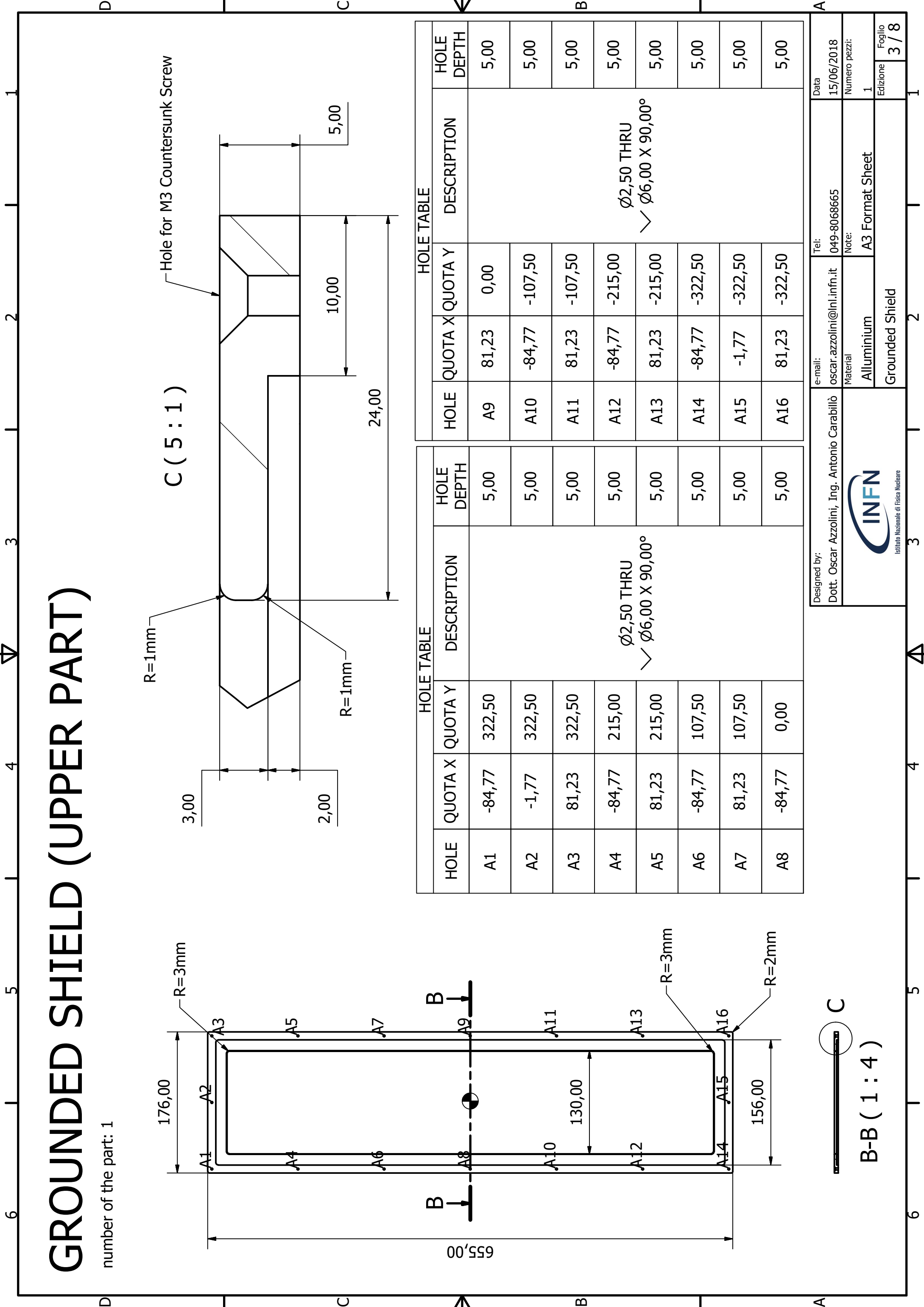
Tel:
049-8068665

Note:
A3 Format Sheet

Data
15/06/2018

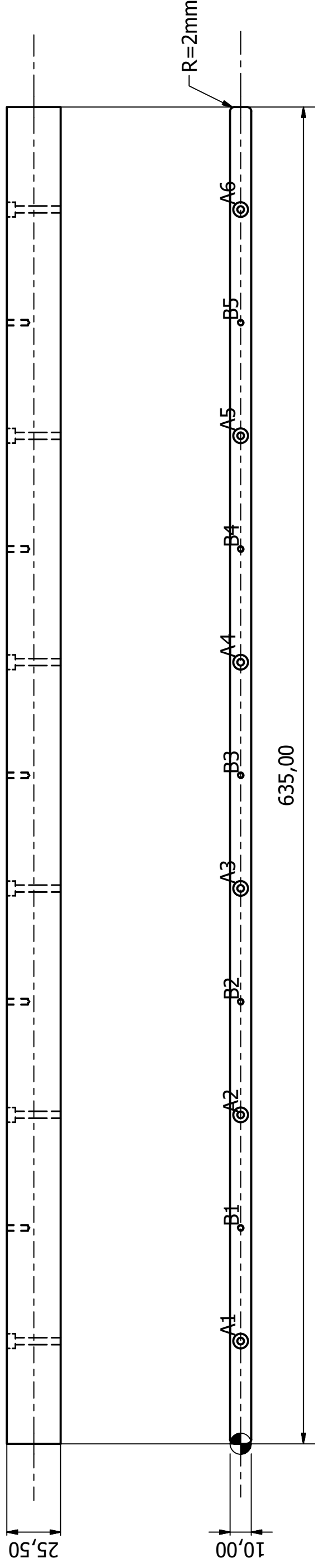
Numero pezzi:
1

Edizione
3 / 8




GROUNDING SHIELD (BOTTOM PART) long parts

number of the part: 2



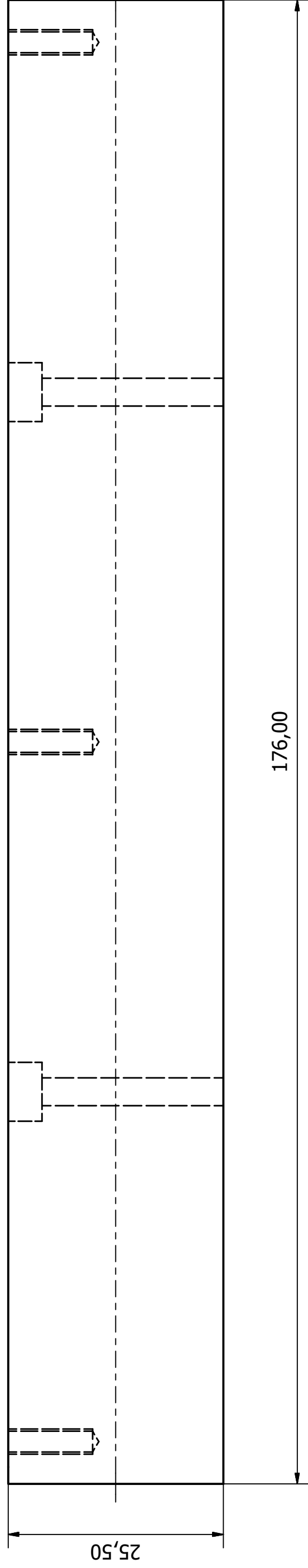
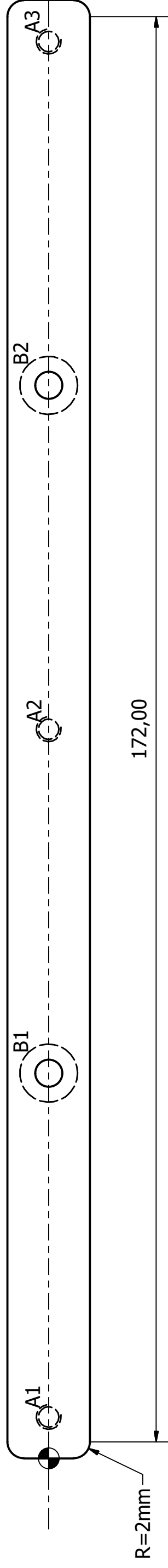
HOLE TABLE			DESCRIPTION
HOLE	QUOTA X	QUOTA Y	
A1	48,75	0,00	Ø3,30 THRU □ □ Ø7,00 ▽ 4,00 HOLE DEPTH: Through All
A2	156,25	0,00	
A3	263,75	0,00	
A4	371,25	0,00	
A5	478,75	0,00	
A6	586,25	0,00	
B1	102,50	0,00	M3x0.5 - 6H HOLE DEPTH: 10mm
B2	210,00	0,00	
B3	317,50	0,00	
B4	425,00	0,00	
B5	532,50	0,00	

SCALA 1:2

Designed by:	e-mail:	Tel:	Data
Dott. Oscar Azzolini, Ing. Antonio Carabillò	oscar.azzolini@lnl.infn.it	049-8068665	15/06/2018
	Material	Note:	Numero pezzi:
	Alluminium	A3 Format Sheet	1
 Istituto Nazionale di Fisica Nucleare			Edizione
Grounded Shield			4 / 8

GROUNDING SHIELD (BOTTOM PART) short parts

number of the part: 2



HOLE TABLE			
HOLE	QUOTA X	QUOTA Y	DESCRIPTION
A1	5,00	0,00	M3x0.5 - 6H HOLE DEPTH: 10mm
A2	88,00	0,00	
A3	171,00	0,00	
B1	46,50	0,00	Ø3,30 THRU └─┘ Ø7,00 ▽ 4,00 HOLE DEPTH: Through All
B2	129,50	0,00	

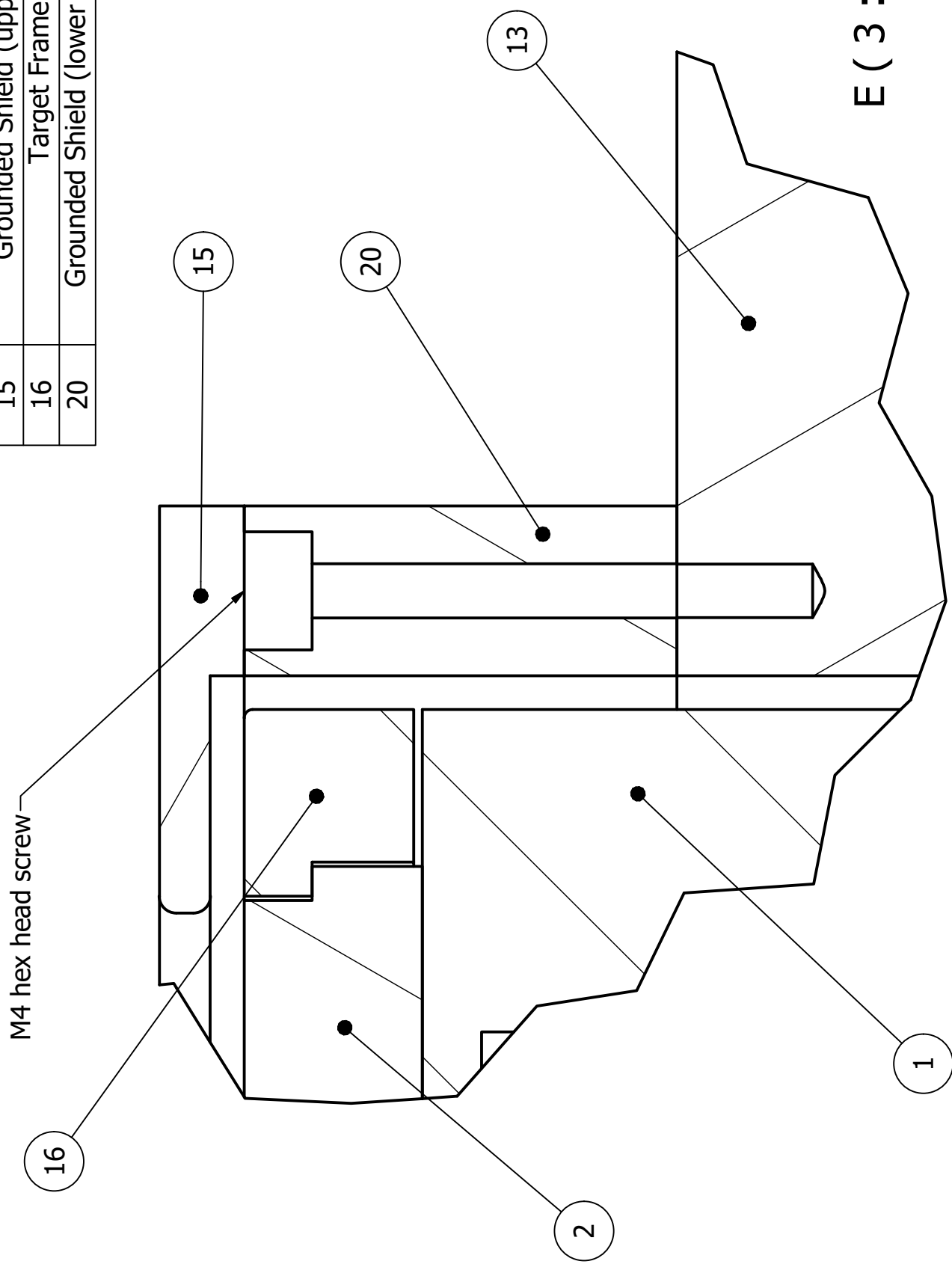
SCALA 2:1

Designed by:	e-mail:	Tel:	Data
Dott. Oscar Azzolini, Ing. Antonio Carabillò	oscar.azzolini@lnl.infn.it	049-8068665	15/06/2018
	Material	Note:	Numero pezzi:
	Alluminium	A3 Format Sheet	1
	Grounded Shield		Edizione
			Foglio
			5 / 8

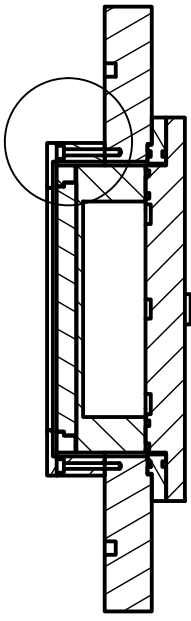
GROUNDING SHIELD UNWELDED VERSION

NOTE: how to connect the shield on the adapter flange.

TABLE	
1	Copper Cover
2	Target
13	Adapter Flange
15	Grounded Shield (upper part)
16	Target Frame
20	Grounded Shield (lower long part)



SCALA 1:4



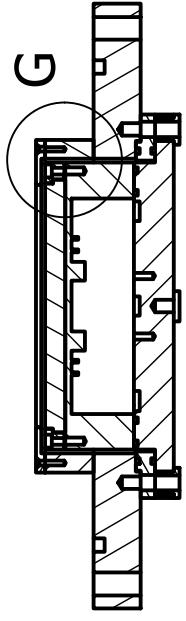
D-D (1:4)

Designed by:	Dott. Oscar Azzolini, Ing. Antonio Carabillò	e-mail:	oscar.azzolini@lnl.infn.it	Tel:	049-8068665	Data	15/06/2018
		Material	Alluminium	Note:	A3 Format Sheet	Numero pezzi:	1
			Grounded Shield			Edizione	6 / 8

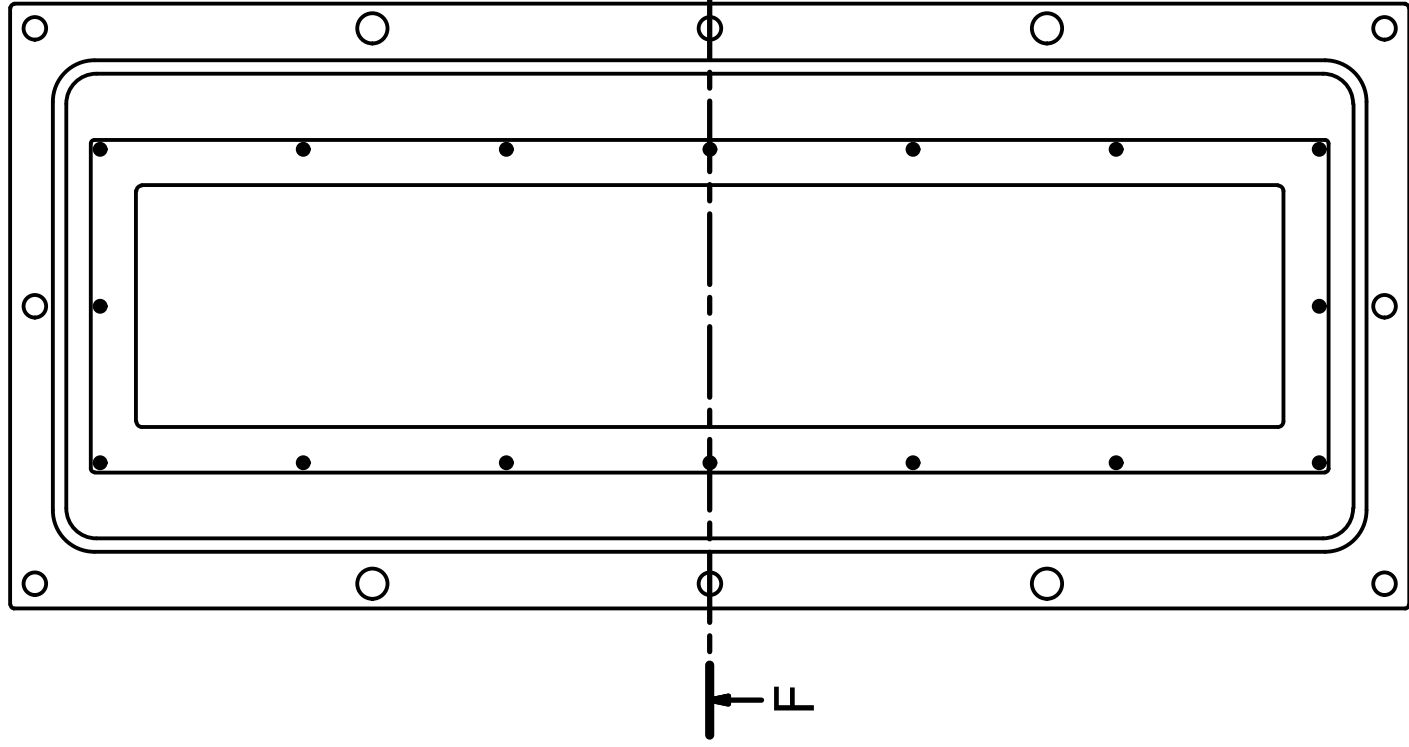


GROUNDING SHIELD UNWELDED VERSION

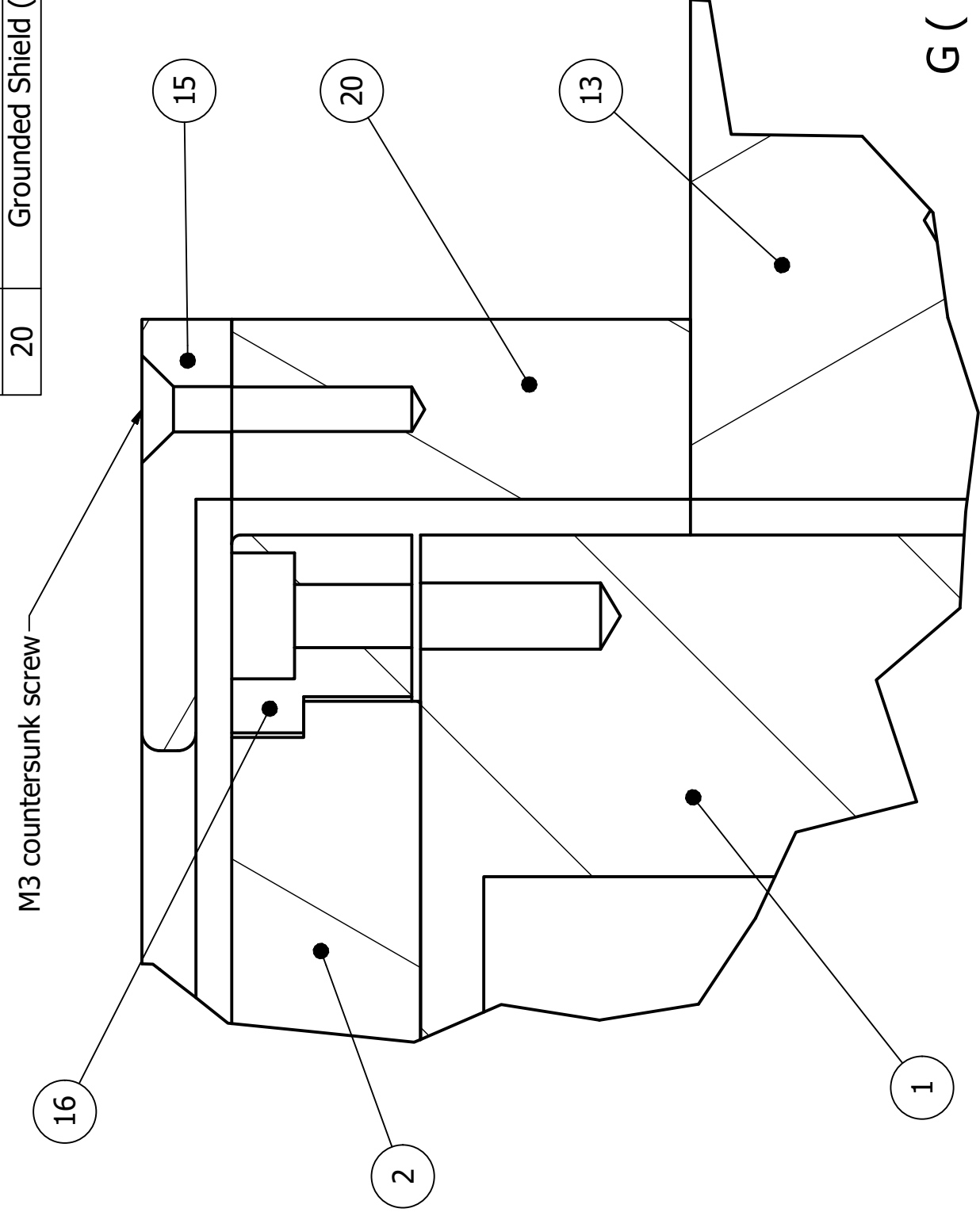
NOTE: how to connect the two parts of the shield.



F-F (1 : 4)



M3 countersunk screw



G (3 : 1)

TABLE

1	Copper Cover
2	Target
13	Adapter Flange
15	Grounded Shield (upper part)
16	Target Frame
20	Grounded Shield (lower long part)

Designed by:

Dott. Oscar Azzolini, Ing. Antonio Carabillò

e-mail:

oscar.azzolini@lnl.infn.it

Tel:

049-8068665

Material

Alluminium

Note:

A3 Format Sheet

Data

15/06/2018

Numero pezzi:

1

Edizione

7 / 8

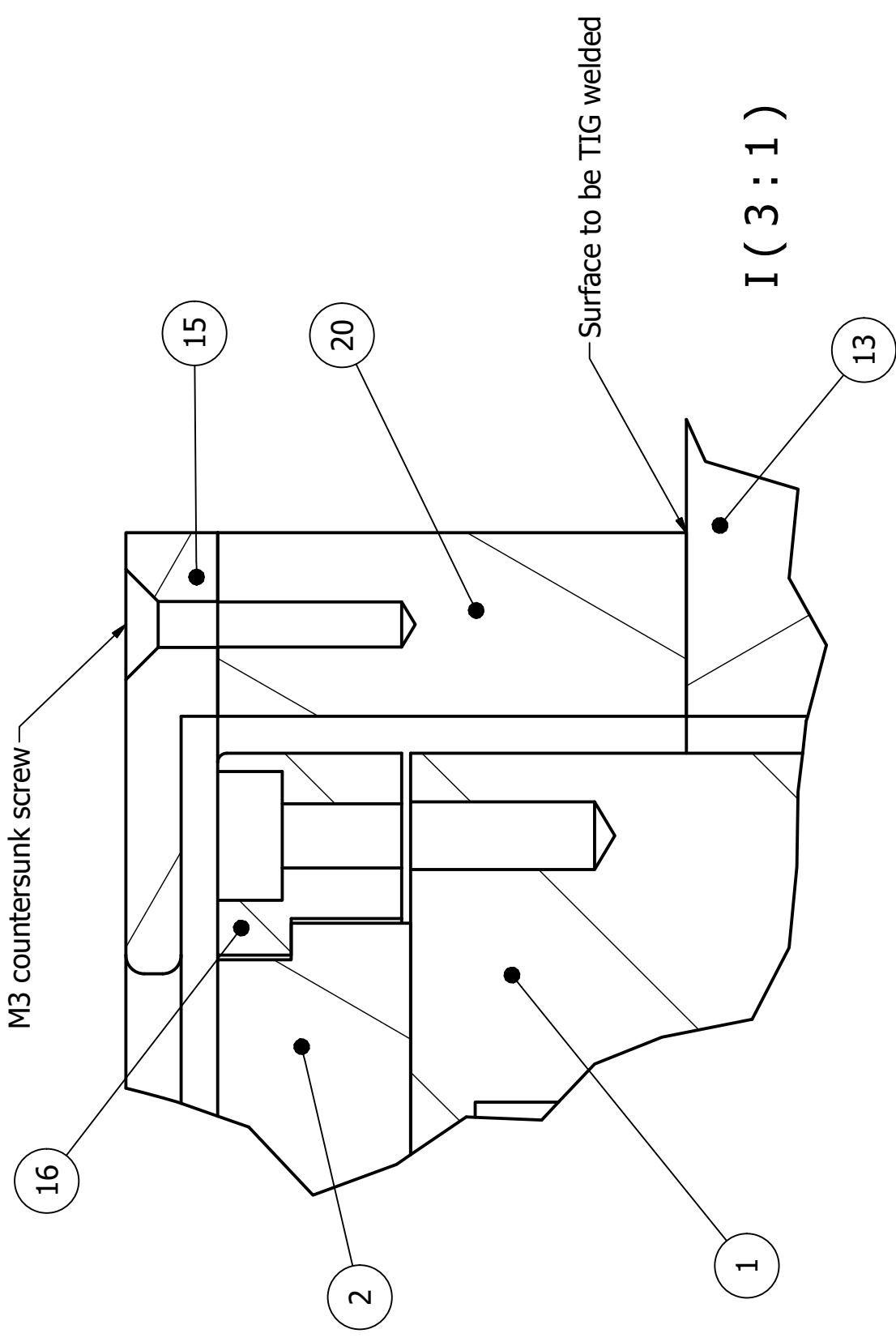
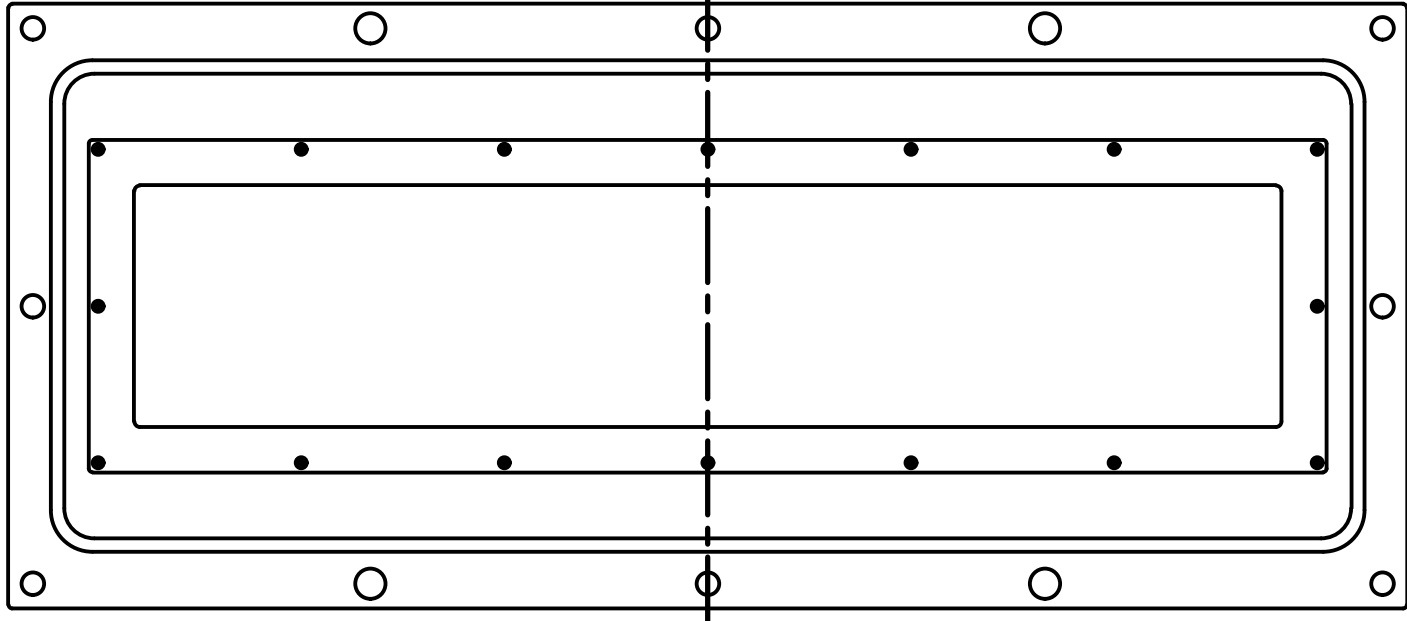
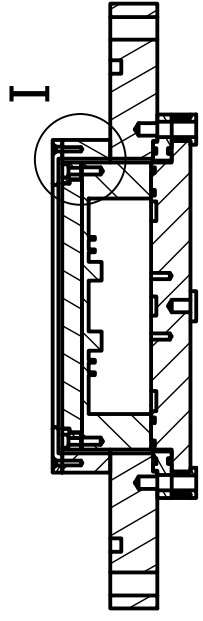
SCALA 1:4




GROUNDING SHIELD WELDED VERSION

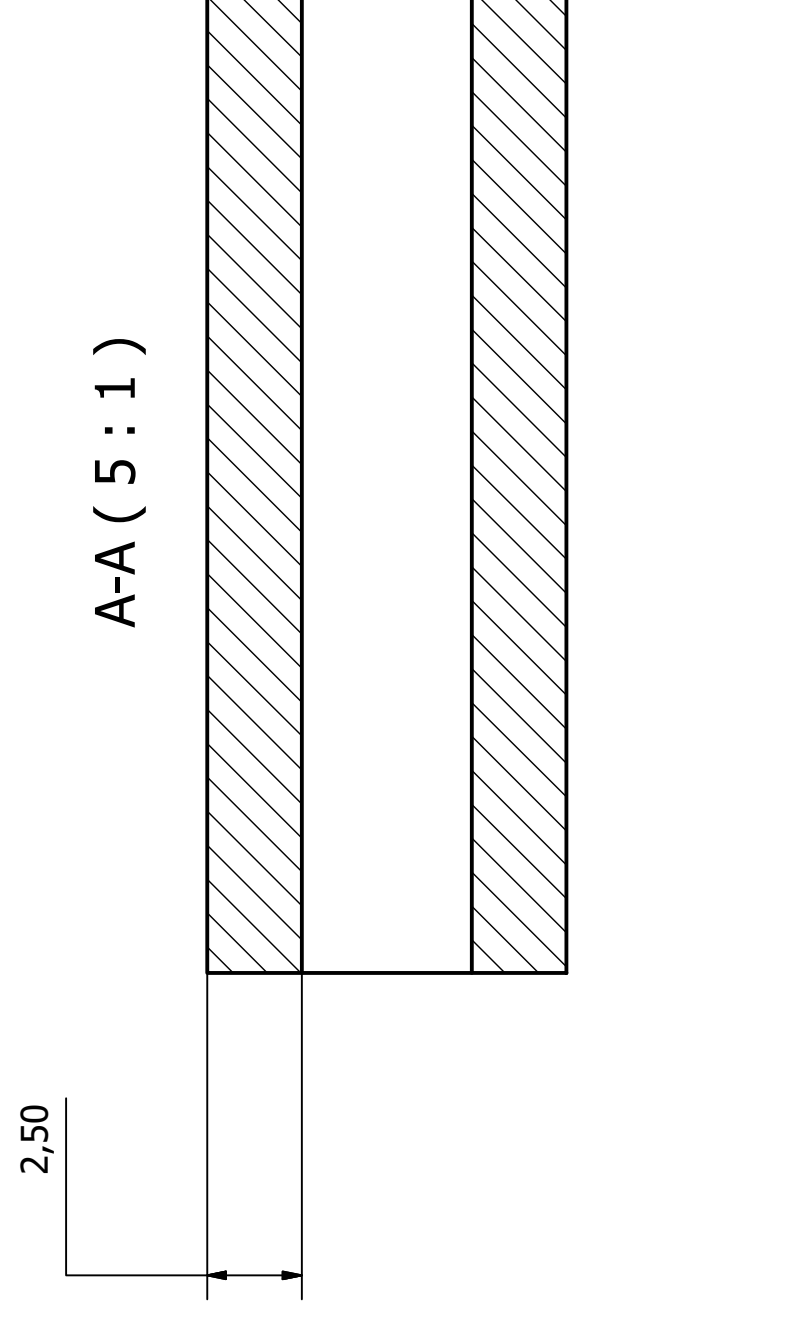
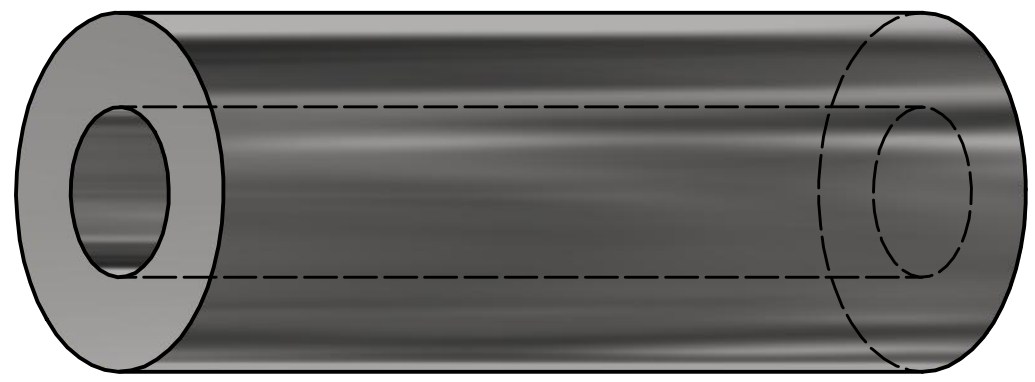
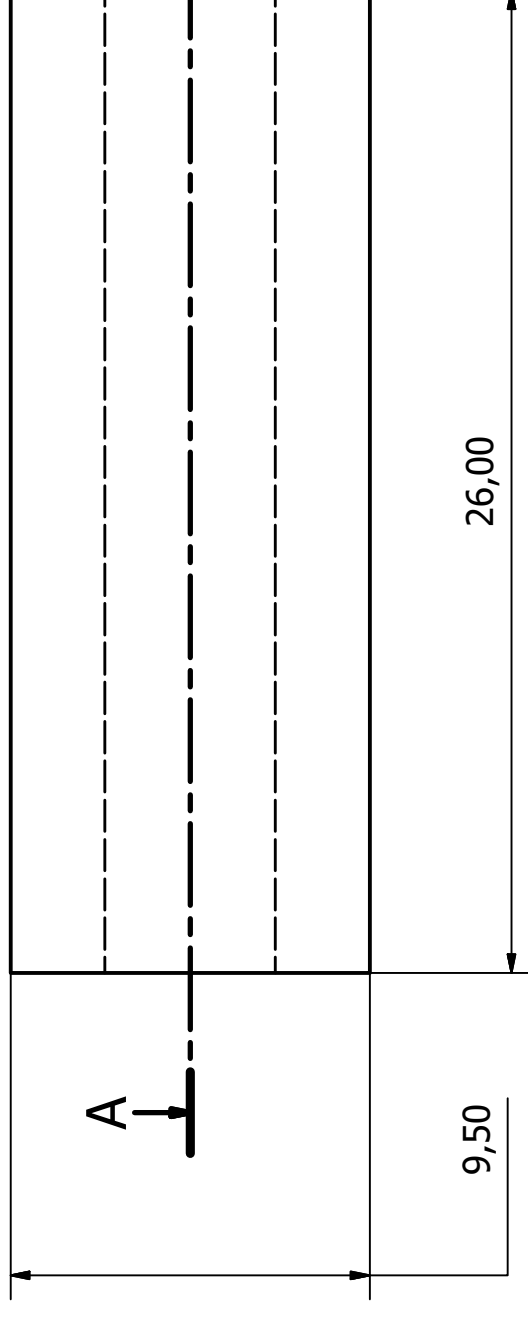
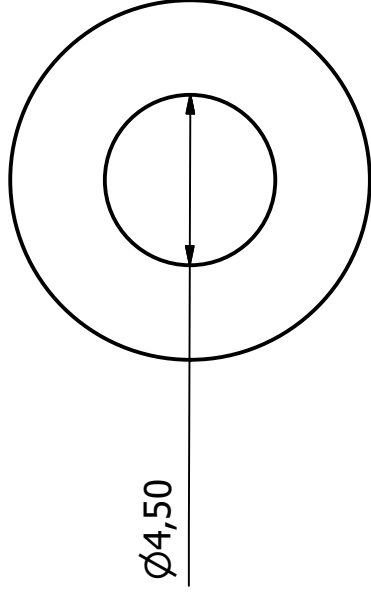
NOTE: the base of the shield is TIG welded on the adapter flange.

TABLE	
1	Cathode body
2	Target
13	Insulating Flange
15	Ground Shield
16	Target Frame
20	Ground Shield




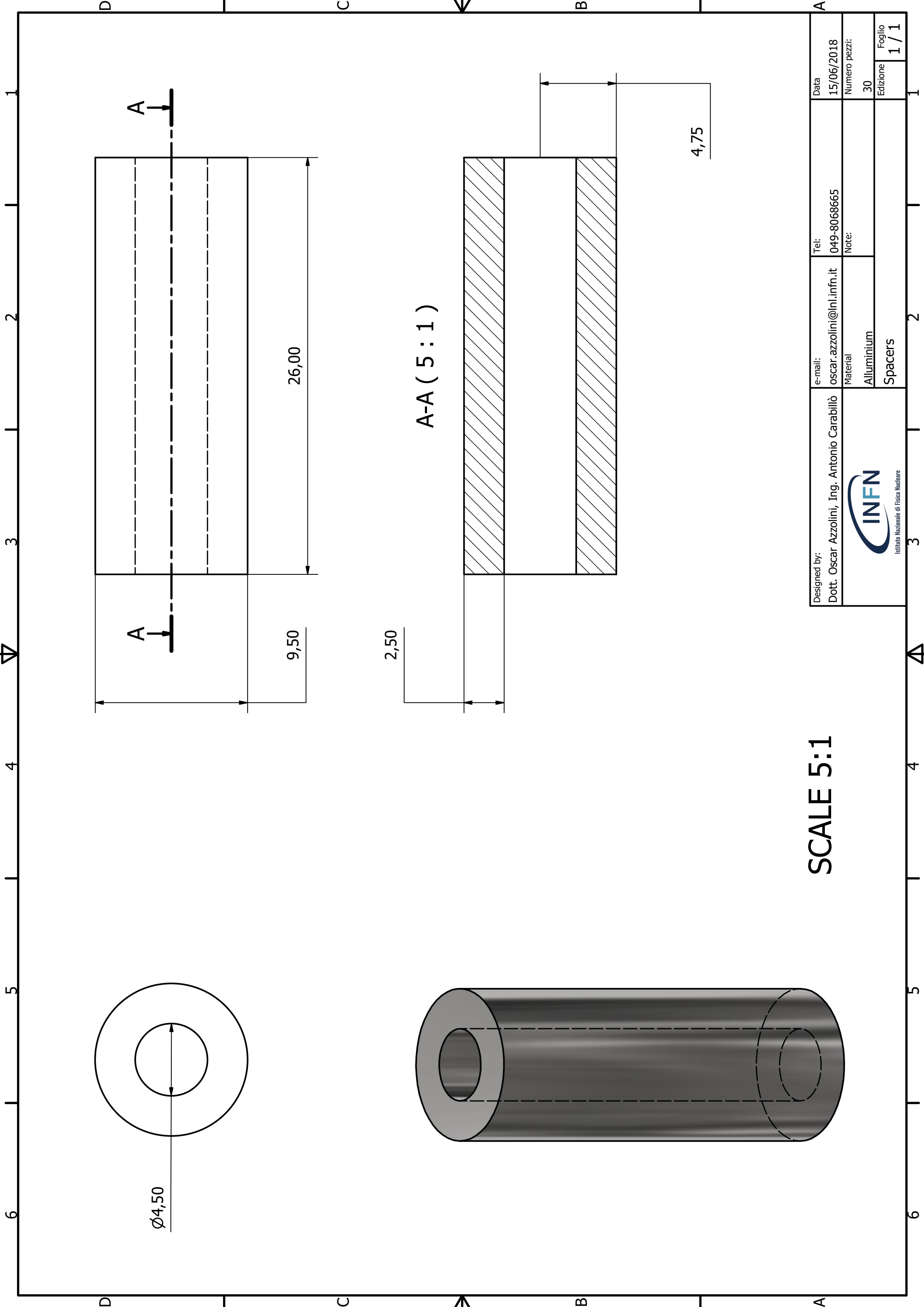
SCALA 1:4

Designed by: Dott. Oscar Azzolini, Ing. Antonio Carabillò	e-mail: oscar.azzolini@lnl.infn.it	Tel: 049-8068665	Data 15/06/2018
 Istituto Nazionale di Fisica Nucleare	Material Alluminium	Note: A3 Format Sheet	Numero pezzi: 1
	Grounded Shield		Edizione 8 / 8



SCALE 5:1

Designed by: Dott. Oscar Azzolini, Ing. Antonio Carabillò	e-mail: oscar.azzolini@lnl.infn.it	Tel: 049-8068665	Data 15/06/2018
	Material Alluminium	Note:	Numero pezzi: 30
 Istituto Nazionale di Fisica Nucleare			Edizione 1 / 1





Dottorati di ricerca

Il tuo indirizzo e-mail

oscar.azzolini@unife.it

Oggetto:

Dichiarazione di conformità della tesi di Dottorato

Io sottoscritto Dott. (Cognome e Nome)

Azzolini Oscar

Nato a:

Bassano del Grappa

Provincia:

Vicenza

Il giorno:

27/04/1979

Avendo frequentato il Dottorato di Ricerca in:

Fisica

Ciclo di Dottorato

32

Titolo della tesi:

RESEARCH ON THIN FILM HARD MATERIALS AND DEVELOPMENT OF A NON-COMMERCIAL PHYSICAL VAPOR DEPOSITION SYSTEM FOR THE COATING OF TUNGSTEN CARBIDE WIRE ROLLS

Titolo della tesi (traduzione):

Tutore: Prof. (Cognome e Nome)

Fiorentini Giovanni

Settore Scientifico Disciplinare (S.S.D.)

Parole chiave della tesi (max 10):

PVD, Sputtering, CVA, Hard coatings

Consapevole, dichiara

CONSAPEVOLE: (1) del fatto che in caso di dichiarazioni mendaci, oltre alle sanzioni previste dal codice penale e dalle Leggi speciali per l'ipotesi di falsità in atti ed uso di atti falsi, decade fin dall'inizio e senza necessità di alcuna formalità dai benefici conseguenti al provvedimento emanato sulla base di tali dichiarazioni; (2) dell'obbligo per l'Università di provvedere al deposito di legge delle tesi di dottorato al fine di assicurarne la conservazione e la consultabilità da parte di terzi; (3) della procedura adottata dall'Università di Ferrara ove si richiede che la tesi sia consegnata dal dottorando in 2 copie, di cui una in formato cartaceo e una in formato pdf non modificabile su idonei supporti (CD-ROM, DVD) secondo le istruzioni pubblicate sul sito : <http://www.unife.it/studenti/dottorato> alla voce ESAME FINALE – disposizioni e modulistica; (4) del fatto che l'Università, sulla base dei dati forniti, archiverà e renderà consultabile in rete il testo completo della tesi di dottorato di cui alla presente dichiarazione attraverso l'Archivio istituzionale ad accesso aperto "EPRINTS.unife.it" oltre che attraverso i Cataloghi delle Biblioteche Nazionali Centrali di Roma e Firenze. DICHIARO SOTTO LA MIA RESPONSABILITA': (1) che la copia della tesi depositata presso l'Università di Ferrara in formato cartaceo è del tutto identica a quella presentata in formato elettronico (CD-ROM, DVD), a quelle da inviare ai Commissari di esame finale e alla copia che produrrà in seduta d'esame finale. Di conseguenza va esclusa qualsiasi responsabilità dell'Ateneo stesso per quanto riguarda eventuali errori, imprecisioni o omissioni nei contenuti della tesi; (2) di prendere atto che la tesi in formato cartaceo è l'unica alla quale farà riferimento l'Università per rilasciare, a mia richiesta, la dichiarazione di conformità di eventuali copie. PER ACCETTAZIONE DI QUANTO SOPRA RIPORTATO

Dichiarazione per embargo

12 mesi

Richiesta motivata embargo

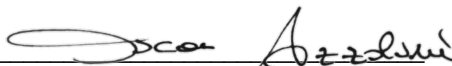
2. Tesi previo accordo con terze parti

Liberatoria consultazione dati Eprints

Consapevole del fatto che attraverso l'Archivio istituzionale ad accesso aperto "EPRINTS.unife.it" saranno comunque accessibili i metadati relativi alla tesi (titolo, autore, abstract, ecc.)

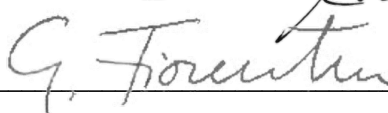
Firma del dottorando

Ferrara, li 20/20/2019 (data) Firma del Dottorando

A handwritten signature in black ink, appearing to read "D. Scari", written over a horizontal line.

Firma del Tutore

Visto: Il Tutore Si approva Firma del Tutore

A handwritten signature in black ink, appearing to read "G. Fiorentin", written over a horizontal line.